Observing air pollution variability with climate change and environmental injustice

Mary Angelique G. Demetillo
Union, New Jersey

B.S. Physics, Seton Hall University, 2017

A Dissertation presented to the Graduate Faculty
Of the University of Virginia in Candidacy for the Degree of
Doctor of Philosophy

Department of Environmental Sciences

University of Virginia
January 2023

Committee Members:
Professor Sally E. Pusede
Professor Xi Yang
Professor Jim Galloway
Professor Kimberly Fields

Abstract. Tropospheric ozone (O_3) and nitrogen dioxide (NO_2) are U.S. Environmental Protection Agency-designated criteria air pollutants regulated to protect human health and public welfare. While air pollution levels have decreased across the U.S., and in many cities around the world, there are still major uncertainties in the sources, the processes affecting their spatiotemporal variability, and their impacts. Climate change will alter many controls over the abundance and distribution of these pollutants, especially for O_3, such that air quality may vary differently in the future than the past. Primary pollutants such as NO_2 are very highly spatially heterogeneous, and their impacts are unequally distributed, with communities of color and low-income communities disproportionately affected in U.S. cities. In this dissertation, I present a landscape-scale analysis of severe drought impacts on O_3 chemistry in California; an evaluation of measurements of the recently-launched satellite sensor, the TROPospheric Ozone Monitoring Instrument (TROPOMI), to resolve NO_2 spatiotemporal variability between neighborhoods in Houston, Texas; and observational constraints on the contribution of diesel engine emissions to NO_2 inequalities in 52 U.S. cities. I found prolonged severe drought conditions impacted O_3 pollution in California by shifting O_3 production to become more NO_x suppressed and decreasing O_3 loss through dry deposition. I show relative NO_2 inequalities measured by TROPOMI combined with a physics-based oversampling algorithm are comparable to those from higher resolution aircraft sensor GCAS. Finally, I find diesel emissions are a large driver of NO_2 inequality in U.S. cities but decreasing these emissions completely would not eliminate air pollution inequality.

Table of Contents

List of tables

List of figures

Acknowledgements

I would first like to express my utmost gratitude to Sally Pusede for this incredible opportunity to have learned from and trained under her mentorship and guidance. Thank you for all the patience, encouragement, confidence, and wisdom in my professional and personal development. I am a better person for it, and I hope to honor your time and efforts in my future endeavors.

I thank my committee members, Jim Galloway, Xi Yang, and Kim Fields for their insight and support. I also thank Dr. Amélie Berger, Chris So, Kinsey Tedford, Solianna Herrera, Laura Barry, Andrew Jablonski, Madeline Miles, and Marion McKenzie for being my home and family in Charlottesville; I am tremendously grateful for growing alongside you all in this journey and am looking forward to crossing paths again.

Gusto ko din, magpasalamat sa pamilya ko dito sa US at sa Pilipinas. Iginagalang ko ang mga skripisyong lumikha ng pagkakataon para magawa ko ito. Salamat kay Nanay at Tatay ko sa pagtitiwala sa akin para ityloy ang pagkakataong ito. Salamat din sa Mark at Chrissy sa pagpananatiling nakaugat at naka-ground sa akin sa prosesong ito. Para sa atin barangáy.

The data used in Chapter 2 was partially provided by the Airborne Research Program (SARP), National Suborbital Research Center (NSRC), and the NASA Airborne Science Program (ASP). SEP was supported by NASA grant NNX16AC17G. I also acknowledge the U.S. Environmental Protection Agency, California Air Resources Board, and San Joaquin Valley Air Pollution Control Board for use of the publicly available isoprene, O_3, NO_2*, temperature, and wind measurements.

The work in Chapter 3 was funded by the University of Virginia (UVA) Office of Sustainability, UVA Data Sciences Institute Presidential Fellowship, a Virginia Space Grant Consortium Graduate Research Fellowship, a NASA Future Investigator NASA Earth and Space Science and Technology (FINESST) award, the UVA Department of Environmental Sciences Hart Family Undergraduate Research Fellowship. I thank Andrew Weinheimer for use of the NASA P-3B NO and NO_2 measurements, John Barrick for use of the NASA P-3B potential temperature data, and Xi Yang for assistance processing the Landsat 8 imagery.

The work in Chapter 4 was funded by a NASA New Investigator Program in Earth Science (20-NIP20-0056), an NSF Career Award (AGS 2047150), the NASA FINESST Graduate Research Fellowship and the Virginia Space Grant Consortium (19-EARTH20-0242). I also acknowledge the FIVE18-19 mobile source inventory was developed with support from NOAAA NRDD Project 19533.

Chapter 1: Introduction

Air quality has improved in the U.S. over the last several decades because of regulations under the U.S. Clean Air Act.[1, 2] However, there still exist inequalities in the distribution of air pollution, alongside associated health impacts, which disproportionately affect communities of color and people with lower socioeconomic status.[3, 4] Climate-change-influenced atmospheric conditions such as air temperature and stagnation have the potential to worsen air pollution in the future, adversely affecting people through their associated health-impacts.[5] Developing effective future air pollution regulatory strategies must therefore consider both environmental injustice and climate change.

Tropospheric ozone (O_3) is a greenhouse gas, an oxidant, and a harmful air pollutant to plants and people, resulting in premature death and chronic and acute respiratory ailments, even when levels are well below the current National Ambient Air Quality Standard (NAAQS) of 70 ppb in eight hours.[6] O_3 is photochemically formed in the atmosphere with a nonlinear dependence on the abundance and chemical reactivity of nitrogen oxides ($NO_x \equiv NO + NO_2$) and volatile organic compounds (VOCs). The abundance of these O_3 precursors have a documented temperature dependence that impact O_3 production.[7]

NO_x drives O_3 production, broadly controls the tropospheric oxidative capacity, and has been linked to adverse health effects largely in respiratory and cardiovascular systems.[8, 9] NO_x sources comprise combustion processes, including those associated with traffic, goods transport, industrial activities, and electricity generation. Substantial changes NO_x emissions have been shown to alter NO_2 chemical lifetime in urban plumes, shifting the dominant chemistry of cities.[10] Even though abundances and lifetime of NO_2 have changed, the unequal NO_2 burden with U.S. cities persists.[11]

The goal of this dissertation is to provide further understanding of the impact of two prominent issues on air quality: climate change and environmental injustice. This dissertation presents observational analyses (1) investigating the impacts of severe drought on the chemical production and loss of O_3 in California, (2) assessing the ability of next-generation, improved-spatial-resolution satellite measurements to resolve NO_2 spatiotemporal variability between neighborhoods of different race-ethnicities and income; and (3) observationally constraining the contribution of diesel vehicle emissions to NO_2 inequality across major U.S. cities.

In Chapter 2, I present a multiyear observational analysis using data collected before, during, and after the record-breaking California drought (2011–2015) at the O_3-polluted locations of Fresno and Bakersfield near the Sierra Nevada foothills. Drought conditions affect O_3 air quality, potentially altering multiple terms in the O_3 mass balance equation. Here, I separately assess drought influences on O_3 chemical production (PO_3) from O_3 mixing ratio. I show that mixing ratios of isoprene, a source of O_3-forming organic reactivity, were relatively insensitive to early drought conditions, but decreased by more than 50% during the most severe drought years (2014–2015). I find drought-driven isoprene effects are temperature dependent, even after accounting for changes in leaf area, consistent with laboratory studies but not previously observed at landscape scales with atmospheric observations. Drought-driven decreases in organic reactivity are cotemporaneous with a change in dominant oxidation mechanisms, with PO_3 becoming more NO_x-suppressed, leading to a decrease in PO_3 of ~20%. I infer reductions in atmospheric O_3 loss of

~15% during the most severe drought period, consistent with past observations of decreases in O_3 uptake by plants. I consider drought-related trends in O_3 variability on synoptic timescales by analyzing statistics of multiday high O_3 events. Finally, I discuss implications for regulating O_3 in Central California and other locations in a future where drought conditions are more prevalent.

In Chapters 3 and 4, I focus on advancing analytical techniques for describing the distribution of NO_2. NO_x ($\equiv NO + NO_2$) is predominantly emitted by anthropogenic combustion, and urban NO_2 abundances co-locate with traffic, power generation, and industrial facilities. NO_2 exhibits steep spatial gradients, and the impacts of NO_2 are heterogeneously distributed and temporally variable at neighborhood scales. We have historically lacked the observations required to describe NO_2 pollution and capture this variability. Recent remote-sensing advancements offer the potential to map intraurban NO_2 levels and provide improved constraints on the NO_2 inequalities experienced by low-income communities and communities of color in U.S. cities.

In Chapter 3, I analyze novel high-spatial-resolution (250 m x 500 m) NO_2 vertical columns measured by the NASA GeoCAPE Airborne Simulator (GCAS) as part of the September-2013 NASA DISCOVER-AQ mission over Houston, Texas, and discuss differences in population-weighted NO_2 at the census-tract scale. Based on the average of 35 repeated flight circuits, I find 37 ± 6% higher NO_2 for people of color living in low-income tracts compared to white residents of high-income tracts, and report NO_2 disparities separately by race-ethnicity (11–32%) and poverty status (15–28%). I observe substantial time-of-day and day-to-day variability in NO_2 differences, driven by the greater prevalence of NO_x emission sources in neighborhoods where residents are people of color and have lower household incomes. I evaluate measurements from the recently launched satellite-based TROPospheric Ozone Monitoring Instrument (TROPOMI), averaged to 0.01° x 0.01° using physics-based oversampling. I demonstrate that TROPOMI resolves similar relative, but not absolute, tract-level differences compared to GCAS. I utilize the Fuel-based Inventory for Vehicle Emissions and National Emissions Inventory NO_x inventories, plus one year of TROPOMI weekday-weekend variability, to attribute tract-level NO_2 disparities to industrial sources and heavy-duty diesel trucking. I show GCAS and TROPOMI spatial patterns correspond to surface patterns measured using aircraft profiling and surface monitors. To conclude, I discuss opportunities for satellite remote sensing to inform decision-making generally.

In Chapter 4, I use observations from TROPOMI to describe NO_2 inequalities with race, ethnicity, and income in 52 U.S. cities over June 2018–February 2020. I report average city-level census tract-scale NO_2 differences of 17 ± 2% higher for Black and African Americans, 19 ± 2% higher for Hispanics/Latinos, 12 ± 2% higher for Asians, and 15 ± 2% higher for Native Americans compared to non-Hispanic/Latino whites; and 17 ± 2% higher for people living below and 10 ± 2% near the poverty line compared to those living above. When combining race-ethnicity and income, NO_2 was 28 ± 2% higher for people of color living in low-income tracts compared to non-Hispanic white residents in high income census tracts, with many populous cities experiencing even greater inequalities. Using observations and inventories, I find diesel traffic is the dominant source of NO_2 inequalities and a 62% reduction in diesel emissions would decrease race-ethnicity and income inequalities by 37%. I add evidence that TROPOMI resolves tract-scale NO_2 differences using relationships with urban segregation patterns and column-to-surface correlations.

In Chapter 5, I synthesize the results of this dissertation and present recommendations for future work.

Chapter 2: Observing Severe Drought Influences on Ozone Air Pollution in California

Adapted from: Demetillo, M. A. G., Anderson, J. F., Geddes, J. A., Najacht, E., Herrera, S. A., Kabasares, K., Kotsakis, A., Yang, X., Lerdau, M T., and Pusede, S. E.: Observing severe drought influences on ozone air pollution in California, *Environ. Sci. Technol.,* 5, *39,* 4695–4706, doi:10.1021/acs.est.8b04852, **2019.**

2.1 Introduction

Climate change is expected to increase the frequency and severity of drought in the future.[12-16] Drought conditions can potentially affect air quality, including concentrations of tropospheric ozone (O_3),[17-19] a harmful pollutant to humans, plants, and ecosystems.[20, 21] While effective future pollution control strategies will require improved understanding of drought-O_3 coupling, these influences are challenging to discern, as drought conditions alter multiple terms in the O_3 mass balance equation simultaneously: emission of biogenic O_3 precursors and chemical production rate (PO_3), chemical and depositional loss rate (LO_3), and change in O_3 concentration on synoptic timescales with atmospheric transport and mixing (Eq. 2.1).

$$\text{(E2.1)} \qquad \frac{\partial[O_3]}{\partial t} = PO_3 + LO_3 \pm \text{transport/mixing}$$

The response of any individual term in $\partial[O_3]/\partial t$ to drought may vary in sign and magnitude as a function of drought duration, drought severity, availability of non-rainwater sources, and PO_3 chemical regime. Moreover, because droughts may extend over multi-month to multiyear timescales, emissions regulations, seasonal patterns, and climatic events (e.g., El Nino Southern Oscillation) may confound interpretation, causing simultaneous variations in the $\partial[O_3]/\partial t$ terms influencing O_3 mixing ratios.

Past research has focused on two key drought-$\partial[O_3]/\partial t$ perturbations, decreased isoprene emissions as they affect PO_3 and reduced stomatal conductance with regard to LO_3. In many locations, plants emit the majority of O_3-forming organic compounds reactive with the hydroxyl radical (OH).[22-24] Isoprene is the most abundant source of organic OH reactivity in the terrestrial atmosphere,[25] a significant contributor to PO_3 in the summertime even in cities,[26] and among the most-studied biogenic reactive carbon species. Detailed laboratory studies have demonstrated that on timescales of hours to weeks, water deficits initially enhance isoprene emissions under mild drought,[27-29] but ultimately suppress isoprene fluxes under sustained, severe water stress.[7, 30] Both types of drought-isoprene response have been inferred at landscape scales[19, 31-35] and soil moisture (i.e. plant water status) has been found to control a major portion of the interannual variability in isoprene flux in many locations.[31]

Plant stomatal O_3 uptake is a major LO_3 pathway that is also drought sensitive.[36, 37] Drought lowers stomatal deposition rates because apertures close to prevent water loss via transpiration and because, at longer time scales, overall leaf area is reduced. Decreased LO_3 has been directly observed using O_3 flux measurements in the late summer/early fall in Mediterranean climates, when water-deficient conditions are prevalent, including the Sierra Nevada Mountains of California.[38-41] Chemical transport and chemistry-climate models, which allow isolation of LO_3 from $\partial[O_3]/\partial t$, have found that drought-driven LO_3 decreases may be large enough to enhance O_3

concentrations.[18, 42] Huang et al.[18] found monthly mean O_3 deposition velocities (v_d), where LO_3 to deposition equals $v_d[O_3]$, decreased over Texas forests during a 2011 drought leading to higher O_3 concentrations. In simulating the 1988 North American Drought, Lin et al.[32] reduced v_d by 35%, increasing O_3 concentrations and improving model-measurement agreement. By contrast, while Wang et al.[19] found elevated O_3 mixing ratios during drought periods, v_d was relatively insensitive to drought conditions.

In 2011–2015, California experienced the most severe drought over the 120-year observational record[16, 43, 44] and the last millennium.[45] During this period, California saw a historic combination of annual high temperatures[5] and precipitation deficits.[43, 44] California is also home to poor O_3 air quality, with many of the most O_3-polluted cities in the U.S. located in the state.[46] Here, I present observations of isoprene, O_3, and nitrogen dioxide concentrations before, during, and after the California drought (2002–2017) to investigate the influence of drought conditions on O_3 air quality. Data were collected in Central California in the San Joaquin Valley (SJV), with monitoring sites proximate to isoprene-emitting oak savanna regions in the Sierra Nevada Mountain foothills (Fig. 2.1). I combine interpretation of variability in interannual, weekday-weekend, and day-to-day O_3 concentrations to observationally distinguish effects temporally corresponding to drought on PO_3 from other influences on O_3 concentration. I infer changes in LO_3 and analyze multiyear trends in synoptic-timescale high O_3 events and meteorological variables. I discuss the implications of these results for regulating O_3 air pollution in a potentially more drought-prone future in Central California and in locations where isoprene dominates OH reactivity.

2.2 Observations

Isoprene mixing ratio data are 3-h integrated samples collected in pressurized stainless-steel canisters and analyzed offline by gas chromatography-flame-ionization-mass spectrometric detection with pre-concentration (EPA method code 177)[47] as part of the U.S. Environmental Protection Agency (EPA) Photochemical Assessment Monitoring Stations (PAMS) program. A near-continuous data record (2002–2017) for "Fresno" is reported at Clovis-N Villa Avenue (36.819°N, 119.716°W). I produce a "Bakersfield" record by combining isoprene observations at Shafter-Walker Street (35.503°N, 119.273°W) (2002–2010 and 2012–2017), Arvin Bear Mountain Boulevard (35.208°N, 118.776°W) (2002–2009), and Bakersfield Golden State Highway (35.386°N, 119.015°W) (2012–2017). In accordance with PAMS protocols, isoprene observations are made for three months each year during O_3 season, typically spanning June–September. At most sites, data collection occurred in June–August for the years 2002–2007, 2009, 2014 and in July–September for the years 2008, 2010–2013, 2015–2017, with exceptions: Shafter, 2012–2013 in June–August; Arvin, 2008 in June–August; and Arvin, 2002–2007 and 2009 in August–September. Isoprene data were downloaded from the U.S. Environmental Protection Agency (EPA) AQS Data Mart (https://aqs.epa.gov/api).

Hourly O_3 and NO_2* measurements are made by UV absorption and chemiluminescence, respectively, and provided to the public by the California Air Resources Board (CARB) (https://www.arb.ca.gov/aqmis2/aqdselect.php). NO_2* data have a well-known positive interference from higher nitrogen oxides,[48] which have been shown to add uncertainty to absolute, but not relative NO_2* concentrations.[49] This interference is acknowledged by using NO_2* rather than NO_2. "Fresno" data are the mean of available hourly observations from Clovis-N Villa Avenue, Skypark (36.842°N, 119.874°W), Drummond (36.706°N, 119.741°W), Fresno-Garland

(36.785°N, 119.773°W), and First Street (36.782°N, 119.773°W) stations (Fig. 2.1b). "Bakersfield" data are mean of available hourly measurements from Shafter-Walker Street, California Avenue (35.357°N, 119.063°W), and Edison (35.346°N, 118.852°W) stations (Fig. 2.1c). In Fresno, extremely elevated NO_2* mixing ratios were observed corresponding to the time period of the nearby Lion Fire (beginning 27 September 2017); these O_3 and NO_2* data were excluded from the analysis. In 2014, at California Avenue, NO_2* measurements prior to 16 September are missing; at Edison, NO_2* measurements prior to 24 July are either missing or were removed because of an apparent persistent negative offset. Hourly temperature, relative humidity, and winds (speed and direction) are also provided by CARB (https://www.arb.ca.gov/aqmis2/metselect.php). I use data from Clovis to represent Fresno. Full annual wind data are not available in Clovis in 2002, 2007, and 2008. In Bakersfield, I combine temperature records at California Avenue (2002–2012, 2015–2016) and Bakersfield Municipal Airport (35.332°N, 119.000°W) (2013–2014, 2017), where temperature measurements were well-correlated (r^2 of 0.99 for 2017 data).

The leaf area index (LAI) product is generated using satellite observations from the Moderate Resolution Imaging Spectrometer (MODIS) instruments and available for download as part of MOD15A2H Version 6. LAI (8-day intervals at 500 m resolution) was averaged for June–September over a series of rectangles that focus observations on the Sierra Nevada foothills adjacent to the Fresno and Bakersfield areas (Fig. A2.1).

2.3 Results and Discussion

2.3.1 Severe drought alters biogenic isoprene emissions and concentrations

A wide variety of plant species produce isoprene within the leaves by the protein isoprene synthase (IsoS) using carbon from the Calvin cycle as the primary carbon source.[50-52] Isoprene is emitted to the atmosphere as a function of sunlight, leaf temperature, leaf area, and species identity. Longer-term field studies indicate emissions are independent of stomatal conductance,[30, 53] while short-term greenhouse experiments suggest a weak dependence on stomatal conductance, attributed to reduced CO_2 uptake and internal CO_2 concentrations that are associated with enhanced isoprene emissions.[54] While drought stress immediately decreases plant photosynthetic activity, laboratory studies have found disproportionately smaller corresponding reductions in isoprene emission rates, implying non-photosynthetic carbon pools are available.[27, 52, 55-57] Severe and/or sustained drought conditions do lead to lower emissions, but only when these alternative pools are depleted[47] and IsoS activity is suppressed.[7] In laboratory studies, recovery is observed to be rapid following soil rewatering, with isoprene emissions temporarily exceeding pre-drought rates in some cases.[27, 29]

Isoprene mixing ratios have been measured in Central California for the last two decades. In Figs. 2.2–b, mean daytime (8 am–8 pm local time, LT) isoprene is shown throughout the pre-drought (2002–2010), early drought (2011–2013), severe drought (2014–2015), and post-drought (2016–2017) periods in Fresno and Bakersfield during O_3-season (June–September). Mixing ratios are enveloped by the 2σ summertime variability; standard mean error uncertainties are given in Table 1. Comparable trends with time are observed if months included in the averages are varied (June–August versus July–September). My categorization of the severe drought is consistent with Exceptional Drought (D4) classification by U.S. Drought Monitor[58] and the lowest Tulare Basin water-year (October–September) rainfall totals over the study period (Table 2.1).[59]

In Fresno, isoprene concentrations during the pre- and early drought were statistically indistinguishable (p = 0.362, Wilcoxon rank-sum test). During the severe drought, isoprene decreased by 54% from pre-drought levels. In the post-drought, isoprene concentrations recovered by 34%, amounting to a 39% return to pre-drought levels. In Bakersfield, predrought isoprene abundances were steady through 2012, but fell by 65% in 2013, suggesting drought-driven emissions decreases occurred earlier in the Southern Sierra Nevada foothills area than in Fresno. While isoprene mixing ratios in Fresno do not appear to decline in 2013, isoprene concentrations fell precipitously in August 2013 (not shown). In Bakersfield, isoprene decreased by an additional 29% during the severe drought. In the post-drought period, isoprene concentrations may have recovered by 16%, but differences between 2014–2015 and 2016–2017 are not significant to the 5% level (p = 0.112). Isoprene mixing ratios are a function of both emissions and chemical loss. When photochemistry is active (summer days), isoprene's loss rate ($k_{\mathrm{isoprene+OH}}$[OH][isoprene]) is proportional to the OH concentration. Isoprene exerts a positive feedback on its own lifetime, as decreased isoprene and consequent higher OH lead to faster isoprene loss rates and, hence, lower isoprene concentrations. As a result, observed differences in isoprene mixing ratio represent an upper bound on changes in isoprene emissions.

Isoprene emissions have a well-known temperature dependence,[25, 60, 61] with critical implications for PO_3 on hot days.[62] A recent laboratory experiment produced evidence that drought stress may alter this temperature dependence for at least weeks after rewetting.[7] They found that while photosynthetic rates rebound fully from drought stress across the range of atmospheric temperatures, IsoS recovery was temperature dependent, with full recovery of emission rates at lower temperatures, but only partial recovery at higher temperatures. The net result was that isoprene fluxes at high and low temperatures were comparable and the temperature dependence was no longer a simple monotonic relationship. While this complex temperature relationship has been seen at leaf and single plant scales previously,[7, 63] these results are the first to demonstrate this relationship at landscape scales.

Isoprene emissions also vary with available leaf area.[64] Plants suffering severe water deficits may reduce leaf area to prevent runaway embolism,[32, 65, 66] as hydraulic conductivity loss in the xylem can inhibit water delivery to leaves.[67] To separate drought effects on the isoprene-temperature response and plant leaf area, in Figs. 2.2c–d, I investigate the slope of correlation between daily maximum temperature and isoprene per unit LAI, where LAI is defined as the ratio of top-level leaf surface area relative to ground surface area over 2002–2017. The slope was derived using an ordinary least squares linear regression, as uncertainties in the y-dimension (isoprene) dominate uncertainties in the x-dimension (temperature). Individual correlation plots are shown in Figs. S2–S3, with on average 32 and 29 daily observations available per year in Fresno and Bakersfield, respectively (Table A2.1). In year 2008 in Fresno and 2010 in Bakersfield, insufficient dynamic range in the observations prevented determination of the slope (Figs. S2–S3).

In Fresno, I find the isoprene-temperature response was similar in the pre- and early drought periods. However, the slope of this correlation (isoprene/LAI versus temperature) fell by 55% during the severe drought, with no apparent post-drought recovery. In Bakersfield, the isoprene-temperature response decreased as early as 2012 (there were no measurements in 2011). During the severe drought, the slope of correlation was 47% lower than in the pre-drought period, with no rebound in 2016–2017. Figs. 2.2c–d are consistent with laboratory observations by Fortunati et al.,[19] offering the first landscape-scale evidence that severe drought alters the temperature dependence of isoprene emissions.

Although I do not find a tight correlation between isoprene and LAI (Fig. 2.3), similar trends in the isoprene temperature-dependence are observed for both isoprene/LAI and isoprene alone (Figs. 2.2c–d). Direct comparison of monthly mean isoprene mixing ratios and LAI suggest reduced isoprene emissions per unit leaf area, but no significant decrease in severe-drought LAI compared to pre-drought (Fig. 2.3). While our MODIS imagery averaging regions (Fig. A2.1) focus on the oak savanna, they also encompass agricultural fields and higher elevation pine forests, which may obscure drought-LAI effects on isoprene-emitting species specifically.[68] Therefore, the observed correlation is a lower bound on the isoprene-emitting LAI response to severe drought. However, congruent with our findings, canopy-scale isoprene emission studies of poplar (*Populus spp.*) demonstrated that as leaves die, the LAI-dependence of isoprene emission rates decline, and emissions become more sensitive to light and temperature.[69] As a constraint on isoprene variation with changes in photosynthesis, solar-induced chlorophyll fluorescence (SIF) observations from the satellite-based Global Ozone Monitoring Experiment-2 (GOME-2) would be a potentially a direct proxy for interannual trends photosynthetic activity;[70, 71] however, the sensor has experienced steady degradation over our study window preventing interpretation of drought impacts.[72]

2.3.2 Observational constraints on PO_3

PO_3 is a nonlinear function of the abundance of nitrogen oxides ($NO_x \equiv NO + NO_2$) and organic gases reactive with OH (Fig. 2.4). At low NO_x concentrations, increases in NO_x increase PO_3, as NO propagates radical recycling and drives PO_3. Under these conditions, organic reactivity to OH (e.g., isoprene) has little effect on PO_3. This chemical regime is known as NO_x-limited and O_3 can be regulated effectively through NO_x emission control. At high NO_x concentrations, NO_x increases reduce PO_3, as NO_2 reacts with OH, yielding closed-shell nitric acid and terminating radical propagation. This PO_3 regime is known as NO_x-suppressed, with organic emission reductions leading to decreased PO_3 and NO_x reductions leading to worsened O_3 pollution. Changes in organic reactivity not only affect PO_3 at higher NO_x levels, it also alters the NO_x concentration at which PO_3 is maximized (Fig. 2.4). Steady reductions in NO_x emissions over the past few decades in California[73] and across the U.S.,[74] have led to the prevalence of O_3 chemistry that is increasingly NO_x limited, which has been observed in Central California[75, 76] and cities U.S. wide.[77, 78]

Drought effects on the NO_x-dependence of PO_3 can be tested independently from the loss and mixing terms in $\partial[O_3]/\partial t$ (eq. 1) using the well-documented weekday-weekend experiment, which takes advantage of known day-of-week patterns in emissions of NO_x and organic reactivity to OH. In U.S. cities, NO_x concentrations have historically been much lower (40–60%) on weekends than weekdays due to reduced weekend traffic from heavy-duty diesel vehicles (HDDVs).[74, 79] HDDVs are a major source of NO_x emissions, although they comprise a small fraction (~3%) of the overall U.S. vehicle fleet.[80] Weekend NO_x decreases occur without equivalently large changes in organic reactivity to OH,[81] as HDDVs are a relatively small source of total organic reactivity emissions. This has been demonstrated to be true in Central California where there are abundant non-traffic organic emission sources.[82-84] When statistics are sufficient to minimize meteorological variability, observed weekday-weekend differences in the mixing ratio of O_x ($\Delta O_{x\ wd-we}$) trace a single PO_3

versus NO_x curve (i.e. constant organic reactivity with varying NO_x).[66] O_x ($O_x \equiv O_3 + NO_2$) includes the portion of O_3 temporarily stored as NO_2.

In 2007, the EPA established more stringent HDDV NO_x emission standards using NO_x selective catalytic reduction (SCR) technology.[85] HDDV regulations affect the weekday-weekend experiment, as reductions mostly occur on weekdays, causing diminishing weekday-weekend differences. HDDVs have long service lifetimes and slow fleet turnover; therefore, their NO_x control will take place gradually over decades. In California, HDDV NO_x reductions have been accelerated through statewide programs requiring all vehicle owners to retrofit or replace older engines with SCRs by 2023.[86] As a result, SCR-equipped vehicles represent a growing fraction of HDDVs on California roads.[87, 88] While there have been conflicting reports on the real-world efficiency and durability of SCRs,[89, 90] SCR-equipped HDDV fleet infiltration is suggested by decreases in weekday-weekend NO_2^* differences ($\Delta NO_2^*{}_{wd-we}$) in Central California (Table 1).

Trends toward smaller $\Delta NO_2^*{}_{wd-we}$ are also consistent with increases in the relative contribution of other non-HDDV weekday-weekend-independent NO_x emission sources, for example soils and fires, which are also drought dependent. Almaraz et al.[91] demonstrated that fertilized soils contributed almost half of NO_x emissions in late July–early August 2016 in Central California (Fresno, Tulare, and Kings counties) and increases in fire activity, and hence NO_x emissions, attributed to greater fuel aridity[92] and the lengthening of the summer fire season,[93] have been observed in the Western U.S. and California over the past several decades.

To investigate drought effects on PO_3 separately from effects on O_x mixing ratios, I present trends in $\Delta O_{x\ wd-we}$ during the pre- (2002–2010), early (2011–2013), severe (2014–2015), and post- (2016–2017) drought periods in Fresno and Bakersfield (Fig. 2.5). To account for simultaneous interannual changes in $\Delta NO_2^*{}_{wd-we}$, I normalize $\Delta O_{x\ wd-we}$ by $\Delta NO_2^*{}_{wd-we}$, which linearly approximates the derivative $\partial PO_3/\partial NO_x$, representing $\Delta O_{x\ wd-we}$ per 1 ppb change in NO_2^*. Comparison of $\Delta O_{x\ wd-we}$ / $\Delta NO_2^*{}_{wd-we}$ and $\Delta O_{x\ wd-we}$ indicates that lack of regard for decreasing $\Delta NO_2^*{}_{wd-we}$ would lead to an interpretation of PO_3 that is more NO_x-limited early in the record (in Fresno) and more NO_x-suppressed later on (in Fresno and Bakersfield) than is observed using $\Delta O_{x\ wd-we}$ / $\Delta NO_2^*{}_{wd-we}$. In Fig. 2.5a–b, $\Delta O_{x\ wd-we}$ / $\Delta NO_2^*{}_{wd-we}$ shown are afternoon (12–5 pm LT) hourly measurements during the June–September O_3 season. Weekdays are defined as Wednesday–Friday and weekends are Sunday to reduce memory effects of the previous day. Any drought influence over PO_3 will have occurred alongside longer-term PO_3 trends ascribed to anthropogenic emission controls. In Central California, NO_x emission controls have led to decreases NO_2^* concentrations (Table 2.1, Fig. A2.4) and increasingly NO_x-limited PO_3.[75, 76, 94, 95] This is evident in Figs. 5a–b as $\Delta O_{x\ wd-we}$/ $\Delta NO_2^*{}_{wd-we}$ increased from 1.7 ± 0.4 to 4.5 ± 0.6 during the pre-drought in Fresno and from 1.7 ± 0.5 to 6.7 ± 0.6 in Bakersfield; at the same time, NO_2^* decreased by ~35% in both locations.

In Fresno, during the early drought $\Delta O_{x\ wd-we}$ / $\Delta NO_2^*{}_{wd-we}$ continued to increase compared to the most recent pre-drought 3-year mean ratio (33%), while in Bakersfield $\Delta O_{x\ wd-we}$ / $\Delta NO_2^*{}_{wd-we}$ decreased by ~20% with respect to 2008–2010 $\Delta O_{x\ wd-we}$ / $\Delta NO_2^*{}_{wd-we}$. During the severe drought, $\Delta O_{x\ wd-we}$ / $\Delta NO_2^*{}_{wd-l}$fell in Fresno by 53% and in Bakersfield by 29% relative to early drought averages. Average post-drought $\Delta O_{x\ wd-we}$ / $\Delta NO_2^*{}_{wd-we}$ may have increased in Fresno by ~35% and decreased slightly by ~15% in Bakersfield compared to the severe drought period; however, differences are within uncertainties defined as 1σ standard mean errors. Trends in $\Delta O_{x\ wd-we}$ /

$\Delta NO_2*_{wd\text{–}we}$ imply PO_3 became more NO_x-suppressed (although was still NO_x-limited) during the severe drought in Fresno and early and severe drought in Bakersfield. From 2008 to 2017, weekend O_x mixing ratios were comparable, suggesting weekend PO_3 was sufficiently NO_x limited that drought did not perturb the chemical regime. A shift toward more NO_x-suppressed PO_3 can happen by either an increase in NO_x concentrations or by a decrease in organic reactivity to OH (Fig. 2.4). In Fresno and Bakersfield, afternoon (12–5 pm LT) NO_2* mixing ratios declined by 18% and ~35%, respectively, from 2008–2010 to 2014–2015. Downward NO_x trends were slower in Fresno, similar to U.S.-wide trends,[96] decreasing by just 6% between the early and severe drought compared to 30% in Bakersfield (Fig. A2.4). While there may be drought influences over NO_x concentrations, I do not attempt to quantify them here.

Taken together, trends in $\Delta O_{x\ wd\text{–}we}$/ $\Delta NO_2*_{wd\text{–}we}$ and NO_2* are consistent with a reduction in a substantial portion of the O_3-forming organic reactivity. Additionally, temporal changes in $\Delta O_{x\ wd\text{–}we}$ / $\Delta NO_2*_{wd\text{–}we}$ reflect observed trends in isoprene as a function of location, with lower isoprene mixing ratios observed earlier in Bakersfield than Fresno. Isoprene constitutes just a portion of the total organic reactivity to OH in the region,[97] and is known to make a small contribution in Bakersfield.[81] There are currently uncertainties in our knowledge of all specific molecules that comprise the organic reactivity regionally.[81, 84] These results offer evidence that an important fraction of this total reactivity is drought-sensitive and not produced as a simple function of photosynthetic carbon fixation.

A shift toward more NO_x-limited PO_3 caused by reduced organic reactivity requires that absolute PO_3 has also decreased (Fig. 2.4). Here, I approximate the change in PO_3 from the early to severe drought period (ΔPO_3), which I then use (with measured $[O_x]$) to solve eq. 1 for the coincident change in LO_3 + transport/mixing. I apply a known set of analytical equations (eqs. S1–S3) to calculate instantaneous PO_3.[97, 98] The analytical model is built on three assumptions: odd hydrogen ($HO_x \equiv OH + HO_2$) is conserved, peroxy nitrates are in steady state with radical precursors, and radical propagation dominates termination. These assumptions are valid when photochemistry is rapid, for example during hot summer days, and should be drought independent. The model first solves for OH concentration, followed by PO_3; a full description is provided in the SI. Inputs to the model are NO_2/NO_x, total organic reactivity to OH, air temperature, PHO_x, and the alkyl nitrate branching ratio (α). Following the temperature-dependent O_3 chemistry analysis in Bakersfield by Pusede et al.,[81] I derive values at 35°C of $NO_2/NO_x = 0.75$ and $PHO_x = 0.7$ ppt s^{-1} for both Fresno and Bakersfield. Because these terms are largely a function of O_3 concentration, they are likely similar in the two locations over 2002–2017. While there are observational constraints on pre-drought organic reactivity (at 35°C) in Bakersfield (7–12 s^{-1}),[72] I have no empirical knowledge of the reactivity in Fresno. For Fresno, I test the range of available data (7–25 s^{-1}), including those collected at the Blodgett Forest Research Station in the Sierra Nevada Mountains, which may not be entirely representative.[99] In Fresno, α was set equal 0.10 following Beaver et al.[100] for Sierra Nevada foothill Oak-influenced air parcels. In Bakersfield, α was set equal 0.03 following Pusede et al.[81] I did not vary PHO_x or α between the early and severe drought; however, both may be drought sensitive. While changes in PHO_x and α alter absolute ΔPO_3, they have a smaller effect on the PO_3 NO_x dependence than organic reactivity.[101, 102]

To estimate ΔPO_3, I first determine the decrease in total organic reactivity consistent with measured $\Delta O_{x\ wd\text{–}we}$ / $\Delta NO_2*_{wd\text{–}we}$ (an approximate of $\partial PO_3/\partial NO_x$), $\Delta NO_2*_{wd\text{–}we}$, and the observation that $\Delta PO_{3\ I} \approx 0$ (Figs. 2.4c–d). This step is necessary because while I know the change in isoprene concentration between early and severe drought (Fig. 2.2), I know neither isoprene's contribution to total organic reactivity nor the drought-sensitive portion of total, including unknown reactivity. Due to documented NO_2* inaccuracies, the weekend NO_x concentration is determined as the NO_x concentration at which $\Delta PO_{3\ I} \approx 0$ within a 0.5 ppb tolerance. I compute PO_3 with an initial (early-drought) total organic reactivity value in the range of 7–20 s^{-1} in Fresno and 7–12 s^{-1} in Bakersfield. I then estimate severe-drought PO_3 by varying "severe-drought" total organic reactivity (rounded to the nearest integer), optimizing agreement in observed $\Delta O_{x\ wd\text{–}I}$/ $\Delta NO_2{*}_{wd\text{–}we}$ and $\partial PO_3/\partial NO_x$ (Fig. A2.5). Calculated ΔPO_3 are weighted by one weekend day ($\Delta PO_{3\ I} \approx 0$) and three weekdays, mirroring our weekday-weekend analysis. Regardless of initial reactivity, results were generally consistent (Table A2.2). Severe-drought reductions in organic reactivity of 65–70% in Fresno and 25–30% in Bakersfield were required to match observations. Because I do not account for drought-related changes in PHO_x or α, calculated reactivity changes are an upper estimate, as they account for the full observed change in $\Delta O_{x\ wd\text{–}we}$ / $\Delta NO_2{*}_{wd\text{–}we}$. By comparison, isoprene mixing ratios decreased by 54% in Fresno and 29% in Bakersfield (Fig. 2.2). Trends in $\Delta O_{x\ wd\text{–}we}$ / $\Delta NO_2{*}_{wd\text{–}we}$ are consistent with increased OH concentrations during the severe drought, which would have also led to reductions in non-biogenic and/or drought-insensitive reactivity. In this way, I approximate that ΔPO_3 equals –25% in Fresno and –17% in Bakersfield.

2.3.3 Inferring drought influences over LO_3 and O_x synoptic time-scale variability

Despite large reductions in PO_3 between early and severe drought, O_x decreased by just 6% in both Fresno and Bakersfield (Table 1), indicating compensating changes in other terms in $\partial[O_3]/\partial t$. Lower severe-drought O_x mixing ratios compared to early drought were significant to the 1% level (Fresno, p = 0.010; Bakersfield, p < 0.001). Severe-drought O_x differences were also significant to the 1% level with respect to the early drought (p < 0.001) defined as 2008–2010 to reduce the influence of ongoing NO_x controls since 2002. While there were no ongoing direct LO_3 measurements in California, by solving the O_3 mass balance using the calculated change in PO_3 and treating drought-related changes in mixing effects on the O_3 concentration as negligible (discussion below), I infer estimates of the magnitude of drought LO_3 decreases.

In the surface boundary layer over vegetation, LO_3 is often dominated by chemical reactions between O_3 and biogenic alkenes ($LO_{3\ chemistry}$) and O_3 deposition through stomatal pores ($LO_{3\ deposition}$), [36, 38] although other nonstomatal processes may also be important. Using the isoprene concentration measurements, in Fresno I estimate a decrease in $LO_{3\ chemistry}$ between the early and most severe drought periods of less than 0.3 ppb O_3 day^{-1} ($k_{O3+isoprene} = 1.3\ x\ 10^{-17}$ cm^3 $molecules^{-1}$ s^{-1}; integrated over 12–5 pm). Long-term observations of reactive terpenes are not available; as an upper estimate, if drought similarly reduced other reactive organic gases in Fresno (by 0.45 ppb isoprene), and if these gases had an O_3 reaction rate similar to α-pinene ($k_{O3+\alpha\text{-pinene}} = 8.0\ x\ 10^{-17}$ cm^3 $molecule^{-1}$ s^{-1}), I would calculate that $LO_{3\ chemistry}$ changed by 1.5 ppb O_3 day^{-1} integrated over 24 h, contributing to a ~2.5% increase in O_x concentration. In Bakersfield, I estimate a decrease in $LO_{3\ chemistry}$ from the early to severe drought of 0.03 ppb O_3 day^{-1} due to decreased isoprene mixing ratios and of 0.2 ppb O_3 day^{-1} due to the same hypothetical reduction in other organic gases (0.06 ppb). This suggests a change in $LO_{3\ chemistry}$ during the severe drought of 0.5–3% in Fresno and <0.3% in Bakersfield.

The remainder of the drought-dependent change in LO_3 has been previously attributed to reduced $LO_{3\ \mathrm{deposition}}$ to vegetated canopies because of decreased stomatal conductance and leaf area.[18, 32, 37, 103, 104] Deposition to ground surfaces may also be suppressed during drought, as reduced resistance to soil deposition has been observed at lower relative humilities.[105] Using eq. 1, I estimate drought-driven changes in $LO_{3\ \mathrm{deposition}}$ (stomatal, cuticular, and to soil) of ~18% in Fresno and ~10% in Bakersfield, which are of the same magnitude as modeled changes over Texas forests, where drought led to $LO_{3\ \mathrm{deposition}}$ decreases of 5–15%.[32]

Some models predict drought will result in changes in surface wind speeds and synoptically-driven factors such as greater atmospheric stagnation[19, 106] leading to enhanced O_3 accumulation over multiple days[107, 108] and changes in surface mixing heights.[109] In Fresno and Bakersfield, I find slightly slower daytime (12–5 pm LT) surface wind speeds concurrent with drought years (Table 1). One effect would be to reduce the spatial extent of the upwind footprint. For example, the Clovis monitoring station is located at the eastern edge of the O_3-polluted SJV and 10.5 km northeast of downtown Fresno. Integrated over 6 h, early-drought and severe-drought wind speed differences (corresponding with ΔPO_3) amount to a 5% decrease in the mean upwind footprint. Because high O_3 concentrations are prevalent throughout the SJV,[66] small changes in the size of the source region are not expected to cause large variations in O_3 mixing ratios measured in Fresno or Bakersfield.

As a constraint on whether O_3 variation on synoptic timescales is influenced by drought conditions, I compare the severity, length, and total O_3 accumulation of ev_3 events during the pre-, early, severe, and post-drought periods (Table 1). O_3 events are identified as four or more consecutive days of increasing afternoon (12–5 pm LT) mean O_x mixing ratios during the June–September O_3 season with a 5% tolerance and leading to an O_x increase over the event of at least 10%.[110] Severity and accumulation are defined for each event as the slope of the O_x concentration versus day and the difference between the maximum and minimum measured O_x, respectively.

Through this method, in Fresno, event severity, length, and accumulation in the early ($p = 0.324$, $p = 0.639$, $p = 0.807$) and severe drought ($p = 0.635$, $p = 0.272$, $p = 0.871$) were statistically indistinguishable from the predrought period. While the ensemble event severity distribution is positively skewed over most of the time record, during 2014–2015 the distribution is approximately normal (Table 1). A reduction in the highest severity values, is consistent a reduction in PO_3 during severe-drought O_3 event. Likewise, in Bakersfield, differences in event severity, length, and accumulation in the early ($p = 0.450$, $p = 0.926$, $p = 0.431$) and severe drought ($p = 0.398$, $p = 0.898$, $p = 0.483$) from the predrought period were not significant at the 5% level. While O_3 variations on synoptic timescales (4–13 days over 2002–2017) do not appear to have changed significantly during the severe drought, drought conditions may have still exerted influence over synoptically-driven factors.

2.4 Air Quality Implications, Future O_3 Ecosystem Impacts

These results suggest drought-O_3 influences are both more complex than would be inferred from the atmospheric O_3 temperature and humidity dependence and are a function of drought severity and duration. This observational study, based on trace gas concentrations rather than flux measurements, is not sensitive enough to distinguish early drought-driven isoprene enhancements from interannual variability, but decreased isoprene under severe drought conditions (and with early drought in Bakersfield) is unambiguous. Oak trees are drought tolerant,[111, 112] in part due to their ability to manage water resource limitation[113] and access groundwater through deep root systems;[114] however, the limits of their drought resilience are not entirely known.[113] I find conditions in the Sierra Nevada foothills region in Central California during the California drought were sufficiently severe to suppress isoprene emissions regionally. While isoprene mixing ratios rebounded partially in Fresno (~35%) and possibly in Bakersfield (~15%) in 2016–2017, recovery was impaired at higher atmospheric temperatures. I anticipate results derived in Central California should apply to other ecosystems with isoprene-emitting drought-prone vegetation. While O_3-temperature correlations are often presupposed, in many locations, this correlation is caused by the temperature dependence emissions of biogenic organic reactivity to OH, including isoprene.[62]

Decreased isoprene emissions will alter O_3 plant and ecosystem impacts, as isoprene reduces stresses from O_3 pollution.[115] Isoprene and other biogenic alkenes act as within-leaf chemical sinks of oxidants, including O_3, preventing a variety of O_3 plant injuries[116] and suggesting greater O_3 sensitivity for ecosystems post-drought. However, while Sierra Nevada trees can live for hundreds of years, high O_3 concentrations in the western Sierra Nevada Foothills, which are common during drought and non-drought years, are only a decades-old phenomenon. The combination of serious O_3 pollution and wide-spread tree death, initiates a landscape scale experiment on O_3 influences over plant community dynamics. There is laboratory evidence that elevated atmospheric O_3 affects plant development and growth, including delayed starch biosynthesis, greater isoprene emissions with a larger portion of photosynthetic carbon allocated to isoprene production, and structural changes leading to increased O_3 resistance.[117] It is also predicted that O_3 pollution favors isoprene-emitting plant species, causing a shift in species composition, which unless otherwise perturbed, would take centuries.[118]

Climate change is predicted to affect the chemistry and environmental conditions that control atmospheric O_3 concentrations.[17, 62, 119] There remain critical uncertainties related to effective regulatory design in a warmer and/or otherwise different climate, including more prevalent and extreme drought. Moreover, the magnitude and sign of drought forcing on any individual term in the O_3 mass balance equation will vary as a function of location. This analysis adds to growing literature indicating severe drought has the potential to alter the abundance and temperature-dependence of O_3-forming biogenic organic reactivity, the dominant chemical mechanisms and absolute rates of PO_3, and the O_3 tropospheric lifetime. While less abundant in Central California, isoprene is typically the largest source of OH reactivity in the continental boundary layer; as a result, drought-isoprene effects on PO_3 will likely be more pronounced in locations where isoprene is dominant. I find severe drought conditions worsen the so-called O_3-climate penalty in Central California, defined as diminished NO_x emission control benefits,[76] as biogenic reactivity is reduced to the extent that PO_3 becomes more NO_x suppressed, more substantial decreases in NO_x would be require to have the same effect. In Central California, drought conditions led to decreased PO_3, but air quality benefits were largely negated by concomitant changes in LO_3, suggesting more aggressive regulatory interventions will be required in the future.

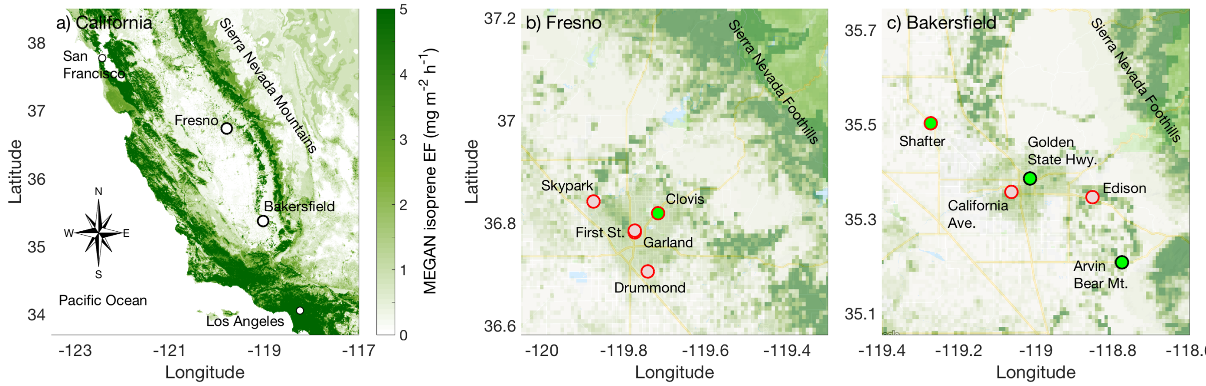

Figure 2.1. Central California (panel a) with MEGAN isoprene emission factors (MEGAN v2.1, version 2011).[120] Fresno (panel b) and Bakersfield (panel c) areas and monitoring station locations with isoprene (green) and O_3 and NO_2* (red outline) measurements available, with MEGAN isoprene emission factors in same color scale as panel a.

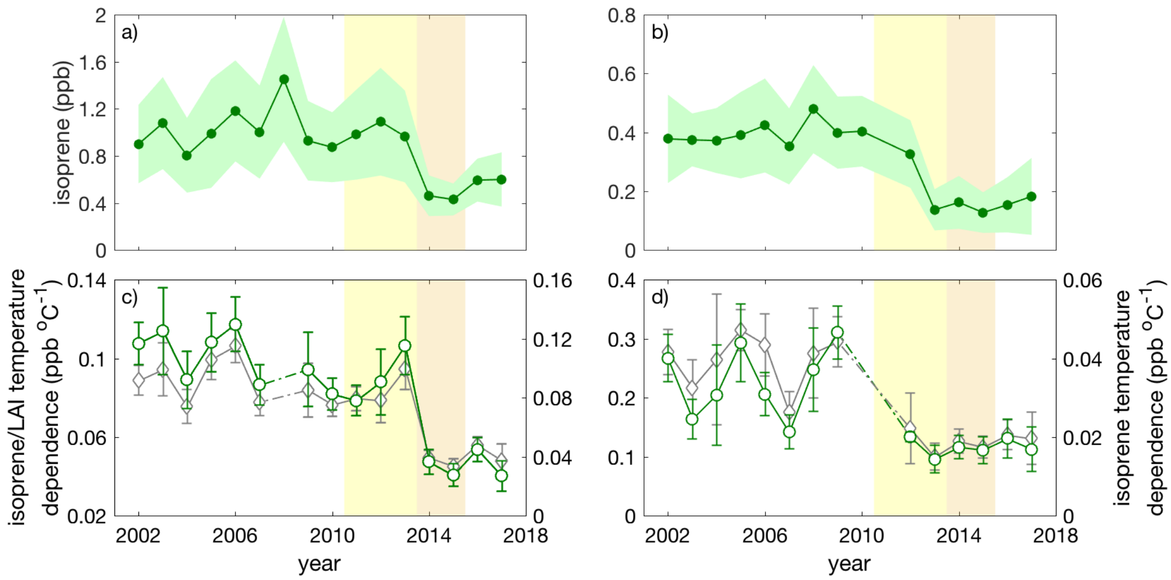

Figure 2.2. Daytime (8 am–8 pm, LT) isoprene mixing ratios (ppb) during O_3-season in Fresno (panel a) and Bakersfield (panel b). Envelopes define the 2σ standard deviation, not the measurement uncertainty. Slopes of the correlation between daily maximum temperature (ºC) and isoprene/LAI (green, left axis) or isoprene (gray, right axis) in Fresno (panel c) and Bakersfield (panel d) with slope errors. Plot fields are tinted to indicate the 2011–2013 early drought (light yellow) and 2014–2015 severe drought (light orange) time periods.

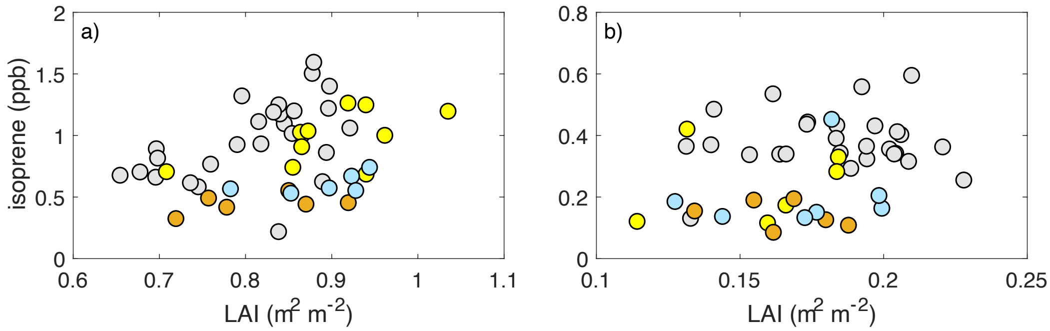

Figure 2.3. Monthly mean isoprene mixing ratios (ppb) versus MODIS-derived LAI (m^2 m^{-2}) in Fresno (panel a) and Bakersfield (panel b). Coloration indicates pre-drought (gray), early-drought (yellow), severe-drought (orange), and post-drought (light blue) time periods.

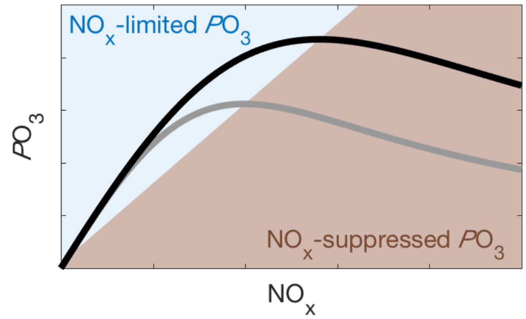

Figure 2.4. Cartoon illustrating PO_3 versus NO_x concentration at high (black) and low (gray) organic reactivity. NO_x-limited PO_3 is indicated in blue and NO_x-suppressed PO_3 is indicated in brown.

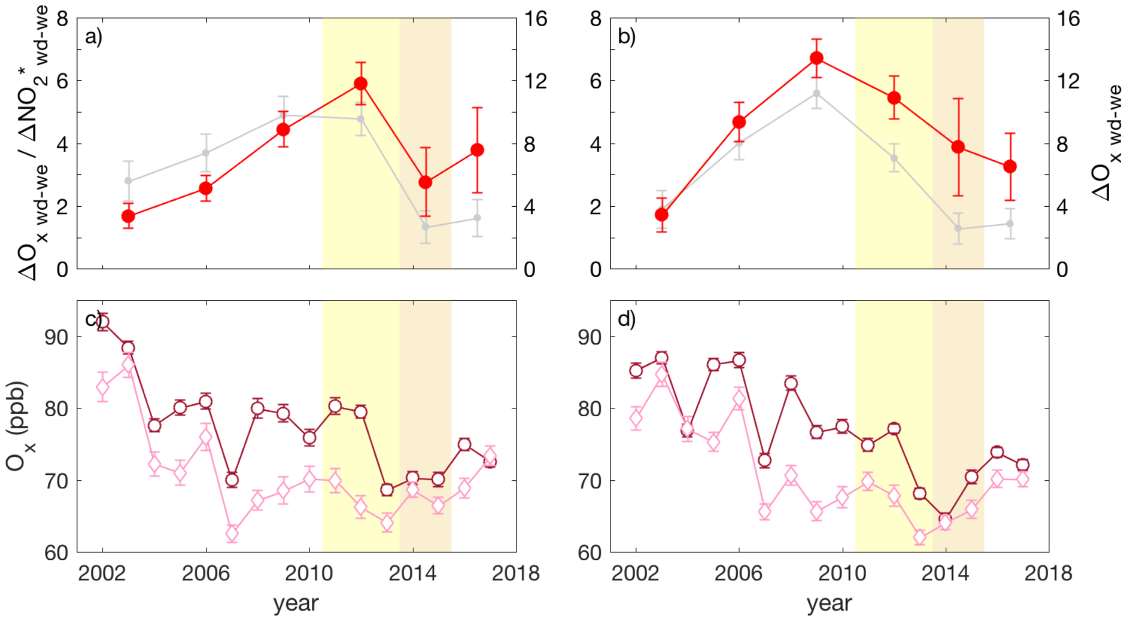

Figure 2.5. Panels a–b, right axis (red): afternoon (12–5 pm, LT) $\Delta O_{x\ wd–we}$ / $\Delta NO_2{}^*{}_{wd–we}$ during O_3 season (June–September) in Fresno and Bakersfield. Left axis (gray): $\Delta O_{x\ wd–we}$ for the same data with standard mean errors. Panels c–d: afternoon (12–5 pm LT) O_x (ppb) during O_3 season on weekdays (burgundy circles) and weekends (pink diamonds) in Fresno (panel c) and Bakersfield (panel d). Error bars are 1σ standard mean errors. Tinted areas indicate the 2011–2013 early-drought (light yellow) and 2014–2015 severe-drought (light orange) time periods.

Table 2.1. Statistics during the pre- (2002–2010), early (2001–2013), severe (2014–215), and post-drought (2016–2017) time periods for Fresno, Bakersfield, and the Tulare Basin during O_3 season (June–September). For O_x and NO_2* metrics, pre-drought is defined as 2008–2010 (italics). Data are reported as means if distributions are generally Gaussian and include medians in parentheses if non-normal. Normality was determined through visual examination of histograms and quantile-quantile plots. Isoprene metrics are daily means (8 am–8 pm, LT); all other metrics are afternoon observations (12–5 pm, LT). Uncertainties are 1σ standard mean errors, with the exception of the isoprene/LAI versus daily maximum temperature slopes, which are slope errors. The number of days with measurements included in each metric is reported in Table A2.1.

	pre-drought ***2008–2010*** **2002–2010**	**early drought** **2011–2013**	**severe drought** **2014–2015**	**post-drought** **2016–2017**
Fresno				
Isoprene mixing ratio (ppb)	1.00 ± 0.03	1.00 ± 0.04	0.45 ± 0.02	0.60 ± 0.02
Isoprene/LAI vs. temperature correlation slope (ppb $^oC^{-1}$)	0.10 ± 0.01	0.10 ± 0.02	0.04 ± 0.01	0.05 ± 0.01
LAI	0.84 ± 0.03	0.89 ± 0.04	0.84 ± 0.04	0.91 ± 0.02
$\Delta O_{x\ wd–I}$/ $\Delta NO_2{*}_{wd–we}$	*4.5 ± 0.6* 2.9 ± 0.5	5.9 ± 0.7	2.8 ± 1.1	3.8 ± 1.4
Percent $\Delta NO_2{*}_{wd–I}$(%)	*42* 42	36	24	23
O_x mixing ratio (ppb)	*75.7 ± 0.4* 78.2 ± 0.4	73.6 ± 0.3	69.5 ± 0.3	72.9 ± 0.2
NO_2* mixing ratio (ppb)	*4.9 (4.3) ± 0.1* 6.0 (5.5) ± 0.1	4.1 (3.7) ± 0.1	3.4 (3.1) ± 0.1	3.4 (3.2) ± 0.1
Daily maximum temperature (^oC)	34.6 ± 0.1	35.2 ± 0.1	35.1 ± 0.1	35.7 ± 0.1
Relative humidity (%)	25 (22)	24 (22)	26 (24)	24 (23)
Wind speed (m s^{-1})	6.4 ± 0.1	6.0 ± 0.1	5.7 ± 0.1	5.9 ± 0.1
Stagnation severity (O_3 ppb day^{-1})	6.3 (5.4) ± 0.2	6.0 (5.3) ± 0.3	5.7 (5.8) ± 0.3	5.3 (4.8) ± 0.3
Stagnation event duration (days)	5.4 (5) ± 0.1	5.4 (5) ± 0.1	5.5 (5) ± 0.2	5.8 (5) ± 0.2
Stagnation accumulation (O_3 ppb $event^{-1}$)	26.8 (23.3) ± 0.8	25.7 (23.1) ± 1.3	24.7 (24.0) ± 1.4	24.9 (23.1) ± 1.4
Bakersfield				
Isoprene mixing ratio (ppb)	0.40 ± 0.01	0.21 ± 0.02	0.15 ± 0.01	0.17 ± 0.01
Isoprene/LAI vs. temperature correlation slope (ppb $^oC^{-1}$)	0.23 ± 0.05	0.11 ± 0.02	0.06 ± 0.01	0.12 ± 0.04
LAI	0.16 ± 0.03	0.20 ± 0.01	0.18 ± 0.02	0.22 ± 0.01
$\Delta O_{x\ wd–I}$/ $\Delta NO_2{*}_{wd–we}$	*6.7 ± 0.6* 4.4 ± 0.6	5.5 ± 0.7	3.9 ± 1.5	3.3 ± 1.1
Percent $\Delta NO_2{*}_{wd–I}$(%)	*36* 31	32	23	29
O_x mixing ratio (ppb)	*76.0 ± 0.2* 79.0 ± 0.1	71.5 ± 0.2	67.0 ± 0.2	72.5 ± 0.2
NO_2* mixing ratio (ppb)	*4.2 (4.0) ± 0.1* 5.3 (4.7) ± 0.1	3.7 (3.4) ± 0.1	2.6 (2.6) ± 0.1	2.9 (2.7) ± 0.1
Daily maximum temperature (^oC)	34.4 ± 0.1	34.1 ± 0.1	34.9 ± 0.1	35.8 ± 0.1
Relative humidity (%)	25 (22)	24 (23)	21 (19)	18 (17)
Wind speed (m s^{-1})	3.2 ± 0.4	3.4 ± 0.3	3.1 ± 0.2	3.1 ± 0.2
Stagnation severity (O_3 ppb day^{-1})	6.0 (5.2) ± 0.2	5.6 (5.1) ± 0.3	6.1 (5.4) ± 0.4	4.8 (4.3) ± 0.3
Stagnation event duration (days)	5.5 (5) ± 0.1	5.5 (5) ± 0.2	5.5 (5) ± 0.2	5.8 (5) ± 0.2
Stagnation accumulation (O_3 ppb $event^{-1}$)	25.7 (22.7) ± 0.8	23.7 (23.7) ± 1.0	25.7 (24.9) ± 1.2	23.0 (20.5) ± 1.4
Tulare Basin				
Water-year rainfall (inches)	56.1	55.2	27.8	72.7

Chapter 3: Observing Air Pollution Inequality Using High Spatial Resolution Nitrogen Dioxide Remote Sensing Measurements in Houston, Texas

Adapted from: Demetillo, M. A. G., Navarro, A., Knowles, K. K., Fields, K. P., Geddes, J. A., Nowlan, C. R., Sun, K., Judd, L. M., Al-Saadi, J., Diskin, G. S., McDonald, B. C., and Pusede, S. E.: Observing Air Pollution Inequality Using High Spatial Resolution Nitrogen Dioxide Remote Sensing Measurements in Houston, Texas, *Environ. Sci. Technol.,* 54, 9882-9895, doi:10.1021/acs.est.0c01864, **2020.**

3.1 Introduction

Houston, Texas is a large, socio-demographically diverse U.S. city that is also a global center for petrochemical manufacturing. Houston experiences among the worst air quality in the U.S.,[121, 122] with documented evidence that local air pollution disproportionately burdens the city's low-income residents and communities of color,[123-126] leading to demonstrated differences in health and life expectancy as a result.[127, 128] Similar racial, ethnic, and income-based inequalities have also been observed in other major U.S. cities.[129-133] Our ability to describe this intra-urban pollutant variability has been limited by the lack of spatially-continuous, temporally-resolved measurements that capture gradients between neighborhoods. In the case of reactive gases with short atmospheric lifetimes, such as nitrogen dioxide (NO_2), intra-urban spatiotemporal variability cannot be directly observed by traditional monitoring approaches, impeding efforts to address air quality disparities through policy.

NO_2 plays a critical role in surface air quality, and knowledge of NO_2 spatiotemporal variability is fundamental to air pollution and public health decision-making. NO_2 is a key control over the atmospheric oxidation capacity, a precursor to ground-level ozone and particulate matter (PM), and a regulated criteria pollutant under the Clean Air Act. In U.S. cities, NO_2 sources are typically dominated by vehicles and electricity generation;[134] in Houston, petrochemical refineries and industrial activities are also large emitters.[135-137] NO_2 is a robust indicator of combustion emissions generally[131] and a common surrogate for traffic-pollutant mixtures, especially toxic diesel exhaust.[138] Epidemiological studies have linked ambient NO_2 concentrations to adverse health outcomes[139-142] and residential proximity to roadways has been associated with reduced lung function and asthma,[143-145] cardiac and pulmonary mortality, and preeclampsia and preterm birth.[146-148]

NO_2 concentrations change rapidly in the near-field of sources, with downwind distance-decay gradients ranging from <0.5 km in unstable to 1–2 km in stable atmospheres.[149, 150] Widely-used monitoring tools such as regulatory surface networks and satellite instruments have historically been unable to resolve such NO_2 gradients. Across the U.S., there are over 400 in situ NO_2 monitoring stations, yet fewer than 1/3 of U.S. urban areas are equipped with even one NO_2 analyzer.[151] In cities with monitors, representative concentrations are not captured for most residents, and, while urban NO_2 is well-correlated with traffic, U.S. Environmental Protection Agency (EPA) guidance generally recommends siting monitors away from roadways.[152] At the same time, satellite remote sensing has contributed substantially to our understanding of inter-urban NO_2 distributions, providing spatially continuous maps of NO_2 columns across cities, but has generally lacked the resolution required to capture intra-urban variability.[74, 151, 153, 154] Fine spatial scale land-use regression (LUR) models, which predict pollutant concentrations as a function of the geographic location of emitters and other land cover elements, have added spatial detail to coarse NO_2 datasets and allowed the creation of NO_2 maps at resolutions of 100 m^2, fine enough to resolve distance-decay gradients away from sources.[155-157] However, these models require substantial a priori geospatial knowledge and rely on temporal averages of pollutant data of at least weeks (surface monitors) to months (satellites). As a result, LUR models typically do not describe pollutant temporal variability, limiting source identification and discovery from time-varying emission patterns, and leading to biases in acute exposure epidemiological studies related to confounding temporal trends and meteorology.[138]

Here, I evaluate the extent that NO_2 remote sensing can resolve intra-urban spatiotemporal variability relevant to NO_2 inequality in Houston, Texas. First, I describe an observationally-based analysis using novel high-spatial-resolution (250 m x 500 m) sub-orbital remote sensing measurements from NASA GCAS (GEOstationary Coastal and Air Pollution Events (GEO-CAPE) Airborne Simulator), collected as part of the September-2013 DISCOVER-AQ study (Deriving Information on Surface Conditions from COlumn and VERtically Resolved Observations Relevant to Air Quality).[158-160] I quantify neighborhood-level (census-tract) differences in population-weighted tropospheric NO_2 vertical columns, with GCAS columns resolving within census-tract variability, and discuss atmospheric controls over the NO_2 spatiotemporal distribution for various socio-demographic groups, specifically race-ethnicity and income. Second, I test whether the recently launched satellite-based TROPOMI sensor, currently producing the highest spatial resolution NO_2 satellite measurements, precisely and/or accurately captures the same NO_2 column differences detected by GCAS. I utilize in situ NO_2 vertical profiles collected onboard the NASA P-3B during DISCOVER-AQ and data from the routine surface monitoring network to demonstrate that columns and surface measurements represent similar NO_2 spatial patterns. I evaluate major source contributions to census-tract-level NO_2 disparities, comparing weekday-weekend column differences in the first full year of TROPOMI data (June 2018–May 2019) to estimates derived from emissions in the high-resolution Fuel-based Inventory of Vehicle Emissions (FIVE) inventory and National Emission Inventory (NEI). Finally, I discuss potential applications and limitations of next-generation satellites observations to inform, evaluate, enforce, and motivate decision-making on air pollution inequality in U.S. cities.

3.2 Materials and Methods

3.2.1 Houston, Texas

Houston-The Woodlands-Sugar Land, referred to in this paper as either Houston or the Houston Metropolitan Area (HMA), is largest metropolitan statistical area in Texas, and among the largest in the U.S., with 6.1 million residents in 2013 and 6.8 million in 2018.[161] Houston is a growing city that is racially, ethnically, and economically diverse, and home to one of the largest Hispanic populations in the U.S. Houston is also the location of ~1/4 of all U.S. chemical refineries[162] and the Houston Ship Channel (HSC), a busy waterway where numerous major industrial facilities are located, extending from the Gulf of Mexico, through Galveston Bay, and along the Buffalo Bayou river between Baytown and Downtown Houston (Fig. A3.1).[163] The unique combination of urban transportation, petrochemical emissions, and the prevalent land-sea breeze contribute to the HMA's poor air quality, including high levels of ozone and hazardous air pollutants.[164-166] Past research has shown that local air pollution is not uniformly distributed across Houston, but is instead concentrated in neighborhoods with larger Hispanic populations, lower rates of educational attainment, and higher rates of poverty.[123-125] Primarily non-white, Hispanic, and lower-income neighborhoods have experienced greater cancer risks, increased chronic and acute air pollutant exposure, and lower overall physical well-being, especially in communities adjacent to facilities on HSC, where low-income households and people of color are statistically overrepresented.[127, 128]

3.2.2 GCAS

The GEOstationary Coastal and Air Pollution Events (GEO-CAPE) Airborne Simulator (GCAS) was developed as a technology-demonstration instrument in support of the GEOstationary Coastal and Air Pollution Events (GEO-CAPE) decadal survey mission.[167] GCAS makes hyperspectral nadir-viewing measurements of backscattered solar radiation in two channels at wavelengths 300–490 nm (air quality species) and 480–900 nm (ocean color). Each channel uses a two-dimensional charge coupled device (CCD) array detector for mapping, with one CCD dimension capturing absorption spectra and the other providing cross-track spatial coverage over a ~45° field of view. GCAS NO_2 column retrievals consisted of a two-step approach similar to algorithms used for other major satellite instruments: GOME, SCIAMACHY, OMI, and the forthcoming TEMPO.[158, 159] First, NO_2 slant column densities were derived by direct spectral fitting of radiances using measured nadir spectra and an averaged unpolluted reference spectrum (over the Gulf of Mexico). Second, slant columns were converted to vertical columns using an air mass factor (AMF), calculated for each scene with scattering weights derived from a radiative transfer model over 56 vertical layers, 45 of which were generated from the Community Multi-scale Air Quality (CMAQ) model. The AMF was a function of the observing geometry, surface reflectance, ozone profile, and trace gas profile shape. GCAS column uncertainties were estimated to range between 20–50% and 18–30% over moderately (0.5–1 x 10^{16} molecules cm^{-2}) and heavily polluted (>2 x 10^{16} molecules cm^{-2}) areas, respectively.[158] In a detailed evaluation of DISCOVER-AQ GCAS observations, Nowlan et al.[158] reported an overall correlation of $r^2 = 0.89$ between integrated P-3B NO_2 columns and GCAS measurements. GCAS was found to underestimate NO_2 columns compared to P-3B measurements for high column densities (GCAS low by 10%) and overestimate columns near background concentrations (by ~1.6 x 10^{15} molecules cm^{-2}), implying our community-level NO_2 difference estimates may be underestimated. Column uncertainties were driven by uncertainties in the AMF and challenges associated with representing species exhibiting high spatiotemporal variability as means. The GCAS instrument and retrieval validation have been described in detail in Nowlan et al.[158, 159] GCAS produced individual spectra with native spatial resolution on the order of tens of m^2, but spectra were spatially averaged to enhance their signal to noise. At a 9-km flight altitude, GCAS produced NO_2 vertical columns at 250 m (across track) x 500 m (along track), with the along-track coverage generated by the host aircraft. During the Houston DISCOVER-AQ deployment, GCAS flew onboard the NASA B-200 and conducted a total of 21 air quality flights in the morning (8 am–12 pm, LT) and afternoon (1 pm–5 pm, LT) over 11 days. I focused on measurements of cloud-free pixels from 9 weekdays that included both morning and afternoon research flights, with two circuits during each flight: September 4, 6, 11–13, 18, and 24–26, 2013. Data from the second circuit of the 12-September morning sortie were omitted because of heavy clouds.

3.2.3 TROPOMI

TROPOspheric Monitoring Instrument (TROPOMI) is the newest space-based NO_2 sensor[168, 169] and the single-payload onboard the sun-synchronous Copernicus Sentinel-5 Precursor (S5P) satellite. TROPOMI measures in the ultraviolet and visible (270–500 nm), near-infrared (675–775 nm), and shortwave infrared (2305–2385 nm) spectral regions to quantify a range of atmospheric trace gases. NO_2 is retrieved by fitting the 405–465 nm band using an updated OMI DOMINO retrieval and based on work from the QA4ECV project.[170-174] At nadir, NO_2 is retrieved at a spatial resolution of 3.5 km x 7 km.[168, 169] Precision of individual tropospheric NO_2 columns over urban/polluted scenes is on the order of 30–60% and dominated by uncertainties in the AMF.[175] Key inputs to the AMF are clouds, the NO_2 profile shape generated using 1° x 1° TM5-MP model output, and the surface albedo from a 0.5° x 0.5° monthly OMI climatology.[176, 177] I used clear-sky Level 2 NO_2 tropospheric columns, quality descriptor: qa value >0.75 as recommended by the Product User Manual.[178] TROPOMI maps at 0.01° x 0.01° were produced using physics-based oversampling.[179] In brief, the approach represents observations on the ground as sensitivity distributions, rather than as points or polygons. For image grating spectrometers like TROPOMI, generalized two-dimensions super Gaussian functions have been shown best to characterize sensitivity distributions.

3.2.4 Surface NO_2* and winds

Hourly ground-based nitrogen dioxide (NO_2*), wind speed, and wind direction measurements were downloaded via the Texas Commission on Environmental Quality Data Report query tool (https://www17.tceq.texas.gov/tamis/index.cfm). NO_2* was measured using chemiluminescence coupled to a heated molybdenum converter that includes a positive interference from nitric acid and organic nitrates, which largely affects absolute rather than relative NO_2* mixing ratios. [49, 180] I use the nomenclature NO_2* rather than NO_2 in acknowledgement of this interference. For September 2013, I analyzed wind data from 16 monitoring stations in the HMA with simultaneous NO_2* and wind observations. To observe interannual trends, I compared daytime (10 am–4 pm LT) annual averaged data for June 2013–May 2014 and June 2018–May 2019 using NO_2* measurements from the 15 stations operating in both time periods. To compare surface and TROPOMI column observations, I included mean midday (12–3 pm LT) measurements from all 17 monitors in the HMA, excluding two designated near-roadway sites (see Fig. A3.14 caption for station information).[181]

3.2.5 Demographic data and boundaries

Household income statistics from the 2010 American Community Survey: 5-Year Dataset and race-ethnicity population tables from the 2010 U.S. Census were downloaded from the IPUMS National Historical Geographic Information System.[182] Year 2013 census tract polygons were downloaded as TIGER/Line shapefiles from the Data.gov library (https://www.census.gov/cgi-bin/geo/shapefiles/index.php).

3.2.6 P-3B dataset and CBL height determination

As part of DISCOVER-AQ, NO_2 and NO were measured onboard the NASA P-3B at 1-s time resolution by the NCAR chemiluminescence system, detecting NO directly and NO_2 following photolysis into NO by a blue light converter. The instrument was calibrated frequently in flight and uncertainties were 0.02 ppb precision (at 1 s averaging) and ±10% accuracy for NO_2. $H_2O_{(v)}$ was measured by the NASA open-path Diode Laser Hygrometer (DLH) and reported at 1-s time resolution with overall uncertainties of 5%. Static air temperature data were collected by a Rosemount model 102 sensor with precision of 0.006°C and accuracy of ±0.2°C.

For each P-3B profile, I identified the CBL height as the altitude of the strongest coincident gradients in potential temperature (θ) and water vapor mixing ratio ($H_2O_{(v)}$), which were also near the top of the region of constant $H_2O_{(v)}$ mixing ratios extending from the surface.[183, 184] To reduce spurious layer determination from instrument noise, I first averaged measurements into 10-m altitude bins and calculated 5-point running mean lapse rates and $H_2O_{(v)}$ gradients. Vertical profiles of NO_2, lapse rate, θ, and $H_2O_{(v)}$ with their corresponding CBL heights over Moody Tower, Channelview, Deer Park, West Houston, Conroe, and Manvel Croix are provided.

3.2.7 FIVE and NEI inventories

The Fuel-based Inventory from Vehicle Emissions (FIVE) is a spatially- and temporally-resolved inventory of mobile source emissions (on-road + off-road engines).[185] I focused on the on-road component, comprised of light-duty gasoline vehicles and heavy-duty trucks, with fuels sales and emission factors updated to 2018. FIVE provided on-road emissions derived from publicly available fuel sales reports, road-level traffic counts, and time-resolved weigh-in-motion traffic counts.[80] Fuel use uncertainties are based on differences between fuel sale reports and truck travel (±13% in Texas) and traffic count site-selection and sample size (±10% for major roads and freeways in large urban areas). Emissions uncertainties were derived from regression analysis of near-road infrared remote sensing and tunnel studies: ±16% and ±15% for light-duty gasoline vehicles and heavy-duty diesel trucks, respectively.[185]

The National Emissions Inventory (NEI) provides a comprehensive and detailed estimate of NO_2 emissions from stationary sources, including industrial facilities, power plants, airports, and commercial facilities. I used estimates from the 2014 NEI Version 1, encompassing reports from state, local, and tribal air agencies and the EPA programs: Toxic Release Inventory, Acid Rain Program, and Maximum Achievable Control Technology standards development. I use emission uncertainties in power plants of ±25% and assume errors in industrial facilities and other less-characterized stationary sources to be ±50%.[90, 186]

3.2.8 Population-weighted NO_2, community-level NO_2 differences, and NO_2 inequality

GCAS and TROPOMI NO_2 columns were averaged within census tract polygons and tagged with geographic identifiers. Population-weighted NO_2 columns were calculated as equal to the product of the tract-unit NO_2 column ($NO_{2,j}$) and demographic group population (p_j) (by race-ethnicity or poverty classification) in the i^{th} tract, summed over all census tracts with NO_2 data (n), and divided by the summation of the group population (p_j) (Eq. 3.1). Errors were defined as standard mean errors, with N representing the number of census tracts with both NO_2 observations and residents of a given demographic group.

$$\text{(E3.1) Population-weighted } NO_{2,j} = \sum_{i=1}^{n} NO_{2,i}\, p_{i,j} \Big/ \sum_{i=1}^{n} p_{i,j}$$

I discussed absolute and relative NO_2 inequality in terms of the absolute and percent difference in population-weighted NO_2 columns between two demographic groups. Race-ethnicity demographics were defined with the following U.S. Census codes: Black and African Americans (JMJE004), excluding individual identifying as Hispanic or Latino; Asians (JMJE006), excluding those identifying as Hispanic or Latino; Hispanics (JMJE012), including all races reporting as Hispanic; and non-Hispanic whites (JMJE003). GCAS sampling was statistically representative of race-ethnicity demographics in the HMA (GCAS, HMA): Black and African American (17%, 12%); Asian (5%, 4%); Hispanic (36%, 37%), and non-Hispanic white (42%, 47%). I also described NO_2 columns for non-whites living in low-income tracts (LIN) defined as NO_2 column densities population-weighted by non-white populations (Black and African American, Asian, and Hispanic) in tracts with median household incomes less than 35,000 USD. NO_2 columns for whites living in high-income tracts (HIW) were defined using population-weighting by non-Hispanic white populations in tracts with median household incomes greater than \$80,000. For reference, lower (upper) annual household-income quintiles were 34,588 (84,905) USD along the GCAS flight path and 33,860 (79,332) USD across the nine counties of the HMA. Along the GCAS track, 13% of the population met the criteria for LIN (16% for HIW), residing in 18% of census tracts (23% for HIW); in the HMA, 16% of the population met the criteria for LIN (13% for HIW), residing in 25% percent of tracks (17% for HIW). Poverty status was categorized following the U.S. Census Bureau definition using the ratio of household income-to-poverty. Households were classified as being below the poverty line if their income was less than the poverty threshold in the U.S. Federal Poverty Guidelines, which scales with the number of people per household. I defined census tracts as below-poverty if >20% of households in the tract were at or below an income-to-poverty ratio of 1. The corresponding number of households was used in Eq. 3.1. Households with an income-to-poverty ratio greater than one in the remaining census tracts comprise the above-poverty population. Near-poverty populations encompassed households in all tracts with an income-to-poverty ratio of 1–1.24.

3.3 Results and Discussion

3.3.1 GCAS, census-tract NO_2 differences, and temporal variability

I focused on GCAS measurements from 35 flight circuits, collected on 9 weekdays (Tuesday–Friday) with sampling conducted in both the morning (8 am–12 pm local time, LT) and afternoon (1 pm–5 pm LT) (Figs. S2–S10). Observations from two example days are shown in Fig. 3.2, with GCAS vertical columns averaged to the underlying census tracts. To investigate differences in neighborhood-level NO_2, I calculated tract-level race-ethnicity population-weighted mean NO_2 columns for census tracts along the GCAS flight path for each circuit, and compared absolute and relative column differences (Tables 1 and 2). Population-weighted NO_2 columns for Hispanic, Black and African American, and Asian residents across all tracts sampled by GCAS were higher than for non-Hispanic whites by 32 ± 11%, 19 ± 7%, and 11 ± 5%, respectively (Table 1). In census tracts defined as below or near the poverty line, NO_2 columns were on average 28 ± 11% and 15 ± 8% higher than those above the poverty line. For non-whites in low-income tracts, population-weighted NO_2 columns were 37 ± 6% higher than for HIWs. Correspondingly, predominantly Hispanic and Black and African American neighborhoods and lower-income neighborhoods of all race-ethnicities were more often located in central Houston and closer proximity to the HSC (Figs. A3.11 and A3.12).

While population-weighted NO_2 columns were always higher for LIN than HIWs, a wider range of NO_2 levels were observed in predominantly non-white, Hispanic, and low-income tracts (Table 2). Variability, defined as two standard deviations of mean population-weighted NO_2 for all 35 flight circuits, was a factor of 2.5 greater for LINs than HIWs. On 25 September, meteorological conditions contributed to late-morning NO_2 columns and LIN-HIW differences (84 ± 8%) that were uniquely high (Table 3.1; Fig. A3.9); however, even after removing all 25-September data, population-weighted NO_2 columns were still 1.8 times more variable for LINs than HIWs. In the afternoon, absolute NO_2 column densities were lower for both LINs and HIWs than in the morning. Afternoon mean surface winds were 8 ± 1 m s^{-1} and usually from the southeast (onshore flow); by comparison, morning surface winds were 6 ± 2 m s^{-1}, and, while typically from the east/east-northeast, were more varied in direction (Table A2.1). The observed variability indicated greater NO_x emission source density in proximity to non-whites living in low-income neighborhoods, as the highest concentrations should co-locate with sources for reactive gases. I test this conclusion against emission inventory data (below), as high-income tracts were also 60% larger than low-income tracts, leading to greater spatial averaging.

3.3.2 Evaluating TROPOMI observations.

GCAS operates as a satellite analog in NASA airborne missions and its high-spatial-resolution observations now provide TROPOMI validation measurements. Launched in October 2017, TROPOMI has been shown to generate detailed NO_2 column maps, revealing hotspots undetectable by past space-based sensors due to its order of magnitude improved spatial resolution.[187-190] Here, I use the high-spatial-resolution, but limited duration, GCAS dataset to evaluate TROPOMI-derived annual-average differences in census tract-scale NO_2 columns, both along the GCAS flight track and across the HMA. The comparison provides an evaluation of the suitability of TROPOMI observations to resolve key horizontal NO_2 gradients for assessing air pollution disparities, where pollutant inequalities with neighborhood demographics in Houston have been independently shown.[123-125, 127, 128]

In Fig. 3.2a–b, TROPOMI observations are weekdays (Tuesday–Friday) over June 2018–May 2019, with data collection occurring at ~1:30 pm LT. Mondays were excluded, as they were considered transition days. TROPOMI measured highly-localized NO_2 column enhancements over the HSC, Texas City Galveston Bay Refinery (the second largest refinery in the U.S.), and the W.A. Parrish Generating Station (a 3.65 GW dual-fired power plant that includes the largest coal-fired plant in Texas at 2.7 GW). To produce TROPOMI maps at 0.01° x 0.01° (~1 km x 1 km over Houston), I employed a physics-based oversampling of daily images.[179] The annual-average weekday NO_2 pattern was spatially similar to GCAS measurements on days with slower surface winds, onshore afternoon air flows, and higher-than-average NO_2, in particular, September 4, 25, and 26.

Population-weighted annual weekday TROPOMI columns were 31 ± 3% higher for LINs than HIWs when sampled along the GCAS flight track (Fig. A3.13a). Across the full HMA (Fig. 3.2b;

Table 1), weekday TROPOMI observations indicated 34 ± 2% higher population-weighted NO_2 columns for LINs than HIWs. Because I utilized population-weighted columns, these results do not simply reflect urban-rural gradients. In Houston's 'urbanized areas' only (Fig. A3.15), which included 79% of tracts in the HMA, population-weighted LIN NO_2 columns were 27 ± 3% higher for HIWs. In September 2018 (Fig. A3.13b), LIN population-weighted weekday TROPOMI NO_2 columns were 42 ± 3% greater than for HIWs. Results from both annual and September TROPOMI weekday means agreed with afternoon GCAS LIN-HIW differences (34 ± 8%) to within uncertainties. Between 2013 and 2018, surface-level NO_2* mixing ratios averaged across the HMA decreased by 6 ± 5% (1.0 ± 7 ppb), with no major changes in the NO_2* spatial distribution and lower absolute and relative changes recorded at monitors nearest to the HSC compared to sites in suburban HMA (Fig. A3.14). In addition to somewhat lower relative LIN-HIW differences, the annually-averaged TROPOMI results yielded significantly lower absolute weekday LIN-HIW differences (9.19×10^{14} molecules cm^{-2}) compared to GCAS (2.6×10^{15} molecules cm^{-2}). Temporally averaging TROPOMI observations would have reduced the impact of individual high pollution episodes, such as on September 25, and contributed to decreased LIN-HIW differences derived from weekday annual compared to September means. Lower absolute column densities were consistent with TROPOMI's coarser spatial resolution and documented TROPOMI biases, with columns biased low under polluted conditions (high NO_2) and biased high at low NO_2 levels, which have been attributed to the lower resolution surface albedo characterization (0.5° OMI LER) and the coarse resolution of the TM5-MP a priori profiles used in the standard product.[188, 191] That being said, annually-averaged TROPOMI maps captured a key portion of LIN-HIW differences (and inequality by other metrics) to GCAS despite the effects of temporal averaging and instrument biases.

TROPOMI and afternoon GCAS measurements were compared as joint probability density functions of household income and fractional census tract race-ethnicity sorted into the lowest (0–20% of the NO_2 column distribution), intermediate (40–60%), and highest-NO_2 (80–100%) quintiles; Fig. 3.3 shows the median contours of each density function. The results showed that neighborhood-level differences were not driven by outliers, but represented broader patterns in the NO_2 distribution with neighborhood demographics. TROPOMI and GCAS described similar patterns: low NO_2 census tracts were more likely to be white and higher income, and intermediate and high NO_2 tracts were more likely to be non-white, Hispanic, and low income. Fig. 3.3 also demonstrated that TROPOMI and GCAS represented the NO_2 column density distributions as normal or log-normal, respectively (represented in the color scales), which was consistent with the coarser spatial resolution of the TROPOMI observations and their reported low bias at high NO_2. In addition, while the high (red) and low (blue) quintiles were comparable between datasets, there was more variation in the mid (yellow) quintile, reflective of these differences in NO_2 distribution.

Finally, census tracts are aspatial administrative units optimally sized around 4000 people that represent fine spatial scales in cities. In Houston's 'urbanized areas' (Fig. A3.15), census tracts were on average 4.7 ± 6.5 km^2 (~2 km x 2 km if square) and the smallest 20% of tracts were on average 1.2 ± 0.3 km^2. Because these smallest tracts are the size of our oversampled TROPOMI product resolution, finer scale analyses are likely limited. On average, the even smaller administrative unit of the U.S. Census block group, optimally sized at ~1500 people, was 2.1 ± 5.5 km^2 in the 'urbanized areas' and just 0.3 ± 0.1 km^2 in the smallest 20% of tracts, with the latter approaching the limit of the GCAS spatial resolution. At the block-group level, I computed LIN-HIW NO_2 differences of 22 ± 5% for TROPOMI and 30 ± 4% for GCAS (all circuits), which were

35% and 17% lower than computed at the tract level, respectively, suggesting even the GCAS resolution was too coarse to fully resolve block-group-scale disparities. Additionally, while finer-scale data hypothetically reveal greater NO_2 inhomogeneity and inequality; higher-resolution NO_2 remote sensing observations potentially underestimate the impacts of NO_x emissions. Because NO_x is primarily emitted as NO and then converted to NO_2 in the presence of ozone, NO_2 remote sensing misses the portion of NO_2 temporarily stored as NO as the system reaches steady state. This is important for a city-wide NO_2 column comparison in differently sized tracts, especially if using NO_2 as a surrogate for other co-emitted species, as sources are more prevalent in low-income neighborhoods, people of color are statistically overrepresented in tracts with higher population densities, and ozone concentrations are spatially variable.

3.3.3 NO_2 column-surface relationships

Satellite and sub-orbital remote sensing instruments observe NO_2 columns and precisely capture surface neighborhood-scale differences when NO_2 vertical distributions do not co-vary with census-tract demographics. NO_2 mixing ratios are typically highest within the convective boundary layer (CBL), the thin layer of air in contact with the Earth's surface during the daytime. While long-lived species are generally well-mixed in the CBL; NO_2 can exhibit steeper vertical gradients, as chemical loss and turbulent mixing timescales are similar.[192] To investigate the extent that NO_2 columns represented surface-level patterns in tract-scale NO_2 inequality (not the surface concentrations themselves), which is a key factor in their application to air pollution decision making, I compared GCAS columns to in situ NO_2 vertical profiles and TROPOMI columns to NO_2* surface measurements.

As part of DISCOVER-AQ, the NASA P-3B aircraft profiled the lower troposphere, spanning altitudes of 3–0.3 km at locations corresponding to the GCAS flight path (Fig. A3.16). I focused on 144 profiles representing tracts of varied population demographics in downtown (Moody Tower), the HSC (Channelview and Deer Park), and suburban Houston (Conroe, West Houston, and Manvel Croix), collected on 8 weekdays in the morning (8:30–10:30 am, LT), at midday (11:30 am–1 pm, LT), and in the afternoon (1:30–3:30, LT). Profiling at Deer Park, Conroe, and West Houston included missed approaches over lightly-trafficked air strips, facilitating sampling below altitudes of 0.1 km. All profiles are provided (Figs. S17–S65).

CBL heights were on average 0.8 ± 0.2 km (±1σ) in the morning, 1.5 ± 0.5 km at midday, and 1.7 ± 0.6 km in the afternoon. CBL heights were not statistically different at any profile location and temporal variability was generally well-correlated across sites (Table A2.3). In the morning, the slope of the correlation between the 3-km column and within-CBL column (Table A2.4; Fig. A3.14 was 0.80 ± 0.18 ($r^2 = 0.99$), and, once the CBL was fully developed (midday and afternoon), the slope was 0.98 ± 0.15 ($r^2 = 0.99$). The slope of correlation between the column within the CBL and below 500 m AGL was 0.83 ± 0.19 ($r^2 = 0.95$) in the morning. Once the CBL was developed, the slope decreased to 0.27 ± 0.05 ($r^2 = 0.80$), consistent with atmospheric conditions in which timescales of turbulent mixing and NO_2 chemical loss are competitive. The high correlation coefficients imply that location-dependent differences in the NO_2 vertical distribution were small and suggest that demographic-based NO_2 comparisons would not substantially differ if derived from surface measurements instead of columns.

I then compared tract-averaged TROPOMI columns and daytime (12–3 pm LT) NO_2* surface mixing ratios measured at monitors across the HMA (Fig. 3.4). I linearly correlated annual (June 2018–May 2019) weekday (Tuesday–Friday) mean observations as a function of the distance between tract center points and the nearest monitors. Surface NO_2* and directly overhead columns (tracts within 1 km of monitors) were strongly correlated (r^2 = 0.92). However, r^2 decreased with increasing distance from the nearest monitor, falling to 0.63–0.75 when tracts were 2–5 km from the local monitor and 0.50–0.58 at distances of 5–10 km. Column-surface correlations have also been shown to improve with monitor density elsewhere using data from the more coarsely resolved satellite OMI sensor.[151] While further analysis would have been required to infer surface concentrations, these results offered strong evidence that TROPOMI captured NO_2 surface patterns and, therefore, surface-level NO_2 inequality. The steep decline in r^2 at 1–2 km corresponds to previously observed NO_2 distance-decay gradients,[149, 150] demonstrating the limits of the routine network to detect representative NO_2 levels for the majority of local residents, and an advantage of TROPOMI, as just 3.4% of census tracts in the HMA (based on tract center points) are located within 2 km of an NO_2 monitor.

3.3.4 NO_x source contributions to census-tract NO_2 differences

To investigate the greater observed temporal variability in the GCAS results and attribute sources of NO_2 disparities for non-whites living in low-income tracts I analyzed LIN-HIW differences reported in the high-spatial-resolution FIVE and stationary source NEI using population-weighting as applied to the NO_2 column observations. Total population-weighted emission sources densities (metric tons NO_2-eq day^{-1} km^{-2}), which included on-road diesel and gasoline-powered vehicles, industrial and petrochemical facilities, and electricity generation, were 82% higher for LINs than HIWs. Stationary emissions in tracts with in low-income tracts were 27% greater (metric tons NO_2-eq day^{-1}) and 7 times more spatially dense than high-income tracts. This was consistent with our inference of greater NO_x emissions in proximity to non-whites living in low-income tracts based on variability in population-weighted GCAS NO_2 columns. Generally, heavy-duty diesel vehicles (HDDVs) represent just 3–6% of the overall U.S. vehicle fleet; however, diesel engines produce ~7 times more NO_x per kg fuel burned than gasoline,[185] contributing the majority of NO_x emissions in many U.S cities.[193] According to the FIVE, population-weighted HDDV emission densities were the largest source of NO_x in both Houston low- and high-income tracts, but were 80% greater for non-whites living in low-income tracts than for HIWs.

Satellite remote sensing has the advantage of capturing temporal variability useful for interpreting NO_x sources, especially NO_2 variations between weekdays and weekends driven by patterns in HDDV traffic.[49, 74] HDDVs have been documented to contribute to air pollution disparities in multiple U.S. cities[194-198] and their exhaust has been associated with a myriad of adverse health effects.[138] Because HDDVs transport commercial goods, their emissions are reduced on weekends,[74, 199] at the same time, passenger vehicle traffic and point source emissions do not exhibit significant weekday-weekend activity differences.[193, 200] To assess HDDV contributions to NO_2 column densities, I compared annual (June 2018–May 2019) weekday (Tuesday–Friday) and weekend (Saturday–Sunday) tract-level population-weighted TROPOMI NO_2 observations (Figs. 2b–c). NO_2 columns unweighted by population were 29% lower on weekends than weekdays, with larger weekend decreases for LINs (24 ± 2%) than HIWs (15 ± 2%). If HDDV traffic caused the entire weekday-weekend difference, then HDDV emissions contributed 25 ± 3% of the LIN-HIW population-weighted NO_2 column inequality across Houston, compared to 22 ± 2% predicted by the inventory, indicating shifting spatial patterns in gasoline vehicle traffic may also play a role. Weekend NO_2 column enhancements were largely confined to the HSC and western shore of Galveston Bay (Fig. 3.2c), indicating industrial and petrochemical sources were the dominant cause of NO_2 differences across the HMA.

3.4 Conclusions and Looking Forward

I quantified the unequal distribution of NO_2 across the city of Houston using high spatial resolution GCAS airborne observations (250 m x 500 m), which were fine enough to resolve census-tract-scale NO_2 spatial variability. I then used this analysis as a basis of comparison to determine that TROPOMI resolved similar tract-level NO_2 disparities. I found that while population-weighted GCAS NO_2 columns were always greater for non-white and Hispanic residents and in primarily low-income tracts, they were also substantially more temporally variable, a consequence of the higher NO_x source density in these neighborhoods. Greater temporal variability has implications for research on the acute health impacts of NO_2, and its surrogates, for LINs, as time-averaged pollutant data and static LUR models do not represent high NO_2 events, such as observed on the morning of September 25, and reflected in the shift in NO_2 column statistical distribution from log-normal (GCAS, 35 flight circuits) to normal (TROPOMI, one year of weekends) (Fig. 3.3). Because long-term averaging does not inherently change the underlying data distribution, and given that TROPOMI has at least the potential for daily coverage, the impact of transient extreme event could still be captured by analyzing other aspects of the NO_2 column distribution. In addition, TROPOMI's multiyear time record and ongoing data collection provides empirical evidence of specific time-varying NO_x source contributions potentially relevant for political and regulatory decision-making; for example, weekday-weekend NO_2 differences in Houston indicate HDDVs cause up to 25% of the city's NO_2 disparities. City-planners, elected officials, and other decision-makers may find such information useful as they develop comprehensive plans, allocate resources for mitigation, invest in public transportation, propose stricter emission requirements, and/or implement vehicle bans.

Spatially and temporally extensive air quality observations are foundational for successful policy design, implementation, and evaluation in every city, especially for controversial issues like environmental justice; this is because they (a) reduce uncertainties about the severity and impact of specific chemicals, which are often at the root of related policy disputes, and (b) lead to more precise identification of the contributing sources. Here, I demonstrated that TROPOMI (oversampled to 0.01° x 0.01°) precisely observed NO_2 disparities between census tracts, and that the spatial patterns in NO_2 columns reflected those measured at the surface. As a result, TROPOMI measurements are well positioned to inform multiple aspects of city-wide decision-making in novel ways: in the development of local and even neighborhood-level interventions, such as ordinances, moratoriums, comprehensive plans, zoning, siting decisions, traffic planning, and permitting; through data-driven regulatory enforcement; and by supporting the prioritization of resources for environmental equity, especially in areas lacking routine surface monitoring. While broader application of satellite NO_2 columns as a surrogate for toxic combustion emissions requires further consideration, as NO_x partitioning favors NO in the nearfield of sources, which are more prevalent in LIN neighborhoods, at least in Houston, TROPOMI observations have the potential to promote targeted and tailored municipal NO_x intervention efforts, as well as illuminate limitations to cities' enforcement capacities (e.g., growth in road transport) and, in so doing, reveal the need for inter-governmental coordination to produce the resources and policies to ensure compliance and equitable outcomes. Finally, the geostationary satellite TEMPO instrument (planned launch date in 2022) will provide hourly column observations of up to 2 km x 4.5 km over North America, resulting in the most spatially and temporally precise space-based NO_2 observations over the U.S. to date.[201] Finer city-wide spatiotemporal detail will further expand our ability to reveal, document and monitor census-tract-level NO_2 disparities, to observe high NO_2 events, to infer source contributions from temporal variability, and to inform decision-making to eliminate the practices, behaviors, and conditions contributing to racial, ethnic, and income-based air quality disparities in major U.S. cities.

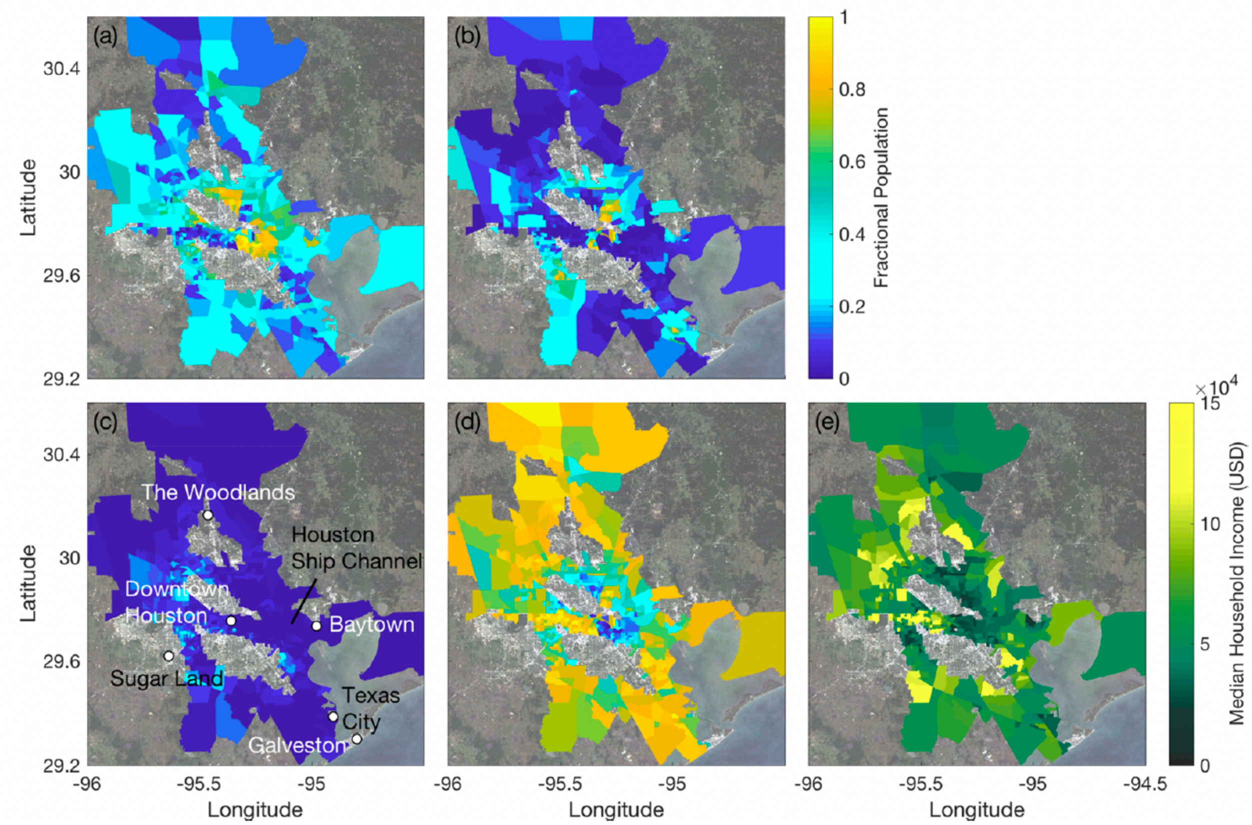

Figure 3.1. Fractional census-tract-level race-ethnicity demographics along the GCAS flight tract: (a) Hispanics, (b) Black and African Americans, (c) Asians, and (d) non-Hispanic whites. Panel (c) includes labels for various locations within the HMA. (e) Fractional median annual household income in USD. While the aircraft flew a repeated circuit, there were slight variations in some circuits between flights; this exact circuit is from the morning of September 4. Background map data: Landsat 8 composite over January 2017 to June 2018.

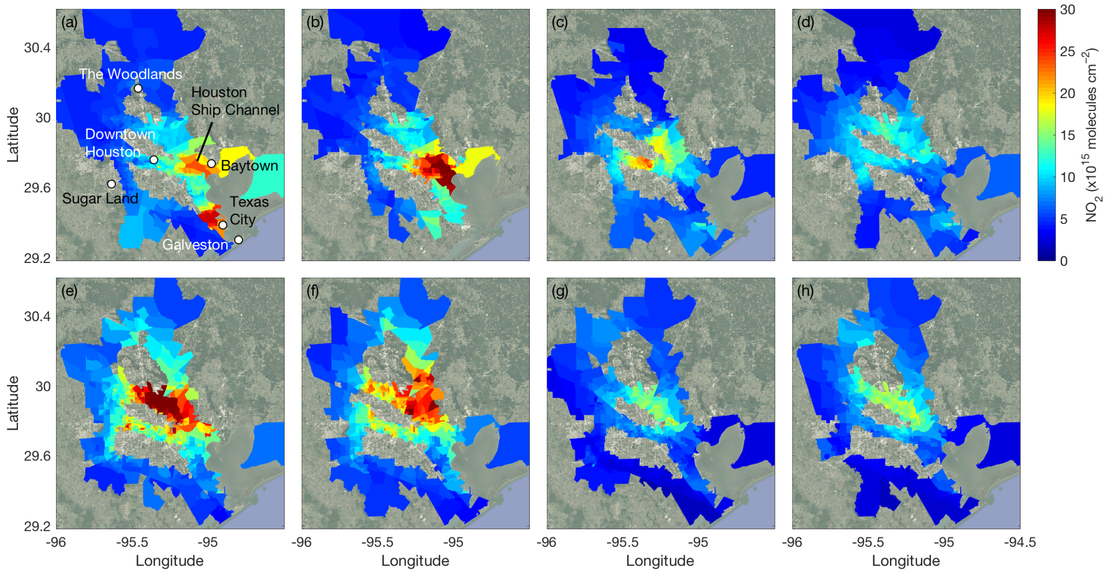

Figure 3.2. GCAS NO_2 column densities (molecules cm^{-2}) averaged to census tracts on two sample days, 4 September (top row; panels a–d) and 26 September (bottom row; panels e–h), during 8 flight circuits in the early morning (8 am–10 am LT; panels a and e), late morning (10 am–12 pm LT; panels b and f), early afternoon (1 pm–3 pm LT; panels c and g), and late afternoon (3 pm–5 pm LT; panels d and h).

Table 3.1. Census-tract-averaged population-weighted NO_2 columns (molecules cm^{-2}) for weekdays (Tuesday–Friday) during morning and afternoon GCAS flights (average of the two circuits) with variability reported as two standard deviations of individual circuit population-weighted NO_2 means for different socio-demographic categories. Annual (June 2018–May 2019) TROPOMI observations sub-sampled along the GCAS flight track (4 September morning) on weekdays and for the HMA on weekdays and weekends (Saturday–Sunday). September-2018 weekdays TROPOMI observations, both along the GCAS flight track (4 September morning) and for the full HMA. GCAS and TROPOMI uncertainties are standard mean errors rounded up to at least one decimal position.

Population-Weighted Census-Tract-Averaged NO_2 ($x10^{15}$ molecules cm^{-2})									
	GCAS Weekday Flights				**TROPOMI**				
	Means		Variability (2σ)		Annual (along GCAS)	Annual (HMA)		September (along GCAS)	September (HMA)
Group	Morning	Afternoon	Morning	Afternoon	Weekdays	Weekdays	Weekends	Weekdays	Weekdays
LIN	13.9 ± 0.5	9.0 ± 0.3	15.3	4.3	3.7 ± 0.1	3.3 ± 0.1	2.6 ± 0.1	4.7 ± 0.1	4.0 ± 0.1
HIW	9.1 ± 0.4	6.3 ± 0.3	4.2	2.4	2.7 ± 0.1	2.2 ± 0.1	1.9 ± 0.1	3.1 ± 0.1	2.9 ± 0.1
Below-poverty	13.0 ± 0.4	8.4 ± 0.3	13.7	4.1	3.5 ± 0.1	3.1 ± 0.1	2.1 ± 0.1	4.4 ± 0.1	3.7 ± 0.1
Near-poverty	11.3 ± 0.2	7.5 ± 0.1	9.8	3.3	3.2 ± 0.1	2.9 ± 0.1	2.0 ± 0.1	4.0 ± 0.1	3.4 ± 0.1
Above-poverty	9.5 ± 0.3	6.5 ± 0.2	5.1	2.5	2.8 ± 0.1	2.6 ± 0.1	1.9 ± 0.1	3.4 ± 0.1	2.9 ± 0.1
Hispanic	12.8 ± 0.4	8.4 ± 0.2	13.3	3.9	3.5 ± 0.1	3.3 ± 0.1	2.2 ± 0.1	4.5 ± 0.1	4.0 ± 0.1
Black/African American	11.4 ± 0.4	7.2 ± 0.2	8.3	3.3	3.2 ± 0.1	3.0 ± 0.1	2.1 ± 0.1	3.9 ± 0.1	3.4 ± 0.1
Asian	10.4 ± 0.3	6.7 ± 0.2	3.3	2.4	3.0 ± 0.1	2.8 ± 0.1	2.0 ± 0.1	3.6 ± 0.1	3.3 ± 0.1
White	8.8 ± 0.3	6.2 ± 0.2	4.9	2.7	2.7 ± 0.1	2.3 ± 0.1	1.7 ± 0.1	3.1 ± 0.1	2.5 ± 0.1

Table 3.2. GCAS census-tract-averaged population-weighted NO_2 columns (molecules cm^{-2}) for each flight circuit in LIN and HIW tracts and their percent difference. For individual circuits, uncertainties are standard mean errors of population-weighted NO_2 across all tracts within the flight path. The second morning pass on 12 September was omitted because most of the circuit was not completed and there were too many clouds.

	MORNING						AFTERNOON					
	First Circuit			Second Circuit			Third Circuit			Fourth Circuit		
	Population-weighted NO_2 (x10^{15} molecules cm^{-2})		Difference (%)	Population-weighted NO_2 (x10^{15} molecules cm^{-2})		Difference (%)	Population-weighted NO_2 (x10^{15} molecules cm^{-2})		Difference (%)	Population-weighted NO_2 (x10^{15} molecules cm^{-2})		Difference (%)
September	LIN	HIW		LIN	HIW		LIN	HIW		LIN	HIW	
4	10.0 ± 0.4	7.5 ± 0.3	28 ± 5	12.4 ± 0.5	8.3 ± 0.5	39 ± 7	12.3 ± 0.5	7.8 ± 0.5	44 ± 7	9.9 ± 0.2	7.4 ± 0.4	28 ± 4
6	11.8 ± 0.4	8.9 ± 0.4	28 ± 6	7.6 ± 0.3	6.0 ± 0.3	24 ± 6	8.6 ± 0.4	6.0 ± 0.3	36 ± 7	7.2 ± 0.4	5.9 ± 0.3	21 ± 5
11	12.4 ± 0.5	8.1 ± 0.4	42 ± 7	10.2 ± 0.5	8.3 ± 0.6	20 ± 9	7.9 ± 0.4	5.7 ± 0.4	33 ± 9	8.0 ± 0.4	6.3 ± 0.4	23 ± 6
12	11.1 ± 0.4	8.7 ± 0.4	25 ± 6	–	–	–	7.7 ± 0.3	4.8 ± 0.2	47 ± 7	10.2 ± 0.5	6.5 ± 0.3	45 ± 6
13	13.7 ± 0.6	9.0 ± 0.5	41 ± 7	11.8 ± 0.5	10.2 ± 0.5	14 ± 7	8.3 ± 0.4	5.3 ± 0.2	45 ± 7	8.6 ± 0.4	5.7 ± 0.2	41 ± 3
18	9.4 ± 0.5	8.0 ± 0.3	17 ± 7	8.7 ± 0.4	7.6 ± 0.4	13 ± 7	6.6 ± 0.2	5.4 ± 0.2	19 ± 5	7.0 ± 0.3	5.7 ± 0.2	20 ± 3
24	8.5 ± 0.3	8.1 ± 0.4	4 ± 6	6.3 ± 0.3	6.2 ± 0.2	2 ± 6	5.7 ± 0.2	4.8 ± 0.2	17 ± 5	6.6 ± 0.2	5.7 ± 0.2	15 ± 3
25	23.9 ± 0.9	13.1 ± 0.7	58 ± 6	37.8 ± 1.9	15.4 ± 1.3	84 ± 9	12.6 ± 0.5	8.9 ± 0.5	35 ± 6	13.8 ± 0.5	10.0 ± 0.5	32 ± 4
26	21.2 ± 1.0	11.2 ± 0.4	61 ± 7	17.3 ± 0.7	12.4 ± 0.5	34 ± 6	10.3 ± 0.4	5.8 ± 0.2	55 ± 6	12.0 ± 0.4	7.0 ± 0.2	44 ± 3
Mean	13.0 ± 0.6	9.2 ± 0.4	34 ± 8	14.0 ± 0.6	9.3 ± 0.5	40 ± 8	8.9 ± 0.4	6.0 ± 0.3	39 ± 6	9.1 ± 0.4	6.7 ± 0.3	30 ± 6

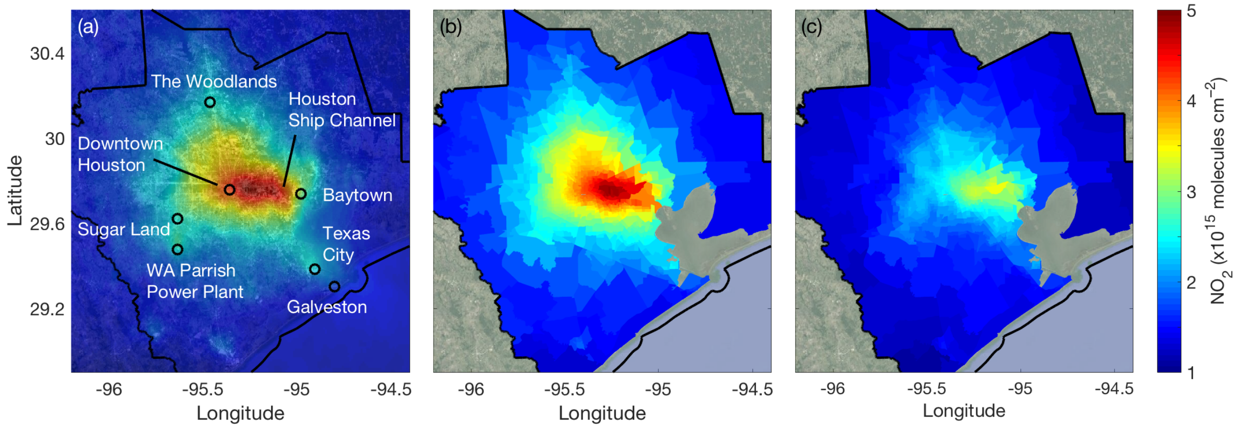

Figure 3.3. Weekday (Tuesday–Friday) TROPOMI NO_2 column densities (molecules cm^{-2}) for June 2018–May 2019 at 0.01° x 0.01° over the greater Houston area (panel a) and averaged within census tracts (panel b). Weekend (Saturday–Sunday) TROPOMI NO_2 columns averaged within census tracts for the HMA (panel c). A 40% transparency is applied to the TROPOMI data in panel (a) to see the underlying land cover. The black outline depicts the HMA.

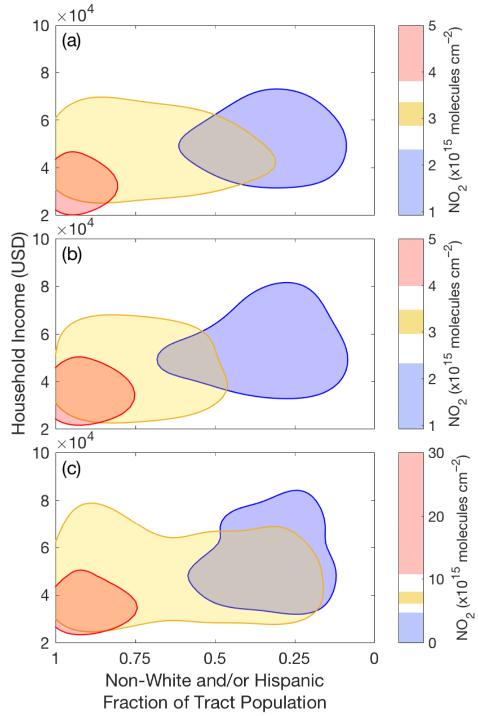

Figure 3.4. HMA population as a function of census tract annual household income (USD) and fraction non-white/Hispanic or fraction non-Hispanic white separated by census-tract-averaged NO_2 column quintile: high NO_2 (80–100% highest column densities) (red), mid-quintile NO_2 (40–60%) (yellow), and low NO_2 (0–20%) (blue). Panels a and b: Annual (June 2018–May 2019) weekday (Tuesday–Friday) TROPOMI observations across the HMA (panel a) and along the GCAS flight track (panel b). Panel c: The composite distribution of all 35 GCAS circuits. Color bars represent vertical column densities (molecule cm^{-2}) corresponding to the NO_2 quintiles.

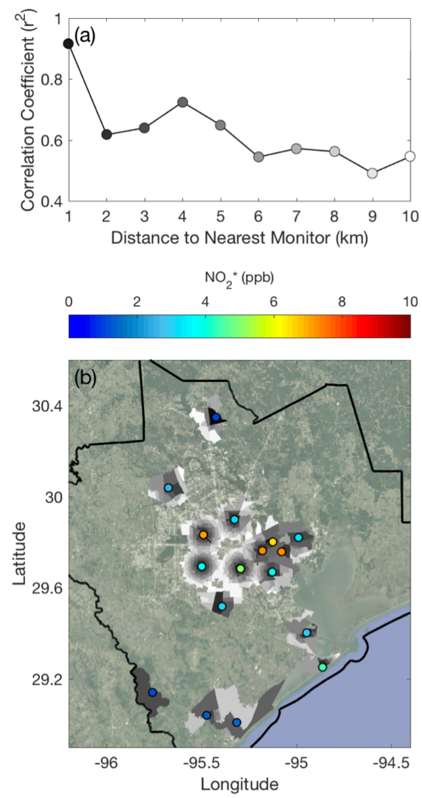

Figure 3.5. Correlation coefficient between tract-averaged NO_2 measured at surface monitors and their overhead columns as a function of distance away from the monitor with respect to the census tract center point (panel a). NO_2* observations are daytime (12–3 pm LT) averages and both datasets include weekdays (Tuesday–Friday) over June 2018–May 2019. Census tracts coloration indicates the distance (km) between the nearest surface NO_2 monitoring station and the census tract center point (panel b) for tracts within a 10 km radius.

Chapter 4: Space-Based Observational Constraints on NO_2 Air Pollution Inequality From Diesel Traffic in Major U.S. Cities

Adapted from: Demetillo, M.A.G., Harkins, C., Mcdonald, B.C., Chodrow, P.S., Sun, K., and Pusede, S.E.: Space-Based Observational Constraints on NO_2 Air Pollution Inequality from Diesel Traffic in Major US Cities. *Geophys. Res. Lett.,* 48, doi:10.1029/2021gl094333, **2021**

4.1 Introduction

In U.S. cities, the concentrations of many air pollutants have been observed, modeled, and inferred to be higher in neighborhoods where residents are primarily people of color and have lower household incomes.[126, 132, 189, 202-204] These disparities have been shown to cause measurable differences in health and life expectancy.[8, 147, 205, 206]. Heavy-duty diesel vehicles (HDDVs) are a major driver of air pollution inequalities, with HDDV exhaust containing nitrogen oxides ($NO_x \equiv NO + NO_2$) and a myriad of hazardous co-emissions.[194-197, 207-211] Source characterization of air quality disparities, including from diesel traffic emissions, has been hindered by the lack of city-wide measurements resolving steep atmospheric pollutant gradients and providing temporal information useful for source identification.

Nitrogen dioxide (NO_2) is a combustion product and a key control over atmospheric oxidation and secondary pollutant formation. Communities of color and those with lower household incomes often experience elevated NO_2 concentrations and exposures.[11, 130, 212-214] Epidemiological studies indicate an association between NO_2 exposure and/or its co-emissions and various adverse health effects.[139, 140, 215] NO_2 is a common surrogate for combustion pollution generally (Levy et al., 2014) and toxins in traffic exhaust specifically.[211] HDDVs contribute a major portion of urban NO_x despite being a small fraction (3–6%) of the U.S. fleet in terms of distance traveled, as diesel engines produce $x7$ more NO_x per kg fuel burned than gasoline.[193, 216] Because its sources are ubiquitous and distributed, NO_2 is highly variable in space and time, with typical distance-decay gradients away from sources of <0.5–2 km.[149, 150, 217] A key advantage to focusing air pollution inequality analyses on NO_2 is that it has recently become possible to observe NO_2 daily from space at the scale of a few kilometers using the TROPospheric Ozone Monitoring Instrument (TROPOMI).

In Chapter 3, I conducted a detailed evaluation of the use of TROPOMI observations to describe intra-urban NO_2 disparities, demonstrating that TROPOMI was indeed well-positioned to inform multiple aspects of NO_2 inequality research in Houston, Texas. I used fine spatial resolution (250 m x 500 m) airborne NO_2 remote sensing measurements from the GEOstationary Coastal and Air Pollution Events Airborne Simulator (GCAS) as a standard, showing that TROPOMI, oversampled to 0.01° x 0.01° using the physics-based algorithm employed here, resolved equivalent NO_2 relative inequalities as GCAS. I assessed the effects of observational uncertainties, retrieval biases, and time averaging on NO_2 inequality estimates, finding that although their influence led to underestimations in absolute census tract-level differences, TROPOMI still captured key variations in NO_2 spatial distribution between tracts.[218] I also showed that spatial patterns in NO_2 columns reflected those at the surface, an essential aspect of their application to air quality environmental justice decision-making and determined that column-based inequalities represented those that would be captured at the surface.

Here I expand this application of TROPOMI, describing NO_2 inequality in 52 major U.S. cities and using these observations as empirical constraints on the contribution of HDDV traffic to NO_2 disparities. I report neighborhood-level (census-tract) disparities with race, ethnicity, and income over an almost two-year period (June 2018–February 2020). I analyze weekday-weekend differences from both TROPOMI and NO_x emissions inventories to quantify the role of diesel traffic in NO_2 inequalities. I discuss results seasonally, as the NO_2 atmospheric lifetime is shorter in the summer, leading to greater co-location between NO_x emission sources and NO_2 columns than in the winter. I further explore analytical issues in the use of TROPOMI for observing tract-scale inequalities in cities where higher spatial resolution measurements are not available, investigating inequality relationships with urban segregation patterns and correlating column and surface measurements as a function of their spatial coincidence.

4.2 Data and Methods

4.2.1 TROPOMI

The TROPOspheric Monitoring Instrument (TROPOMI) detects various atmospheric trace gases in the ultraviolet and visible, near infrared, and shortwave infrared spectral regions.[169, 172] TROPOMI samples at ~1:30 pm local time (LT) almost daily from onboard the sun-synchronous Copernicus Sentinel-5 Precursor satellite. NO_2 is retrieved by fitting the 405–465 nm band using an updated OMI DOMINO algorithm based on the QA4ECV project.[170-174] Before 6 August 2019, NO_2 was retrieved at a nadir spatial resolution of 3.5 km x 7 km. NO_2 tropospheric vertical column densities (TVCDs) have since become available at 3.5 km x 5.5 km. Precision of individual TVCDs over polluted scenes is on the order of 30–60% and dominated by uncertainties in air mass factor inputs, including clouds, NO_2 profile shape (daily 1° x 1° TM5-MP output), and surface albedo (monthly 0.5° x 0.5° OMI climatology).[174, 176, 177]

I use the TROPOMI Level 2 NO_2 product averaged to 0.01° x 0.01° (~1 km x 1 km) with a physics-based oversampling algorithm.[179] I include cloud-free scenes with qa > 0.75. I calculate mean NO_2 TVCDs within census tract boundaries for 52 U.S. cities (Table A4.1) over the time periods of June 2018–February 2020, summer (June–August), and winter (December–February) and separately analyze seasonal NO_2 TVCDs on weekdays (Tuesday–Friday) and weekends (Saturday–Sunday). The mean number of TROPOMI pixels rounded up to the nearest integer averaged in each 0.01° x 0.01° grid are as follows (± 1 σ standard deviation), 77 ± 24 (summer weekdays), 33 ± 10 (summer weekends), 33 ± 21 (winter weekdays), and 18 ± 11 (winter weekends), with reduced wintertime sampling statistics due to increased cloud cover (Table A4.2). TROPOMI observations are spatially continuous (discretized to 0.001° x 0.001°), giving NO_2 TVCDs within tracts smaller in area than 1 km^2. Cities were selected to represent both the largest U.S. urban areas and mid-sized cities for broad country-wide coverage. Cities are defined as U.S. Census-designated 'urbanized areas' (UAs) with two exceptions: I separate New York-Newark, NJ–NY–CT along state lines into New York City, NY and Newark, NJ and San Francisco–Oakland, CA along the San Francisco Bay into San Francisco and Oakland, CA. With a population density threshold of 1,000 people mi^{-2}, UAs represent the urban core of metropolitan areas, and, therefore, results reflect intra-urban rather than urban-suburban differences.[207]

4.2.2 Population-Weighted Census-Tract NO_2 Inequalities

I calculate population-weighted NO_2 census tract-averaged TVCDs with race and ethnicity and sort tracts by household poverty status or median household income using the U.S. Census database for 2019 (Text A4.1). Race-ethnicity groups are defined following the U.S. Census categories of Black and African Americans, Asians, American Indians and Native Alaskans, referred to in the text as Native Americans, and whites, excluding people from each racial group identifying as Hispanic or Latino, and Hispanics/Latinos, including all races also reporting as Hispanic and/or Latino. Poverty status is defined according to the U.S. Census Bureau definition using the household income-to-poverty ratio. Households are categorized as below the poverty line if their income is below the U.S. Federal Poverty Guidelines poverty threshold, which scales with the number of people per household. Census tracts are classified as follows: below the poverty line, >20% of tract households at or below an income-to-poverty ratio of one; near poverty, all tract households having an income-to-poverty ratio of 1–1.24; and above poverty, all tract households having an income-to-poverty ratio >1.24. I discuss the sensitivity of these results to the 1.24 threshold in Text A4.1. I combine race-ethnicity and income categories, reporting results for Black and African Americans, Asians, Native Americans, and/or Hispanic/Latino residents in the lowest median income quintile tracts (LINs) and for non-Hispanic/Latino whites residing in the highest median income quintile tracts (HIWs). Household income quintiles are UA specific.

4.2.3 NO_x Inventories

The Fuel-based Inventory from Vehicle Emissions (FIVE18–19) is a U.S.-wide, 4 km x 4 km mobile source (on-road and off-road, gasoline and diesel engines) NO_x emissions inventory providing monthly mean hourly data, separately for weekdays, Saturdays, and Sundays.[193, 216, 219] Emission rates are based on publicly available fuel sales reports, road-level traffic counts, and time-resolved weigh-in-motion traffic counts. Fuel-use uncertainties are determined from differences between fuel sale reports and truck travel and traffic count site-selection and sample size. Emissions uncertainties are ±16% and ±17% for gasoline and diesel vehicles, respectively, and are derived from a regression analysis of near-road infrared remote sensing and tunnel studies.[90]

NO_x stationary source emissions are from the 2017 National Emissions Inventory (NEI17) updated January 2021 Version.[47] The NEI17 reports annual emission totals of point sources including industrial facilities, electricity generating units, oil and gas operations, and airports. Data for smaller industrial facilities, e.g., dry cleaners and gas stations, are voluntarily submitted by state agencies and counted as area rather than point sources. Here, I focus on annual NEI17 point source emissions and assume they exhibit no seasonal or day-to-day variability. A comparison of monthly time resolved NEI point source NO_x emissions in July and January indicated seasonal differences are indeed small (~5%). Emissions uncertainties in power plants are ±25%; uncertainties in industrial facilities and other stationary sources are larger and assumed to be ±50%.[90, 186]

4.2.4 Surface NO_2* Measurements

I use NO_2* surface measurements from 97 non-roadway monitors in 20 UAs identified as having at least three operating NO_2 monitoring stations during June 2018–February 2020 (Table A4.3).

Almost all of these NO_2 instruments operate by first decomposing NO_2 to NO over a heated molybdenum catalyst and measuring NO by chemiluminescence. NO_2 data collected with this technique have a known positive interference from oxidized and reduced nitrogen compounds, which also thermally decompose across the catalyst but at non-unity efficiency.[48] The nomenclature NO_2* is used in acknowledgement of this interference. Past research has shown the instruments capture NO_2 temporal patterns and NO_2 mixing ratios before substantial oxidation has occurred.[73] Because I are interested in the distance dependence of correlations between surface NO_2* and the overhead TROPOMI TVCDs, rather than the surface NO_2 mixing ratios themselves, I do not apply a correction factor to the NO_2* dataset.

4.2.5 Segregation Extent and Structure

I compute three complementary metrics to quantify and describe city-level racial segregation extent and structure, with segregation structure classified as clustered (mega-regions of segregation) or patch worked (micro-regions of segregation), based on the same 2019 U.S. Census tract-level demographics and UA boundaries as the inequality results. I calculate the Shannon Entropy Index, a measure of diversity and prevalence. Cities with low entropy have a small number of prominent groups, whereas cities with high entropy have roughly equal proportions of groups.[220] I describe the extent of urban segregation through the Information Theory Index, reflecting the amount of information that an individual's location carries about their demographic group.[220, 221] This is an aspatial metric describing the extent of segregation by comparing the demographic representation of a geographic unit to the overall city average.[222] I compute the mean local information density, a measure of the spatial scale of segregation, generating urban segregation structure estimates (clustered or patch worked) based on the Fisher information between spatial and demographic variables.[223]

4.3 Results and Discussion

4.3.1 NO_2 Inequality and the Role of Diesel NO_x Emissions

Across the 52 cities in our study, which represent 130 million residents, population-weighted NO_2 TVCDs are on average 17 ± 2% higher for Black and African Americans, 19 ± 2% higher for Hispanics/Latinos, 12 ± 2% higher for Asians, and 15 ± 2% higher for Native Americans compared to whites (city-level results are weighted by urban population size in the averaging). NO_2 TVCDs are on average higher for people living below (17 ± 2%) and near the poverty line (10 ± 2%) than for those above. When race-ethnicity and income are combined, I report an average of 28 ± 2% greater population-weighted NO_2 for LINs than HIWs, with the highest inequalities observed in Phoenix, Arizona (46 ± 2%), Los Angeles, California (43 ± 1%), and Newark, New Jersey (42 ± 2%) (Figure 4.1). In only one city, San Antonio, Texas, is the sign of LIN-HIW inequality negative over June 2018–February 2020 (–6 ± 3%), although a small number of negative values are also observed for the other metrics. In the five most-populated UAs, representing ~35% of the population, NO_2 TVCDs are 36 ± 3% higher for LINs compared to HIWs. Absolute NO_2 disparities (molecules cm^{-2}) are strongly associated with local city-level NO_2 pollution (Figure 4.1h), for example, the Pearson correlation coefficient (r) is 0.82 for the combined race-ethnicity and income metric (LIN-HIW). At the same time, relative inequalities (%) are only moderately associated with city-level NO_2 (r = 0.46), suggesting that sustained NO_x emission control will reduce but not eliminate NO_2 disparities, a result consistent with previous work investigating trends in NO_2 inequality between 2000 and 2010 using land-use regression NO_2 datasets.[11]

To observationally constrain city-wide effective contributions of HDDVs to NO_2 disparities, I first compare TROPOMI NO_2 inequalities on weekdays and weekends and then contextualize the measured changes using NO_x emission weekday-weekend patterns predicted by the FIVE18–19 (mobile sources) and NEI17 (point sources). HDDVs transport commercial goods and, due to decreased activity, their emissions are substantially reduced on weekends; at the same time, passenger vehicles (largely gasoline powered in the U.S.) and point source emissions exhibit much less weekday-weekend variability, although the timing of their emissions may change.[74, 199, 224] Off-road diesel engines (e.g., construction) also vary weekday to weekend; however, their contribution to total urban NO_x emissions is considerably smaller than on-road HDDVs. While HDDVs with NO_x control are a growing portion of the vehicle fleet, with reports of declining weekday-weekend NO_2 differences, HDDVs still emit an important fraction of urban NO_x.[90, 225] In the 52 UAs at the focus of this work, NO_2 TVCDs are an average of 34 ± 17% (1σ standard deviation) lower on weekends than weekdays (June 2018–February 2020). I define weekdays as Tuesdays–Fridays and weekends as Saturdays–Sundays. Monday and Saturday are considered transition days as they are influenced by carryover of yesterday's NO_2; therefore, I remove Mondays from our analysis but keep Saturdays to improve weekend statistics.

Weekday-weekend differences in city-level census-tract absolute TROPOMI NO_2 inequalities are fit using a weighted bivariate linear regression model with weights derived from errors in city-level NO_2 for the different residential populations (Table A4.4).[226] Because NO_2 concentrations better correlate with NO_x emission rates when the NO_2 atmospheric lifetime is short, I evaluate correlations in the summer separately from winter months. I determine the 'effective' HDDV contributions to inequalities from the regression slope, a combined function of changes in both the total NO_x emissions and the nonlinear NO_2-dependent NO_2 chemical lifetime. This method weights cities equally regardless of population. LIN-HIW disparities decrease by 37 ± 3% on weekends in the summer and 32 ± 2% in the winter (Figure 4.2a). Weekday and weekend inequalities are more strongly correlated in the summer (r = 0.93) than in the winter (r = 0.51), a function of seasonal differences in NO_2 lifetime but also reduced sampling statistics under cloudier wintertime conditions (Table A4.2). For race-ethnicity and poverty metrics, weekday-weekend differences are 28–46% in the summer (mapped in Figure A4.3) and more variable in the winter (0–41%). Weekday-weekend decreases in NO_2 TVCDs are therefore spatially variable within cities and larger in census tracts where residents are primarily people of color and/or have lower household incomes. Observed weekday-weekend NO_2 differences suggest greater weekend NO_x emission reductions in the most polluted neighborhoods, as summertime weekend NO_2 decreases are 50% larger in the highest quintile NO_2 census tracts than in the lowest quintile NO_2 tracts. In the winter, comparable weekday-weekend NO_2 differences are observed for the highest and lowest quintile NO_2 tracts, consistent with longer NO_2 lifetimes and greater distribution of NO_2 TCVDs away from NO_x emission sources in space and time (more day-to-day carryover).

Observed weekday-weekend differences in NO_2 TCVDs are a function of both the direct change in NO_x emissions and the subsequent indirect effects on the NO_x-dependent NO_2 lifetime. Weekday-weekend differences in NO_x emissions are driven by the fraction of total HDDVs that are parked on weekends and, to a smaller extent, weekday-weekend changes in spatiotemporal patterns in other vehicle types. To attribute observed differences in NO_2 disparities to a specific reduction in diesel traffic, I compare TROPOMI-based results with changes in NO_x emission densities (metric tons NO_x day^{-1} km^{-2}) and their resulting inequalities derived from the FIVE18–19 and NEI17. I first degrade the 0.01° x 0.01° oversampled TROPOMI product and FIVE18–19 database (4 km x 4 km) to the same 0.04° x 0.04° grid, average each to underlying census tracts, and calculate inequalities as described in Section 3.2.8. NEI17 sources are represented as points and summed within their respective tracts. Census tract-level FIVE18–19 and NEI17 are combined and normalized by tract areas to produce NO_x emissions densities. I analyze inventory-based results, and their comparison with TROPOMI, separately in the summer and winter.

Because I expect the coarser 0.04° x 0.04° grid to influence the observed inter-tract differences, I first compare census tract-averaged disparities based on the 0.01° x 0.01° oversampled TVCDs to those determined using the 0.04° x 0.04° TVCDs. I calculate the normalized mean biases and errors in the absolute and relative inequalities separately on summer and winter weekdays, using the 0.01° x 0.01° TROPOMI-based results as our reference values. Despite the loss of spatial detail, U.S.-wide normalized mean biases for the different inequality metrics are just <1–6% (Figure A4.1, Table A4.5). In fact, I generally calculate slightly higher NO_2 inequalities with the coarser-resolution NO_2 product than the 0.01° x 0.01° TVCDs, suggesting larger pixels have the effect of distributing NO_x emissions over larger spatial areas with similar demographic and income characteristics. The largest city-level normalized mean biases (8–22%) are observed in Oakland, San Diego, and San Francisco, CA, all cities that encompass narrow geographical areas along coasts that may even challenge the satellite analysis at 0.01° x 0.01°. While normalized mean biases are low on average across UAs, normalized mean errors for each metric are higher (3–13%), indicating inaccuracies are larger in individual cities because of the loss of spatial resolution. That said, I find the 0.04° x 0.04° TVCDs give comparable weekday-weekend NO_2 differences to the 0.01° x 0.01° product for all inequality metrics (Table A4.5). The coarse-resolution TVCDs yield weekday-weekend decreases in LIN-HIW disparities of 37 ± 4% and 38 ± 2% in the summer and winter, respectively, equaling results with the 0.01° x 0.01° TVCDs within uncertainties in the summer. This agreement is similar for the other metrics, indicating datasets resolved to 0.04° x 0.04° capture crucial census tract-scale patterns in the intra-urban spatiotemporal distribution.

Using the FIVE18–19 and NEI17, I calculate mean summertime weekday-weekend reductions in LIN-HIW disparities in NO_x emissions densities of 43 ± 4% (includes all source sectors), in agreement with TROPOMI-based weekday-weekend differences using the 0.04° x 0.04° TVCDs within associated uncertainties (Table A4.4). For race-ethnicity and poverty status, weekday to weekend decreases in emissions disparities equal empirical estimates to within 3–15%, with the inventories generally predicting comparable or slightly larger weekend reductions than TROPOMI. There is greater disagreement between NO_2 TVCDs and the inventories in the winter, with TROPOMI weekday-weekend differences in some race-ethnicity metrics being much smaller than estimated by the FIVE18–19 and NEI17. These wintertime discrepancies are consistent with seasonal patterns in NO_2 mesoscale transport (greater day-to-day carryover), further displacement of NO_2 away from NO_x emission sources, and more NO_x-suppressed chemistry, but may also be related to the reduced wintertime sampling statistics on weekdays and weekends.

Finally, I partition NO_x emission inequalities and weekday-weekend differences in disparities by source sector, focusing on the role of HDDVs. I limit the analysis to summer months, when NO_2 TVCDs are most responsive to NO_x emissions changes (Figure 4.2a). On weekdays, on-road

HDDVs cause on average (unweighted by urban population) 45 ± 5% of LIN-HIW NO_x emissions-based inequalities (Figure 4.2b; Table A4.6). The remainder is due to on-road gasoline-powered vehicles (38 ± 5%), gasoline and diesel off-road vehicles (13 ± 6%), and stationary sources (4 ± 6%), largely electricity generating units. Across the 52 UAs, HDDVs contribute significantly to mean (weighted by urban population) NO_x emissions inequalities for Black and African Americans (63 ± 13%), Hispanics/Latinos (52 ± 10%), Asians (36 ± 7%), and Native Americans (62 ± 12%) and for people living below and near the poverty line (56 ± 11%) (Figure A4.3). While HDDVs are the largest source of UA-level disparities, stationary sources may increase in importance if the analysis was conducted across more suburban metropolitan areas. Regulatory controls on gasoline-powered vehicles and electricity generation between 2000 and 2010 have been shown to have caused decreases in NO_2 inequalities (based on mixing ratios) from these sources across the U.S.[11, 193] HDDV NO_x emission densities decrease by 62 ± 2% on weekends, with diesel traffic still causing 26 ± 6% of LIN-HIW NO_x emissions inequalities on weekends. If the entire effective weekday-weekend change in NO_2 inequality observed by TROPOMI is caused by HDDVs, then a 62 ± 2% reduction in summertime weekday on-road HDDV emissions leads to a 37 ± 3% decrease in the corresponding NO_2 LIN-HIW disparities. I find that on average LIN-HIW NO_x emission densities from the other major source of emissions-based disparities, gasoline-powered vehicles, decrease by 10% weekday to weekend; however, NO_x emission inequalities change by less than 1% (Table A4.6), indicating that weekday-weekend differences in disparities are driven by HDDVs. If HDDV emissions were fully controlled (or their distribution was equalized), summer weekday LIN-HIW NO_x emissions-based inequalities would decrease by almost 50%. Likewise, elimination of on-road HDDV inequalities would lower disparities with race-ethnicity and poverty by 59% and 49%, respectively (Table A4.7). These predicted changes represent upper bounds, as U.S. urban chemical oxidation is trending toward NO_x-limitation.[10]

4.3.2 Resolving Census Tract-Scale Inequality from Space

Application of satellite remote sensing to NO_2 inequality requires demonstration that oversampled TROPOMI TVCDs capture inter-census-tract differences and spatial patterns that reflect those at the surface. In Demetillo et al. (2020), I found that TROPOMI-based results were comparable to NO_2 census tract-scale disparities determined using the high spatial resolution airborne sensor GCAS in Houston, TX. In addition, I used in situ NO_2 aircraft profiles and surface data to show similar spatial patterns in NO_2 columns and surface NO_2 mixing ratios. Because I do not have aircraft measurements for the 52 cities in our domain, I instead test the dependence of tract-level NO_2 inequalities on spatial heterogeneities in UA demographics. To evaluate relationships between column and surface NO_2 spatial distributions, I analyze Pearson correlation coefficients of TVCDs and surface NO_2* mixing ratios as a function of observation proximity.

Because of historical and contemporary racial discrimination, U.S. cities are segregated by race, ethnicity, and income—without segregation, air pollution disparities would not be possible. I find city-level race-ethnicity NO_2 inequalities are weakly associated with overall segregation extent ($r = 0.35$; $p = 0.010$) (Figure A4.4), suggesting UAs are sufficiently segregated to support intra-urban NO_2 disparities and NO_2 inequalities are more sensitive to changes in overall NO_2 pollution level. Segregation structure can be characterized along an axis between clustered segregation, where segregated census tracts spatially aggregate into larger contiguous regions (mega-regions of segregation), and patch-worked segregation, where the spatial scale of segregated tracts is small and adjacent tracts are more likely to have different demographic populations (micro-regions of segregation).[220, 223, 227] Segregation extent is typically higher in cities with patch-worked segregation; however, this is not always true (Figure A4.4).[223] For reference, Atlanta, GA typifies clustering, while New York City, NY exhibits segregation that is patch worked (Figure A4.5). This structural distinction is informative for the application of TROPOMI, as the 0.01° x 0.01° spatial resolution is coarser than many densely-populated tracts and oversampling has the effect of smoothing spatial gradients through averaging. Because NO_2 spatially varies at sub-census-tract scales, if the tract unit challenges the TROPOMI resolution, NO_2 disparities would positively correlate with increasing clustering, providing a test of the TROPOMI resolution at the tract scale.[111] Here, I compare race-ethnicity summer weekday NO_2 inequalities with urban race-ethnicity segregation structure (Figure A4.4). I find that city-level race-ethnicity NO_2 disparities are uncorrelated with segregation structure ($r = 0.07$, $p = 0.619$) and not positively associated with clustering, implying TROPOMI is indeed able to resolve inter-tract differences even when segregated tracts do not spatially aggregate. Past research has shown city-level NO_2 co-varies with urban form and density.[155, 228, 229] However, because I focus on the urban core, I cross-cut this variability, largely excluding urban-suburban form and density gradients.

To assess whether spatial distributions in NO_2 TVCDs reflect those at the surface, I compare NO_2 columns and mean daytime (12−3 pm LT) NO_2* surface mixing ratios as a function of the spatial proximity between tract-averaged TVCDs and the NO_2* nearest monitor.[151, 207] Census tract coverage is spatially continuous; however, there are instances where no tracts are identified within a given 1-km interval (i). Here, tract-averaged TVCDs are set equal the column value in the $i + 1$ distance interval, or infrequently the $i + 2$ interval. This largely occurs when comparing directly overhead tract-averaged TVCDs, so I limit the correction to columns ≤1 km from the nearest NO_2* monitor. The highest mean r values are observed when TVCDs and surface measurements are spatially coincident, 0.69 ± 0.05 in the summer and 0.60 ± 0.09 in the winter (Figure A4.6). However, I anticipate that r values (≤1 km) would be even higher if comparisons were instead based on the 0.01° x 0.01° product. At distances of 6–10 km, r values fall to 0.42 ± 0.07 (summer) and 0.30 ± 0.09 (winter). These results indicate that TROPOMI TVCDs indeed capture similar spatial patterns as measured at the surface, but also highlight that the NO_2* network is too spatially sparse to collect locally-relevant NO_2* levels for most residents.

4.4 Summary

I use TROPOMI observations to quantify NO_2 inequality in 52 major U.S. cities over June 2018–February 2020. I report average census tract-level population-weighted NO_2 disparities for Black and African Americans (17 ± 2%), Hispanics/Latinos (19 ± 2%), Asians (12 ± 2%), and Native Americans (15 ± 2%) compared to non-Hispanic/Latino whites, and for people living below (17 ± 2%) and near the poverty line (10 ± 2%) compared to those living above. Higher inequalities are found when race-ethnicity and income are combined, with 28 ± 2% greater population-weighted NO_2 for LINs than HIWs. For all metrics, much greater disparities are observed in some larger U.S. cities. Absolute NO_2 inequalities are strongly associated with UA NO_2 pollution; however, correlations between relative inequalities and city-level NO_2 are weaker. I use weekday-weekend differences in NO_2 TVCDs as empirical constraints on the impact of regulating HDDV NO_x emissions, showing that a 62% reduction in on-road diesel traffic would lead to a 37% decrease in LIN-HIW inequalities. While HDDV emissions contribute to the majority of NO_2 inequalities—63 ± 13% for Black and African Americans, 52 ± 10% for Hispanics/Latinos, 36 ± 7% for Asians, 62 ± 12% for Native Americans, and 56 ± 11% for people living below or near poverty line—

controlling them entirely would not eliminate NO_2 disparities. Finally, I provide additional evidence that oversampled TROPOMI observations resolve key patterns in the census tract-scale NO_2 distribution with NO_2 disparities being invariant with segregation structure and that spatial patterns in directly-overhead NO_2 columns reflect surface-level NO_2 spatial patterns.

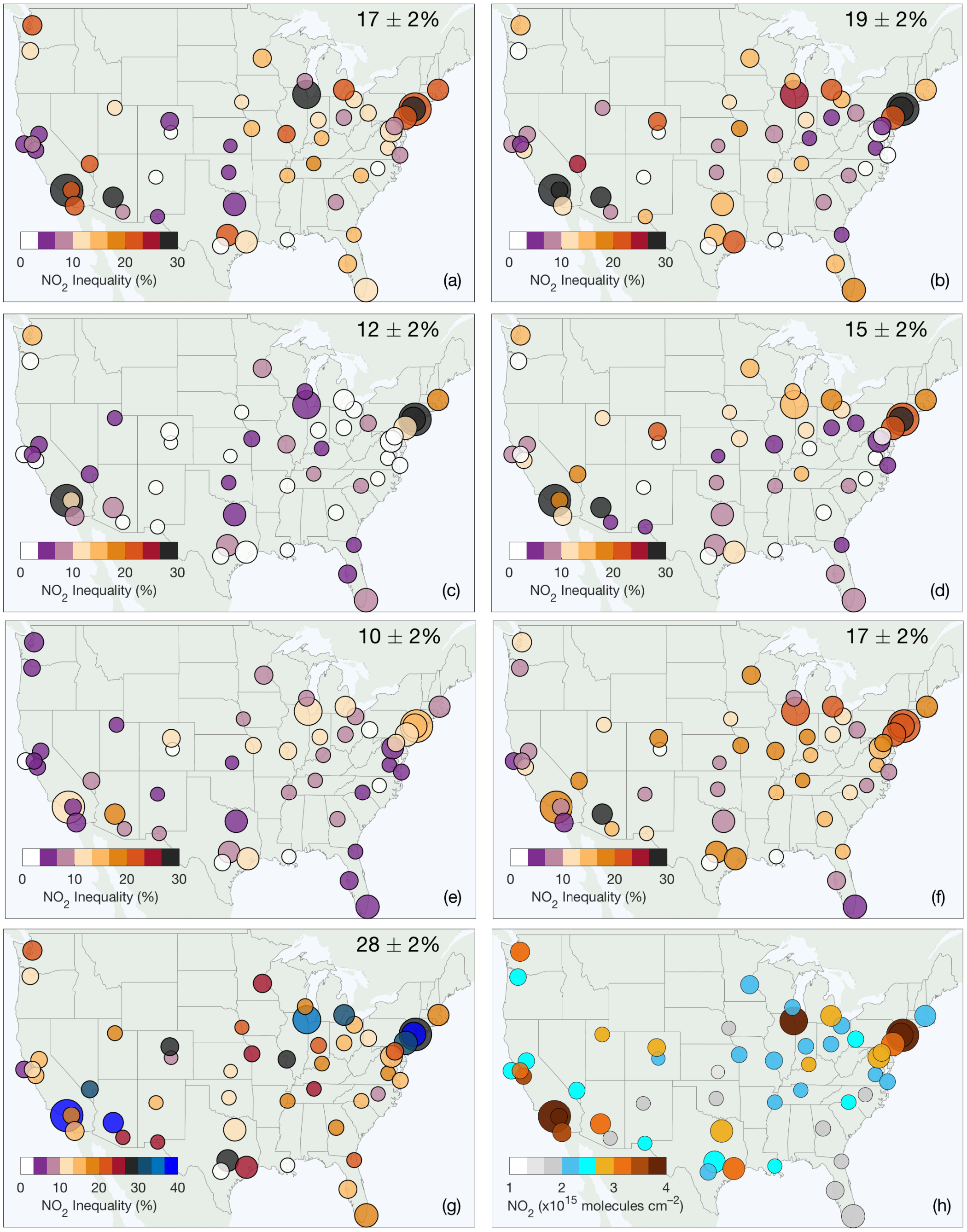

Figure 4.1. Relative NO_2 inequalities (percentage difference between population-weighted NO_2 means) for 52 major U.S. cities over all days in June 2018–February 2020. Marker size reflects the total city population with the smallest markers representing cities with <1.5 million residents and the largest markers for cities with >10 million residents. Average NO_2 inequalities are shown for Black and African American (a), Hispanic/Latino (b), Asian (c), and Native American (d) compared to white residents. Inequalities are also mapped for people living near (e) and below (f) versus above the poverty line and for LINs compared to HIWs (g). Displayed mean values for each group are weighted by urban population size. City-averaged NO_2 TVCDs are shown (h).

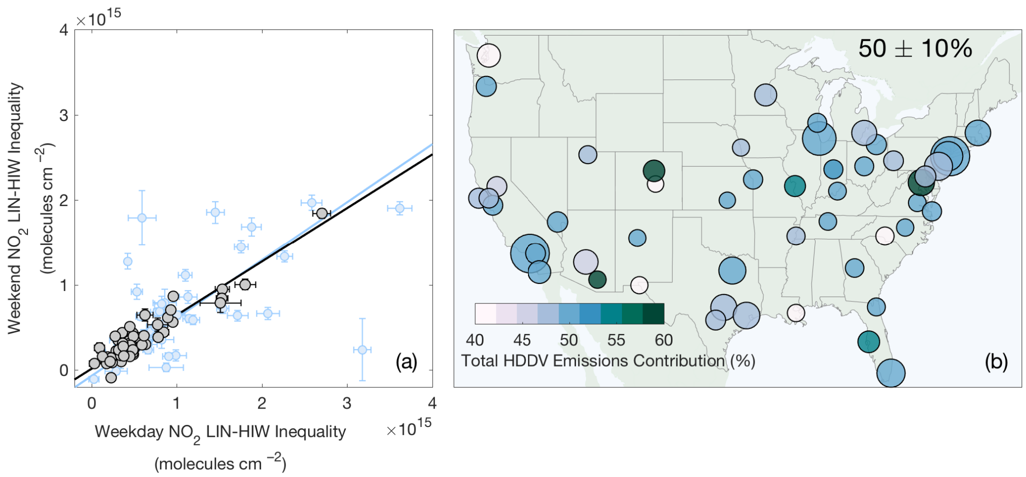

Figure 4.2. Absolute differences (molecules cm^{-2}) in population-weighted TVCDs NO_2 between LINs and HIWs on weekdays and weekends (a) in the summer (black) and winter (light blue). Percent contributions of on-road HDDVs to NO_x emission density-based LIN-HIW inequalities during summer months from the FIVE18–19 and NEI17 (b). The mean HDDV contribution to emissions inequality is displayed, weighted by urban population size.

Chapter 5: Concluding Remarks

5.1 Summary and Conclusions

In Chapter 2, I conducted a landscape-scale, observationally-based chemical analysis demonstrating that prolonged severe drought shifted the dominant PO_3 mechanisms in California. I found isoprene mixing ratios and their temperature-dependence remained steady throughout the pre and early drought periods, but under prolonged, severe drought conditions, decrease by 50%, with only partial recovery in the post-drought peak period. I found O_x weekday-to-weekend differences decreased from the early to severe drought period, indicating drought shifted PO_3 from NO_x-limited to more NO_x-suppressed, which must have been attended by sizable decrease in PO_3, estimated to be ~25%. I found high O_3 events between pre, early, and severe drought periods were statistically indistinguishable, indicating drought impacts on mixing were negligible. I also showed the O_3 abundance was relatively unaffected during the severe drought, with only a 6% decrease. Drought-related changes in LO_3 through chemistry were found to be only 1% of the total change in LO_3, leaving dry deposition to be the major loss pathway. As drought events are expected to increase in severity and frequency, steeper NO_x emissions declines will be required for these controls to be effective.[12, 13]

In Chapter 3, I presented a detailed methods-focused analysis demonstrating that current satellite-based NO_2 remote sensing captured the unequal burden between communities as a function of race-ethnicity and income in Houston, Texas. Prior to this analysis, intraurban inequality analyses were predominantly model-based and limited by lack of spatially continuous observations with sufficient resolution to resolve steep spatial gradients of NO_2. Using a novel sub-kilometer resolution NASA airborne dataset, I calculated NO_2 inequalities, defined as differences in population-weighted NO_2 means with on average 37 ± 6% higher NO_2 for people of color living in low-income census tracts than for white residents in high-income tracts. I found that NO_2 inequalities were always present despite considerable temporal variability, and that severe neighborhood-level NO_2 differences corresponded to an atmospheric stagnation event with hazardous levels of O_3. I repeated this analysis using the first full year of observations collected by TROPOMI, averaged with physics-based oversampling to increase the nadir spatial resolution of 3.5 km x 7 km to 0.01° x 0.01° (~ 1 km x 1 km). Relative NO_2 inequalities derived from these next-generation satellite observations were comparable to those from aircraft observations to within associated uncertainties, with long-term averaging effects and instrument uncertainties biasing space-based NO_2 observations low. Surface representation of these column-based NO_2 inequalities was confirmed through (1) an analysis of vertical NO_2 distribution within the convective boundary layer using 144 in situ vertical profiles and (2) a column-surface distance-dependent correlation analysis. The column-surface correlations declined steeply at the scale of typical NO_2 distance-decay gradients. I evaluated source contribution to inequality by combining these inequalities with assessment of emissions estimates from the National Emissions Inventory and the Fuel-based Inventory for Vehicle Emissions. In Houston, Texas, stationary sources were found to be the largest contributor to inequality (~75%) while mobile emissions sources were dominant by diesel emissions (~25%).

In Chapter 4, I extended the analysis developed in Chapter 3 to 52 major U.S. cities, and I observationally constrained the contribution of diesel traffic emissions to inequalities. Using two years of TROPOMI measurements combined with physics-based oversampling, I reported that NO_2 was 17 ± 2% higher for Black and African Americans, 19 ± 2% higher for Hispanics/Latinos, 12 ± 2% higher for Asians, and 15 ± 2% higher for Native Americans compared to non-Hispanic/Latino whites; and 17 ± 2% higher for people living below and 10 ± 2% near the poverty line compared to those living above. When race-ethnicity and income were combined, inequality was higher with 28 ± 2% greater population-weighted NO_2 for people of color living in low-income census tracts compared to non-Hispanic white residents in high income census tracts. I found absolute differences in tract-level NO_2 are strongly associated with NO_2 pollution; however, correlations between relative inequalities and city-level NO_2 are weaker. I conducted a column-surface correlation analysis and a resolution test using city segregation patterns providing further evidence of TROPOMI's ability to represent NO_2 spatial patterns at the surface and resolve NO_2 differences at the census tract level. I provide constraints on the impact of regulations on diesel NO_x emissions by calculating weekday-weekend differences in NO_2 and show that a 62% reduction in on-road diesel traffic would lead to a 37% decrease in LIN-HIW inequalities. The Biden Administration recently put forth tightened diesel emissions standards that will reduce diesel NO_x emissions by 60% by 2045, and my work in Chapter 4 tests the outcome of this rule on NO_2 inequalities. In fact, Demetillo et al. (2021) was cited multiple times during the EPA's public comment period on the proposed rule. Still, while diesel emissions are the largest contributor to intraurban NO_2 inequalities in U.S. on average, the dominant source type can vary between cities, for example in Houston, and controlling diesel emissions alone will not eliminate inequalities.

5.2 Future Directions

The work in this dissertation contributes to a larger body of literature providing material evidence of air pollution injustice within cities. Here, I have demonstrated that publicly available measurements offer new insights into which emissions sources drive neighborhood-level inequalities. While satellite data are useful for describing and informing policy making around the unequal distribution of a limited number of pollutants, much work is needed to address air pollution injustice within the multiscale framework in which inequality impacts people. Among these include: (1) to what degree equitable strategies can be both efficient and effective at reducing air pollution inequality and (2) how do location-specific characteristics (local meteorology, differences in dominant source type and distribution, urban landscape, surrounding geography, etc…) constrain the structure and scale of a potential solution framework, or put another way, how scalable are solutions? Because the issue of air pollution inequality is multidisciplinary, so must be the answers to the above considerations; however, atmospheric chemistry will remain a critical player in solutions-focused research.

While the Clean Air Act has improved air quality across the U.S., equity has not been central to its efforts, and air pollution inequalities have persisted. Future regulations should include equitable solutions. Studies investigating different storylines of mitigation efforts will be the most useful for optimizing efforts and resources towards environmental justice. Consideration of spatial scale is important, and to develop equitable and effective strategies towards addressing air pollution inequality in cities, we will need to understand the implications of focusing on city-wide and air basin scales. Cities across the U.S. have both shared and unique histories and presents that influence pollutant source compositions, landscapes, geographies, meteorology, and political processes and practices that can affect the efficacy air pollution controls.

We now have the spatial resolution to observe differences in air pollution at neighborhood levels and the computational and statistical tools with which to analyze these measurements and model potential solutions. It is important to leverage the informational strengths of each type of dataset available. Next-generation satellite observations from TROPOMI, and the upcoming TEMPO sensor, are powerful in their spatiotemporal continuity but lack longitudinal insight, such as provided by ground-based monitoring, which give context on how air pollution has changed over time. Aircraft, vehicle, and low-cost distributed network observations provide the spatial detail that further enhance information in satellite and ground-based observational analyses. Additionally, as modelling and data science techniques become more advanced, it will be even more critical to understand the strength, limitations, and information truly present in each dataset.

Finally, technical advancements are not enough and must be accompanied by community-centered research to make progress towards environmental justice. Local knowledge gained through mutually beneficial collaboration with people at the forefront of these issues can create new opportunities for innovative solutions. For instance, a longitudinal analysis using satellite observations can compare the efficacy of city-wide sector-based emission controls and location-specific (for instance those in neighborhoods of predominantly nonwhite and/or low-income communities) source regulation. Even more generally, community concerns and preferences may not be known by scientists, which when readily and seriously considered can open pathways towards more effective solutions.

Appendix A2

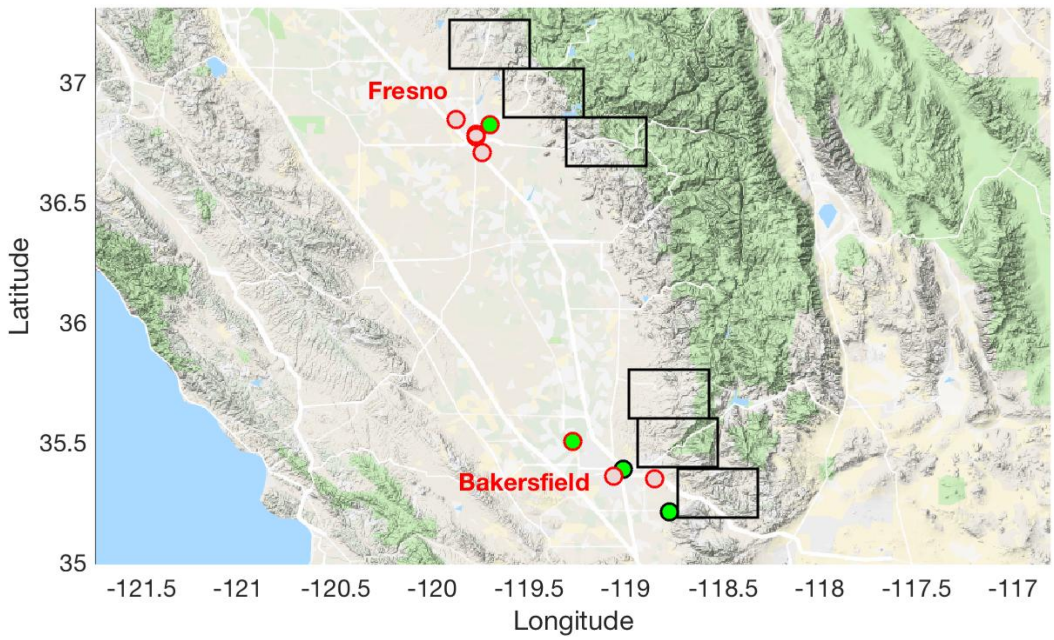

Figure A2.1 Areas included in EVI and LAI averages (black outlines). Isoprene (green), O_3, and NO_2* (red outline) measurement stations in the Clovis (Fresno) and Bakersfield area.

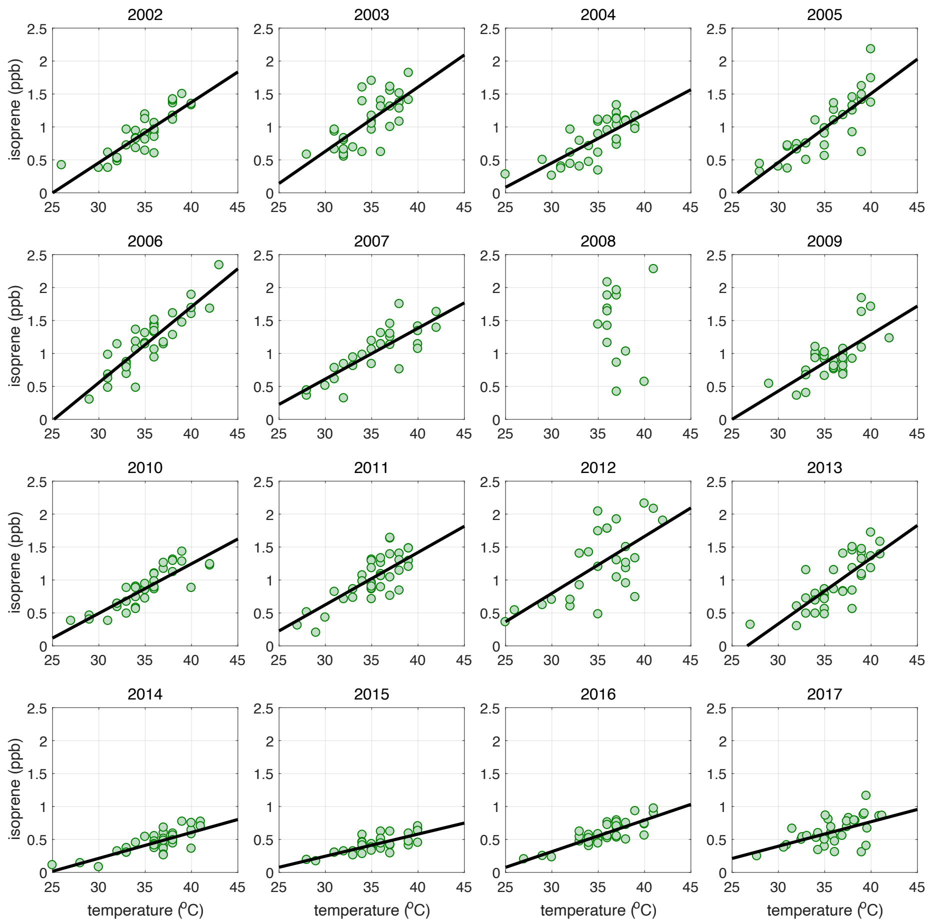

Figure A2.2. Daytime (10 am–6 pm LT) mean isoprene (ppb) versus daily maximum temperature (green circle) in Clovis for each day with observations over June–September. The fit is an ordinary least squares linear regression (black line).

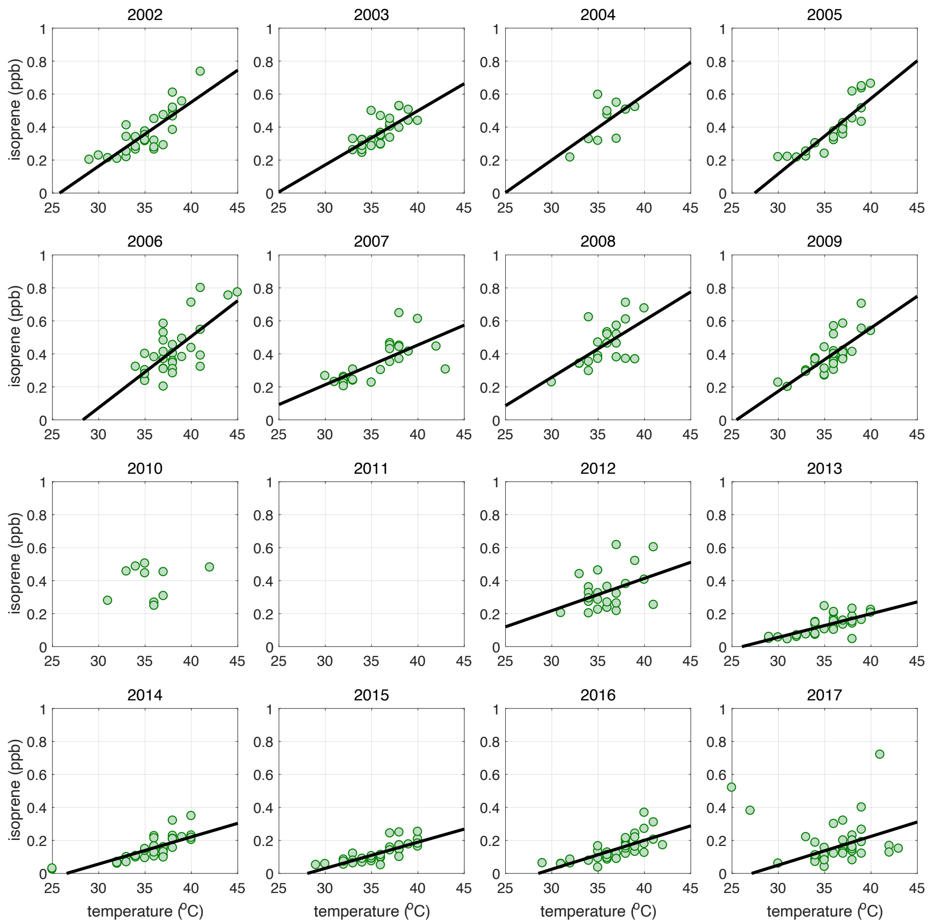

Figure A2.3. Daytime (10 am–6 pm LT) mean isoprene (ppb) versus daily maximum temperature (green circle) in Bakersfield for each day with observations over June–September. The fit is an ordinary least squares linear regression (black line).

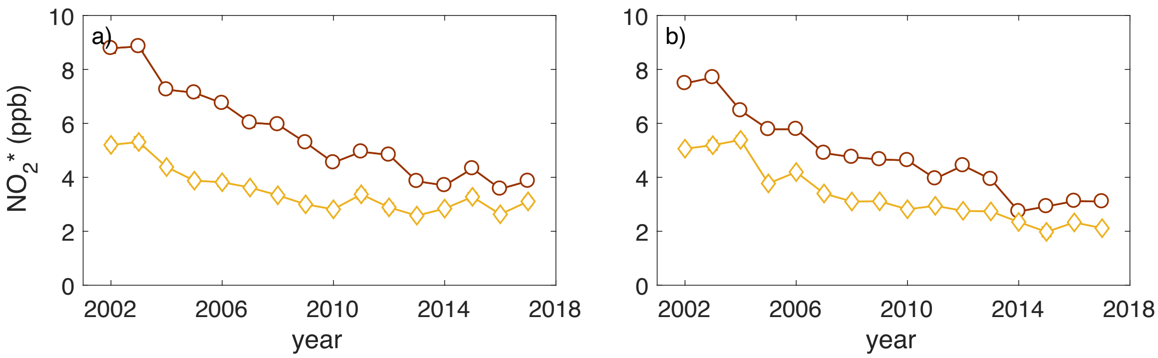

Figure A2.4. Afternoon (12–5 pm LT) NO_2* during O_3 season on weekdays (brown circles) and weekends (golden diamonds) in Fresno (panel a) and Bakersfield (panel b). Error bars representing standard mean errors are included but generally smaller than the markers.

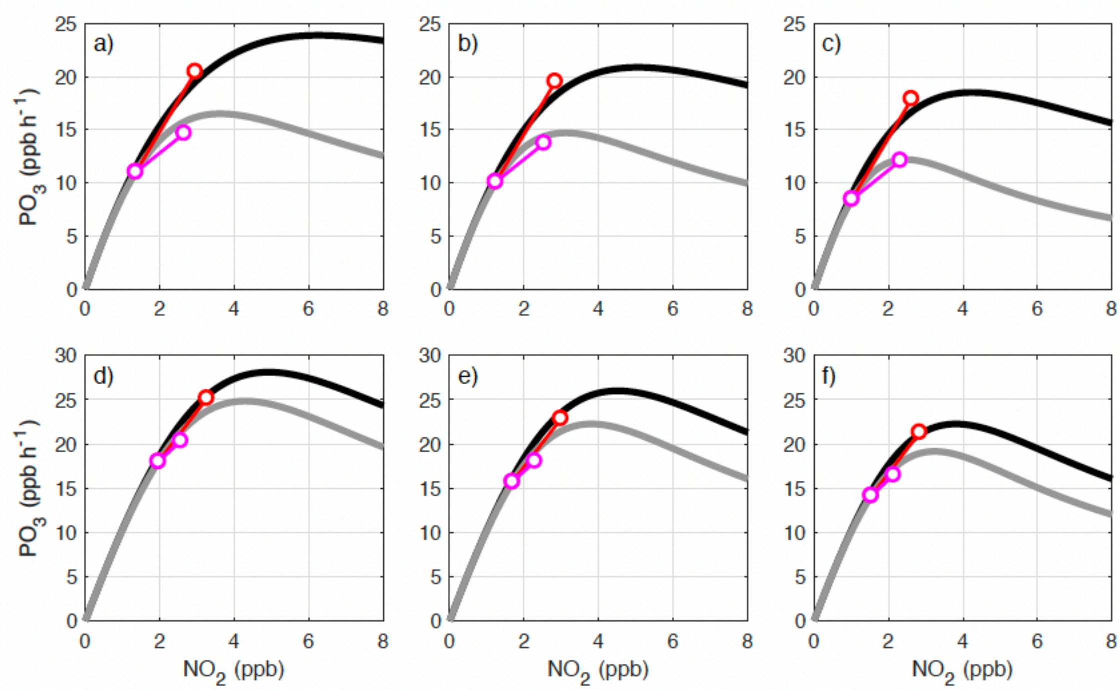

Figure A2.5. Modeled $P\mathrm{O}_3$ versus NO_2 at two organic reactivity to OH values for Fresno (panels a–c) and Bakersfield (panels d–f) under three example initial organic reactivity conditions. Observational constraints are measured $\Delta O_{x\ wd–we}$ / $\Delta NO_2{}^*{}_{wd–we}$ (an approximate of $\partial PO_3/\partial NO_x$), $\Delta NO_2{}^*{}_{wd–we}$, and the observation that $\Delta P\mathrm{O}_{3\ we}$ ~0. Early drought $\Delta O_{x\ wd–we}$ / $\Delta NO_2{}^*{}_{wd–we}$ are in red and severe drought $\Delta O_{x\ wd–we}$ / $\Delta NO_2{}^*{}_{wd–we}$ in magenta. In Fresno, calculated $\Delta P\mathrm{O}_3$ are (left to right): 25%, 25%, and 27%. In Bakersfield, calculated $\Delta P\mathrm{O}_3$ are (left to right): 16%, 17%, and 18%.

Table A2.1. Mean number of days with measurements (rounded to the nearest whole number) included in Table 1 calculations.

	pre-drought 2002–2010	**early drought 2011–2013**	**severe drought 2014–2015**	**post-drought 2016–2017**
Fresno				
Isoprene mixing ratio (ppb)	284	103	72	69
EVI (June–September)	72	24	16	16
LAI (June–September)	144	48	32	32
O_3 mixing ratio (ppb)	816	306	130	171
Weekday O_3 mixing ratio (ppb)	347	133	54	73
Weekend O_3 mixing ratio (ppb)	118	43	19	24
Weekday NO_2* mixing ratio (ppb)	415	158	72	90
Weekend NO_2* mixing ratio (ppb)	140	52	24	30
Daily maximum temperature (ºC)	992	372	248	214
Relative humidity (%)	271	90	59	58
Wind speed (m s^{-1})	712	363	244	241
Bakersfield				
Isoprene mixing ratio (ppb)	243	57	69	73
EVI (June–September)	72	24	16	16
LAI (June–September)	144	48	32	32
O_3 mixing ratio (ppb)	749	306	204	203
Weekday O_3 mixing ratio (ppb)	318	133	85	89
Weekend O_3 mixing ratio (ppb)	108	43	30	28
Weekday NO_2* mixing ratio (ppb)	386	158	101	106
Weekend NO_2* mixing ratio (ppb)	130	52	32	34
Daily maximum temperature (ºC)	924	372	248	247
Relative humidity (%)	555	196	128	132
Wind speed (m s^{-1})	547	79	132	131

Text A2.1 Analytical PO_3 model description

The analytical model is established set of equations to calculate PO_3[97, 230] built on the assumptions that HO_x ($HO_x \equiv OH + HO_2$) is conserved (eq. A2.1), peroxy nitrates (RO_2NO_2) are in steady state with radical precursors, and radical propagation dominates termination (eq. A2.2):

$$PHO_x = 2k_{HO_2+HO_2}[HO_2]^2 + 2k_{HO_2+RO_2}[HO_2][RO_2] + 2k_{RO_2+RO_2}[RO_2]^2 \qquad (A2.1)$$

$$+ k_{NO_2+OH}[NO_2][OH] + \alpha k_{NO+RO_2}[NO][RO_2]$$

$$[HO_2] = [RO_2] = \frac{k_{OH+RH}[RH][OH]}{(1-\alpha)k_{HO_2+NO}[NO]} \qquad (A2.2)$$

RH is any generic gas-phase organic compound. Radical propagation reactions are R1–R5 and termination reactions are R6–R10. Rate expressions are temperature dependent. The termination reaction rate expressions are (at 295 K): $k_{NO_2+OH} = 2.58\ x\ 10^{-11}$,[231] $k_{RO_2+RO_2} = 6.8\ x\ 10^{-12}$, $k_{RO_2+HO_2} = 8.0\ x\ 10^{-12}$, and $k_{HO_2+HO_2} = 2.74\ x\ 10^{-14}$.[232] RO_2 rates are for $C_2H_5O_2$.[98, 233]

(R1) $RH + OH \rightarrow R + H_2O$

(R2) $R + O_2 \rightarrow RO_2$

(R3) $RO_2 + NO \rightarrow RO + NO_2$

(R4) $RO + O_2 \rightarrow RCHO + HO_2$

(R5) $HO_2 + NO \rightarrow OH + NO_2$

(R6) $OH + NO_2 + M \rightarrow HNO_3 + M$

(R7) $RO_2 + NO + M \rightarrow RONO_2 + M$

(R8) $RO_2 + R'O_2 \rightarrow ROOR + O_2$

(R9) $RO_2 + HO_2 \rightarrow ROOH + O_2$

(R10) $HO_2 + HO_2 \rightarrow HOOH + O_2$

The OH concentration is solved for using the quadratic equation with PO_3 is approximately equal to (eq. A2.3):

$$PO_3 = k_{HO_2+NO}[NO][HO_2] + k_{RO_2+NO}[NO][RO_2] \qquad (A2.3)$$

Appendix A3

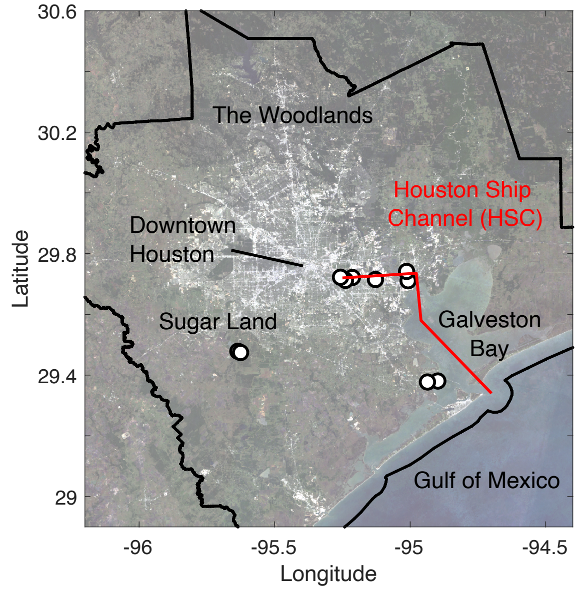

Figure A3.1. Study area with major NO_x sources, including oil refineries and power plants (circles) and the Houston Shipping Channel (HSC) (red line). Background map data: Landsat 8 composite over January 2017–June 2018.

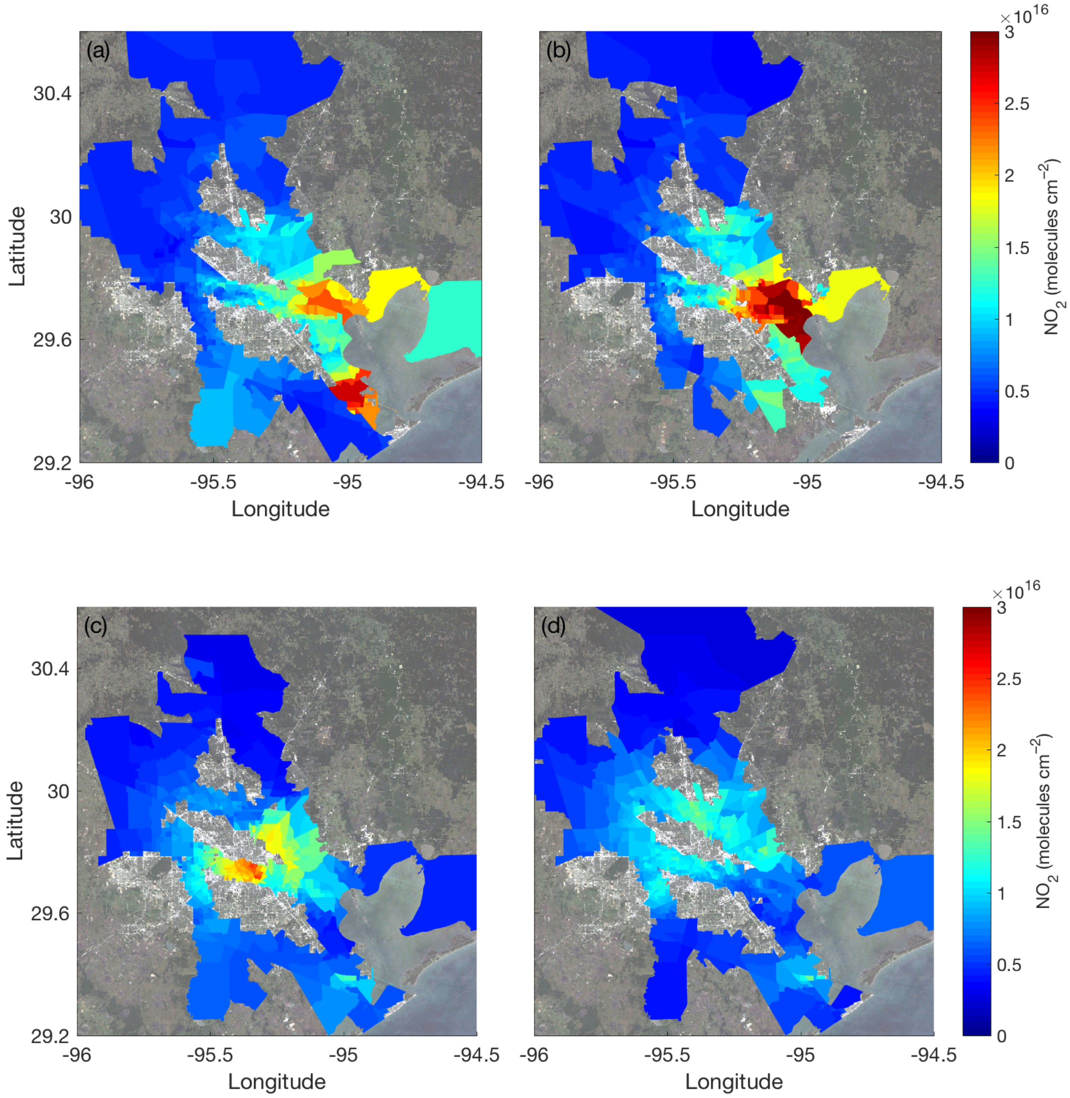

Figure A3.2. September 4, 2013 GCAS column observations (molecules cm^{-2}) averaged to census tracts for the early morning (panel a) and late morning (panel b) circuits and the early afternoon (panel c) and late afternoon (panel d) circuits. Background map data: Landsat 8 composite over January 2017–June 2018.

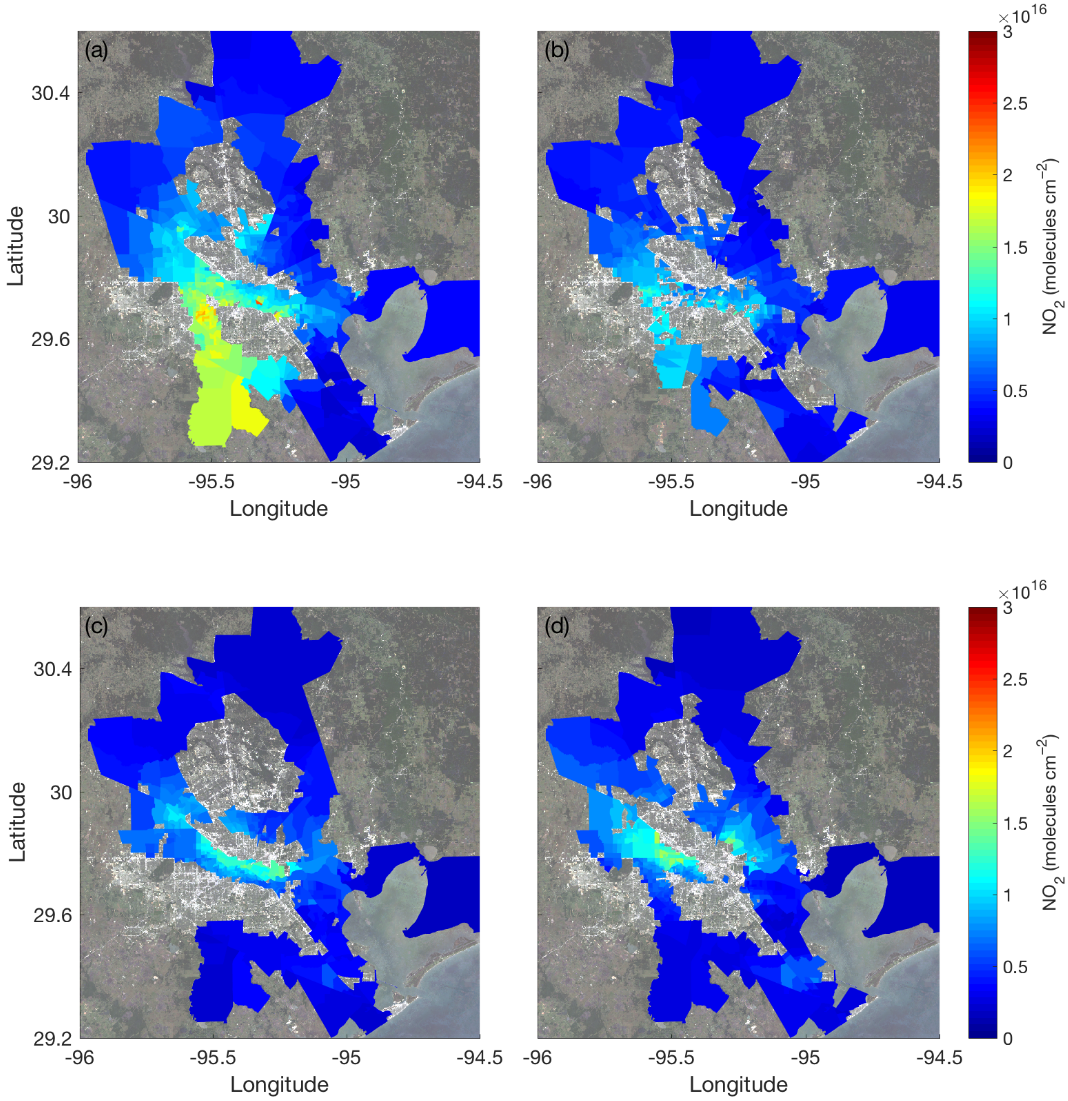

Figure A3.3. September 6, 2013 GCAS column observations (molecules cm^{-2}) averaged to census tracts for the early morning (panel a) and late morning (panel b) circuits and the early afternoon (panel c) and late afternoon (panel d) circuits. Background map data: Landsat 8 composite over January 2017–June 2018.

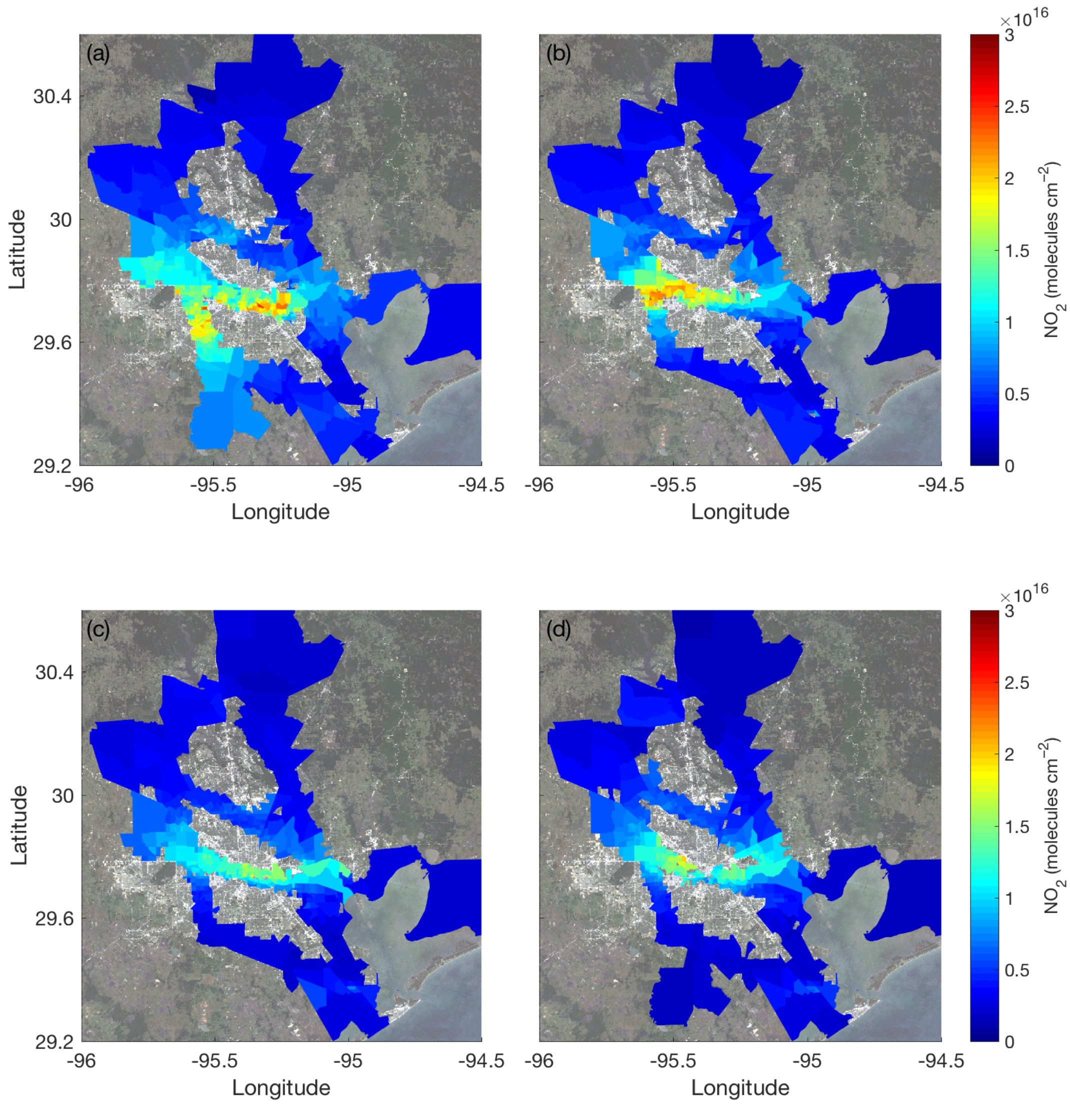

Figure A3.4. September 11, 2013 GCAS column observations (molecules cm^{-2}) averaged to census tracts for the early morning (panel a) and late morning (panel b) circuits and the early afternoon (panel c) and late afternoon (panel d) circuits. Background map data: Landsat 8 composite over January 2017–June 2018.

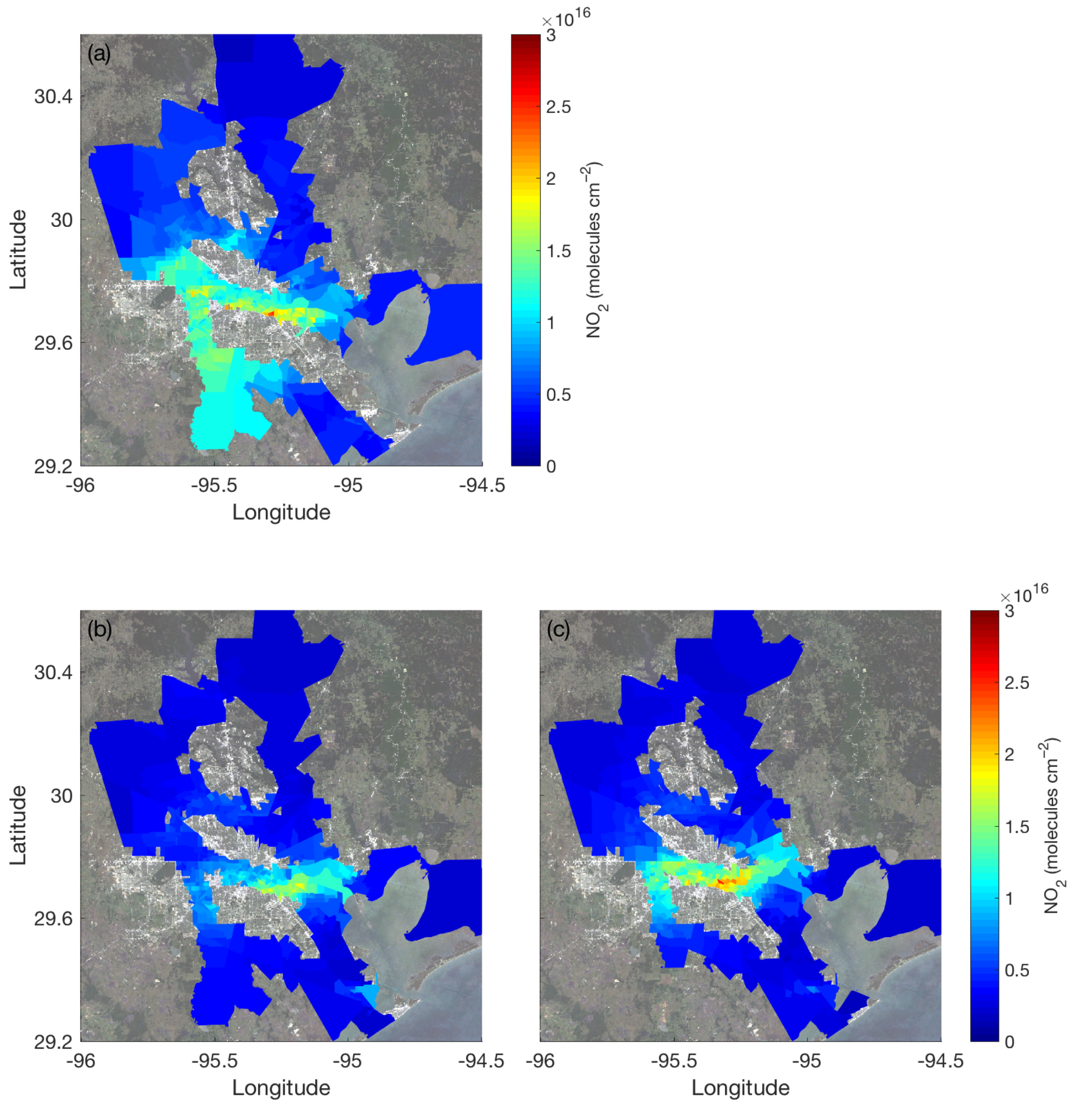

Figure A3.5. September 12, 2013 GCAS column observations (molecules cm^{-2}) averaged to census tracts for the early morning (panel a), early afternoon (panel b), and late afternoon (panel c) circuits. There were insufficient data collected during the second circuit in the morning flight to include. Background map data: Landsat 8 composite over January 2017–June 2018.

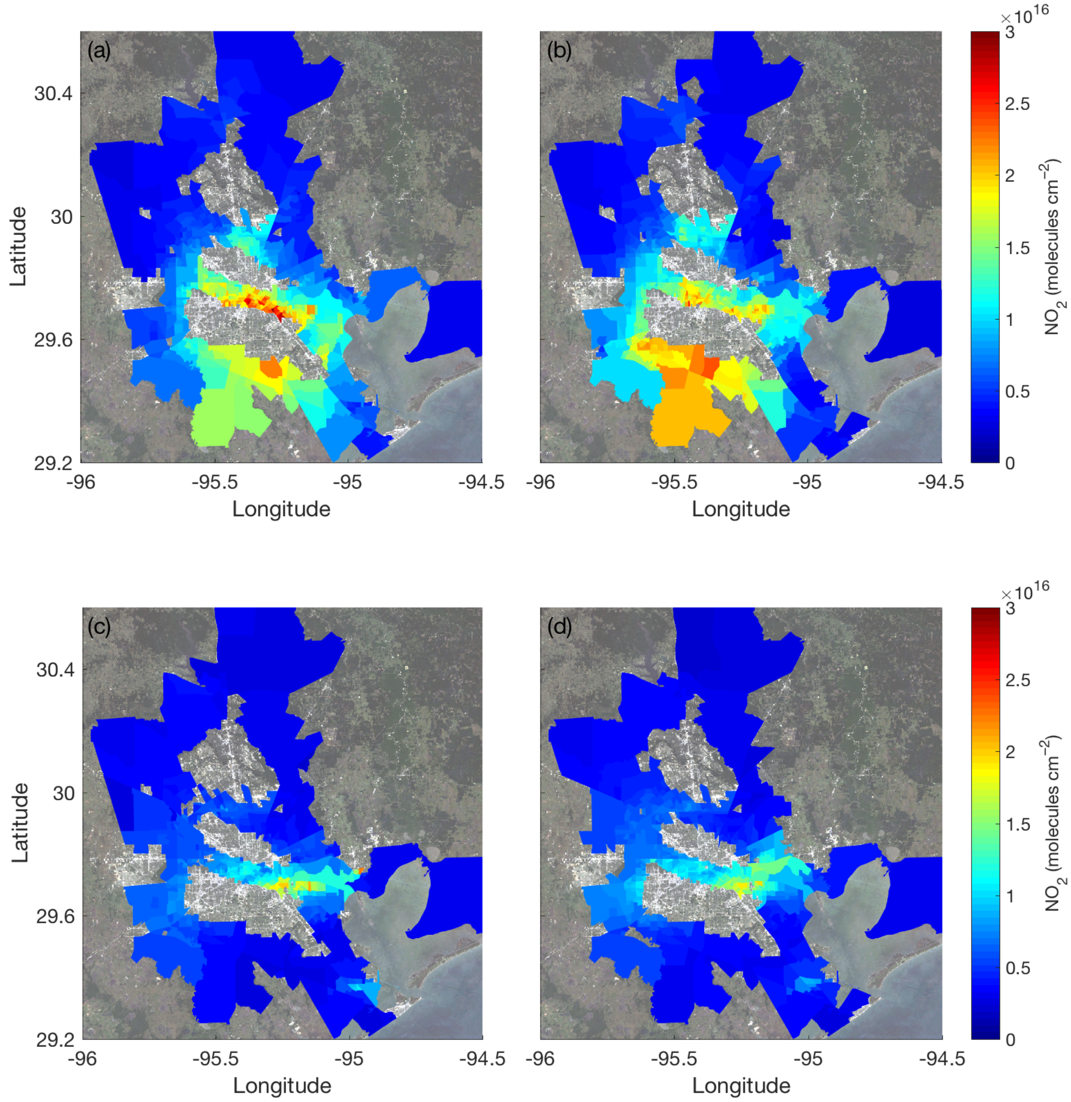

Figure A3.6. September 13, 2013 GCAS column observations (molecules cm^{-2}) averaged to census tracts for the early morning (panel a) and late morning (panel b) circuits and the early afternoon (panel c) and late afternoon (panel d) circuits. Background map data: Landsat 8 composite over January 2017–June 2018.

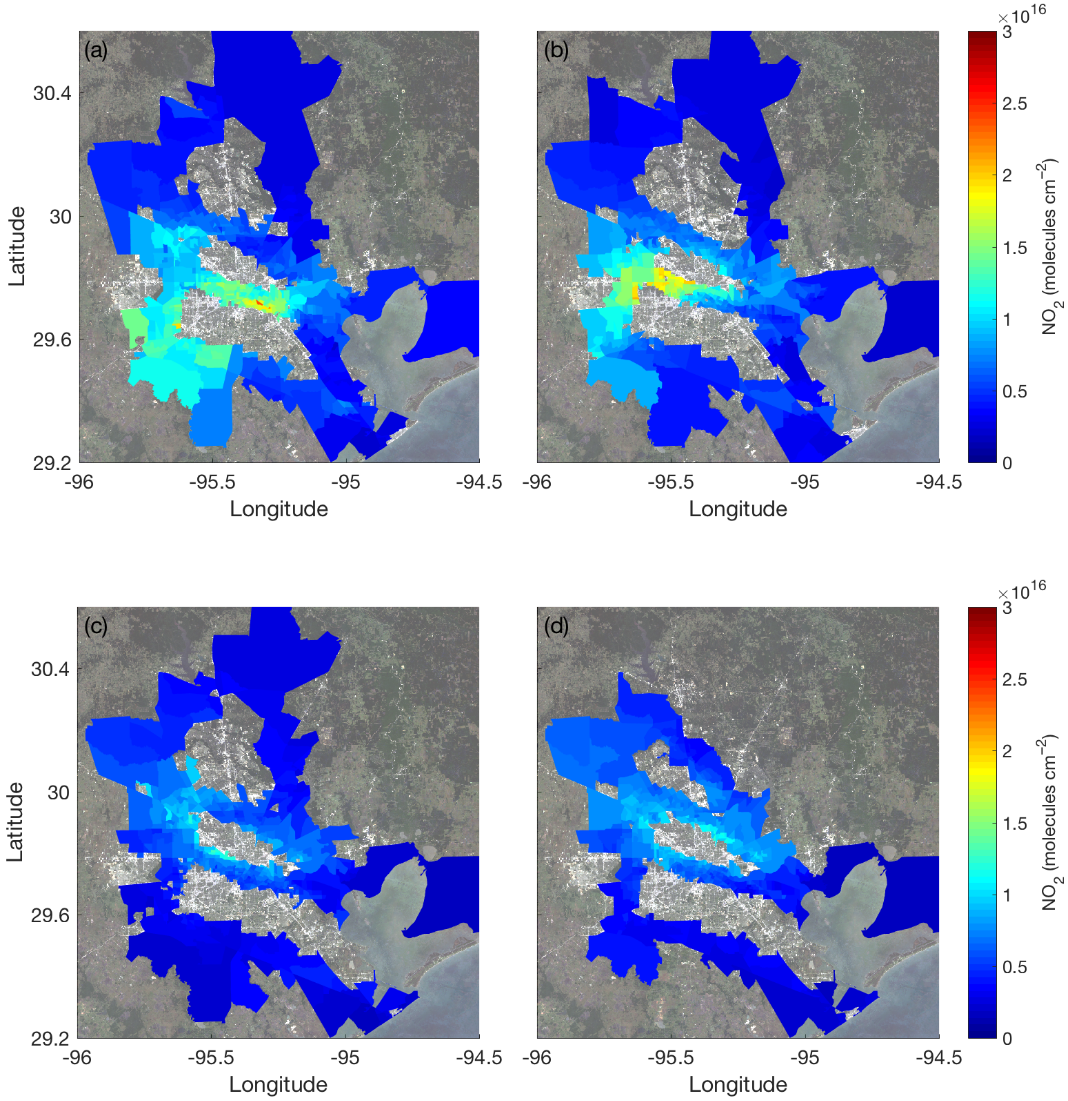

Figure A3.7. September 18, 2013 GCAS column observations (molecules cm^{-2}) averaged to census tracts for the early morning (panel a) and late morning (panel b) circuits and the early afternoon (panel c) and late afternoon (panel d) circuits. Background map data: Landsat 8 composite over January 2017–June 2018.

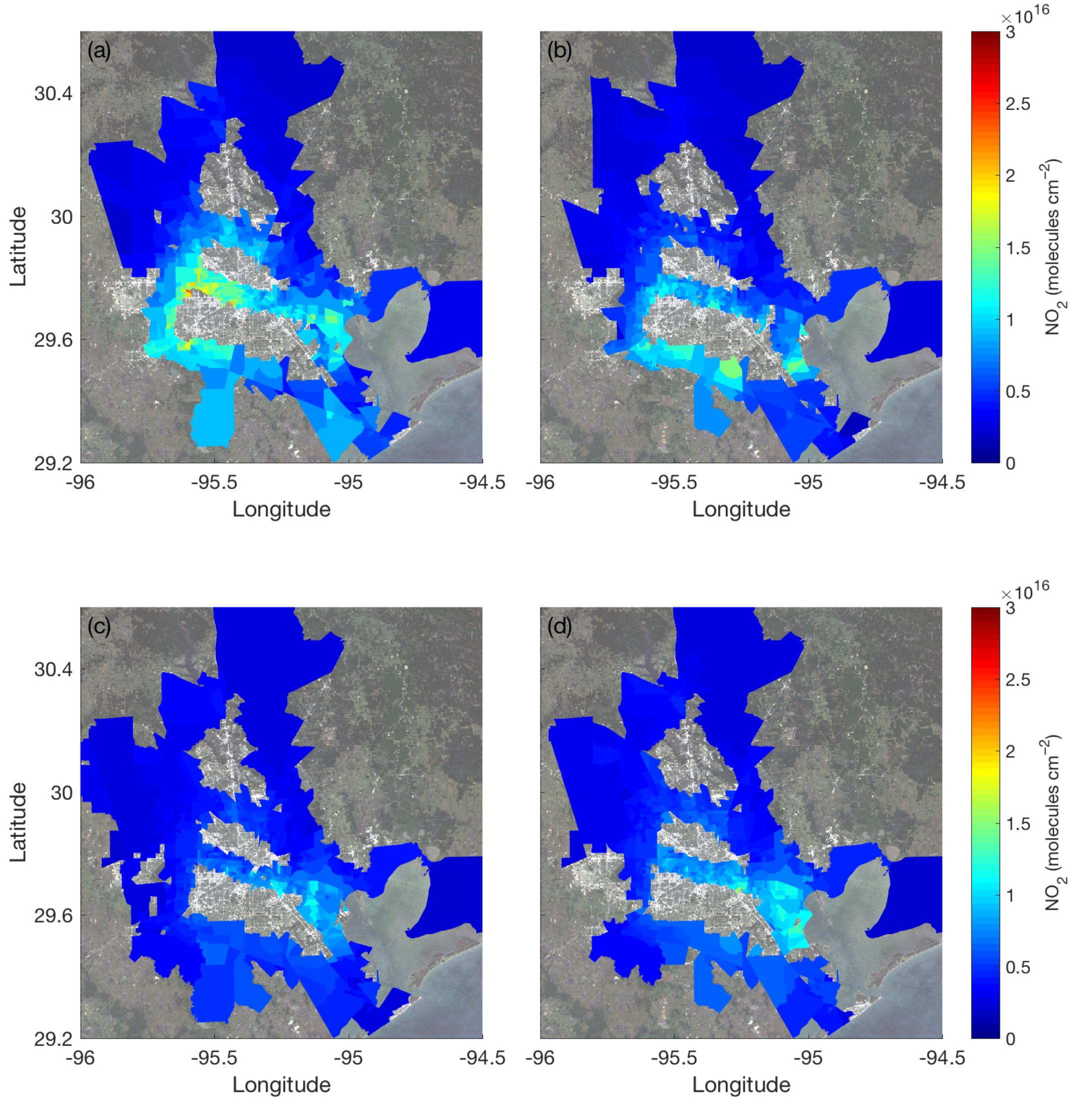

Figure A3.8. September 24, 2013 GCAS column observations (molecules cm^{-2}) averaged to census tracts for the early morning (panel a) and late morning (panel b) circuits and the early afternoon (panel c) and late afternoon (panel d) circuits. Background map data: Landsat 8 composite over January 2017–June 2018.

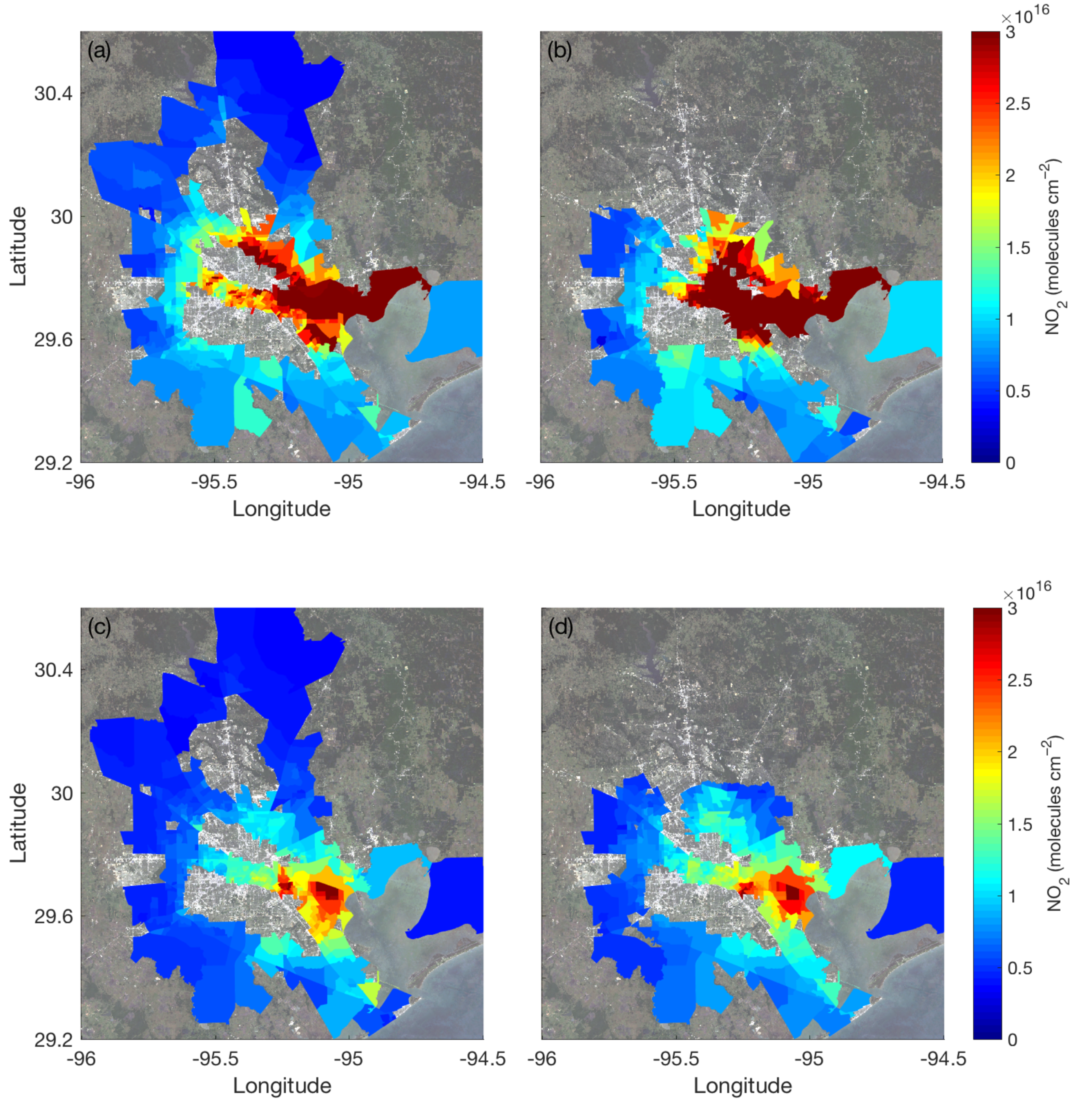

Figure A3.9. September 25, 2013 GCAS column observations (molecules cm^{-2}) averaged to census tracts for the early morning (panel a) and late morning (panel b) circuits and the early afternoon (panel c) and late afternoon (panel d) circuits. Background map data: Landsat 8 composite over January 2017–June 2018.

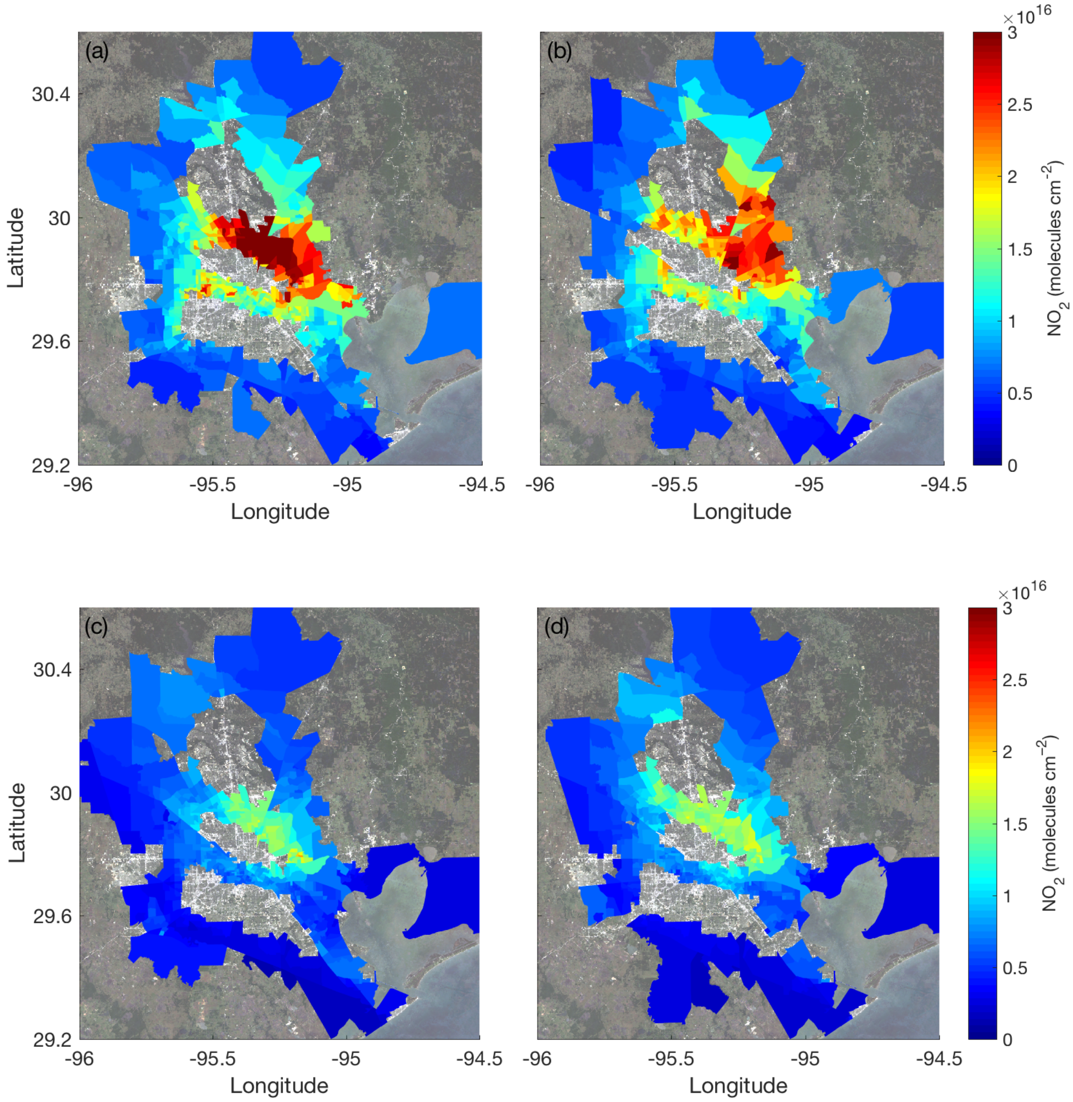

Figure A3.10. September 26, 2013 GCAS column observations (molecules cm^{-2}) averaged to census tracts for the early morning (panel a) and late morning (panel b) circuits and the early afternoon (panel c) and late afternoon (panel d) circuits. Background map data: Landsat 8 composite over January 2017–June 2018.

Table A3.1. Mean morning (7 am–12 pm LT) and afternoon (12–6 pm LT) wind direction and speed with 1σ standard deviation corresponding to each GCAS flight day as measured by surface monitors across the HMA (Methods).

	Morning		**Afternoon**	
	Wind Direction (Degrees)	Wind Speed (m/s)	Wind Direction (Degrees)	Wind Speed (m/s)
4 September	201 ± 96	4 ± 1	138 ± 24	7 ± 2
6 September	67 ± 36	7 ± 1	119 ± 12	8 ± 1
11 September	85 ± 17	8 ± 1	114 ± 11	9 ± 1
12 September	63 ± 14	8 ± 2	106 ± 22	9 ± 1
13 September	85 ± 80	6 ± 1	112 ± 33	8 ± 1
18 September	95 ± 21	8 ± 2	119 ± 7	10 ± 1
24 September	59 ± 76	7 ± 2	72 ± 89	7 ± 2
25 September	248 ± 78	4 ± 1	179 ± 87	5 ± 1
26 September	165 ± 40	6 ± 3	136 ± 10	8 ± 1

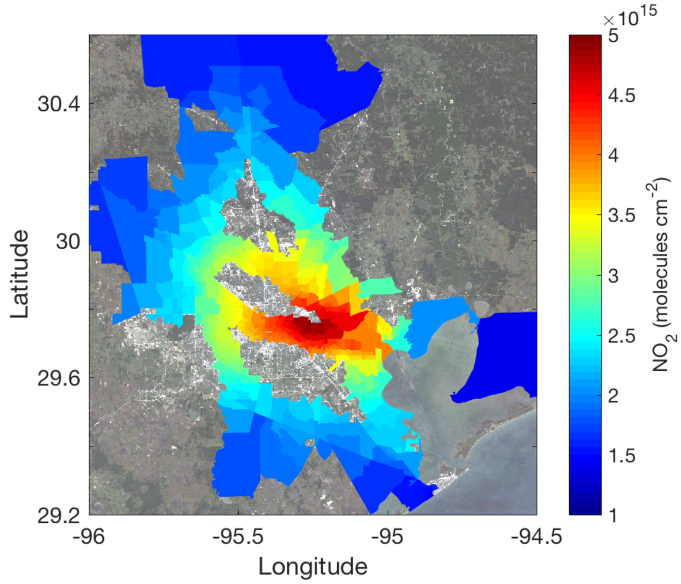

Figure A3.11. Weekday (Tuesday–Friday) TROPOMI NO_2 columns (molecules cm^{-2}) for June 2018–May 2019 averaged within census tracts along the 4-September morning flight track. Background map data: Landsat 8 composite over January 2017–June 2018.

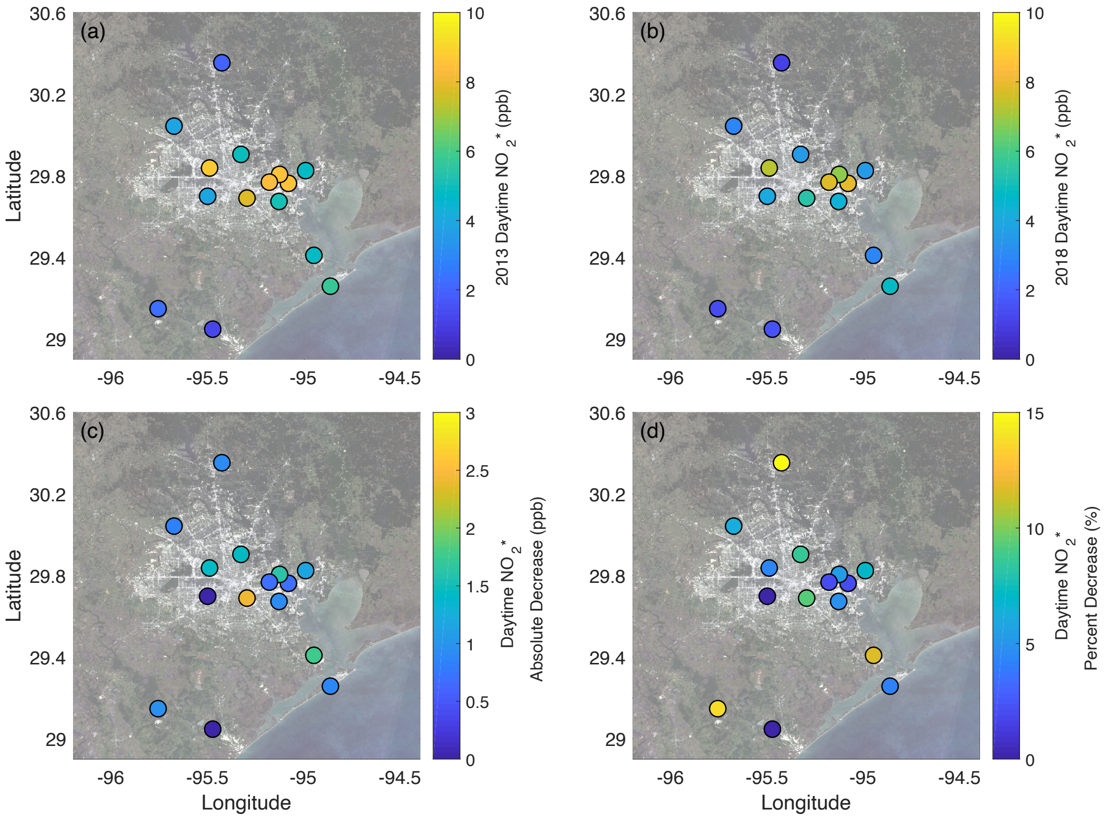

Figure A3.12. Annual (June–May), weekday (Tuesday–Friday), daytime (10 am–4 pm LT) averaged NO_2* (ppb) in 2013 (panel a) and 2018 (panel b). Absolute (panel c) and percent (panel d) change in daytime NO_2* between 2013 and 2018 (data in panels a and b). Monitoring sites included those with measurements in both 2013 and 2018: Houston Aldine (29.901°N, 95.326°W), Channelview (29.803°N, 95.125°W), Northwest Harris County (30.040°N, 95.674°W), Houston Bayland Park, (29.696°N, 95.499°W), Texas City 34th Street (29.406°N, 94.947°W), Conroe Relocated (30.350°N, 95.425°W), Park Place (29.686°N, 95.295°W), Wallisville Road (29.821°N, 94.990°W), Mustang Bayou (29.309°N, 95.200°W), Danciger (29.144°N, 95.757°W), HRM #3 Haden Road (29.765°N, 95.179°W), Manvel Croix Park (29.520°N, 95.393°W), Lynchburg Ferry (29.759°N, 95.079°W), Lake Jackson (29.044°N, 95.473°W), Galveston 99th Street (29.254°N, 94.861°W), and Houston Deer Park #2 (29.670°N, 95.129°W).

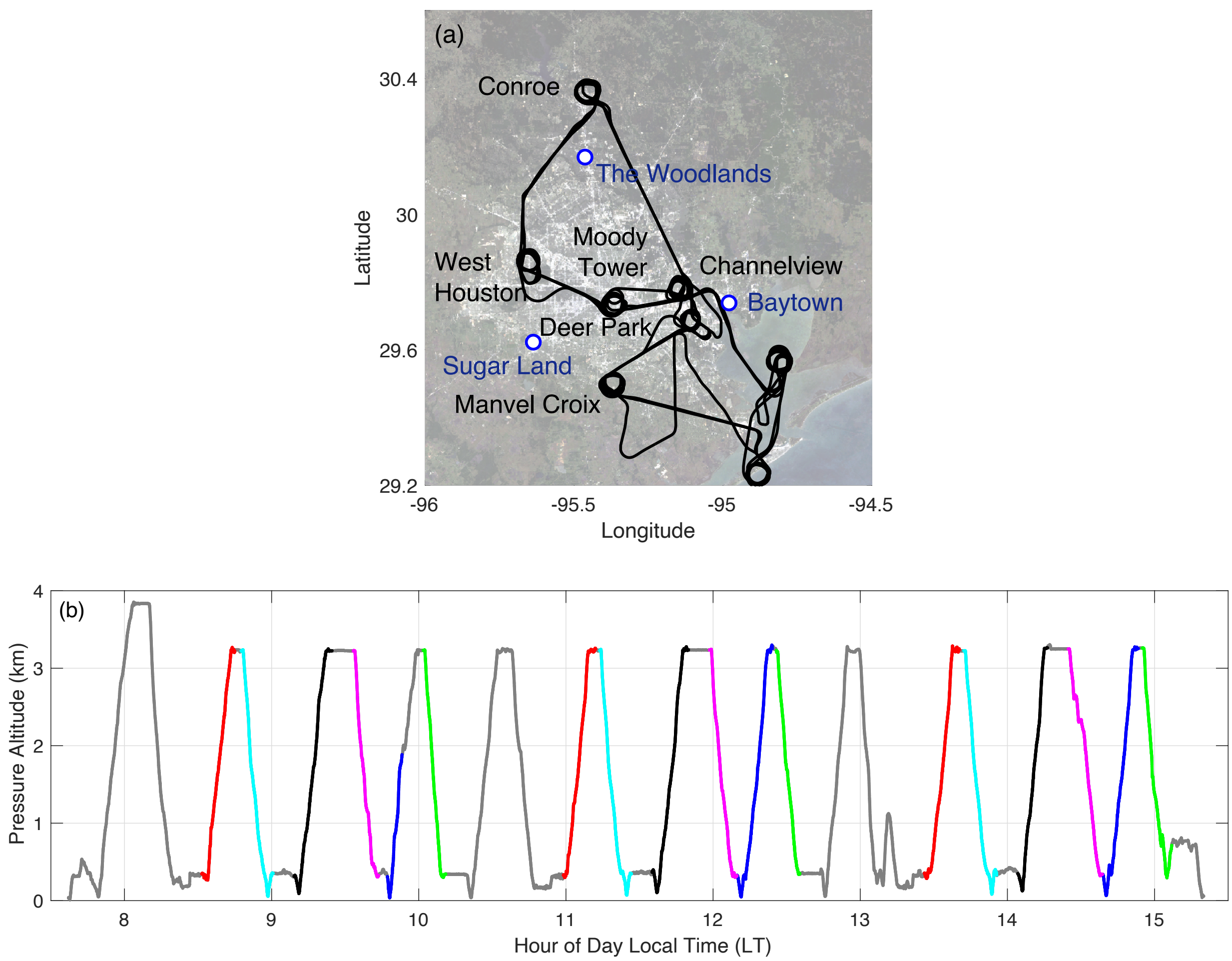

Figure A3.13. Sample NASA P-3B flight track (9/24) with profile locations (panel a) and altitude profile (km above sea level) (panel b) used in this analysis: Moody Tower (red), West Houston (cyan), Conroe (black), Channelview (magenta), Deer Park (blue), and Manvel Croix (green). Panel a background map data: Google.

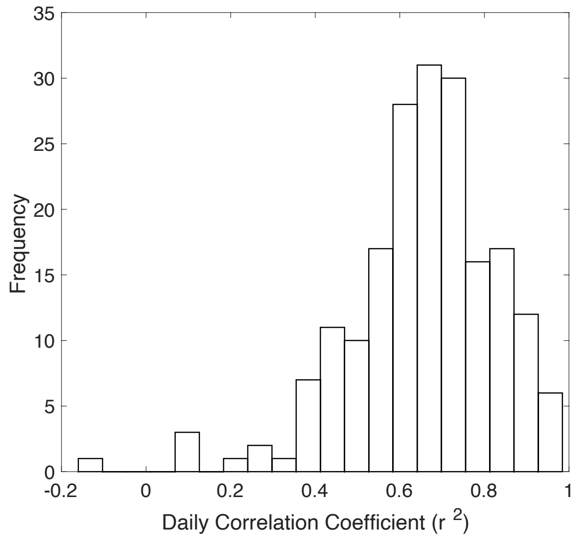

Figure A3.14. Linear correlation coefficients between overhead (within 1 km) tract-level TROPOMI columns, averaged annually (June 2018–May 2019), and individual daily (12–3 pm LT) NO_2* surface mixing ratios, both on weekdays (Tuesday–Friday). Correlation coefficients were only computed for days when at least 75% of monitoring stations provided data (at least 14 of 18 stations).

Table A3.2. P-3B profile time and convective boundary layer (CBL) height (above ground level, agl), fraction of the NO_2 column measured up to 3 km located below the CBL as measured and after interpolating the lowest-altitude NO_2 data point to the surface.

	Time			**CBL Height (agl)***			**Fraction NO_2 (Measured) below CBL**			**Fraction NO_2 (Interpolated to Surface) below CBL**		
	Profile 1	Profile 2	Profile 3	Profile 1	Profile 2	Profile 3	Profile 1	Profile 2	Profile 3	Profile 1	Profile 2	Profile 3
Channel View												
4-Sep	10.10	13.22	-	1.05	1.00	-	0.88	0.90	-	0.88	0.93	-
6-Sep	9.74	-	-	0.94	-	-	0.65	-	-	0.73	-	-
11-Sep	9.75	12.34	14.83	0.94	1.25	0.86	0.93	0.84	0.79	0.95	0.87	0.82
12-Sep	9.76	12.48	15.21	0.99	1.60	1.49	0.86	0.94	0.96	0.87	0.95	0.97
13-Sep	9.62	12.08	14.58	0.38	1.27	1.90	0.42	0.74	0.84	0.78	0.78	0.92
24-Sep	9.64	12.07	14.53	0.87	1.64	1.51	0.69	0.82	0.91	0.75	0.83	0.94
25-Sep	9.82	12.31	14.80	0.43	2.12	2.27	0.75	0.97	0.96	0.92	0.98	0.97
26-Sep	-	12.40	14.85	-	1.47	2.35	-	0.95	0.99	-	0.96	1.00
Mean	*9.77*	*12.41*	*14.80*	*0.80*	*1.48*	*1.73*	*0.74*	*0.88*	*0.91*	*0.84*	*0.90*	*0.94*
Moody Tower												
4-Sep	8.75	11.99	15.14	0.72	1.30	0.92	0.79	0.88	0.80	0.90	0.91	0.84
6-Sep	8.62	10.76	13.39	0.71	0.88	0.76	0.84	0.66	0.79	0.85	0.69	0.85
11-Sep	8.60	11.31	13.86	0.83	1.24	1.18	0.85	0.96	0.65	0.96	0.97	0.69
12-Sep	8.63	11.37	14.09	0.55	1.31	1.66	0.82	0.94	0.93	0.89	0.96	0.94
13-Sep	8.59	11.13	13.50	0.50	1.30	1.87	0.81	0.90	0.87	0.88	0.92	0.89
24-Sep	8.64	11.09	13.55	0.77	1.98	1.74	0.85	0.96	0.95	0.90	0.97	0.96
25-Sep	8.65	11.39	13.76	0.34	2.18	2.42	0.51	0.98	0.98	0.88	0.98	0.99
26-Sep	-	11.35	13.82	-	1.24	2.37	-	0.95	0.99	-	0.96	1.00
Mean	*8.64*	*11.30*	*13.89*	*0.63*	*1.43*	*1.61*	*0.78*	*0.90*	*0.87*	*0.89*	*0.92*	*0.90*
West Houston												
4-Sep	9.09	-	-	0.69	-	-	0.85	-	-	0.85	-	-
6-Sep	8.89	11.07	13.70	0.84	1.13	0.65	0.93	0.85	0.84	0.93	0.84	0.84
11-Sep	8.87	11.55	14.11	0.68	1.15	1.75	0.89	0.76	0.94	0.89	0.76	0.94
12-Sep	8.91	11.64	14.36	0.73	1.35	1.69	0.92	0.90	0.87	0.92	0.90	0.87
13-Sep	8.84	11.35	-	0.48	1.66	-	0.84	0.96	-	0.85	0.96	-
24-Sep	8.90	11.34	13.81	1.30	1.64	1.40	0.92	0.91	0.83	0.93	0.91	0.84
25-Sep	8.95	11.61	13.99	0.45	2.20	2.32	0.62	0.96	0.97	0.66	0.96	0.97
26-Sep	-	11.63	14.05	-	1.24	2.29	-	0.90	0.99	-	0.91	0.99
Mean	*8.92*	*11.46*	*14.01*	*0.74*	*1.48*	*1.68*	*0.85*	*0.89*	*0.91*	*0.86*	*0.89*	*0.91*
	Time			**CBL Height (agl)***			**Fraction NO_2 (Measured) below CBL**			**Fraction NO_2 (Interpolated to Surface) below CBL**		

	Profile 1	Profile 2	Profile 3	Profile 1	Profile 2	Profile 3	Profile 1	Profile 2	Profile 3	Profile 1	Profile 2	Profile 3
Conroe												
4-Sep	9.64	12.77	-	0.85	1.50	-	0.78	0.80	-	0.79	0.79	-
6-Sep	9.32	-	14.14	0.81	-	1.58	0.77	-	0.81	0.78	-	0.81
11-Sep	9.32	11.93	14.49	0.45	1.20	1.25	0.63	0.77	0.76	0.70	0.77	0.77
12-Sep	9.33	12.07	14.79	0.51	1.17	1.75	0.58	0.71	0.86	0.60	0.72	0.86
13-Sep	9.24	11.72	-	0.49	1.22	-	0.81	0.70	-	0.83	0.71	-
24-Sep	9.28	11.71	14.17	0.70	1.45	1.74	0.65	0.85	0.85	0.70	0.85	0.86
25-Sep	9.40	11.96	14.41	0.28	2.20	2.33	0.53	0.95	0.96	0.59	0.95	0.96
26-Sep	-	12.03	14.42	-	1.41	2.11	-	0.87	0.96	-	0.88	0.97
Mean	*9.36*	*12.03*	*14.40*	*0.58*	*1.45*	*1.79*	*0.68*	*0.81*	*0.87*	*0.71*	*0.81*	*0.87*
Deer Park												
4-Sep	10.41	13.55	-	0.75	0.42	-	0.75	0.69	-	0.72	0.70	-
6-Sep	9.99	-	14.75	0.74	-	0.52	0.80	-	0.74	0.78	-	0.72
11-Sep	10.02	12.63	15.12	0.70	1.08	0.82	0.89	0.90	0.89	0.89	0.90	0.89
12-Sep	10.04	12.76	-	1.08	1.54	-	0.94	0.96	-	0.94	0.96	-
13-Sep	9.85	12.30	14.91	0.55	2.71	1.94	0.93	1.00	0.96	0.93	1.00	0.96
24-Sep	9.84	12.29	14.77	1.08	1.99	1.99	0.93	0.96	0.98	0.94	0.96	0.98
25-Sep	10.07	12.54	15.00	0.56	2.40	2.31	0.79	1.00	0.99	0.81	1.00	0.99
26-Sep	-	12.62	15.11	-	1.23	2.33	-	0.93	0.99	-	0.94	0.99
Mean	*10.03*	*12.67*	*14.94*	*0.78*	*1.62*	*1.65*	*0.86*	*0.92*	*0.92*	*0.86*	*0.92*	*0.92*
Manvel Croix												
4-Sep	10.75	13.88	-	0.59	0.91	-	0.70	0.74	-	0.72	0.76	-
6-Sep	10.24	12.81	15.07	0.84	0.83	1.14	0.62	0.47	0.79	0.62	0.55	0.85
11-Sep	10.30	12.91	15.44	1.07	1.03	0.90	0.64	0.63	0.47	0.72	0.70	0.53
12-Sep	10.31	13.03	-	1.10	1.35	-	0.82	0.90	-	0.85	0.91	-
13-Sep	10.12	12.53	15.14	0.83	2.61	2.64	0.94	0.99	1.00	0.96	0.99	1.00
24-Sep	10.10	12.51	15.01	0.62	1.15	1.65	0.75	0.68	0.93	0.85	0.78	0.97
25-Sep	10.34	12.79	15.20	0.87	2.17	2.22	0.84	0.94	0.97	0.88	0.98	0.99
26-Sep	-	12.85	15.41	-	1.53	2.38	-	0.80	0.96	-	0.87	0.98
Mean	*10.31*	*12.91*	*15.21*	*0.84*	*1.44*	*1.82*	*0.76*	*0.77*	*0.85*	*0.80*	*0.82*	*0.89*

*Elevation: Channelview, 10 m; Moody Tower, 50 m; Conroe, 60 m; Deer Park, 20 m; West Houston, 30 m, and Manvel Croix, 20 m.

Table A3.3. P-3B profile time, mean NO_2 (ppb) within the CBL, mean NO_2 (ppb) below 500 m agl, and mean NO_2:NO_x below 500 m agl.

	Time			**Mean NO_2 below CBL height**			**Mean NO_2 below 500 m**			**NO_2:NO_x below 500 m**		
	Profile 1	Profile 2	Profile 3	Profile 1	Profile 2	Profile 3	Profile 1	Profile 2	Profile 3	Profile 1	Profile 2	Profile 3
Channel View												
4-Sep	10.10	13.22	-	11.56	5.90	-	11.07	8.22	-	0.68	0.81	-
6-Sep	9.74	-	-	1.04	-	-	1.59	-	-	0.74	-	-
11-Sep	9.75	12.34	14.83	2.29	2.10	3.73	3.09	2.45	3.94	0.73	0.74	0.76
12-Sep	9.76	12.48	15.21	1.39	0.95	2.95	1.88	0.98	4.76	0.77	0.79	0.79
13-Sep	9.62	12.08	14.58	3.76	1.23	0.94	1.87	2.24	2.29	0.79	0.80	0.83
24-Sep	9.64	12.07	14.53	0.93	0.61	0.72	1.27	0.69	1.30	0.74	0.84	0.78
25-Sep	9.82	12.31	14.80	8.43	2.02	1.78	5.52	3.71	3.17	0.79	0.86	0.89
26-Sep	-	12.40	14.85	-	3.38	1.36	-	5.19	5.33	-	0.82	0.82
Mean	*9.77*	*12.41*	*14.80*	*4.20*	*2.31*	*1.91*	*3.75*	*3.35*	*3.47*	*0.75*	*0.81*	*0.81*
Moody Tower												
4-Sep	8.75	11.99	15.14	3.02	6.39	2.03	4.07	6.86	2.09	0.54	0.80	0.82
6-Sep	8.62	10.76	13.39	4.39	2.95	3.12	5.73	3.25	2.95	0.69	0.75	0.72
11-Sep	8.60	11.31	13.86	3.99	2.75	3.27	11.09	3.48	3.32	0.73	0.74	0.84
12-Sep	8.63	11.37	14.09	4.08	1.68	2.02	4.48	2.21	2.67	0.71	0.78	0.82
13-Sep	8.59	11.13	13.50	5.65	2.81	1.57	5.44	3.45	1.27	0.79	0.80	0.85
24-Sep	8.64	11.09	13.55	4.39	0.93	1.04	5.35	2.08	1.55	0.66	0.79	0.79
25-Sep	8.65	11.39	13.76	7.30	1.22	1.79	2.62	3.56	2.48	0.83	0.85	0.87
26-Sep	-	11.35	13.82	-	1.58	0.88	-	1.62	1.62	-	0.84	0.83
Mean	*8.64*	*11.30*	*13.89*	*4.69*	*2.54*	*1.96*	*5.54*	*3.31*	*2.24*	*0.71*	*0.79*	*0.82*
West Houston												
4-Sep	9.09	-	-	2.27	-	-	2.27	-	-	0.66	-	-
6-Sep	8.89	11.07	13.70	3.84	1.40	3.75	4.49	1.60	3.99	0.71	0.81	0.81
11-Sep	8.87	11.55	14.11	3.72	2.46	1.65	4.40	2.63	2.08	0.74	0.84	0.87
12-Sep	8.91	11.64	14.36	3.99	1.12	0.93	4.74	1.14	1.05	0.73	0.86	0.86
13-Sep	8.84	11.35	-	3.30	1.85	-	3.19	2.09	-	0.79	0.84	-
24-Sep	8.90	11.34	13.81	1.26	0.42	0.51	2.97	0.56	0.64	0.74	0.82	0.86
25-Sep	8.95	11.61	13.99	1.96	0.50	0.59	1.76	0.70	0.79	0.82	0.85	0.88
26-Sep	-	11.63	14.05	-	1.09	0.80	-	1.22	1.06	-	0.85	0.87
Mean	*8.92*	*11.46*	*14.01*	*2.91*	*1.26*	*1.37*	*3.40*	*1.42*	*1.60*	*0.74*	*0.84*	*0.86*

	Time			Mean NO_2 below CBL height			Mean NO_2 below 500 m			NO_2:NO_x below 500 m		
	Profile 1	Profile 2	Profile 3	Profile 1	Profile 2	Profile 3	Profile 1	Profile 2	Profile 3	Profile 1	Profile 2	Profile 3
Conroe												
4-Sep	9.64	12.77	-	1.33	0.57	-	1.61	0.63	-	0.72	0.86	-
6-Sep	9.32	-	14.14	0.89	-	0.33	1.09	-	0.38	0.78	-	0.85
11-Sep	9.32	11.93	14.49	1.15	0.28	0.34	1.15	0.31	0.40	0.78	0.79	0.82
12-Sep	9.33	12.07	14.79	0.68	0.30	0.30	0.68	0.31	0.35	0.78	0.86	0.87
13-Sep	9.24	11.72	-	2.31	0.38	-	2.27	0.40	-	0.79	0.87	-
24-Sep	9.28	11.71	14.17	0.53	0.36	0.30	0.51	0.43	0.31	0.79	0.84	0.92
25-Sep	9.40	11.96	14.41	2.97	0.35	0.52	1.96	0.63	0.80	0.87	0.84	0.87
26-Sep	-	12.03	14.42	-	2.08	0.84	-	2.42	0.96	-	0.87	0.90
Mean	*9.36*	*12.03*	*14.40*	*1.41*	*0.62*	*0.44*	*1.32*	*0.73*	*0.53*	*0.79*	*0.85*	*0.87*
Deer Park												
4-Sep	10.41	13.55	-	9.52	4.82	-	9.77	4.16	-	0.60	0.80	-
6-Sep	9.99	-	14.75	2.60	-	1.40	2.50	-	1.40	0.74	-	0.68
11-Sep	10.02	12.63	15.12	1.83	1.39	1.55	2.17	1.53	2.31	0.72	0.76	0.80
12-Sep	10.04	12.76	-	2.74	2.05	-	3.48	2.32	-	0.75	0.81	-
13-Sep	9.85	12.30	14.91	6.32	1.48	2.24	6.81	2.10	2.47	0.77	0.82	0.83
24-Sep	9.84	12.29	14.77	4.00	1.22	1.55	5.88	2.88	2.56	0.71	0.72	0.77
25-Sep	10.07	12.54	15.00	44.92	5.98	5.17	46.26	6.56	5.56	0.75	0.86	0.91
26-Sep	-	12.62	15.11	-	1.49	0.65	-	1.92	1.76	-	0.84	0.85
Mean	*10.03*	*12.67*	*14.94*	*10.28*	*2.63*	*2.09*	*10.98*	*3.07*	*2.68*	*0.72*	*0.80*	*0.81*
Manvel Croix												
4-Sep	10.75	13.88	-	1.61	0.85	-	1.70	0.93	-	0.70	0.83	-
6-Sep	10.24	12.81	15.07	1.90	0.38	0.53	1.57	0.46	0.65	0.83	0.75	0.76
11-Sep	10.30	12.91	15.44	0.42	0.30	0.42	0.52	0.32	0.51	0.79	0.77	0.82
12-Sep	10.31	13.03	-	0.79	0.71	-	0.69	0.95	-	0.80	0.83	-
13-Sep	10.12	12.53	15.14	4.87	0.30	0.42	5.61	0.65	0.63	0.80	0.84	0.88
24-Sep	10.10	12.51	15.01	4.88	1.08	1.18	5.52	1.19	1.50	0.75	0.81	0.87
25-Sep	10.34	12.79	15.20	2.77	0.84	1.15	4.03	1.02	1.60	0.81	0.86	0.91
26-Sep	-	12.85	15.41	-	0.24	0.19	-	0.23	0.42	-	0.87	0.88
Mean	*10.31*	*12.91*	*15.21*	*2.46*	*0.59*	*0.65*	*2.80*	*0.72*	*0.89*	*0.78*	*0.82*	*0.85*

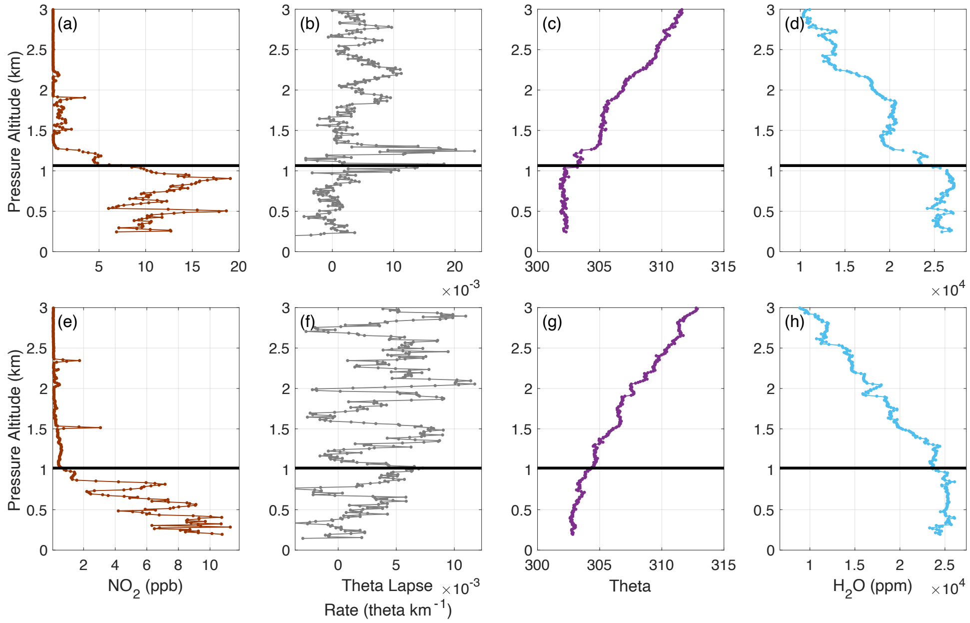

Figure A3.15. Channelview on September 4, 2013: P-3B vertical profile measurements averaged into 10-m altitude bins during the morning (panels a–d) and midday (panels e–h) circuits: NO_2 (ppb) (panels a and e), theta lapse rate (K km^{-1}) (panels b and f), theta (K) (panels c and g), and $H_2O_{(v)}$ (ppm) (panels d and h). Altitude data are pressure altitude above sea level (km). Lapse rates are 5-point running means of binned data. CBL heights (Methods) are shown as heavy black lines.

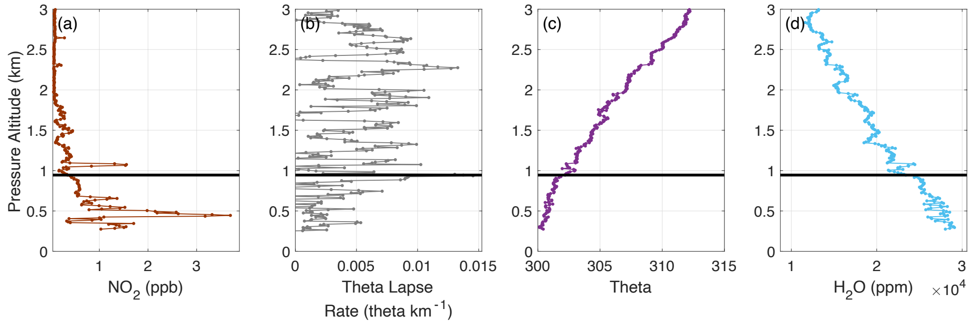

Figure A3.16. Channelview on September 6, 2013: P-3B vertical profile measurements averaged into 10-m altitude bins during the morning (panels a–d) circuit: NO_2 (ppb) (panel a), theta lapse rate (K km^{-1}) (panel b), theta (K) (panel c), and $H_2O_{(v)}$ (ppm) (panel d). Altitude data are pressure altitude above sea level (km). Lapse rates are 5-point running means of binned data. CBL heights (Methods) are shown as heavy black lines.

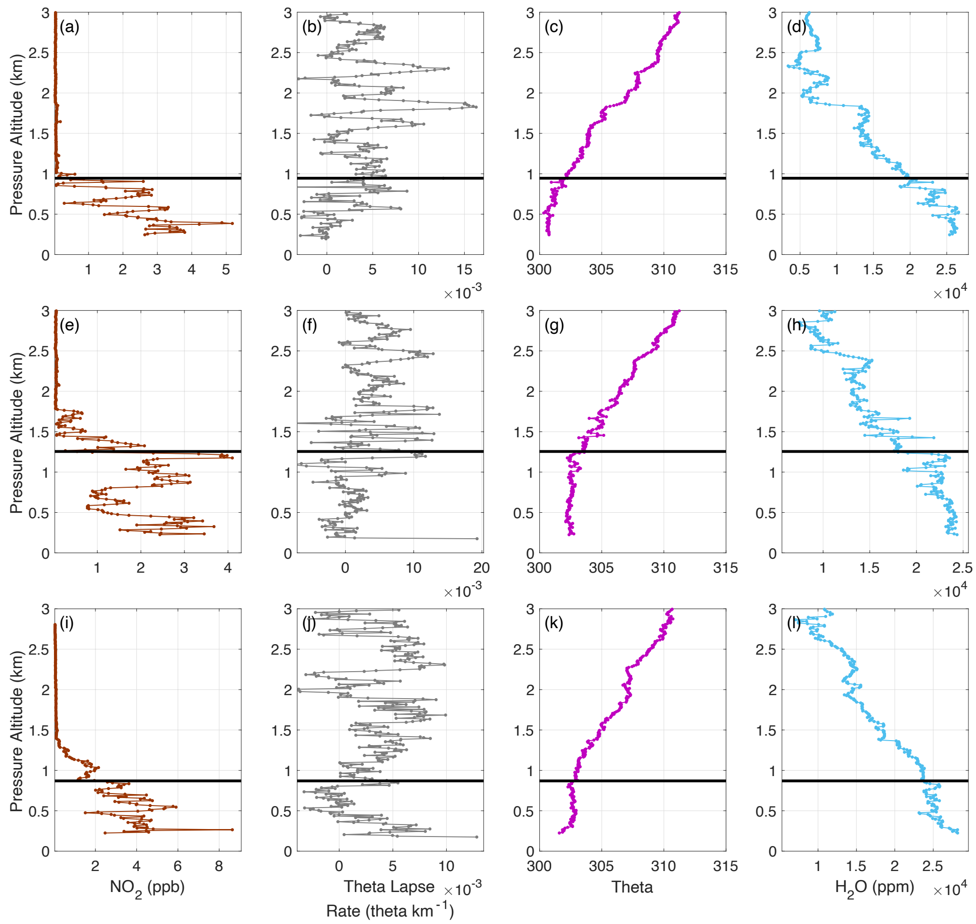

Figure A3.17. Channelview on September 11, 2013: P-3B vertical profile measurements averaged into 10-m altitude bins during the morning (panels a–d), midday (panels e–h), and afternoon (panels i–l) circuits: NO_2 (ppb) (panels a, e, and i), theta lapse rate (K km^{-1}) (panels b, f, and j), theta (K) (panels c, g, and k), and $H_2O_{(v)}$ (ppm) (panels d, h, and l). Altitude data are pressure altitude above sea level (km). Lapse rates are 5-point running means of binned data. CBL heights (Methods) are shown as heavy black lines.

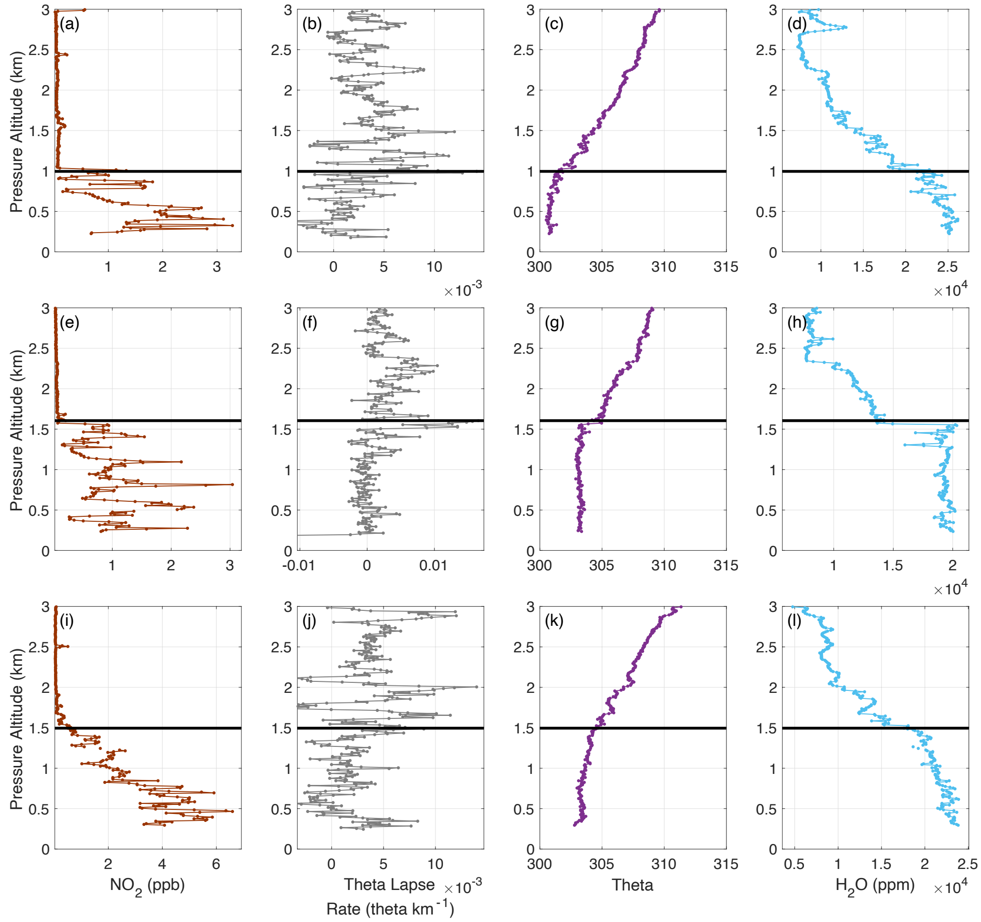

Figure A3.18. Channelview on September 12, 2013: P-3B vertical profile measurements averaged into 10-m altitude bins during the morning (panels a–d), midday (panels e–h), and afternoon (panels i–l) circuits: NO_2 (ppb) (panels a, e, and i), theta lapse rate (K km^{-1}) (panels b, f, and j), theta (K) (panels c, g, and k), and $H_2O_{(v)}$ (ppm) (panels d, h, and l). Altitude data are pressure altitude above sea level (km). Lapse rates are 5-point running means of binned data. CBL heights (Methods) are shown as heavy black lines.

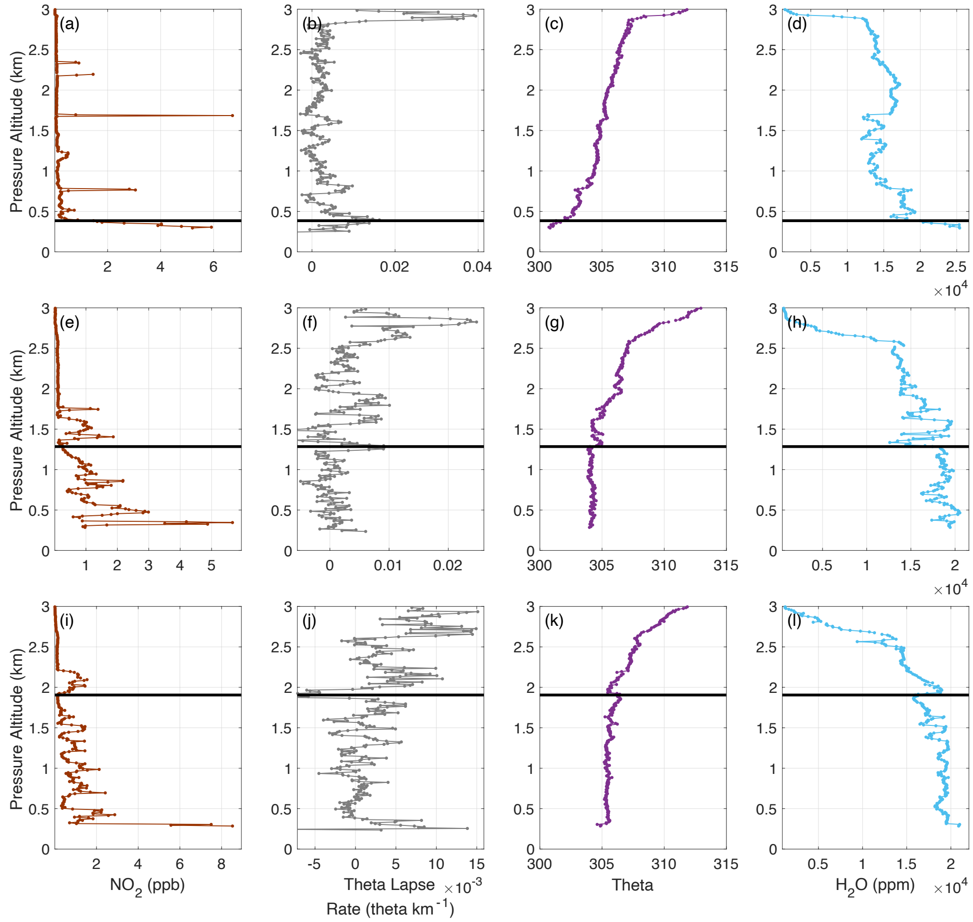

Figure A3.19. Channelview on September 12, 2013: P-3B vertical profile measurements averaged into 10-m altitude bins during the morning (panels a–d), midday (panels e–h), and afternoon (panels i–l) circuits: NO_2 (ppb) (panels a, e, and i), theta lapse rate (K km^{-1}) (panels b, f, and j), theta (K) (panels c, g, and k), and $H_2O_{(v)}$ (ppm) (panels d, h, and l). Altitude data are pressure altitude above sea level (km). Lapse rates are 5-point running means of binned data. CBL heights (Methods) are shown as heavy black lines.

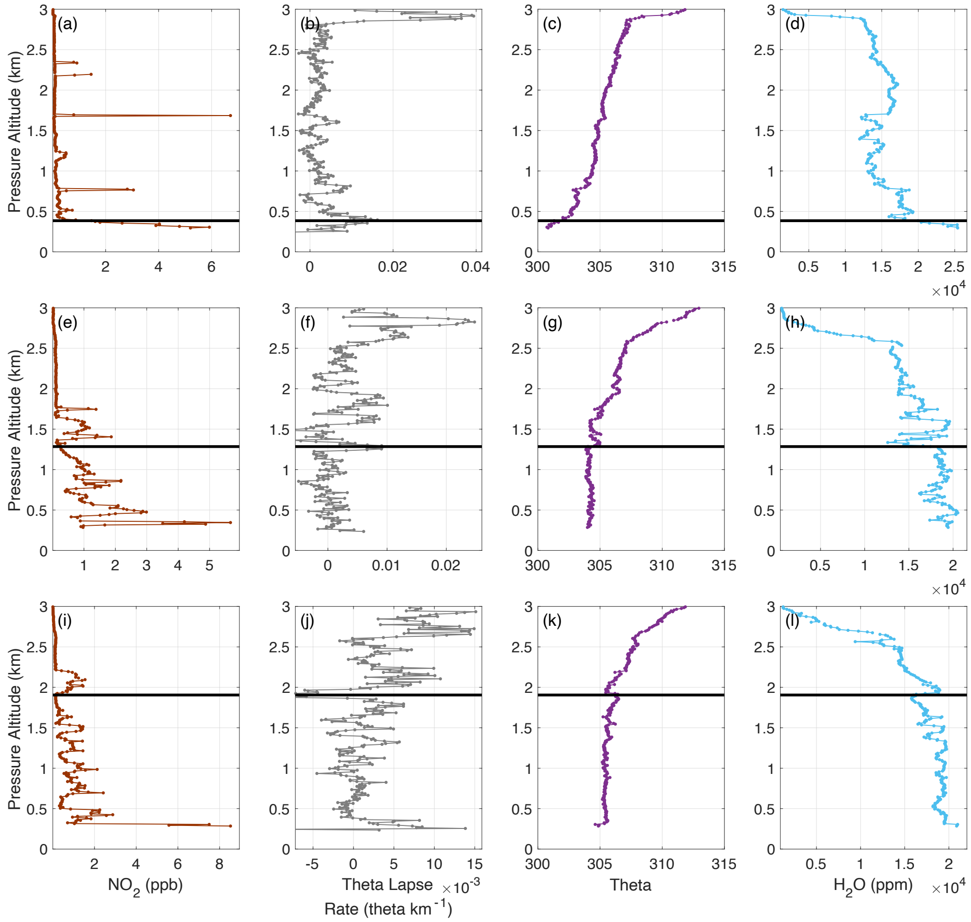

Figure A3.20. Channelview on September 13, 2013: P-3B vertical profile measurements averaged into 10-m altitude bins during the morning (panels a–d), midday (panels e–h), and afternoon (panels i–l) circuits: NO_2 (ppb) (panels a, e, and i), theta lapse rate (K km^{-1}) (panels b, f, and j), theta (K) (panels c, g, and k), and $H_2O_{(v)}$ (ppm) (panels d, h, and l). Altitude data are pressure altitude above sea level (km). Lapse rates are 5-point running means of binned data. CBL heights (Methods) are shown as heavy black lines.

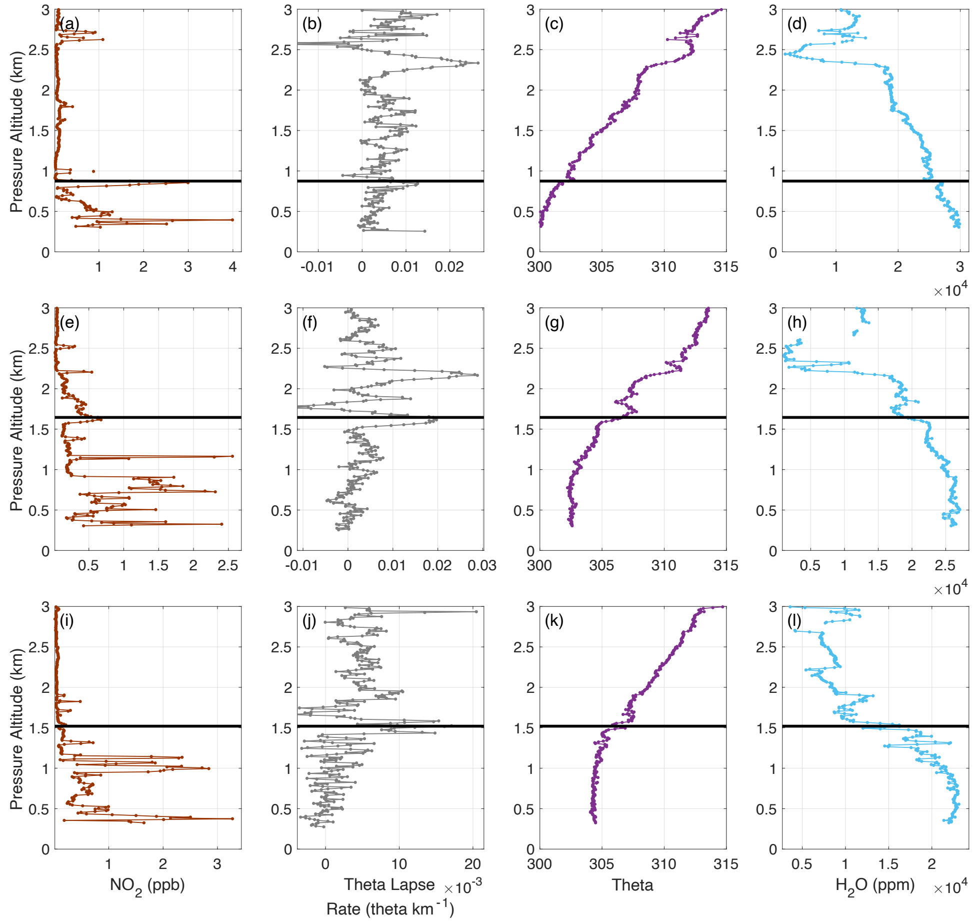

Figure A3.21. Channelview on September 24, 2013: P-3B vertical profile measurements averaged into 10-m altitude bins during the morning (panels a–d), midday (panels e–h), and afternoon (panels i–l) circuits: NO_2 (ppb) (panels a, e, and i), theta lapse rate (K km^{-1}) (panels b, f, and j), theta (K) (panels c, g, and k), and $H_2O_{(v)}$ (ppm) (panels d, h, and l). Altitude data are pressure altitude above sea level (km). Lapse rates are 5-point running means of binned data. CBL heights (Methods) are shown as heavy black lines.

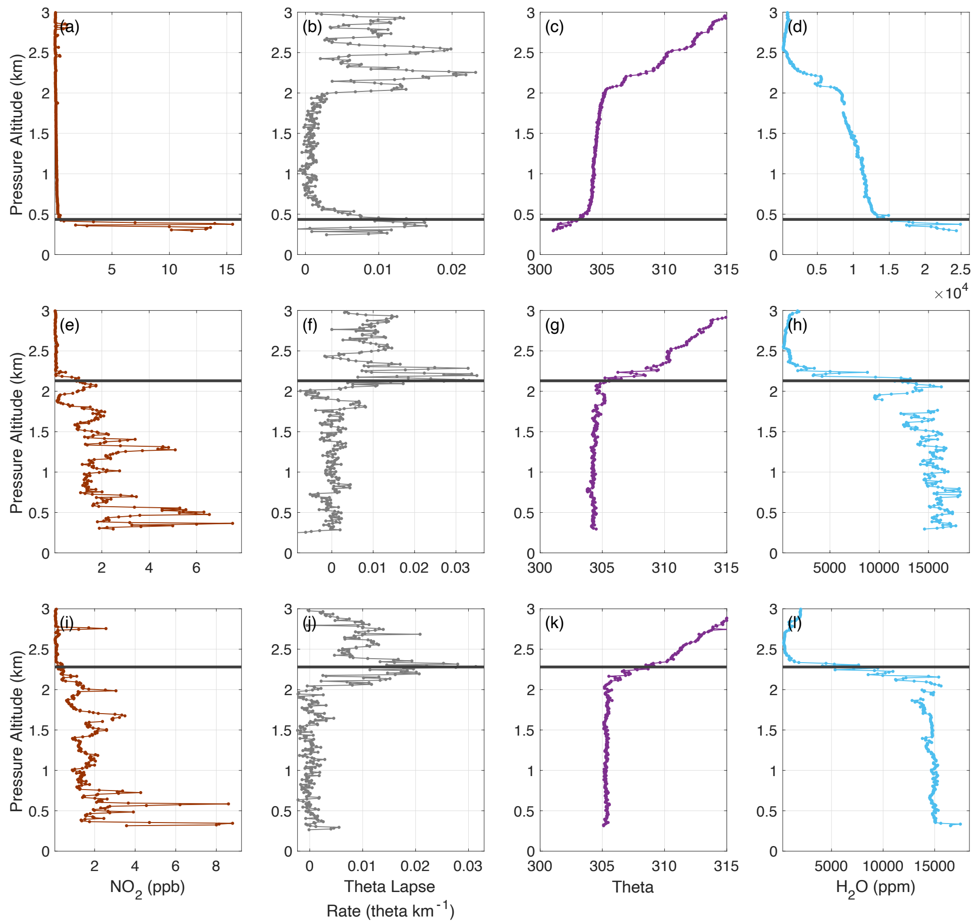

Figure A3.22. Channelview on September 25, 2013: P-3B vertical profile measurements averaged into 10-m altitude bins during the morning (panels a–d), midday (panels e–h), and afternoon (panels i–l) circuits: NO_2 (ppb) (panels a, e, and i), theta lapse rate (K km^{-1}) (panels b, f, and j), theta (K) (panels c, g, and k), and $H_2O_{(v)}$ (ppm) (panels d, h, and l). Altitude data are pressure altitude above sea level (km). Lapse rates are 5-point running means of binned data. CBL heights (Methods) are shown as heavy black lines.

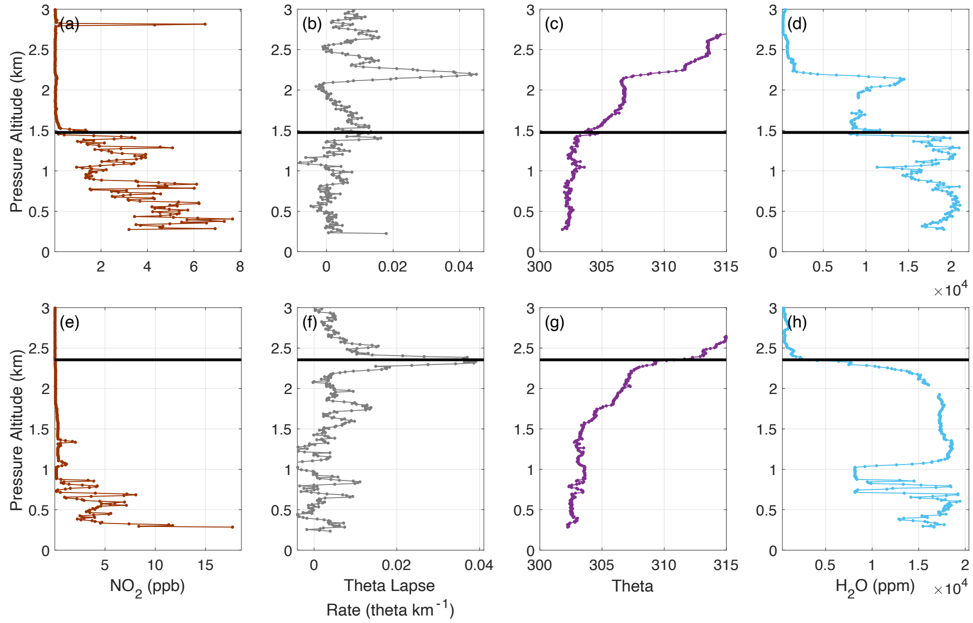

Figure A3.23. Channelview on September 26, 2013: P-3B vertical profile measurements averaged into 10-m altitude bins during the midday (panels a–d) and afternoon (panels e–h) circuits: NO_2 (ppb) (panels a and e), theta lapse rate (K km^{-1}) (panels b and f), theta (K) (panels c and g), and $H_2O_{(v)}$ (ppm) (panels d and h). Altitude data are pressure altitude above sea level (km). Lapse rates are 5-point running means of binned data. CBL heights (Methods) are shown as heavy black lines.

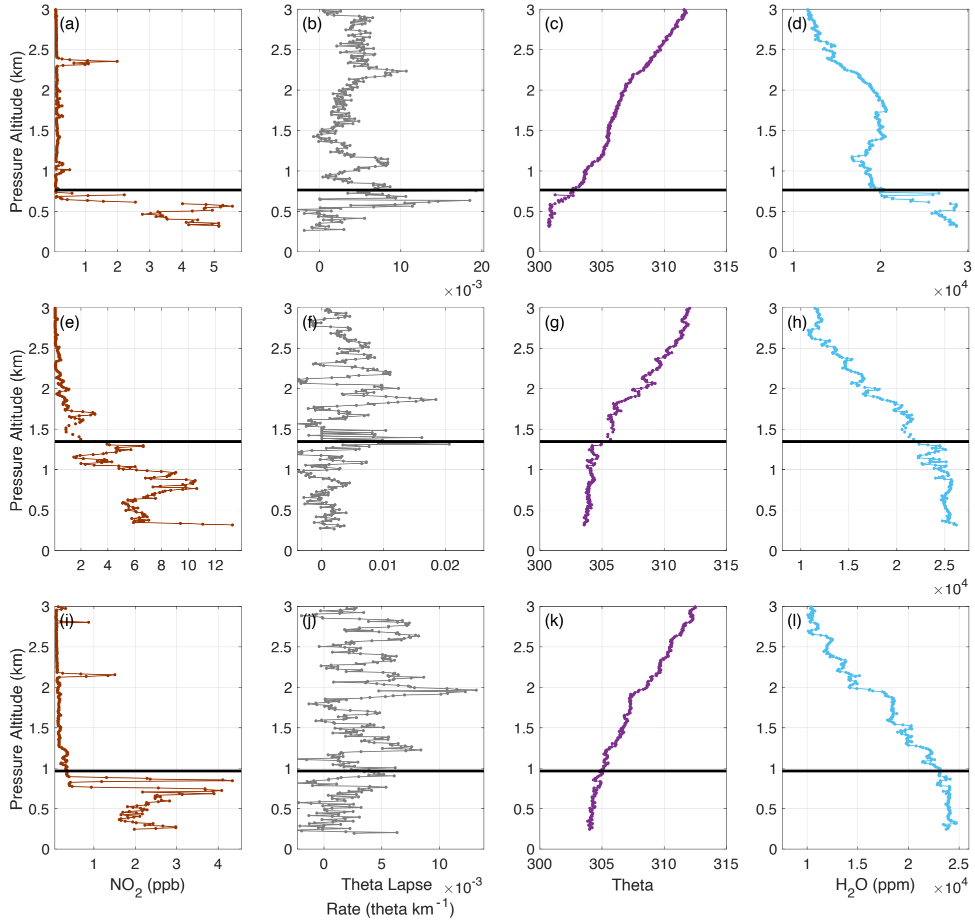

Figure A3.24. Moody Tower on September 4, 2013: P-3B vertical profile measurements averaged into 10-m altitude bins during the morning (panels a–d), midday (panels e–h), and afternoon (panels i–l) circuits: NO_2 (ppb) (panels a, e, and i), theta lapse rate (K km^{-1}) (panels b, f, and j), theta (K) (panels c, g, and k), and $H_2O_{(v)}$ (ppm) (panels d, h, and l). Altitude data are pressure altitude above sea level (km). Lapse rates are 5-point running means of binned data. CBL heights (Methods) are shown as heavy black lines.

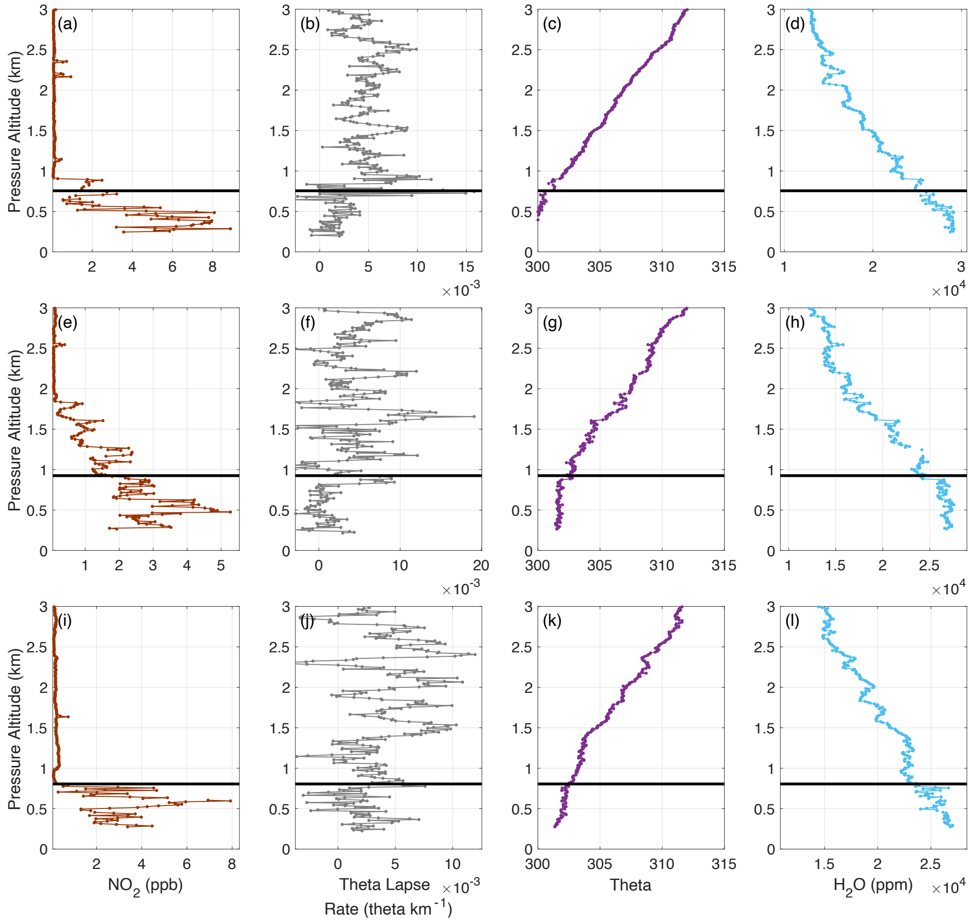

Figure A3.25. Moody Tower on September 6, 2013: P-3B vertical profile measurements averaged into 10-m altitude bins during the morning (panels a–d), midday (panels e–h), and afternoon (panels i–l) circuits: NO_2 (ppb) (panels a, e, and i), theta lapse rate (K km^{-1}) (panels b, f, and j), theta (K) (panels c, g, and k), and $H_2O_{(v)}$ (ppm) (panels d, h, and l). Altitude data are pressure altitude above sea level (km). Lapse rates are 5-point running means of binned data. CBL heights (Methods) are shown as heavy black lines.

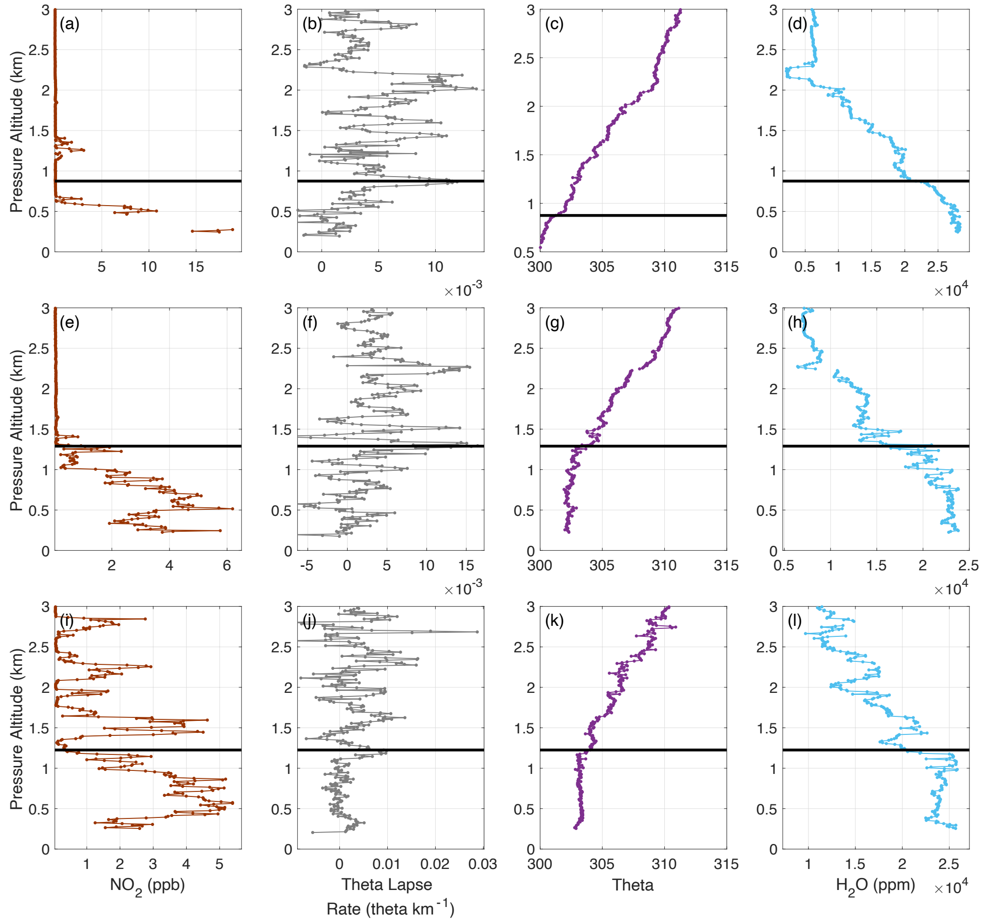

Figure A3.26. Moody Tower on September 11, 2013: P-3B vertical profile measurements averaged into 10-m altitude bins during the morning (panels a–d), midday (panels e–h), and afternoon (panels i–l) circuits: NO_2 (ppb) (panels a, e, and i), theta lapse rate (K km^{-1}) (panels b, f, and j), theta (K) (panels c, g, and k), and $H_2O_{(v)}$ (ppm) (panels d, h, and l). Altitude data are pressure altitude above sea level (km). Lapse rates are 5-point running means of binned data. CBL heights (Methods) are shown as heavy black lines.

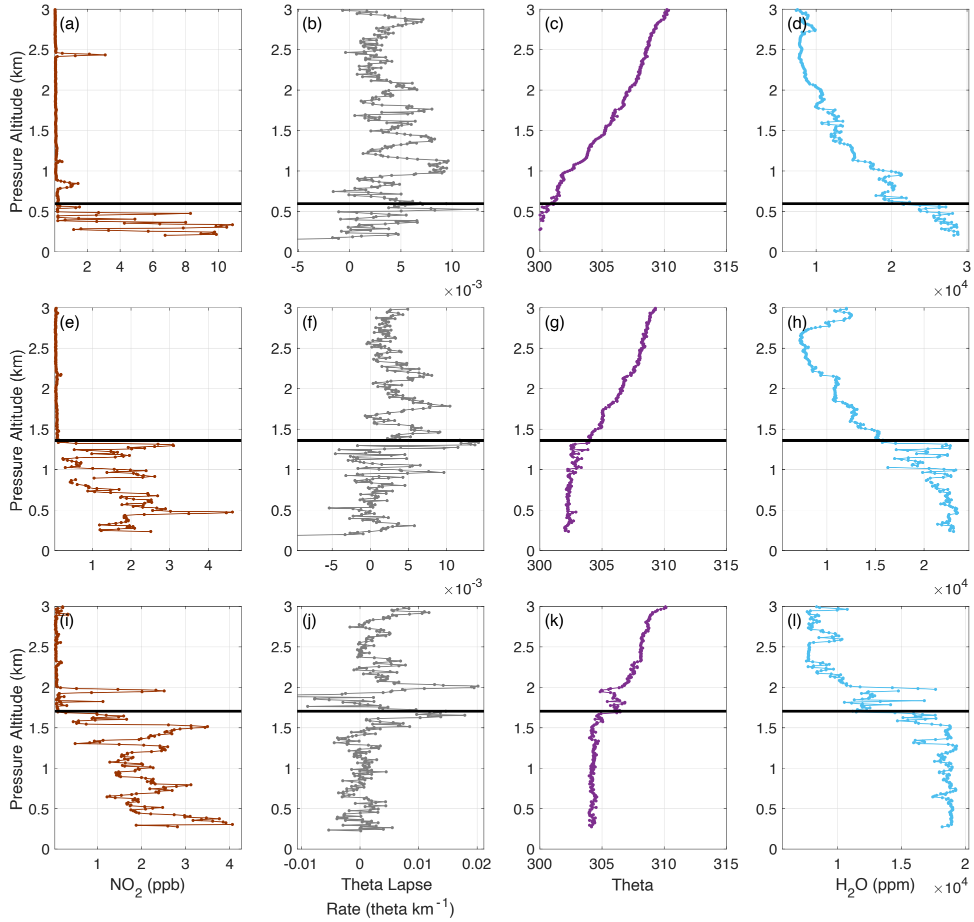

Figure A3.27. Moody Tower on September 12, 2013: P-3B vertical profile measurements averaged into 10-m altitude bins during the morning (panels a–d), midday (panels e–h), and afternoon (panels i–l) circuits: NO_2 (ppb) (panels a, e, and i), theta lapse rate (K km^{-1}) (panels b, f, and j), theta (K) (panels c, g, and k), and $H_2O_{(v)}$ (ppm) (panels d, h, and l). Altitude data are pressure altitude above sea level (km). Lapse rates are 5-point running means of binned data. CBL heights (Methods) are shown as heavy black lines.

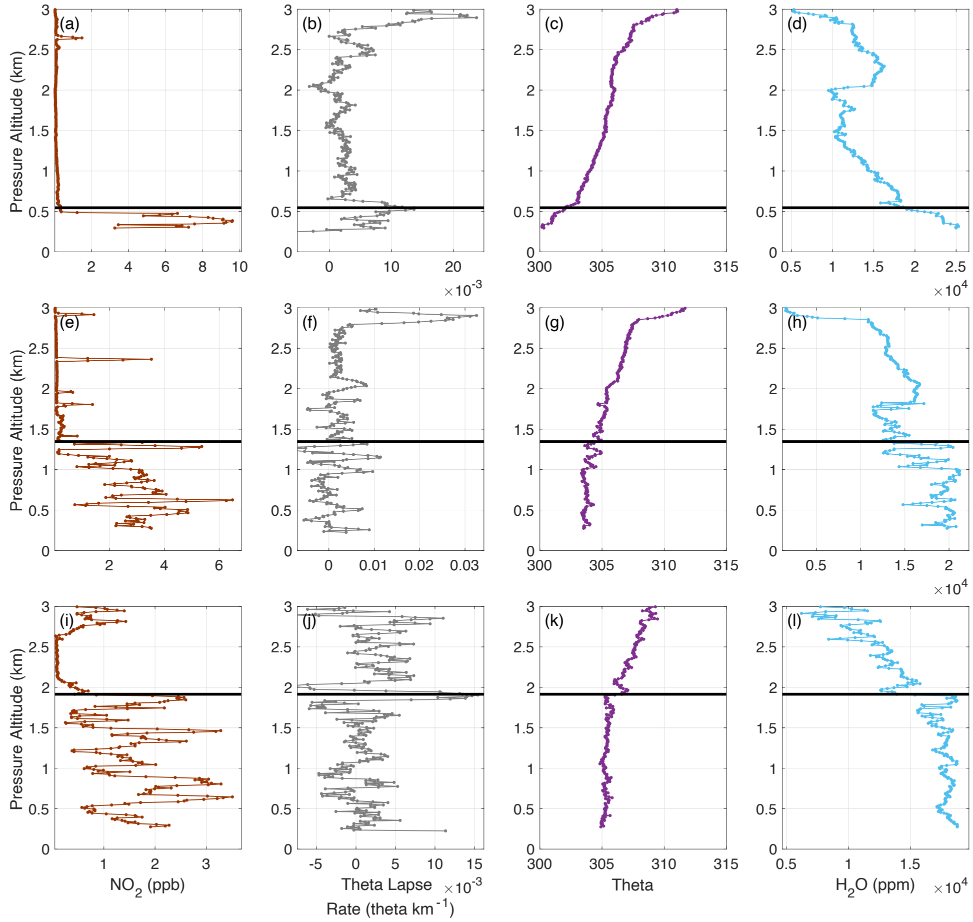

Figure A3.28. Moody Tower on September 13, 2013: P-3B vertical profile measurements averaged into 10-m altitude bins during the morning (panels a–d), midday (panels e–h), and afternoon (panels i–l) circuits: NO_2 (ppb) (panels a, e, and i), theta lapse rate (K km^{-1}) (panels b, f, and j), theta (K) (panels c, g, and k), and $H_2O_{(v)}$ (ppm) (panels d, h, and l). Altitude data are pressure altitude above sea level (km). Lapse rates are 5-point running means of binned data. CBL heights (Methods) are shown as heavy black lines.

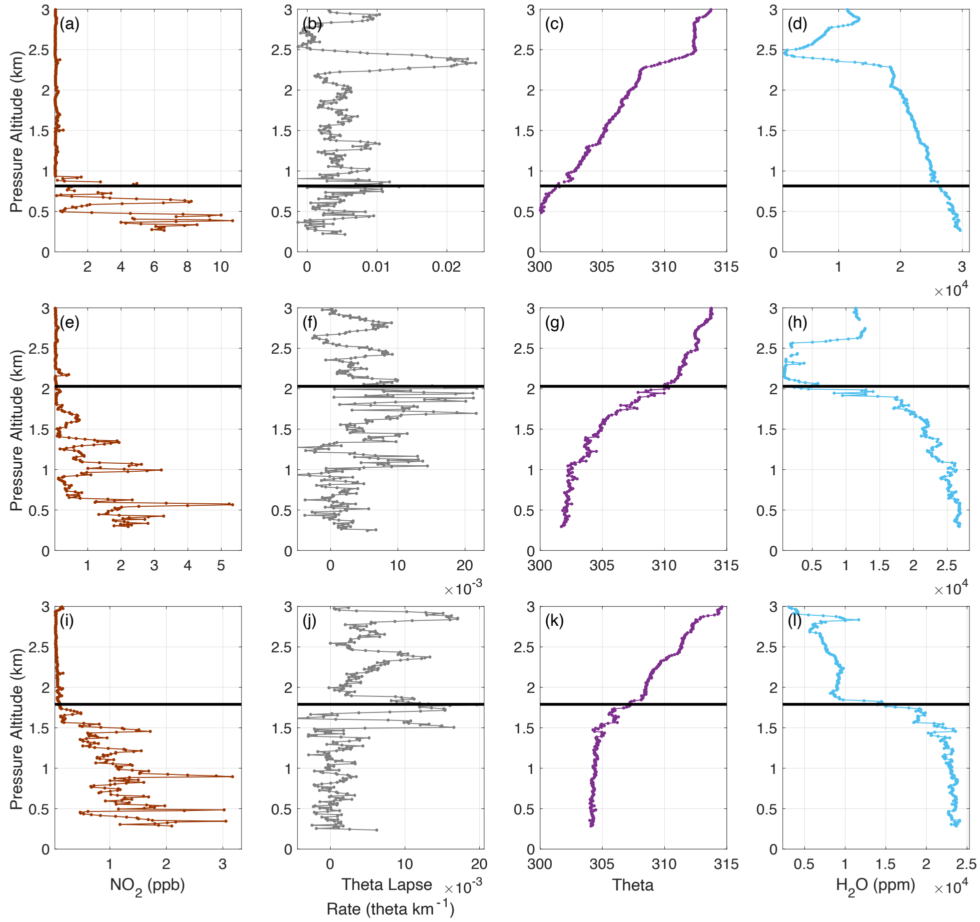

Figure A3.29. Moody Tower on September 24, 2013: P-3B vertical profile measurements averaged into 10-m altitude bins during the morning (panels a–d), midday (panels e–h), and afternoon (panels i–l) circuits: NO_2 (ppb) (panels a, e, and i), theta lapse rate (K km^{-1}) (panels b, f, and j), theta (K) (panels c, g, and k), and $H_2O_{(v)}$ (ppm) (panels d, h, and l). Altitude data are pressure altitude above sea level (km). Lapse rates are 5-point running means of binned data. CBL heights (Methods) are shown as heavy black lines.

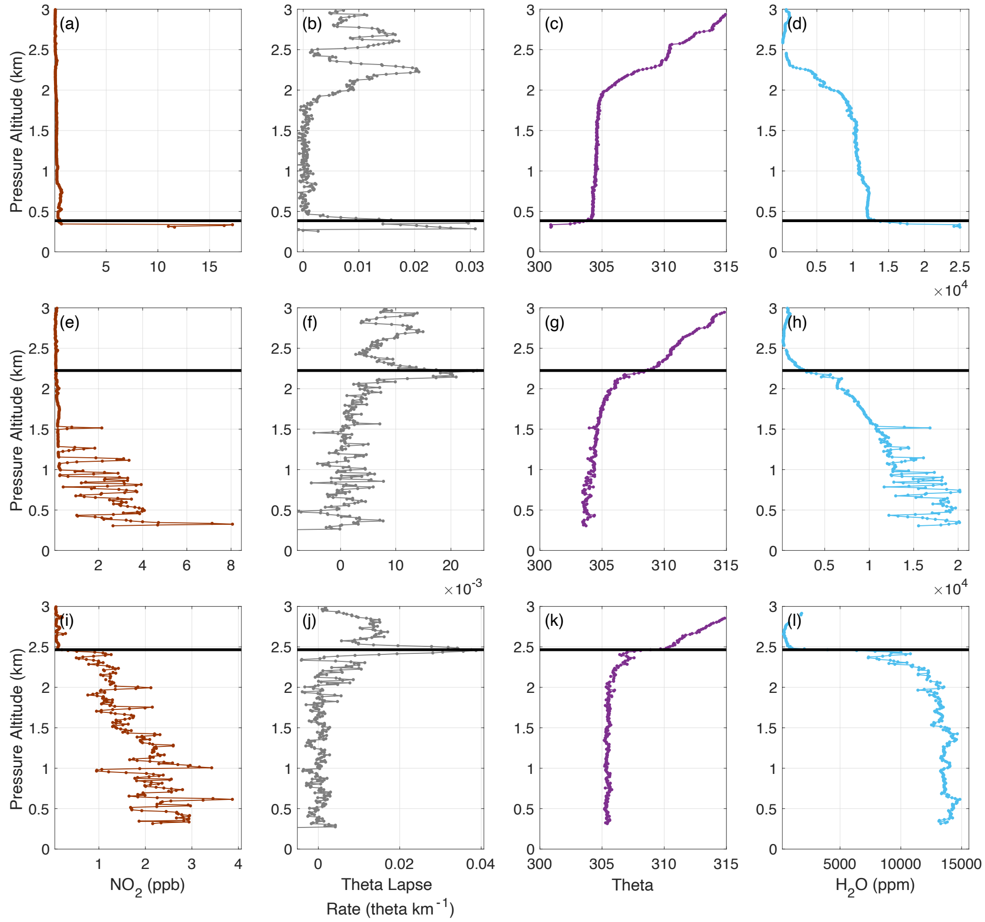

Figure A3.30. Moody Tower on September 25, 2013: P-3B vertical profile measurements averaged into 10-m altitude bins during the morning (panels a–d), midday (panels e–h), and afternoon (panels i–l) circuits: NO_2 (ppb) (panels a, e, and i), theta lapse rate (K km^{-1}) (panels b, f, and j), theta (K) (panels c, g, and k), and $H_2O_{(v)}$ (ppm) (panels d, h, and l). Altitude data are pressure altitude above sea level (km). Lapse rates are 5-point running means of binned data. CBL heights (Methods) are shown as heavy black lines.

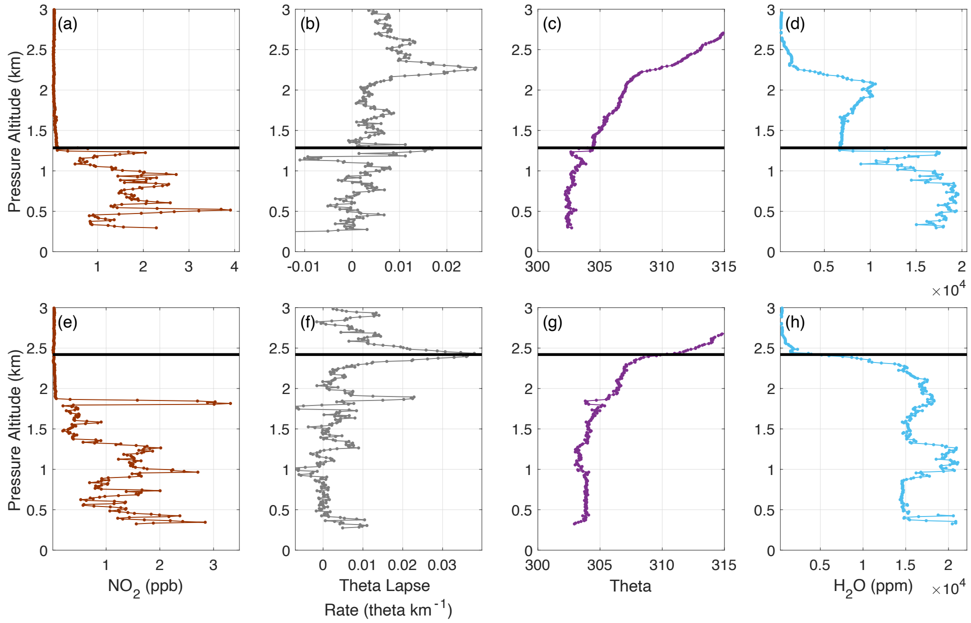

Figure A3.31. Moody Tower on September 26, 2013: P-3B vertical profile measurements averaged into 10-m altitude bins during the midday (panels a–d) and afternoon (panels e–h) circuits: NO_2 (ppb) (panels a and e), theta lapse rate (K km^{-1}) (panels b and f), theta (K) (panels c and g), and $H_2O_{(v)}$ (ppm) (panels d and h). Altitude data are pressure altitude above sea level (km). Lapse rates are 5-point running means of binned data. CBL heights (Methods) are shown as heavy black lines.

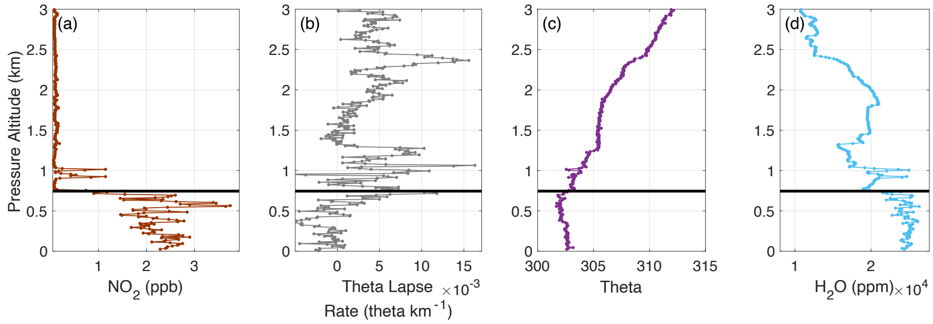

Figure A3.32. West Houston on September 4, 2013: P-3B vertical profile measurements averaged into 10-m altitude bins during the morning (panels a–d) circuit: NO_2 (ppb) (panel a), theta lapse rate (K km^{-1}) (panel b), theta (K) (panel c), and $H_2O_{(v)}$ (ppm) (panel d). Altitude data are pressure altitude above sea level (km). Lapse rates are 5-point running means of binned data. CBL heights (Methods) are shown as heavy black lines.

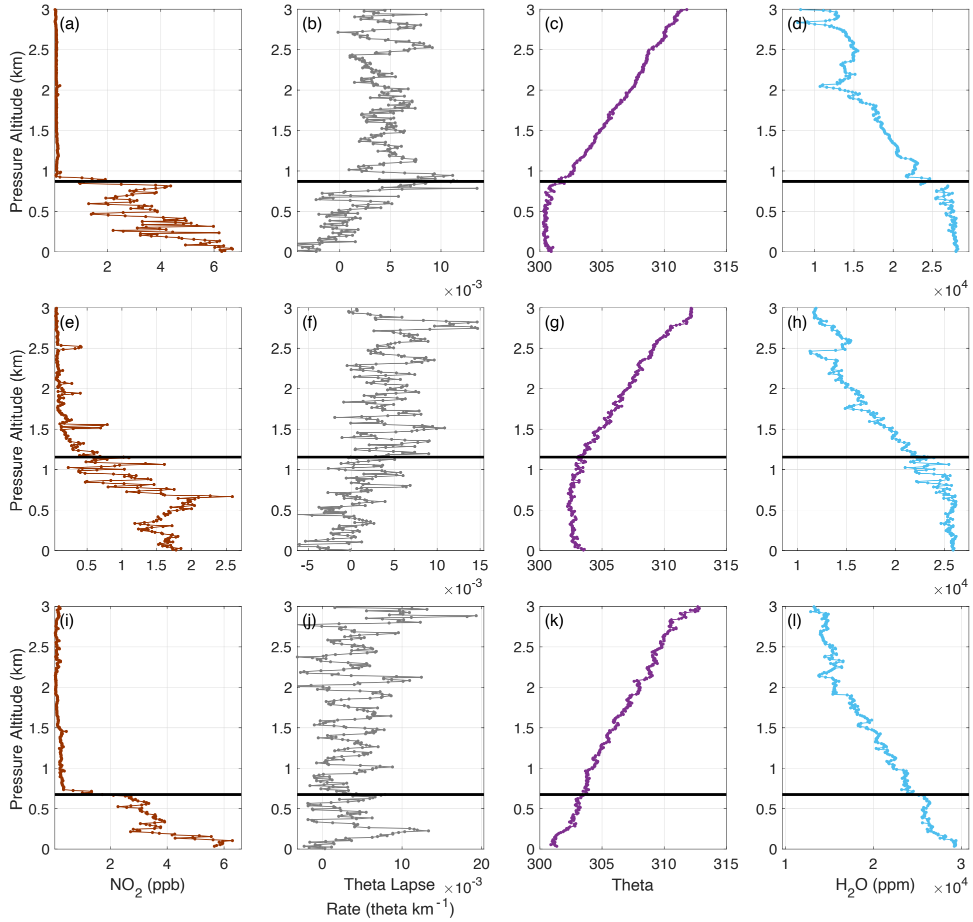

Figure A3.33. West Houston on September 6, 2013: P-3B vertical profile measurements averaged into 10-m altitude bins during the morning (panels a–d), midday (panels e–h), and afternoon (panels i–l) circuits: NO_2 (ppb) (panels a, e, and i), theta lapse rate (K km^{-1}) (panels b, f, and j), theta (K) (panels c, g, and k), and $H_2O_{(v)}$ (ppm) (panels d, h, and l). Altitude data are pressure altitude above sea level (km). Lapse rates are 5-point running means of binned data. CBL heights (Methods) are shown as heavy black lines.

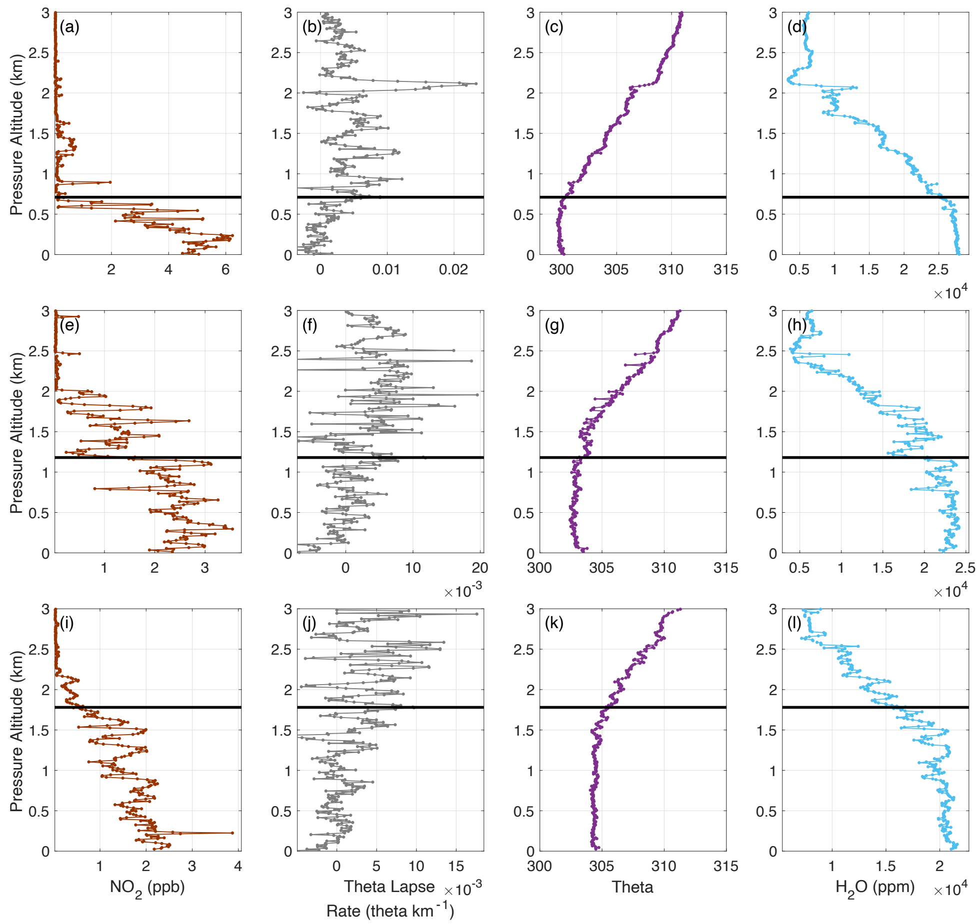

Figure A3.34. West Houston on September 11, 2013: P-3B vertical profile measurements averaged into 10-m altitude bins during the morning (panels a–d), midday (panels e–h), and afternoon (panels i–l) circuits: NO_2 (ppb) (panels a, e, and i), theta lapse rate (K km^{-1}) (panels b, f, and j), theta (K) (panels c, g, and k), and $H_2O_{(v)}$ (ppm) (panels d, h, and l). Altitude data are pressure altitude above sea level (km). Lapse rates are 5-point running means of binned data. CBL heights (Methods) are shown as heavy black lines.

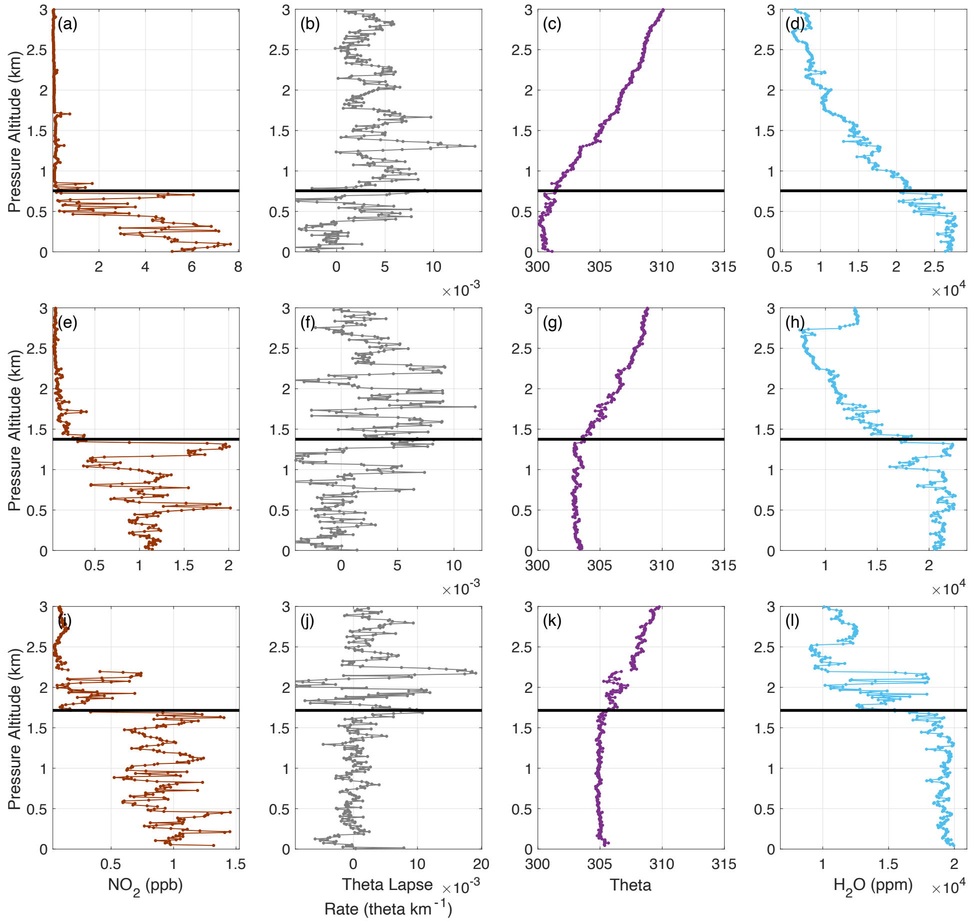

Figure A3.35. West Houston on September 12, 2013: P-3B vertical profile measurements averaged into 10-m altitude bins during the morning (panels a–d), midday (panels e–h), and afternoon (panels i–l) circuits: NO_2 (ppb) (panels a, e, and i), theta lapse rate (K km^{-1}) (panels b, f, and j), theta (K) (panels c, g, and k), and $H_2O_{(v)}$ (ppm) (panels d, h, and l). Altitude data are pressure altitude above sea level (km). Lapse rates are 5-point running means of binned data. CBL heights (Methods) are shown as heavy black lines.

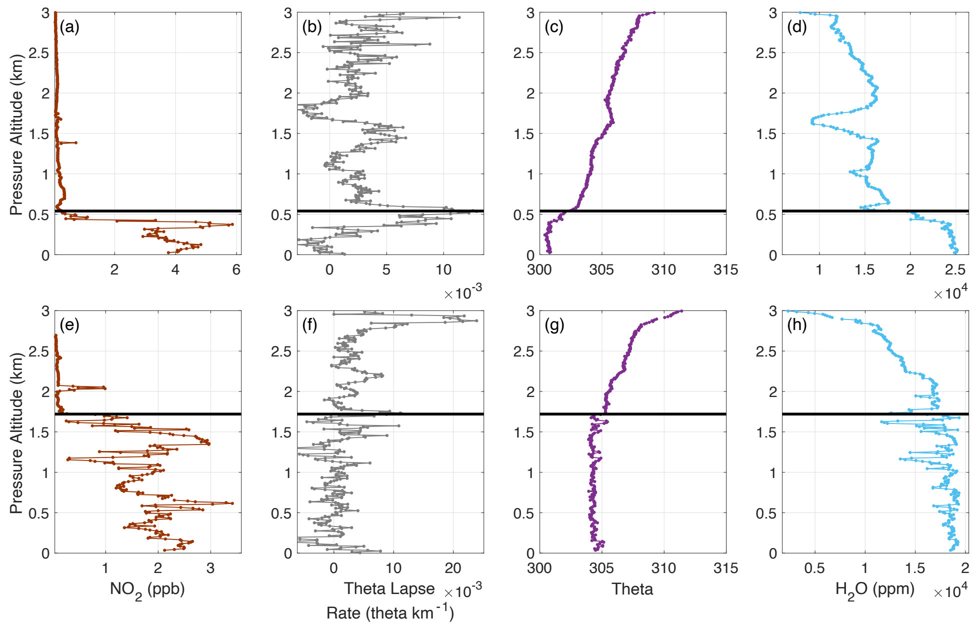

Figure A3.36. West Houston on September 13, 2013: P-3B vertical profile measurements averaged into 10-m altitude bins during the morning (panels a–d) and midday (panels e–h) circuits: NO_2 (ppb) (panels a and e), theta lapse rate (K km^{-1}) (panels b and f), theta (K) (panels c and g), and $H_2O_{(v)}$ (ppm) (panels d and h). Altitude data are pressure altitude above sea level (km). Lapse rates are 5-point running means of binned data. CBL heights (Methods) are shown as heavy black lines.

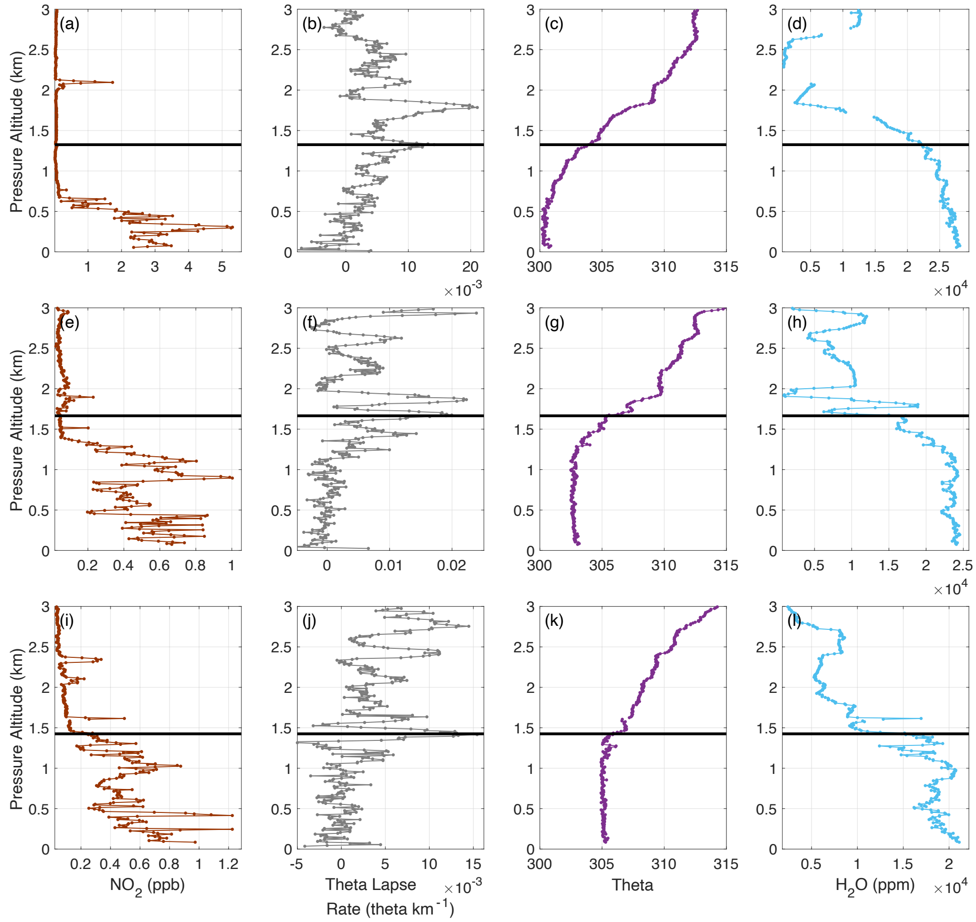

Figure A3.37. West Houston on September 24, 2013: P-3B vertical profile measurements averaged into 10-m altitude bins during the morning (panels a–d), midday (panels e–h), and afternoon (panels i–l) circuits: NO_2 (ppb) (panels a, e, and i), theta lapse rate (K km^{-1}) (panels b, f, and j), theta (K) (panels c, g, and k), and $H_2O_{(v)}$ (ppm) (panels d, h, and l). Altitude data are pressure altitude above sea level (km). Lapse rates are 5-point running means of binned data. CBL heights (Methods) are shown as heavy black lines.

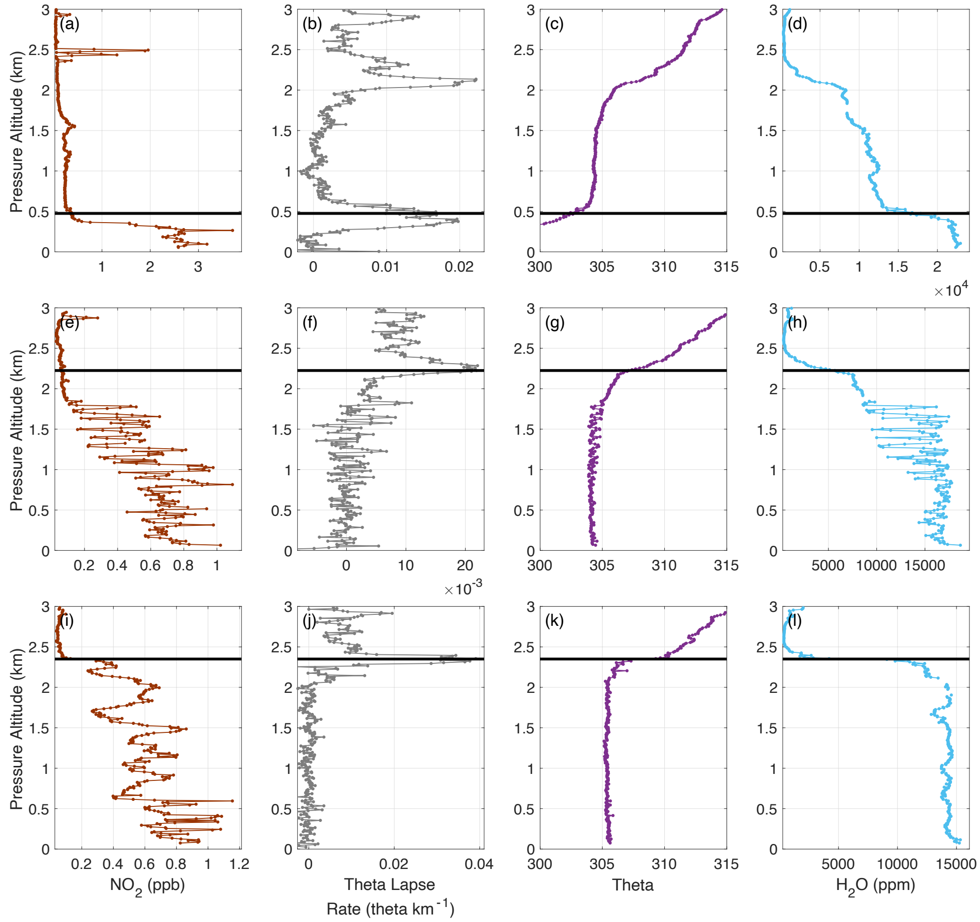

Figure A3.38. West Houston on September 25, 2013: P-3B vertical profile measurements averaged into 10-m altitude bins during the morning (panels a–d), midday (panels e–h), and afternoon (panels i–l) circuits: NO_2 (ppb) (panels a, e, and i), theta lapse rate (K km^{-1}) (panels b, f, and j), theta (K) (panels c, g, and k), and $H_2O_{(v)}$ (ppm) (panels d, h, and l). Altitude data are pressure altitude above sea level (km). Lapse rates are 5-point running means of binned data. CBL heights (Methods) are shown as heavy black lines.

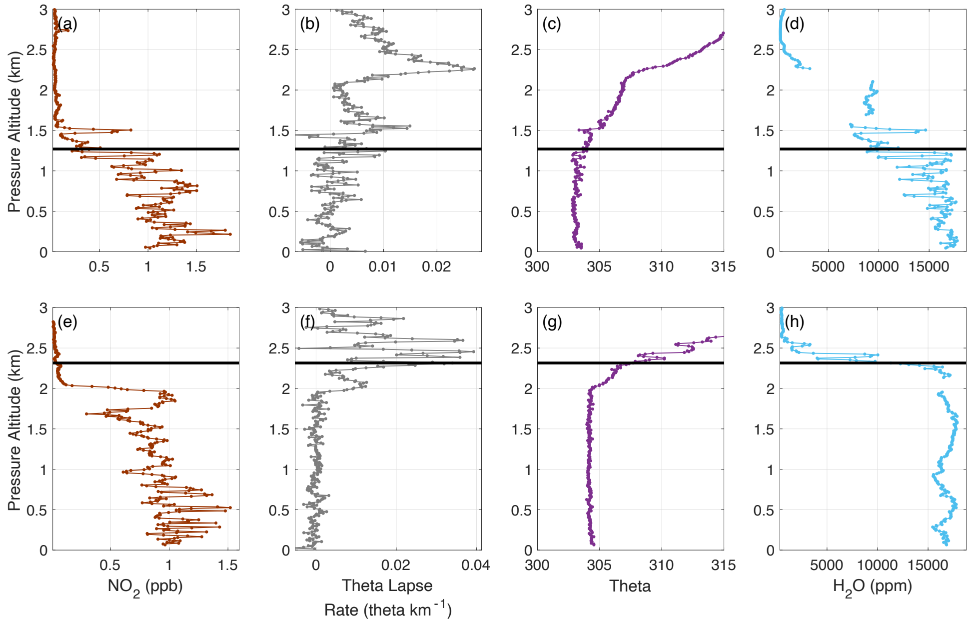

Figure A3.39. West Houston on September 26, 2013: P-3B vertical profile measurements averaged into 10-m altitude bins during the midday (panels a–d) and afternoon (panels e–h) circuits: NO_2 (ppb) (panels a and e), theta lapse rate (K km^{-1}) (panels b and f), theta (K) (panels c and g), and $H_2O_{(v)}$ (ppm) (panels d and h). Altitude data are pressure altitude above sea level (km). Lapse rates are 5-point running means of binned data. CBL heights (Methods) are shown as heavy black lines.

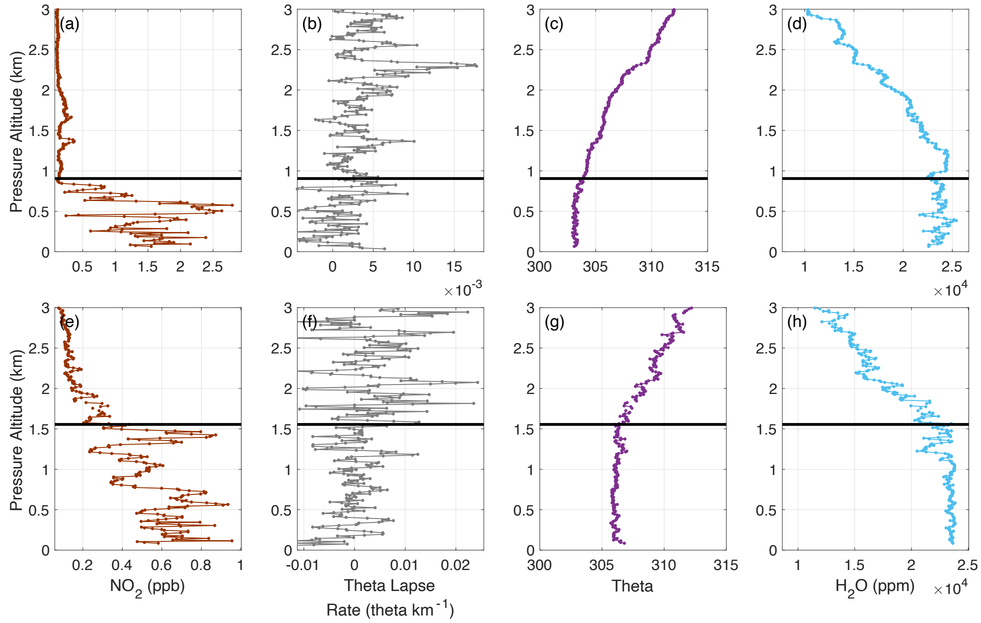

Figure A3.40. Conroe on September 4, 2013: P-3B vertical profile measurements averaged into 10-m altitude bins during the morning (panels a–d) and midday (panels e–h) circuits: NO_2 (ppb) (panels a and e), theta lapse rate (K km^{-1}) (panels b and f), theta (K) (panels c and g), and $H_2O_{(v)}$ (ppm) (panels d and h). Altitude data are pressure altitude above sea level (km). Lapse rates are 5-point running means of binned data. CBL heights (Methods) are shown as heavy black lines.

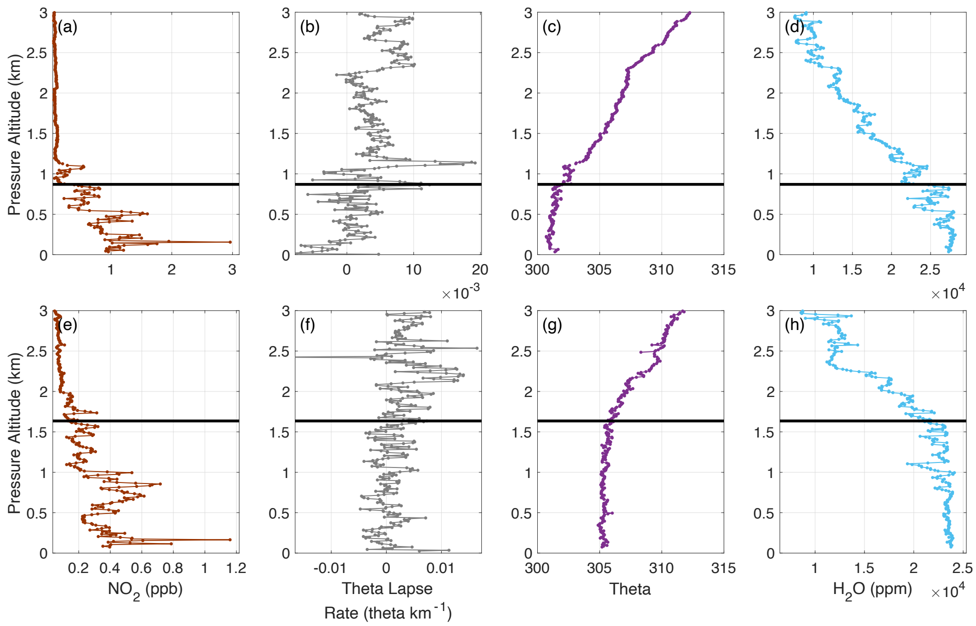

Figure A3.41. Conroe on September 6, 2013: P-3B vertical profile measurements averaged into 10-m altitude bins during the morning (panels a–d) and afternoon (panels e–h) circuits: NO_2 (ppb) (panels a and e), theta lapse rate (K km^{-1}) (panels b and f), theta (K) (panels c and g), and $H_2O_{(v)}$ (ppm) (panels d and h). Altitude data are pressure altitude above sea level (km). Lapse rates are 5-point running means of binned data. CBL heights (Methods) are shown as heavy black lines.

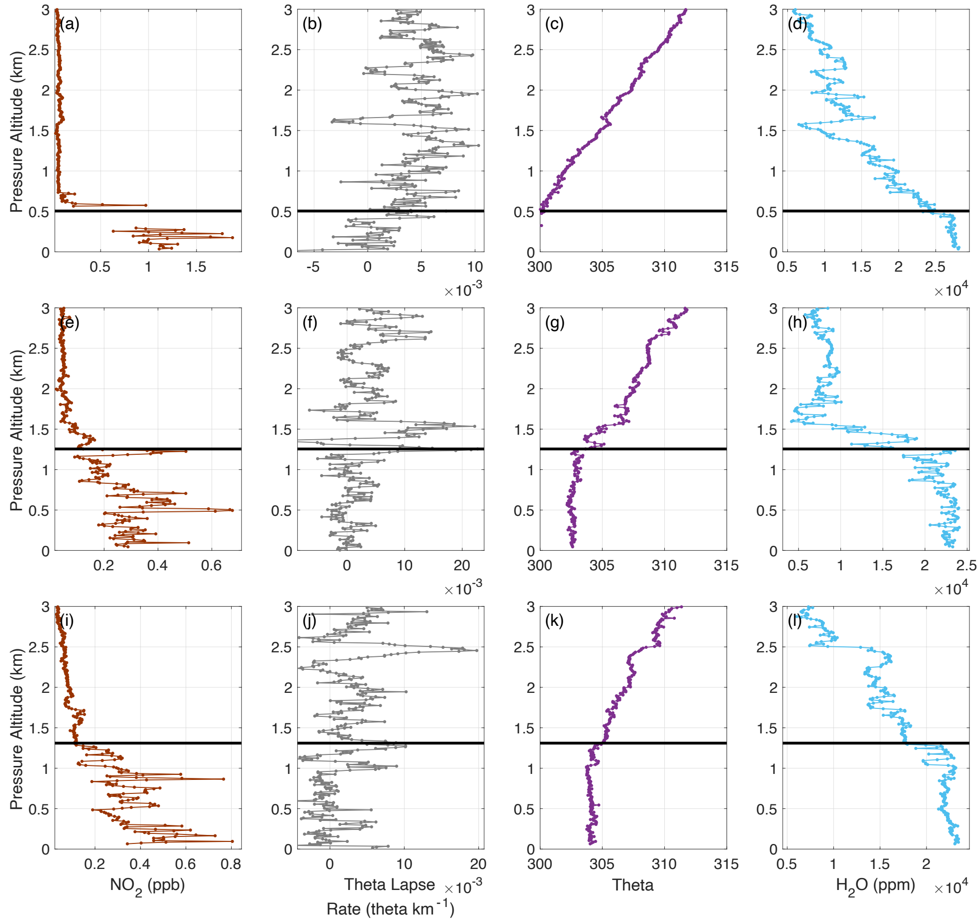

Figure A3.42. Conroe on September 11, 2013: P-3B vertical profile measurements averaged into 10-m altitude bins during the morning (panels a–d), midday (panels e–h), and afternoon (panels i–l) circuits: NO_2 (ppb) (panels a, e, and i), theta lapse rate (K km^{-1}) (panels b, f, and j), theta (K) (panels c, g, and k), and $H_2O_{(v)}$ (ppm) (panels d, h, and l). Altitude data are pressure altitude above sea level (km). Lapse rates are 5-point running means of binned data. CBL heights (Methods) are shown as heavy black lines.

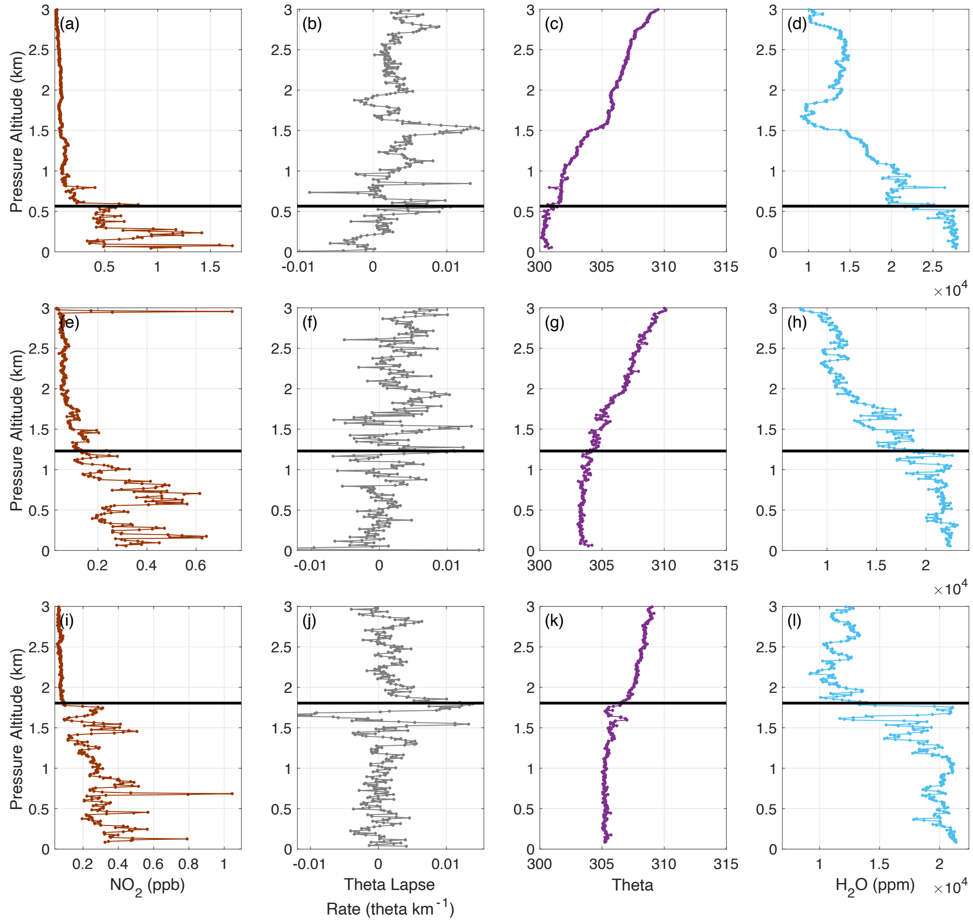

Figure A3.43. Conroe on September 12, 2013: P-3B vertical profile measurements averaged into 10-m altitude bins during the morning (panels a–d), midday (panels e–h), and afternoon (panels i–l) circuits: NO_2 (ppb) (panels a, e, and i), theta lapse rate (K km^{-1}) (panels b, f, and j), theta (K) (panels c, g, and k), and $H_2O_{(v)}$ (ppm) (panels d, h, and l). Altitude data are pressure altitude above sea level (km). Lapse rates are 5-point running means of binned data. CBL heights (Methods) are shown as heavy black lines.

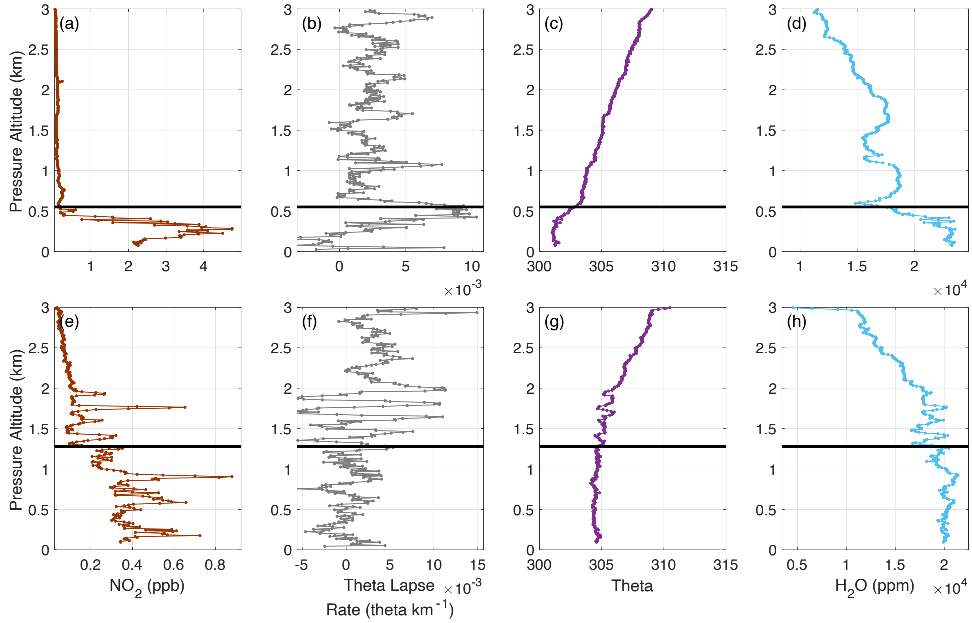

Figure A3.44. Conroe on September 13, 2013: P-3B vertical profile measurements averaged into 10-m altitude bins during the morning (panels a–d) and midday (panels e–h) circuits: NO_2 (ppb) (panels a and e), theta lapse rate (K km^{-1}) (panels b and f), theta (K) (panels c and g), and $H_2O_{(v)}$ (ppm) (panels d and h). Altitude data are pressure altitude above sea level (km). Lapse rates are 5-point running means of binned data. CBL heights (Methods) are shown as heavy black lines.

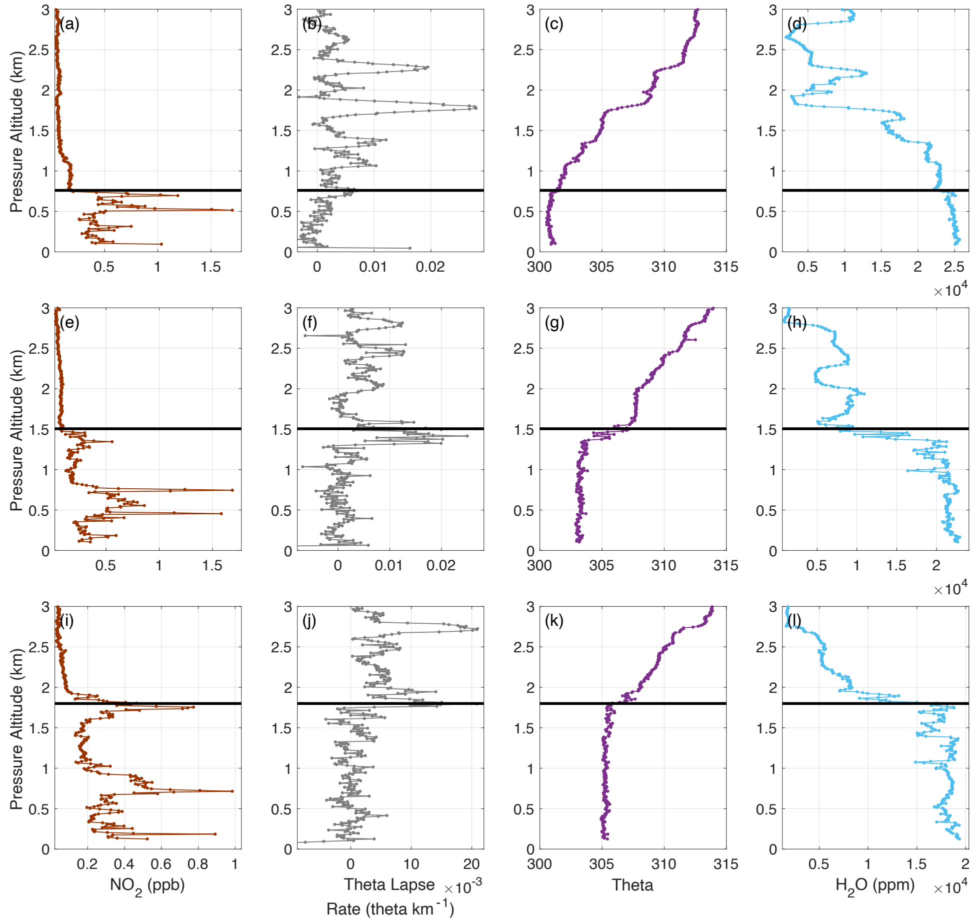

Figure A3.45. Conroe on September 24, 2013: P-3B vertical profile measurements averaged into 10-m altitude bins during the morning (panels a–d), midday (panels e–h), and afternoon (panels i–l) circuits: NO_2 (ppb) (panels a, e, and i), theta lapse rate (K km^{-1}) (panels b, f, and j), theta (K) (panels c, g, and k), and $H_2O_{(v)}$ (ppm) (panels d, h, and l). Altitude data are pressure altitude above sea level (km). Lapse rates are 5-point running means of binned data. CBL heights (Methods) are shown as heavy black lines.

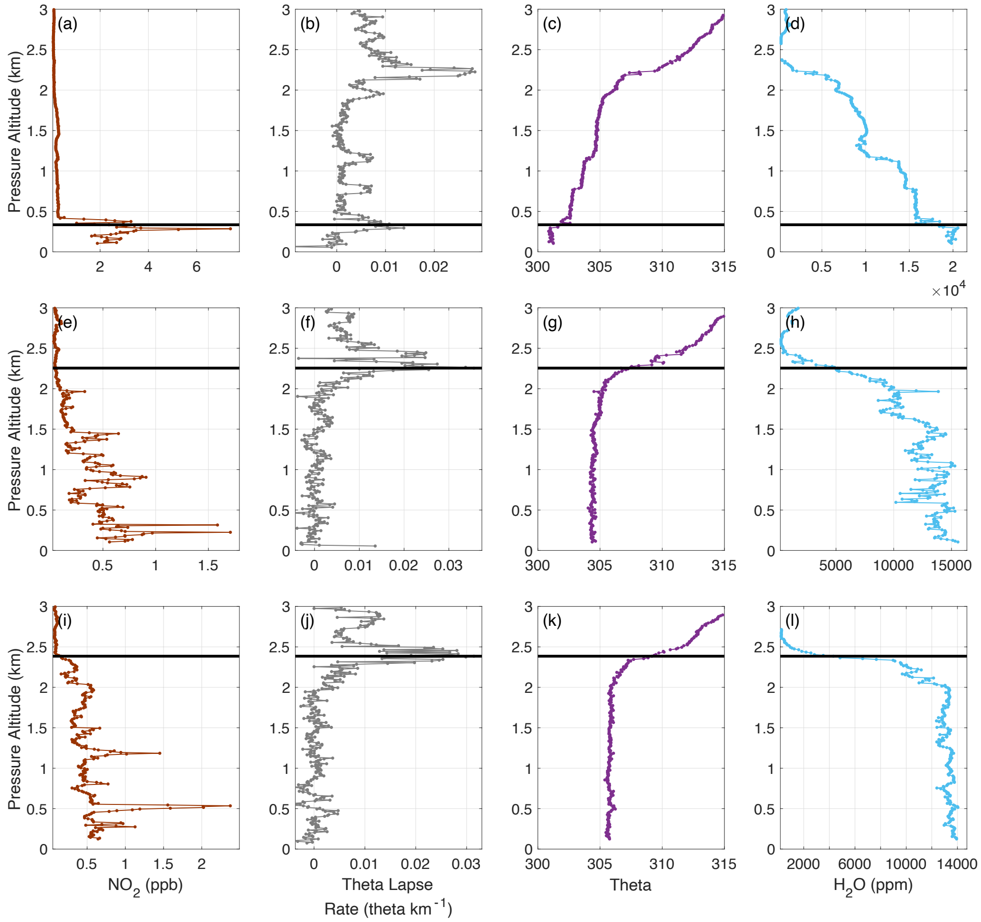

Figure A3.46. Conroe on September 25, 2013: P-3B vertical profile measurements averaged into 10-m altitude bins during the morning (panels a–d), midday (panels e–h), and afternoon (panels i–l) circuits: NO_2 (ppb) (panels a, e, and i), theta lapse rate (K km^{-1}) (panels b, f, and j), theta (K) (panels c, g, and k), and $H_2O_{(v)}$ (ppm) (panels d, h, and l). Altitude data are pressure altitude above sea level (km). Lapse rates are 5-point running means of binned data. CBL heights (Methods) are shown as heavy black lines.

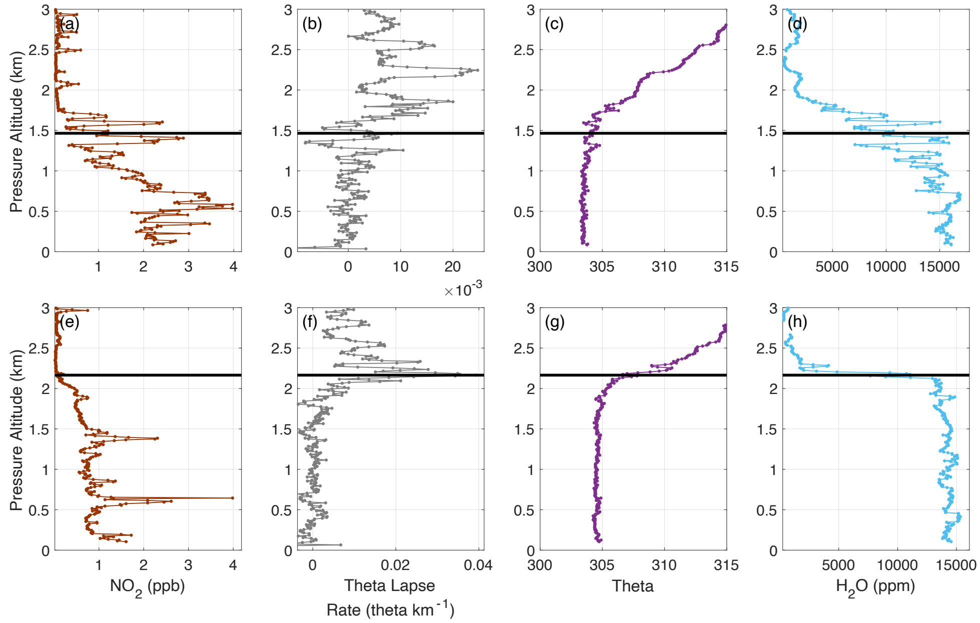

Figure A3.47. Conroe on September 26, 2013: P-3B vertical profile measurements averaged into 10-m altitude bins during the midday (panels a–d) and afternoon (panels e–h) circuits: NO_2 (ppb) (panels a and e), theta lapse rate (K km^{-1}) (panels b and f), theta (K) (panels c and g), and $H_2O_{(v)}$ (ppm) (panels d and h). Altitude data are pressure altitude above sea level (km). Lapse rates are 5-point running means of binned data. CBL heights (Methods) are shown as heavy black lines.

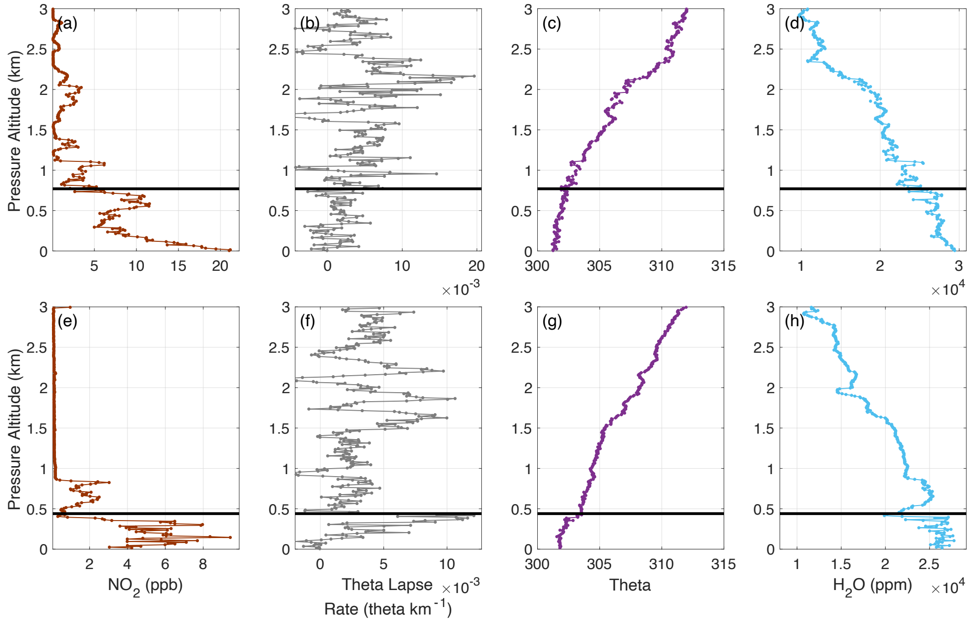

Figure A3.48. Deer Park on September 4, 2013: P-3B vertical profile measurements averaged into 10-m altitude bins during the morning (panels a–d) and midday (panels (e–h) circuits: NO_2 (ppb) (panels a and e), theta lapse rate (K km^{-1}) (panels b and f), theta (K) (panels c and g), and $H_2O_{(v)}$ (ppm) (panels d and h). Altitude data are pressure altitude above sea level (km). Lapse rates are 5-point running means of binned data. CBL heights (Methods) are shown as heavy black lines.

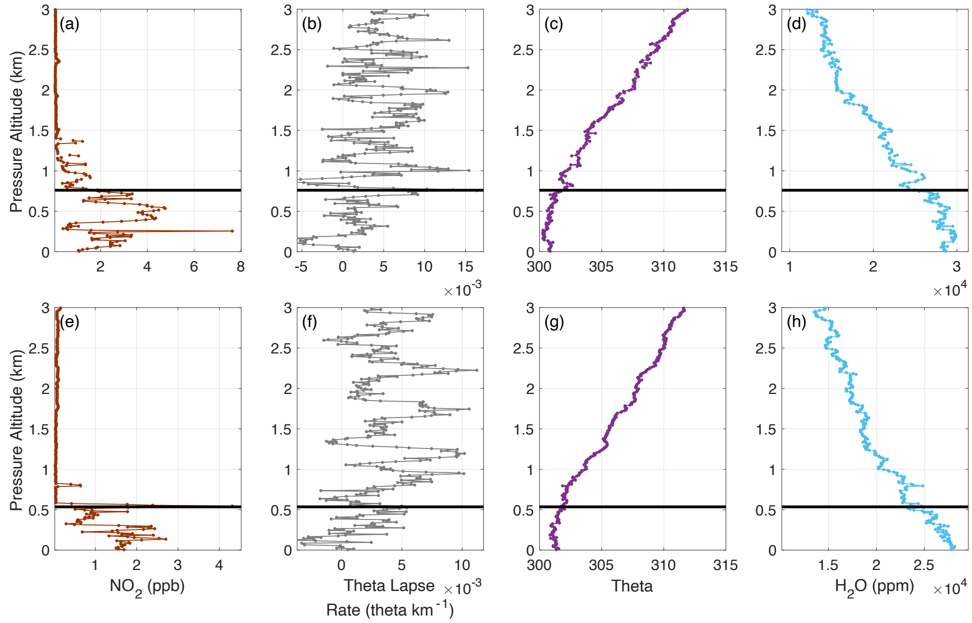

Figure A3.49. Deer Park on September 6, 2013: P-3B vertical profile measurements averaged into 10-m altitude bins during the morning (panels a–d) and afternoon (panels e–h) circuits: NO_2 (ppb) (panels a and e), theta lapse rate (K km^{-1}) (panels b and f), theta (K) (panels c and g), and $H_2O_{(v)}$ (ppm) (panels d and h). Altitude data are pressure altitude above sea level (km). Lapse rates are 5-point running means of binned data. CBL heights (Methods) are shown as heavy black lines.

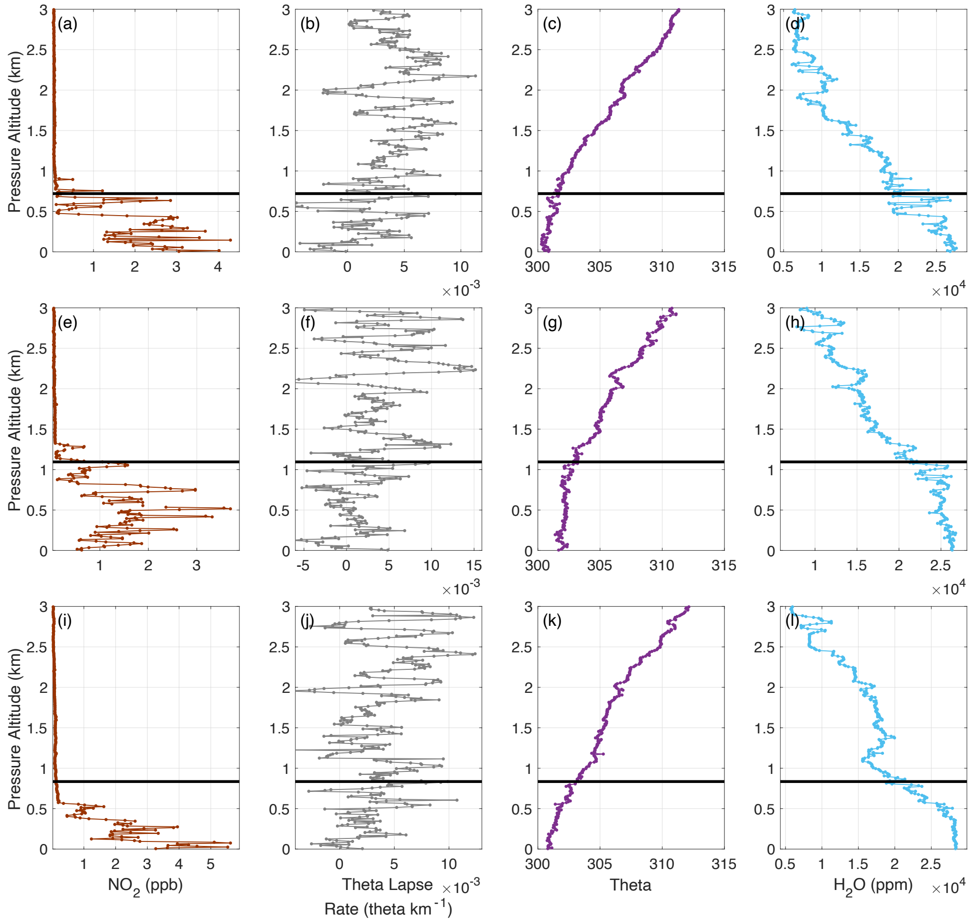

Figure A3.50. Deer Park on September 11, 2013: P-3B vertical profile measurements averaged into 10-m altitude bins during the morning (panels a–d), midday (panels e–h), and afternoon (panels i–l) circuits: NO_2 (ppb) (panels a, e, and i), theta lapse rate (K km^{-1}) (panels b, f, and j), theta (K) (panels c, g, and k), and $H_2O_{(v)}$ (ppm) (panels d, h, and l). Altitude data are pressure altitude above sea level (km). Lapse rates are 5-point running means of binned data. CBL heights (Methods) are shown as heavy black lines.

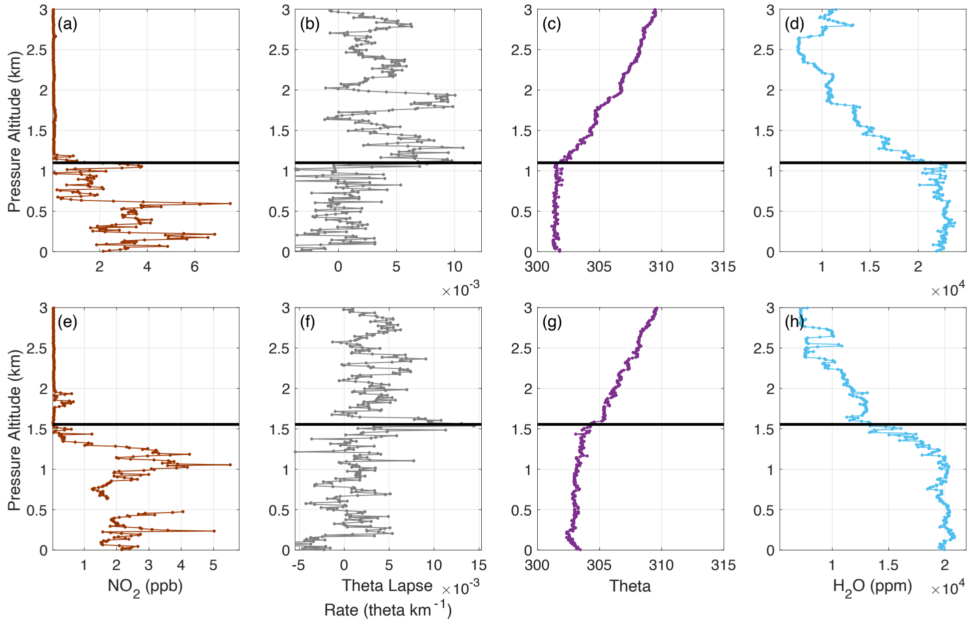

Figure A3.51. Deer Park on September 12, 2013: P-3B vertical profile measurements averaged into 10-m altitude bins during the morning (panels a–d) and midday (panels (e–h) circuits: NO_2 (ppb) (panels a and e), theta lapse rate (K km^{-1}) (panels b and f), theta (K) (panels c and g), and $H_2O_{(v)}$ (ppm) (panels d and h). Altitude data are pressure altitude above sea level (km). Lapse rates are 5-point running means of binned data. CBL heights (Methods) are shown as heavy black lines.

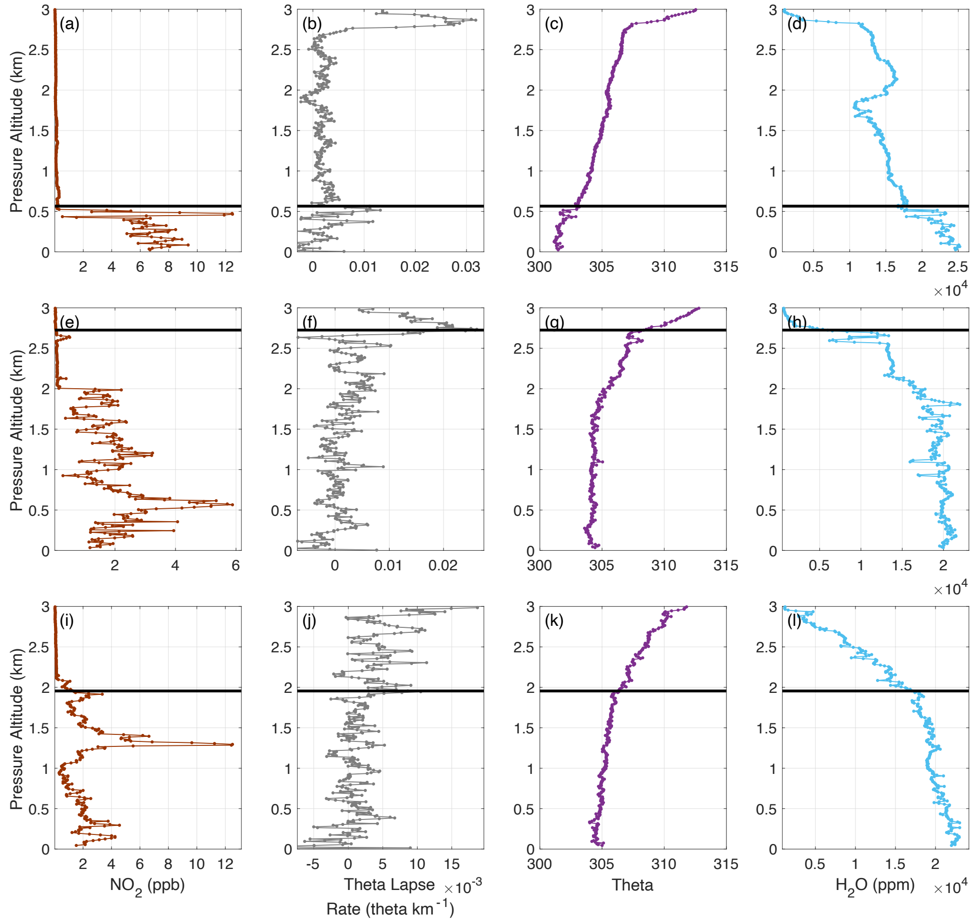

Figure A3.52. Deer Park on September 13, 2013: P-3B vertical profile measurements averaged into 10-m altitude bins during the morning (panels a–d), midday (panels e–h), and afternoon (panels i–l) circuits: NO_2 (ppb) (panels a, e, and i), theta lapse rate (K km^{-1}) (panels b, f, and j), theta (K) (panels c, g, and k), and $H_2O_{(v)}$ (ppm) (panels d, h, and l). Altitude data are pressure altitude above sea level (km). Lapse rates are 5-point running means of binned data. CBL heights (Methods) are shown as heavy black lines.

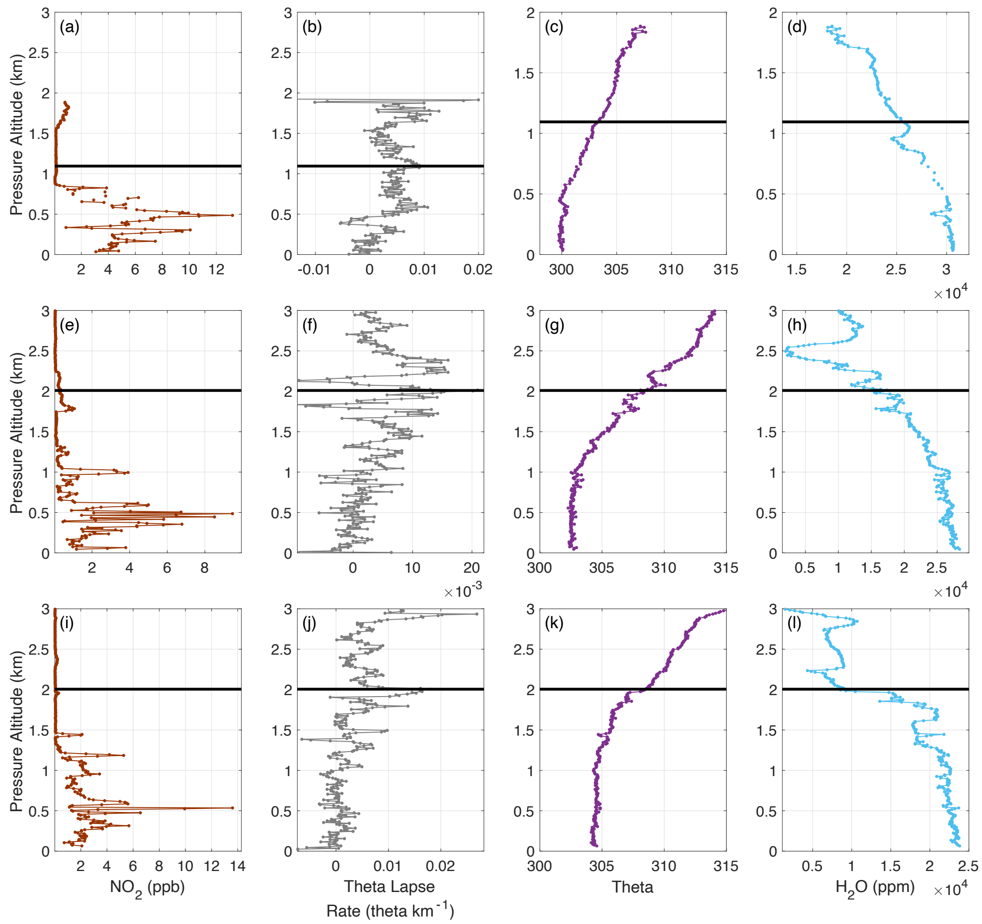

Figure A3.53. Deer Park on September 24, 2013: P-3B vertical profile measurements averaged into 10-m altitude bins during the morning (panels a–d), midday (panels e–h), and afternoon (panels i–l) circuits: NO_2 (ppb) (panels a, e, and i), theta lapse rate (K km^{-1}) (panels b, f, and j), theta (K) (panels c, g, and k), and $H_2O_{(v)}$ (ppm) (panels d, h, and l). Altitude data are pressure altitude above sea level (km). Lapse rates are 5-point running means of binned data. CBL heights (Methods) are shown as heavy black lines.

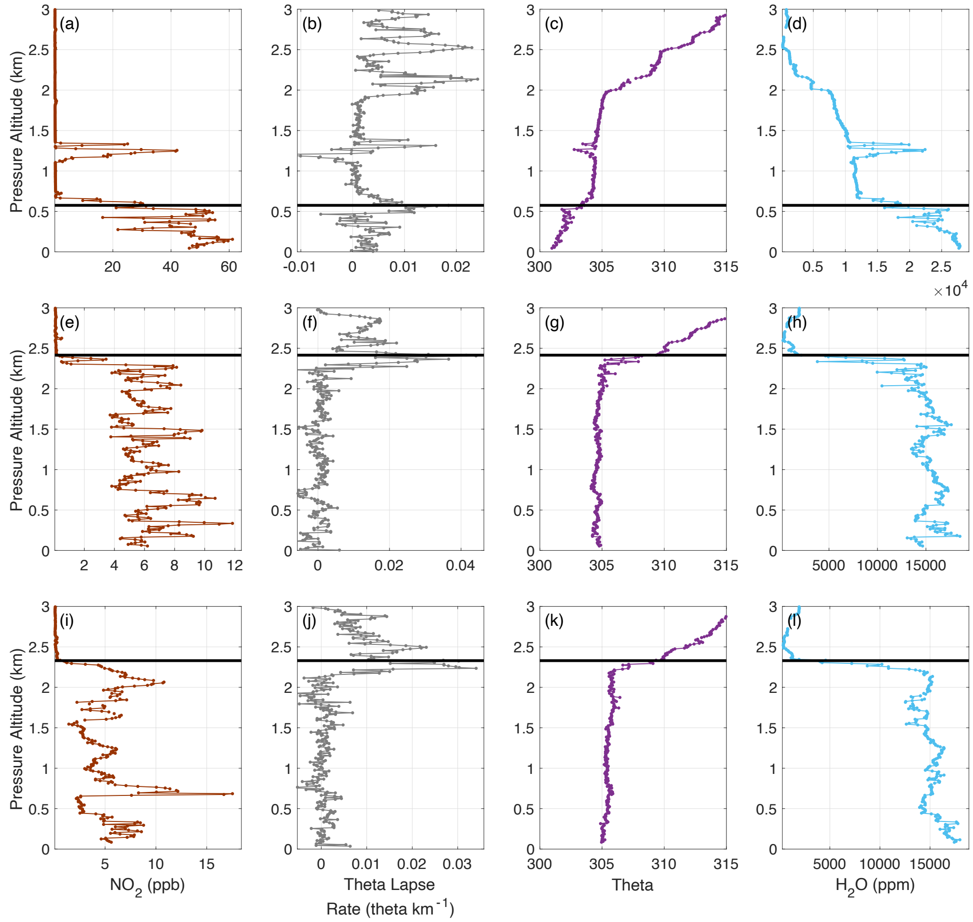

Figure A3.54. Deer Park on September 25, 2013: P-3B vertical profile measurements averaged into 10-m altitude bins during the morning (panels a–d), midday (panels e–h), and afternoon (panels i–l) circuits: NO_2 (ppb) (panels a, e, and i), theta lapse rate (K km^{-1}) (panels b, f, and j), theta (K) (panels c, g, and k), and $H_2O_{(v)}$ (ppm) (panels d, h, and l). Altitude data are pressure altitude above sea level (km). Lapse rates are 5-point running means of binned data. CBL heights (Methods) are shown as heavy black lines.

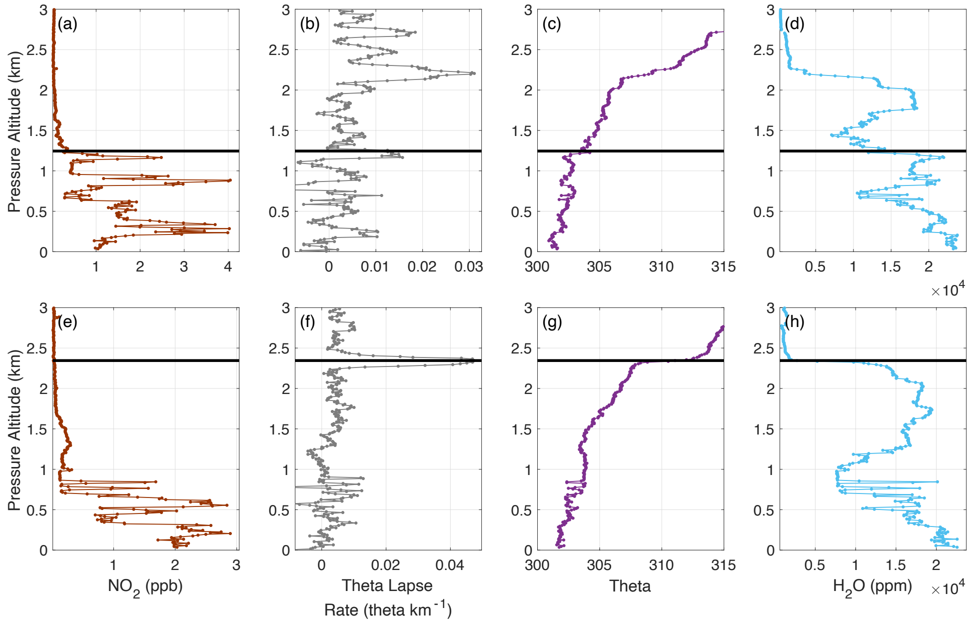

Figure A3.55. Deer Park on September 26, 2013: P-3B vertical profile measurements averaged into 10-m altitude bins during the midday (panels a–d) and afternoon (panels e–h) circuits: NO_2 (ppb) (panels a and e), theta lapse rate (K km^{-1}) (panels b and f), theta (K) (panels c and g), and $H_2O_{(v)}$ (ppm) (panels d and h). Altitude data are pressure altitude above sea level (km). Lapse rates are 5-point running means of binned data. CBL heights (Methods) are shown as heavy black lines.

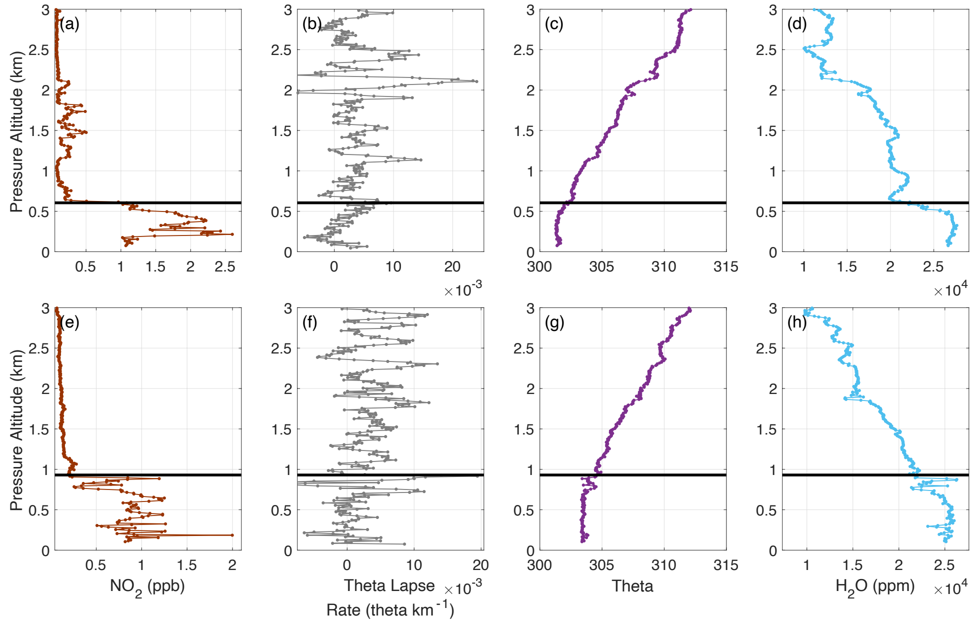

Figure A3.56. Manvel Croix on September 4, 2013: P-3B vertical profile measurements averaged into 10-m altitude bins during the morning (panels a–d) and midday (panels e–h) circuits: NO_2 (ppb) (panels a and e), theta lapse rate (K km^{-1}) (panels b and f), theta (K) (panels c and g), and $H_2O_{(v)}$ (ppm) (panels d and h). Altitude data are pressure altitude above sea level (km). Lapse rates are 5-point running means of binned data. CBL heights (Methods) are shown as heavy black lines.

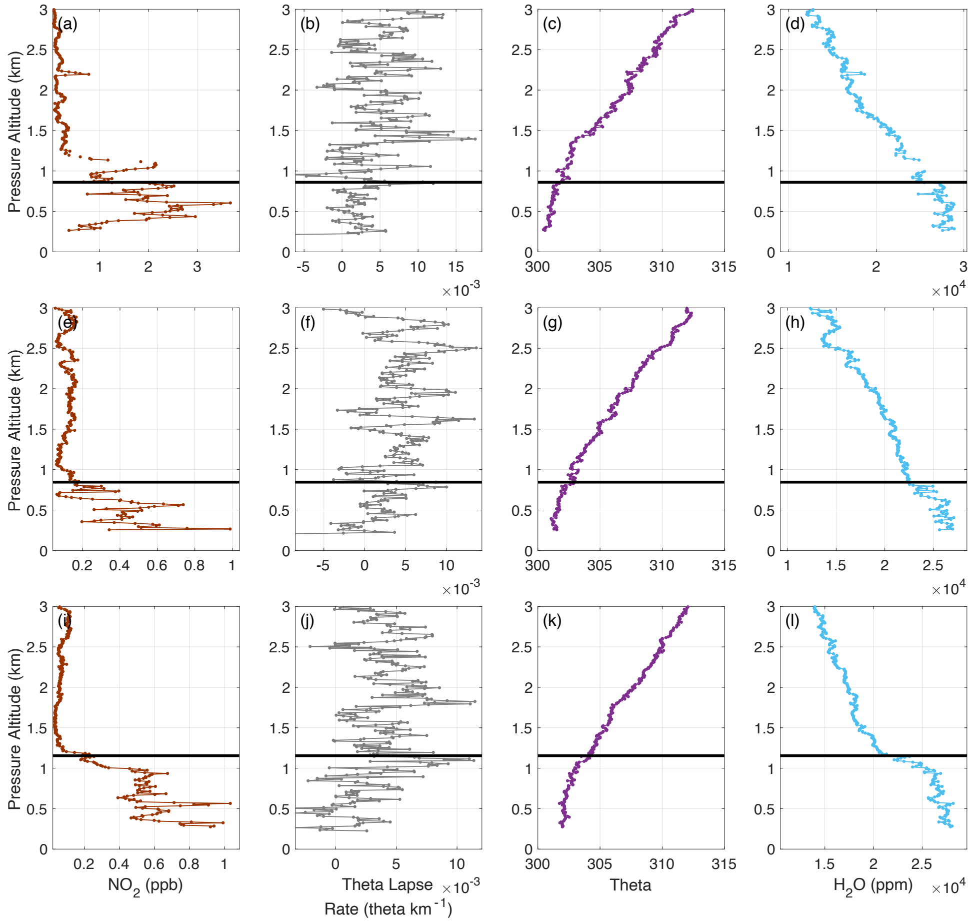

Figure A3.57. Manvel Croix on September 6, 2013: P-3B vertical profile measurements averaged into 10-m altitude bins during the morning (panels a–d), midday (panels e–h), and afternoon (panels i–l) circuits: NO_2 (ppb) (panels a, e, and i), theta lapse rate (K km^{-1}) (panels b, f, and j), theta (K) (panels c, g, and k), and $H_2O_{(v)}$ (ppm) (panels d, h, and l). Altitude data are pressure altitude above sea level (km). Lapse rates are 5-point running means of binned data. CBL heights (Methods) are shown as heavy black lines.

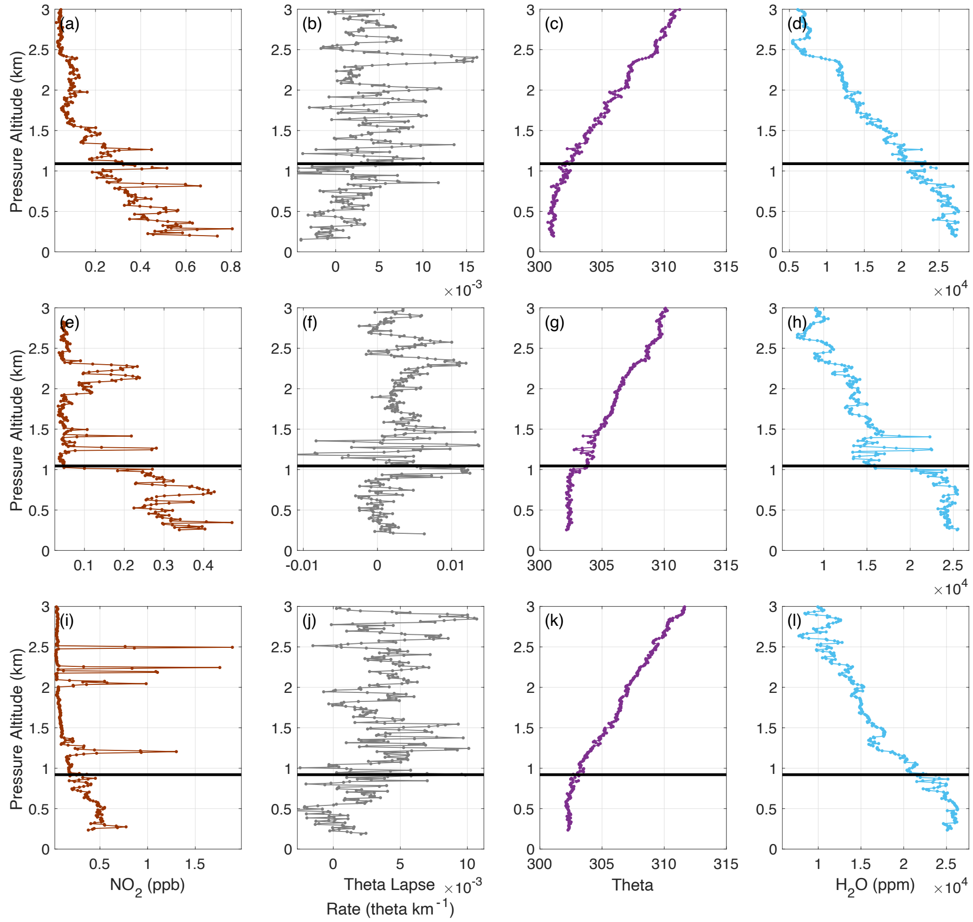

Figure A3.58. Manvel Croix on September 11, 2013: P-3B vertical profile measurements averaged into 10-m altitude bins during the morning (panels a–d), midday (panels e–h), and afternoon (panels i–l) circuits: NO_2 (ppb) (panels a, e, and i), theta lapse rate (K km^{-1}) (panels b, f, and j), theta (K) (panels c, g, and k), and $H_2O_{(v)}$ (ppm) (panels d, h, and l). Altitude data are pressure altitude above sea level (km). Lapse rates are 5-point running means of binned data. CBL heights (Methods) are shown as heavy black lines.

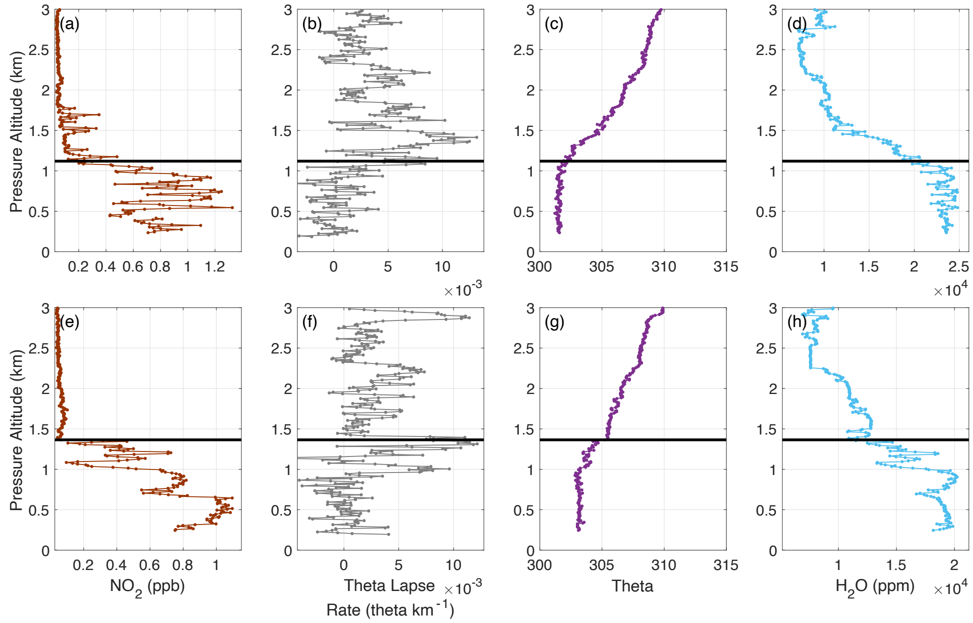

Figure A3.59. Manvel Croix on September 12, 2013: P-3B vertical profile measurements averaged into 10-m altitude bins during the morning (panels a–d) and midday (panels e–h) circuits: NO_2 (ppb) (panels a and e), theta lapse rate (K km^{-1}) (panels b and f), theta (K) (panels c and g), and $H_2O_{(v)}$ (ppm) (panels d and h). Altitude data are pressure altitude above sea level (km). Lapse rates are 5-point running means of binned data. CBL heights (Methods) are shown as heavy black lines

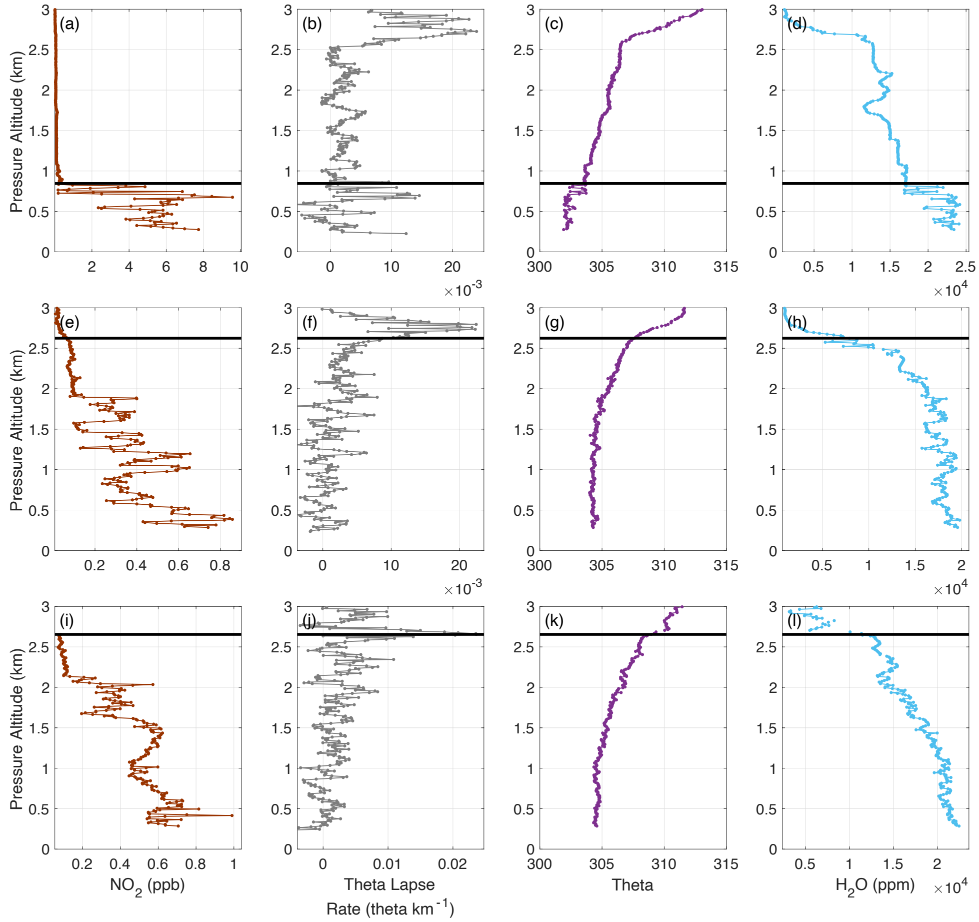

Figure A3.60. Manvel Croix on September 13, 2013: P-3B vertical profile measurements averaged into 10-m altitude bins during the morning (panels a–d), midday (panels e–h), and afternoon (panels i–l) circuits: NO_2 (ppb) (panels a, e, and i), theta lapse rate (K km^{-1}) (panels b, f, and j), theta (K) (panels c, g, and k), and $H_2O_{(v)}$ (ppm) (panels d, h, and l). Altitude data are pressure altitude above sea level (km). Lapse rates are 5-point running means of binned data. CBL heights (Methods) are shown as heavy black lines.

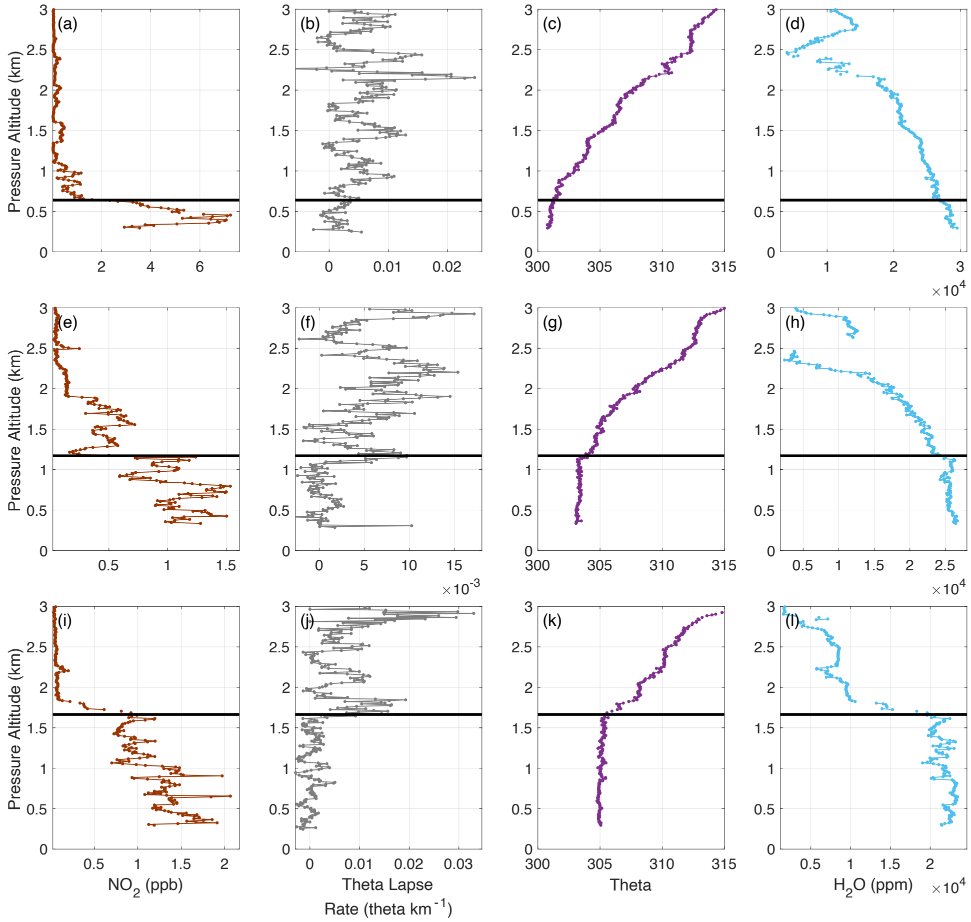

Figure A3.61. Manvel Croix on September 24, 2013: P-3B vertical profile measurements averaged into 10-m altitude bins during the morning (panels a–d), midday (panels e–h), and afternoon (panels i–l) circuits: NO_2 (ppb) (panels a, e, and i), theta lapse rate (K km^{-1}) (panels b, f, and j), theta (K) (panels c, g, and k), and $H_2O_{(v)}$ (ppm) (panels d, h, and l). Altitude data are pressure altitude above sea level (km). Lapse rates are 5-point running means of binned data. CBL heights (Methods) are shown as heavy black lines.

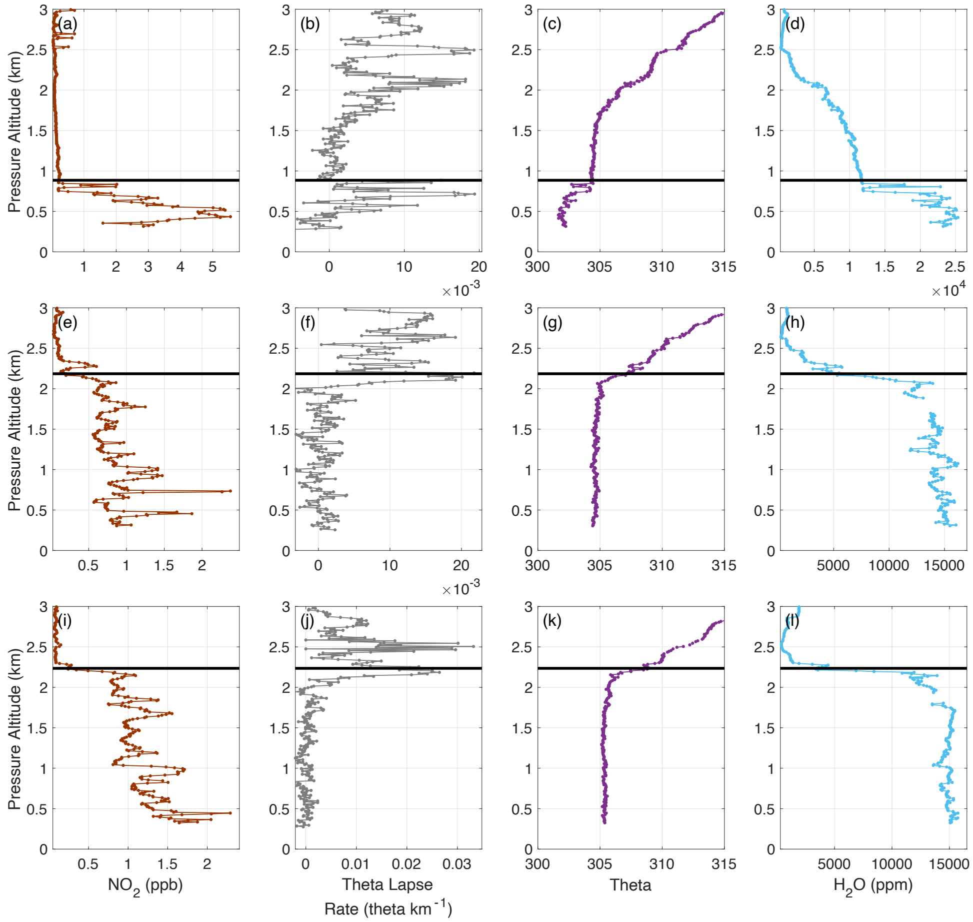

Figure A3.62. Manvel Croix on September 25, 2013: P-3B vertical profile measurements averaged into 10-m altitude bins during the morning (panels a–d), midday (panels e–h), and afternoon (panels i–l) circuits: NO_2 (ppb) (panels a, e, and i), theta lapse rate (K km^{-1}) (panels b, f, and j), theta (K) (panels c, g, and k), and $H_2O_{(v)}$ (ppm) (panels d, h, and l). Altitude data are pressure altitude above sea level (km). Lapse rates are 5-point running means of binned data. CBL heights (Methods) are shown as heavy black lines.

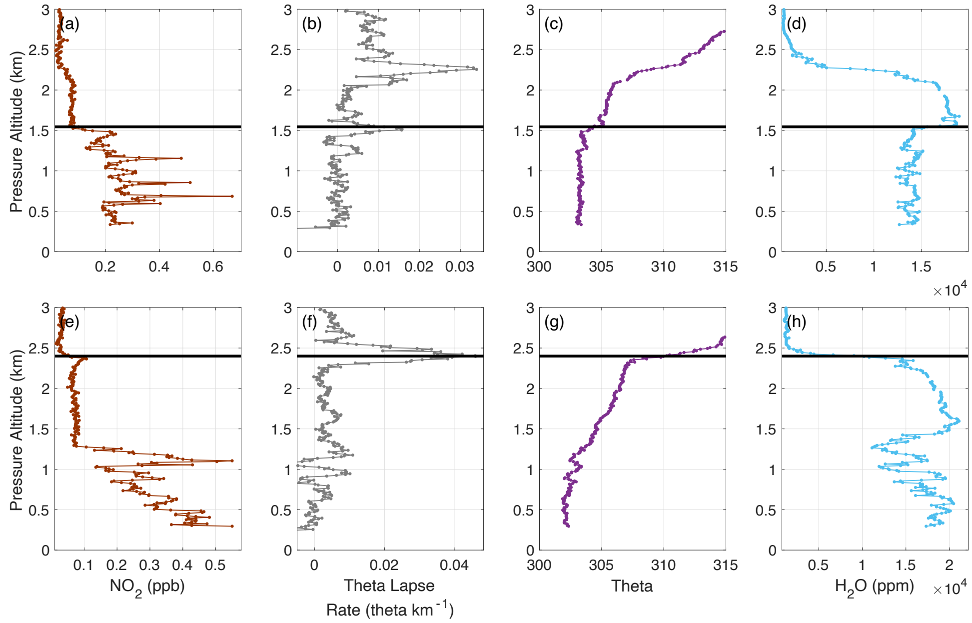

Figure A3.63. Manvel Croix on September 26, 2013: P-3B vertical profile measurements averaged into 10-m altitude bins during the midday (panels a–d) and afternoon (panels e–h) circuits: NO_2 (ppb) (panels a and e), theta lapse rate (K km^{-1}) (panels b and f), theta (K) (panels c and g), and $H_2O_{(v)}$ (ppm) (panels d and h). Altitude data are pressure altitude above sea level (km). Lapse rates are 5-point running means of binned data. CBL heights (Methods) are shown as heavy black lines.

Appendix A4

Text A4.1 Oversampled TROPOMI NO_2 TVCDs were averaged to underlying census-tract polygons within UA boundaries for each city. Census tract demographics and corresponding tract-level NO_2 were linked through their GEOIDs. Population-weighted NO_2 inequalities were calculated according to Eq. A4.4. Population-weighted NO_2 for the j^{th} race-ethnicity group in the i^{th} census tract were equal to the summation across the products of tract-level (NO_2, i) and group populations (p_i, j) for all n tracts in the UA divided by the total demographic group population in the UA.

$$Eq. A4.4 \qquad Population - weighted\ NO_{2,j} = \sum_{i=1}^{n} NO_{2,i}\, p_{i,j} \,/ \sum_{i=1}^{n} p_{i,j}$$

Race-ethnicity and income groups are categorized using U.S. Census designations: Black and African Americans (ALUKE004), Asians (ALUKE006), American Indians and Native Alaskans (ALUKE005), and whites (ALUKE003), excluding people from each racial group identifying as Hispanic or Latino; Hispanics/Latinos (ALUKE012), including all races also reporting as Hispanic and/or Latino; below the poverty line, >20% of tract households at or below an income-to-poverty ratio of one (ALWVE002 and ALWVE003); near the poverty line, all tract households having an income-to-poverty ratio of 1–1.24 (ALWVE004); and above the poverty line, all tract households having an income-to-poverty ratio >1.24 (ALWVE005, ALWVE006, ALWVE007, and ALWVE008).

Poverty-based NO2 inequalities are sensitive to the definition of the poverty line of 1.24. For example, if were defined 'above poverty' as all tract households having an income-to-poverty ratio >1.49 (ALWVE006, ALWVE007, and ALWVE008), and separately analyze NO_2 disparities near, but still above, the poverty line (ALWVE005), we find 7 ± 4%, 6 ± 4%, 9 ± 6%, and 6 ± 6% higher NO_2 for tracts near-above (ALWVE005) than significantly above poverty (ALWVE006, ALWVE007, and ALWVE008) for summer weekdays, summer weekends, winter weekdays, and winter weekends, respectively. Likewise, we compute 11 ± 6%,10 ± 5%, 12 ±6%, and 9±5% higher NO_2 for tracts below (ALWVE002 and ALWVE 003) and 14 ± 7%,11 ± 6%,17 ± 11%, and 11 ± 6% higher NO_2 for tracts near, but still below (ALWVE004), than significantly above the poverty line (ALWVE006, ALWVE007, and ALWVE008) for summer weekdays, summer weekends, winter weekdays, and winter weekends, respectively. Sensitivity to the definition of poverty indicates a scaling between household income and census-tract NO_2 TVCD, where, as income-to-poverty increases, NO_2 column densities decrease.

Appendix A4

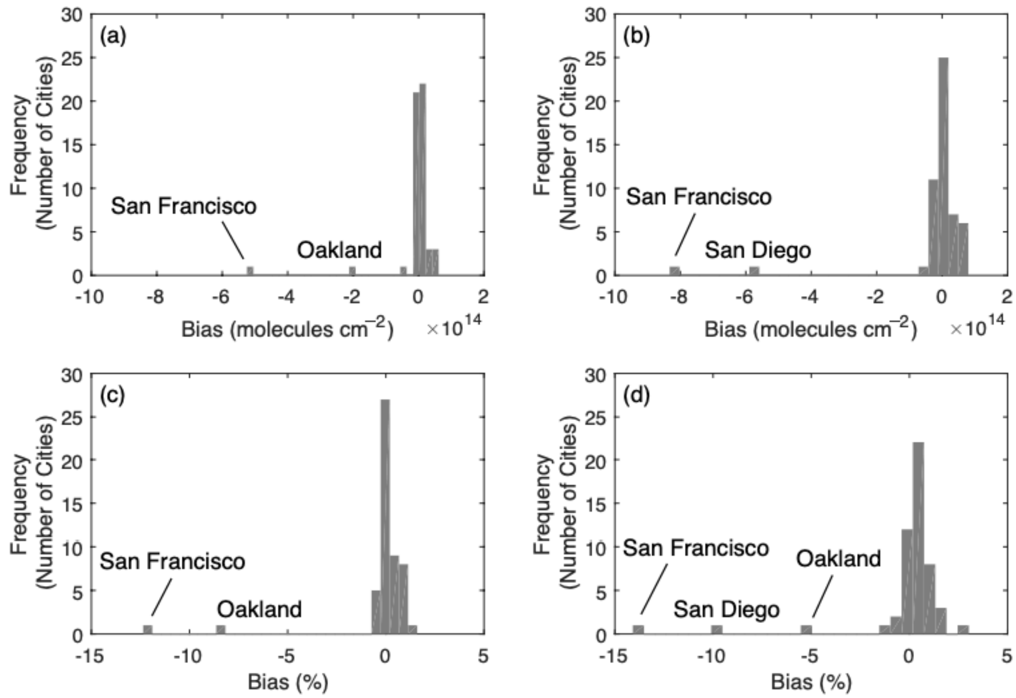

Figure A4.1. City-level bias in census tract-averaged absolute (a–b) and relative (c–d) LIN-HIW differences for summer (a and c) and winter (b and d) weekday TROPOMI observations, oversampled to 0.01° x 0.01° and degraded to 0.04° x 0.04°, compared to TROPOMI observations oversampled to 0.01° x 0.01°. Positive values indicate greater LIN-HIW differences in the 0.01° x 0.01° than the 0.04° x 0.04° product.

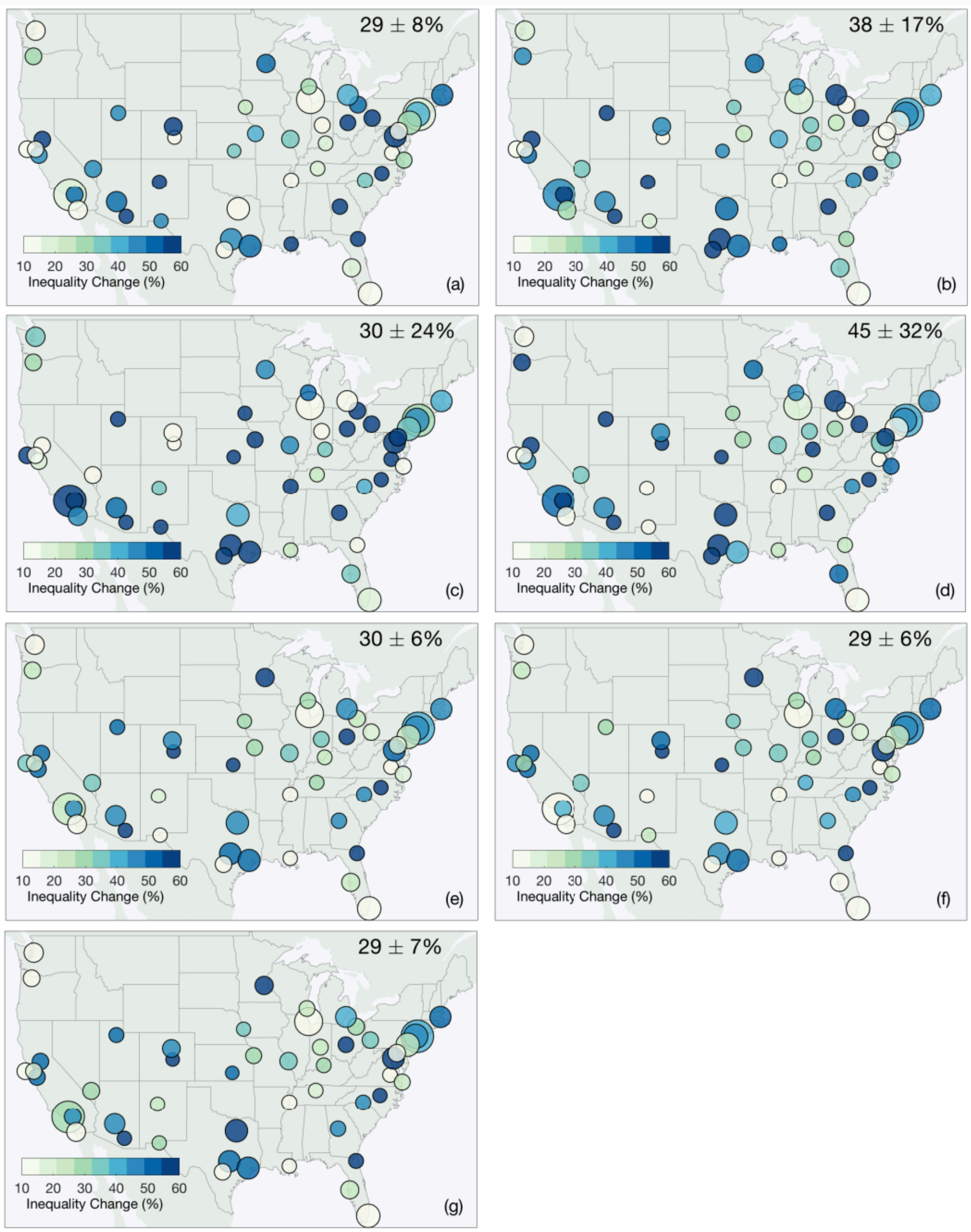

Figure A4.2. Summer weekday-weekend percentage difference in inequality in the 52 UAs for Black and African American (a), Hispanic and Latino (b), Asian (c), and Native American (d) compared to white residents. Inequalities are also mapped for people living near (e) and below (f) versus above the poverty line and for LINs compared to HIWs (g). Mean values for each group weighted by urban population size are also reported.

Appendix A4

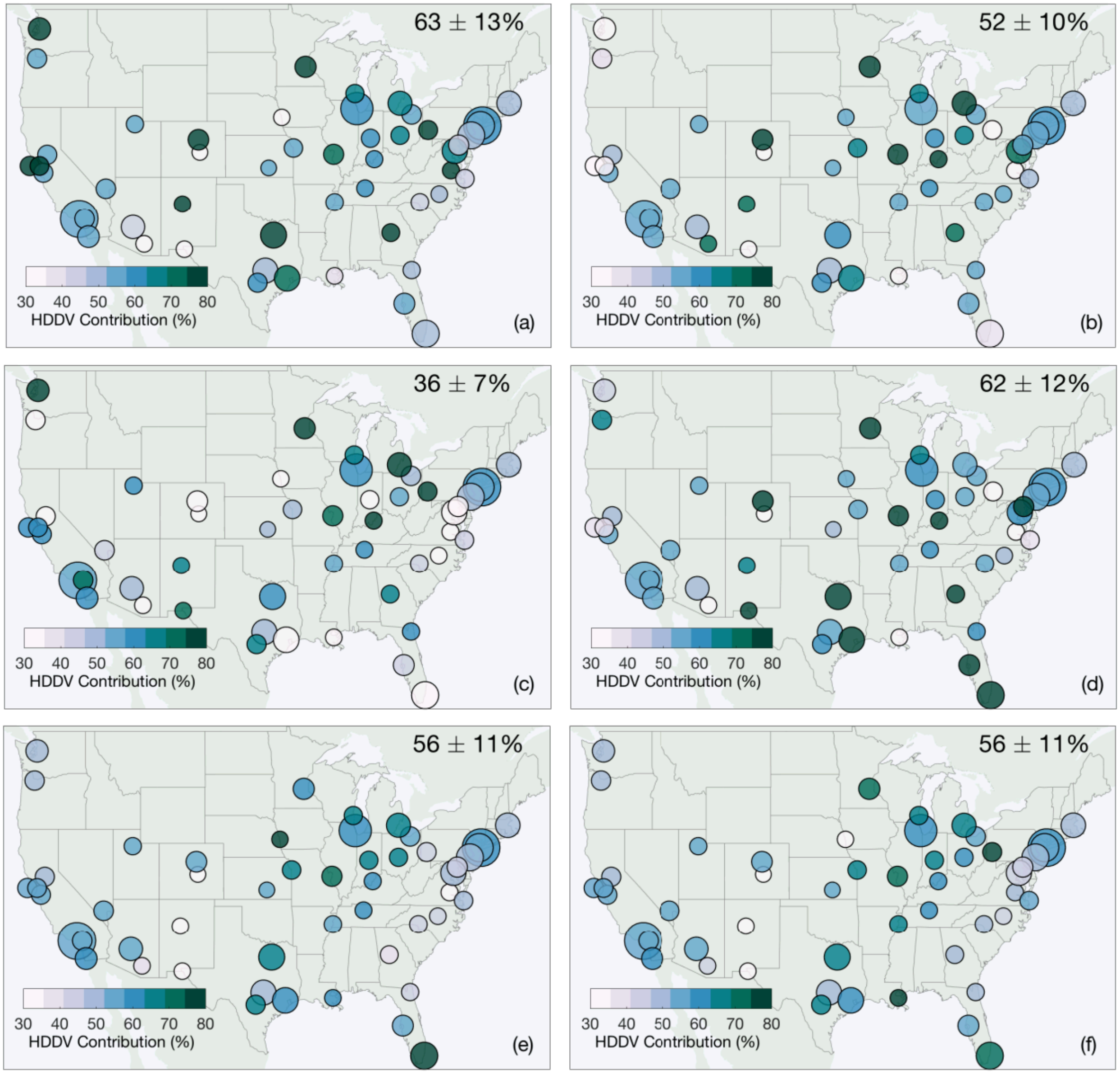

Figure A4.3. Percent contributions of on-road HDDVs to NOx emission density LIN-HIW inequalities during summer months for Black and African American (a), Hispanic and Latino (b), Asian (c), and Native American (d) compared to white residents. Inequalities are also mapped for people living near (e) and below (f) versus those living above the poverty line. Mean values for each group weighted by urban population size are also reported.

Appendix A4

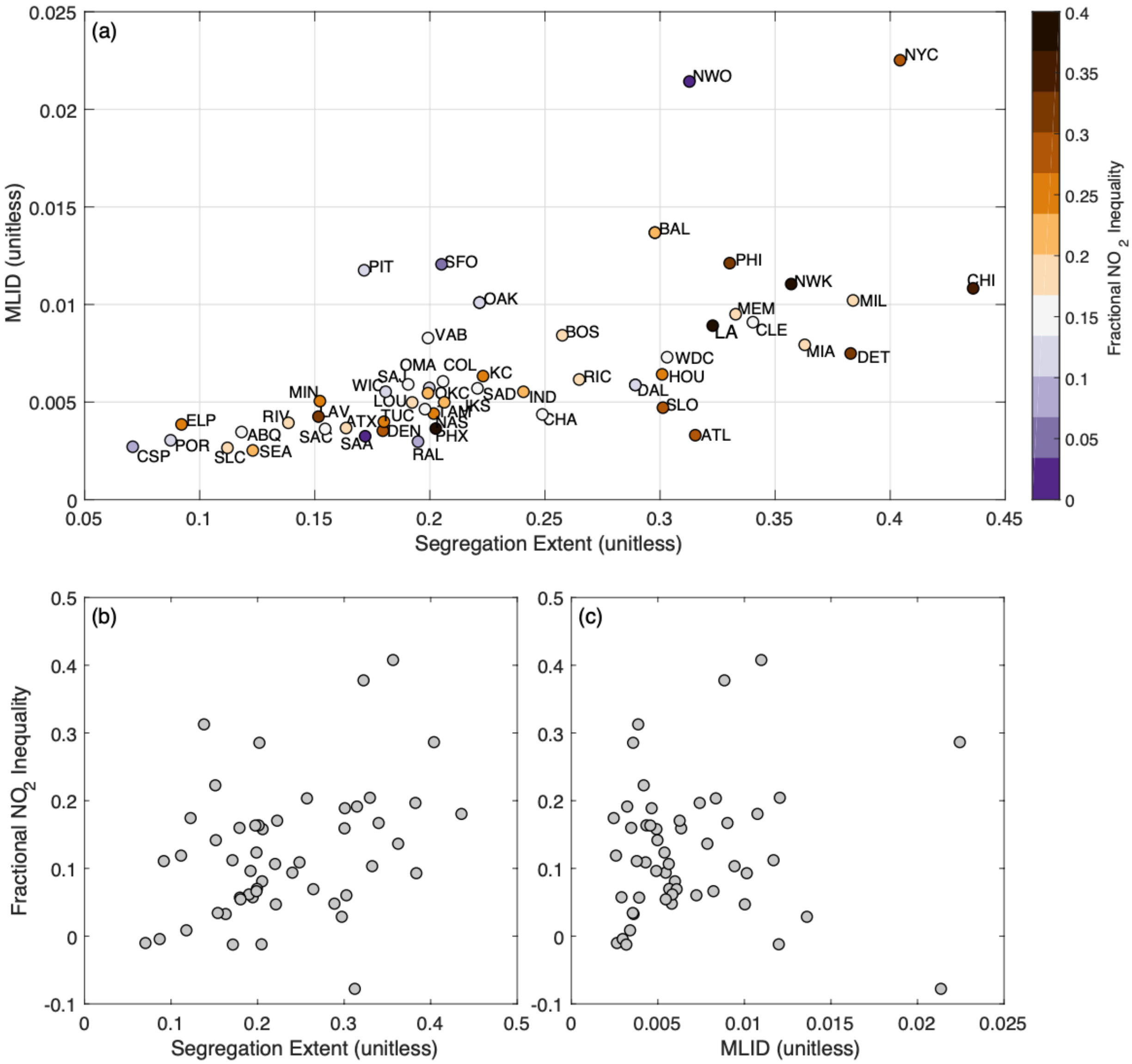

Figure A4.4. Relationships between racial-ethnic segregation extent and structure (mean local information density, MLID) (a), segregation extent and race-ethnicity inequality (b), and segregation structure and race-ethnicity inequality (c), where race-ethnicity inequality is defined as the summer weekday population-weighted NO_2 difference between Black and African Americans, Hispanics and Latinos, Asians, and Native Americans compared to non-Hispanic whites. Higher MLID values indicate segregation is characterized as patch worked and lower MLID values indicate segregation is characterized by clustering.

Appendix A4

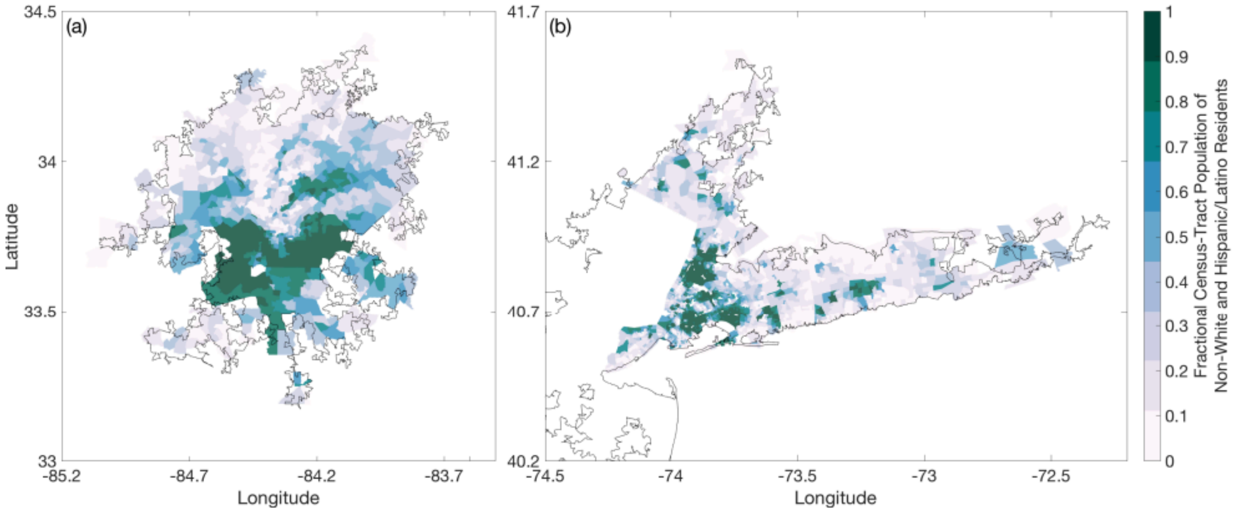

Figure A4.5. Fraction of residents that are Black or African American, Asian, Native American, and Hispanic/Latino in each census tract in the Atlanta, GA (a) and New York City, NY (b) UAs

Appendix A4

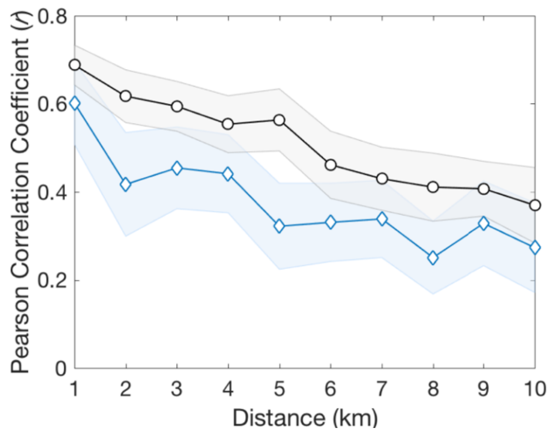

Figure A4.6. Average Pearson correlation coefficients (*r*) between tract-averaged TVCDs and surface NO_2* mixing ratios as a function of distance between monitoring stations and census tract center points on summer (black circles) and winter weekdays (blue diamonds) for the 20 UAs with at least three monitors. Envelopes represent the 1s standard mean errors of the city-specific *r* values.

Appendix A4

Table A4.1. Census-designated 'urbanized areas' (UAs) in this study, with boundaries from the U.S. Census Bureau (https://www.census.gov/cgi-bin/geo/shapefiles/index.php). There are the following exceptions: (a) the New York City–Newark, NJ–NY–CT UA was divided along state lines to create distinct estimates for New York City, NY and Newark, NJ and (b) the San Francisco–Oakland, CA UA was divided through San Francisco Bay to create distinct estimates for Oakland, CA and San Francisco, CA.

Abbreviation	Urbanized Area
ABQ	Albuquerque, NM
ATL	Atlanta, GA
ATX	Austin, TX
BAL	Baltimore, MD
BOS	Boston, MA–NH–RI
CHA	Charlotte, NC–SC
CHI	Chicago, IL–IN
CLE	Cleveland, OH
COL	Columbus, OH
CSP	Colorado Springs, CO
DAL	Dallas–Fort Worth–Arlington, TX
DEN	Denver–Aurora, CO
DET	Detroit, MI
ELP	El Paso, TX–NM
HOU	Houston, TX
IND	Indianapolis, IN
JKS	Jacksonville, RL
KC	Kansas City, MO–KS
LA	Los Angeles–Long Beach–Anaheim, CA
LAV	Las Vegas–Henderson, NV
LOU	Louisville/Jefferson County, KY–IN
MEM	Memphis, TN–MS–AR
MIA	Miami, FL
MIL	Milwaukee, WI
MIN	Minneapolis–St. Paul, MN–WI
NAS	Nashville–Davidson, TN
NWK	Newark, NJ
NWO	New Orleans, LA
NYC	New York, NY
OAK	Oakland, CA
OKC	Oklahoma City, OK
OMA	Omaha, NE–IA
PHI	Philadelphia, PA–NJ–DE–MD
PHX	Phoenix–Mesa, AZ
PIT	Pittsburgh, PA
POR	Portland, OR–WA
RAL	Raleigh, NC
RIC	Richmond, VA
RIV	Riverside–San Bernardino, CA
SAA	San Antonio, TX
SAC	Sacramento, CA
SAD	San Diego, CA
SAJ	San Jose, CA
SEA	Seattle, WA
SFO	San Francisco, CA
SLC	Salt Lake City–West Valley City, UT
SLO	St. Louis, MO-IL
TAM	Tampa–St. Petersburg, FL
TUC	Tucson, AZ
VB	Virginia Beach, VA
WDC	Washington, DC–VA–MD
WIC	Wichita, KS

Appendix A4

Table A4.2. Mean UA-level oversampled TROPOMI sampling statistics rounded up to the nearest integer.

Average of Number of Overlapping Pixels Per 0.01° x 0.01° Grid Box				
Urbanized Area	**Summer Weekdays**	**Summer Weekends**	**Winter Weekdays**	**Winter Weekends**
ABQ	95	42	51	28
ATL	60	21	41	20
ATX	85	36	52	35
BAL	57	27	19	11
BOS	66	29	14	11
CHA	70	30	41	27
CHI	67	26	9	6
CLE	56	30	5	6
COL	44	23	9	6
CSP	63	25	29	11
DAL	82	35	42	31
DEN	86	24	23	9
DET	58	22	4	7
ELP	100	43	72	45
HOU	60	21	44	29
IND	61	31	10	13
JKS	41	21	49	24
KC	76	32	18	12
LA	114	48	67	27
LAV	109	47	65	31
LOU	56	25	15	13
MEM	63	22	27	21
MIA	50	19	52	27
MIL	68	24	2.4	3
MIN	70	24	13	4
NAS	53	21	26	14
NWK	62	32	19	10
NWO	53	19	45	25
NYC	62	32	19	10
OAK	125	52	37	18
OKC	92	33	38	24
OMA	82	33	13	8
PHI	55	30	16	10
PHX	113	48	74	38
PIT	36	24	9	6
POR	84	43	11	2
RAL	73	28	42	19
RIC	64	28	22	15
RIV	116	50	71	27
SAA	73	36	51	35
SAC	123	50	40	16
SAD	110	45	74	33
SAJ	127	53	37	17
SEA	72	35	10	1
SFO	119	49	36	17
SLC	103	43	17	4
SLO	71	30	13	11
TAM	41	21	58	31
TUC	97	44	77	42
VB	76	35	36	16
WDC	58	27	20	11
WIC	89	37	20	15
Mean ± 1 σ	77 ± 24	33 ± 10	33 ± 21	18 ± 11

Appendix A4

Table A4.3. Weekday-weekend differences in UA-level TVCD inequalities in the summer and winter computed from the slope of the weekday versus weekend census-tract-averages based on the 0.01° x 0.01° and 0.04° x 0.04° products and the FIVE and NEI inventories. For the observations, the *y*-intercepts have units of x10^{14} molecules cm^{-2} and errors are derived from the fit, a weighted bivariate linear regression model. For the inventories, the *y*-intercepts have units of metric tons NO_x km^{-1} day^{-1}; the slope and intercept errors are negligible and not included. The Pearson correlation coefficients are also reported.

	Slope	**Intercept**	***r***	**Slope**	**Intercept**	***r***
			Fine (0.01° x 0.01°)			
		Summer			**Winter**	
LINs	0.63 ± 0.03	0.15 ± 0.25	0.93	0.68 ± 0.02	–0.69 ± 0.28	0.51
Black/African Americans	0.73 ± 0.05	–0.19 ± 0.24	0.93	0.82 ± 0.03	–0.92 ± 0.26	0.65
Hispanics and Latinos	0.52 ± 0.05	0.28 ± 0.20	0.95	0.89 ± 0.04	–1.77 ± 0.27	0.55
Asians	0.57 ± 0.05	–0.02 ± 0.17	0.97	1.07 ± 0.06	–0.43 ± 0.23	0.70
Native Americans	0.53 ± 0.05	0.16± 0.20	0.95	0.90 ± 0.05	–1.66 ± 0.27	0.61
Below poverty	0.66 ± 0.06	–0.05 ± 0.29	0.89	0.68 ± 0.03	–0.68 ± 0.28	0.47
Near poverty	0.62 ± 0.10	0.06 ± 0.26	0.93	0.59 ± 0.06	–0.04 ± 0.26	0.48
			Coarse (0.04° x 0.04°)			
		Summer			**Winter**	
LINs	0.63 ± 0.04	0.09 ± 0.26	0.93	0.62 ± 0.02	–0.23 ± 0.28	0.54
Black/African Americans	0.72 ± 0.06	–0.21 ± 0.25	0.93	0.74 ± 0.03	–0.60 ± 0.26	0.70
Hispanics and Latinos	0.52 ± 0.04	0.27 ± 0.20	0.95	0.81 ± 0.04	–1.43 ± 0.27	0.60
Asians	0.58 ± 0.06	–0.02 ± 0.18	0.97	1.01 ± 0.05	–0.45 ± 0.23	0.75
Native Americans	0.54 ± 0.05	0.13 ± 0.20	0.96	0.82 ± 0.04	–1.33 ± 0.23	0.67
Below poverty	0.66 ± 0.07	–0.05 ± 0.30	0.88	0.63 ± 0.02	–0.41 ± 0.28	0.50
Near poverty	0.62 ± 0.10	0.05 ± 0.26	0.93	0.56 ± 0.06	0.04 ± 0.26	0.54
			Inventories (0.04° x 0.04°)			
		Summer			**Winter**	
LINs	0.59	2.3 x 10^{-8}	0.99	0.62	1.9 x 10^{-8}	0.99
Black/African Americans	0.56	1.4 x 10^{-8}	0.99	0.61	9.0 x 10^{-9}	0.99
Hispanics and Latinos	0.58	7.5 x 10^{-9}	0.99	0.61	7.1 x 10^{-9}	0.99
Asians	0.59	2.3 x 10^{-9}	0.99	0.62	2.6 x 10^{-9}	0.99
Native Americans	0.59	5.5 x 10^{-9}	0.99	0.61	5.0 x 10^{-9}	0.99
Below poverty	0.61	1.3 x 10^{-8}	0.99	0.63	1.2 x 10^{-8}	0.99
Near poverty	0.61	1.3 x 10^{-8}	0.99	0.62	6.4 x 10^{-9}	0.99

Appendix A4

Table A4.4. Normalized biases and errors for census tract-averaged TROPOMI observations, oversampled to 0.01° x 0.01° over and degraded to 0.04° x 0.04°, compared to TROPOMI observations, oversampled 1° x 1° only. Positive values indicate greater inequalities in the 0.01° x 0.01° than 0.04° x 0.04° product.

Absolute Inequality	**LINs**	**Black and African Americans**	**Hispanic and Latino**	**Asian**	**Native Americans**	**Near poverty**	**Below poverty**
Mean Bias (x10^{13} molecules cm^{-2})							
Summer weekdays	–0.8	–1.8	–0.4	–0.3	–0.6	0.01	–0.4
Winter weekdays	–1.9	–29.2	–22.2	–9.7	–18.9	–14.1	–26.4
Normalized Mean Bias (x10^{-2})							
Summer weekdays	–1.4	–5.6	–1.1	–2.1	–2.5	0.2	–1.2
Winter weekdays	–2.0	–94.2	–63.9	–73.6	–73.0	–69.3	–717
Mean Error (x10^{13} molecules cm^{-2})							
Summer weekdays	2.6	2.7	1.9	1.1	1.7	0.8	0.2
Winter weekdays	4.9	40.3	32.2	16.8	25.0	17.5	33.0
Normalized Mean Error (x10^{-2})							
Summer weekdays	4.4	8.6	5.6	8.2	6.7	3.7	5.1
Winter weekdays	5.2	1300	94.5	12.8	96.1	86.2	89.7
Relative Inequality	**LINs**	**Black and African Americans**	**Hispanic and Latino**	**Asian**	**Native Americans**	**Near poverty**	**Below poverty**
Mean Bias (%)							
Summer weekdays	–0.41	–0.74	–0.22	–0.15	–0.32	–0.02	–0.21
Winter weekdays	–0.09	–0.56	–0.29	–0.29	–0.26	0.02	–0.15
Normalized Mean Bias							
Summer weekdays	–1.78	–5.90	–1.63	–2.68	–2.96	–0.20	–1.49
Winter weekdays	–0.36	–3.64	–1.97	–4.82	–2.21	0.24	–0.94
Mean Error (%)							
Summer weekdays	1.01	1.08	0.74	0.44	0.70	0.29	0.71
Winter weekdays	1.44	1.35	1.11	0.78	1.03	0.50	1.13
Normalized Mean Error							
Summer weekdays	4.35	8.55	5.41	7.92	6.55	3.47	4.96
Winter weekdays	5.66	8.77	7.58	12.94	8.65	5.43	7.04

Appendix A4

Table A4.5. Weekday-weekend percent differences in NO_x emission densities and NO_x emissions inequality.

	Weekday-Weekend Percent Differences (%)			
Urbanized Area	**Summer Emission Densities**	**Winter Emission Densities**	**Summer LIN-HIW Inequalities**	**Winter LIN-HIW Inequalities**
ABQ	10	9	2	0
ATL	11	11	0	0
ATX	11	10	0	0
BAL	11	11	0	0
BOS	11	11	0	0
CHA	11	11	0	0
CHI	10	10	0	0
CLE	10	10	0	0
COL	11	11	0	0
CSP	9	9	3	0
DAL	11	10	0	0
DEN	10	9	0	0
DET	11	11	0	0
ELP	9	8	0	0
HOU	11	10	0	0
IND	11	11	0	0
JKS	11	153	1	0
KC	10	10	0	0
LA	9	9	0	0
LAV	9	9	0	0
LOU	11	11	0	0
MEM	11	10	1	0
MIA	11	10	0	0
MIL	10	9	0	0
MIN	11	10	0	0
NAS	11	10	0	0
NWK	11	11	0	0
NWO	11	10	0	0
NYC	11	11	0	0
OAK	8	8	0	0
OKC	11	10	1	0
OMA	11	10	0	0
PHI	11	11	0	0
PHX	10	9	1	0
PIT	11	11	0	0
POR	9	9	0	0
RAL	11	11	0	0
RIC	11	11	1	0
RIV	9	8	1	0
SAA	11	10	0	0
SAC	9	9	0	0
SAD	9	9	0	0
SAJ	9	9	0	0
SEA	9	9	0	0
SFO	8	8	0	0
SLC	9	9	0	0
SLO	11	10	0	0
TAM	11	11	1	0
TUC	10	9	1	0
VB	11	11	0	0
WDC	11	11	0	0
WIC	11	10	0	0
Mean	10 ± 1	13 ± 20	0 ± 0	0 ± 0

Appendix A4

Table A4.6. On-road HDDV emissions contribution to inequality and summer weekday inequality from inventory emissions estimates with HDDV emissions completely controlled for each sociodemographic group. Data are unweighted by urban population size.

On-Road Diesel Contributions to NO_x Emissions Inequality	Summer Weekdays (%)	Summer Weekends (%)	Winter Weekdays (%)	Winter Weekends (%)
LINs	45 ± 5	26 ± 5	39 ± 5	25 ± 5
Black or African Americans	43 ± 5	25 ± 5	47 ± 5	28 ± 5
Hispanics/Latinos	41 ± 5	23 ± 5	36 ± 5	32 ± 5
Asians	35 ± 5	19 ± 5	38 ± 5	25 ± 5
Native Americans	43 ± 5	25 ± 5	38 ± 5	33 ± 5
Non-white and/or Hispanic/Latino	55 ± 9	35 ± 9	49 ± 9	42 ± 13
Below Poverty	46 ± 5	27 ± 5	40 ± 5	25 ± 5
Near Poverty	45 ± 5	26 ± 5	39 ± 5	25 ± 5

Summer Weekday On-Road Diesel Contributions to NO_x Emissions Inequality	Inequality with HDDVs (%)	Inequality without HDDVs (%)	Change in inequality (%)
LINs	127 ± 16	121 ± 15	49 ± 18
Black or African Americans	62 ± 14	51 ± 13	57 ± 35
Hispanics/Latinos	64 ± 13	52 ± 14	55 ± 32
Asians	39 ± 15	33 ± 13	60 ± 59
Native Americans	50 ± 37	40 ± 13	64 ± 118
Non-white and/or Hispanic/Latino	54 ± 14	44 ± 14	59 ± 42
Below Poverty	88 ± 13	83 ± 13	48 ± 21
Near Poverty	56 ± 13	52 ± 12	49 ± 33

References

(1) Kim, S. W.; Heckel, A.; McKeen, S. A.; Frost, G. J.; Hsie, E. Y.; Trainer, M. K.; Richter, A.; Burrows, J. P.; Peckham, S. E.; Grell, G. A. Satellite-observed U.S. power plant NOx emission reductions and their impact on air quality. *Geophysical Research Letters* **2006**, *33* (22). DOI: 10.1029/2006gl027749.
(2) De Gouw, J. A.; Parrish, D. D.; Frost, G. J.; Trainer, M. Reduced emissions of CO2, NOx, and SO2. *Earth's Future* **2014**, *2* (2), 75-82. DOI: 10.1002/2013ef000196.
(3) Wang, Y.; Apte, J. S.; Hill, J. D.; Ivey, C. E.; Patterson, R. F.; Robinson, A. L.; Tessum, C. W.; Marshall, J. D. Location-specific strategies for eliminating US national racial-ethnic PM2.5 exposure inequality. *Proceedings of the National Academy of Sciences* **2022**, *119* (44). DOI: 10.1073/pnas.2205548119.
(4) Hong, C.; Zhang, Q.; Zhang, Y.; Davis, S. J.; Tong, D.; Zheng, Y.; Liu, Z.; Guan, D.; He, K.; Schellnhuber, H. J. Impacts of climate change on future air quality and human health in China. *Proceedings of the National Academy of Sciences* **2019**, *116* (35), 17193-17200. DOI: 10.1073/pnas.1812881116.
(5) Di, Q.; Dai, L.; Wang, Y.; Zanobetti, A.; Choirat, C.; Schwartz, J. D.; Dominici, F. Association of Short-term Exposure to Air Pollution With Mortality in Older Adults. *Journal of the American Medical Association* **2017**, *318* (24), 2446. DOI: 10.1001/jama.2017.17923.
(6) Fortunati, A.; Barta, C.; Brilli, F.; Centritto, M.; Zimmer, I.; Schnitzler, J. R.-P.; Loreto, F. Isoprene emission is not temperature-dependent during and after severe drought-stress: a physiological and biochemical analysis. *The Plant Journal* **2008**, *55* (4), 687-697. DOI: 10.1111/j.1365-313x.2008.03538.x.
(7) Adar, S. D.; Kaufman, J. D. Cardiovascular Disease and Air Pollutants: Evaluating and Improving Epidemiological Data Implicating Traffic Exposure. *Inhalation Toxicology* **2007**, *19* (sup1), 135-149. DOI: 10.1080/08958370701496012.
(8) Crouse, D. L.; Peters, P. A.; Hystad, P.; Brook, J. R.; van Donkelaar, A.; Martin, R. V.; Villeneuve, P. J.; Jerrett, M.; Goldberg, M. S.; Pope, C. A., 3rd; et al. Ambient PM2.5, O_3, and NO_2 Exposures and Associations with Mortality over 16 Years of Follow-Up in the Canadian Census Health and Environment Cohort (CanCHEC). *Environmental Health Perspectives* **2015**, *123* (11), 1180-1186. DOI: 10.1289/ehp.1409276 .
(9) Laughner Joshua, L.; Cohen Ronald, C. Direct observation of changing NOx lifetime in North American cities. *Science* **2019**, *366* (6466), 723-727. DOI: 10.1126/science.aax6832.
(10) Clark, L. P.; Millet, D. B.; Marshall, J. D. Changes in Transportation-Related Air Pollution Exposures by Race-Ethnicity and Socioeconomic Status: Outdoor Nitrogen Dioxide in the United States in 2000 and 2010. *Environmental Health Perspectives* **2017**, *125* (9), 097012. DOI: doi:10.1289/EHP959.
(11) Demetillo, M. A. G.; Anderson, J. F.; Geddes, J. A.; Yang, X.; Najacht, E. Y.; Herrera, S. A.; Kabasares, K. M.; Kotsakis, A. E.; Lerdau, M. T.; Pusede, S. E. Observing Severe Drought Influences on Ozone Air Pollution in California. *Environmental Science & Technology* **2019**, *53* (9), 4695-4706. DOI: 10.1021/acs.est.8b04852.
(12) Coumou, D.; Rahmstorf, S. A decade of weather extremes. *Nature Climate Change* **2012**, *2* (7), 491-496. DOI: 10.1038/nclimate1452.
(13) Dai, A. Increasing drought under global warming in observations and models. *Nature Climate Change* **2013**, *3* (1), 52-58. DOI: 10.1038/nclimate1633.

(14) Funk, C.; Peterson, P.; Landsfeld, M.; Pedreros, D.; Verdin, J.; Shukla, S.; Husak, G.; Rowland, J.; Harrison, L.; Hoell, A.; et al. The climate hazards infrared precipitation with stations—a new environmental record for monitoring extremes. *Scientific Data* **2015**, *2* (1), 150066. DOI: 10.1038/sdata.2015.66.
(15) Cook, B. I.; Ault, T. R.; Smerdon, J. E. Unprecedented 21st century drought risk in the American Southwest and Central Plains. *Science Advances* **2015**, *1* (1), e1400082. DOI: 10.1126/sciadv.1400082.
(16) Diffenbaugh, N. S.; Swain, D. L.; Touma, D. Anthropogenic warming has increased drought risk in California. *Proceedings of the National Academy of Sciences* **2015**, *112* (13), 3931-3936. DOI: 10.1073/pnas.1422385112.
(17) Jacob, D. J.; Winner, D. A. Effect of climate change on air quality. *Atmospheric Environment* **2009**, *43* (1), 51-63. DOI: 10.1016/j.atmosenv.2008.09.051.
(18) Huang, L. M.-B., E. C.; McGaughey, G.; Kimura, Y.; Allen, D. T. . The Impact of Drought on Ozone Dry Deposition over Eastern Texas. *Atmospheric Environment* **2016**, *127*, 176-186.
(19) Wang, Y.; Xie, Y.; Dong, W.; Ming, Y.; Wang, J.; Shen, L. Adverse effects of increasing drought on air quality via natural processes. *Atmospheric Chemistry and Physics* **2017**, *17* (20), 12827-12843. DOI: 10.5194/acp-17-12827-2017.
(20) Jerrett, M.; Burnett, R. T.; Pope, C. A.; Ito, K.; Thurston, G.; Krewski, D.; Shi, Y.; Calle, E.; Thun, M. Long-Term Ozone Exposure and Mortality. *New England Journal of Medicine* **2009**, *360* (11), 1085-1095. DOI: 10.1056/nejmoa0803894.
(21) Ashmore, M. R. Assessing the future global impacts of ozone on vegetation. *Plant, Cell & Environment* **2005**, *28* (8), 949-964. DOI: 10.1111/j.1365-3040.2005.01341.x.
(22) Di Carlo, P. Missing OH Reactivity in a Forest: Evidence for Unknown Reactive Biogenic VOCs. *Science* **2004**, *304* (5671), 722-725. DOI: 10.1126/science.1094392.
(23) Kaiser, J.; Skog, K. M.; Baumann, K.; Bertman, S. B.; Brown, S. B.; Brune, W. H.; Crounse, J. D.; De Gouw, J. A.; Edgerton, E. S.; Feiner, P. A.; et al. Speciation of OH reactivity above the canopy of an isoprene-dominated forest. *Atmospheric Chemistry and Physics* **2016**, *16* (14), 9349-9359. DOI: 10.5194/acp-16-9349-2016.
(24) Kim, S.; Guenther, A.; Karl, T.; Greenberg, J. Contributions of primary and secondary biogenic VOC tototal OH reactivity during the CABINEX (Community Atmosphere-Biosphere INteractions Experiments)-09 field campaign. *Atmospheric Chemistry and Physics* **2011**, *11* (16), 8613-8623. DOI: 10.5194/acp-11-8613-2011.
(25) Guenther, A.; Hewitt, C. N.; Erickson, D.; Fall, R.; Geron, C.; Graedel, T.; Harley, P.; Klinger, L.; Lerdau, M.; McKay, W. A.; et al. A global model of natural volatile organic compound emissions. *Journal of Geophysical Research* **1995**, *100* (D5), 8873. DOI: 10.1029/94jd02950.
(26) Jacob, D. J.; Logan, J. A.; Yevich, R. M.; Gardner, G. M.; Spivakovsky, C. M.; Wofsy, S. C.; Munger, J. W.; Sillman, S.; Prather, M. J.; Rodgers, M. O.; et al. Simulation of summertime ozone over North America. *Journal of Geophysical Research* **1993**, *98* (D8), 14797. DOI: 10.1029/93jd01223.
(27) Sharkey, T. D. L., F. Water Stress, Temperature, and Light Effects on the Capacity for Isoprene Emission and Photosynthesis of Kudzu Leaves. *Oecologia* **2005**, *146* (1), 120-129.
(28) Pegoraro, E.; Rey, A.; Barron-Gafford, G.; Monson, R.; Malhi, Y.; Murthy, R. The interacting effects of elevated atmospheric CO2 concentration, drought and leaf-to-air vapour pressure deficit on ecosystem isoprene fluxes. *Oecologia* **2005**, *146* (1), 120-129. DOI: 10.1007/s00442-005-0166-5.

(29) Brilli, F.; Barta, C.; Fortunati, A.; Lerdau, M.; Loreto, F.; Centritto, M. Response of isoprene emission and carbon metabolism to drought in white poplar (Populus alba) saplings. *New Phytologist* **2007**, *175* (2), 244-254. DOI: 10.1111/j.1469-8137.2007.02094.x.
(30) Lerdau, M.; Keller, M. Controls on isoprene emission from trees in a subtropical dry forest. *Plant, Cell & Environment* **1997**, *20* (5), 569-578. DOI: 10.1111/j.1365-3040.1997.00075.x.
(31) Tawfik, A. B. S., R.; Goldstein, A.; Pressley, S.; Steiner, A. L. . Quantifying the Contribution of Environmental Factors to Isoprene Flux Interannual Variability. *Atmospheric Environment* **2012**, *54*, 216-224.
(32) Huang, L.; McDonald-Buller, E.; McGaughey, G.; Kimura, Y.; Allen, D. T. Comparison of regional and global land cover products and the implications for biogenic emission modeling. *Journal of the Air & Waste Management Association* **2015**, *65* (10), 1194-1205. DOI: 10.1080/10962247.2015.1057302.
(33) Zheng, Y.; Unger, N.; Barkley, M. P.; Yue, X. Relationships between photosynthesis and formaldehyde as a probe of isoprene emission. *Atmospheric Chemistry and Physics* **2015**, *15* (15), 8559-8576. DOI: 10.5194/acp-15-8559-2015.
(34) Abeleira, A. J.; Farmer, D. K. Summer ozone in the northern Front Range metropolitan area: weekend–weekday effects, temperature dependences, and the impact of drought. *Atmospheric Chemistry and Physics* **2017**, *17* (11), 6517-6529. DOI: 10.5194/acp-17-6517-2017.
(35) Zheng, Y.; Unger, N.; Tadić, J. M.; Seco, R.; Guenther, A. B.; Barkley, M. P.; Potosnak, M. J.; Murray, L. T.; Michalak, A. M.; Qiu, X.; et al. Drought impacts on photosynthesis, isoprene emission and atmospheric formaldehyde in a mid-latitude forest. *Atmospheric Environment* **2017**, *167*, 190-201. DOI: 10.1016/j.atmosenv.2017.08.017.
(36) Clifton, O. E.; Fiore, A. M.; Munger, J. W.; Malyshev, S.; Horowitz, L. W.; Shevliakova, E.; Paulot, F.; Murray, L. T.; Griffin, K. L. Interannual variability in ozone removal by a temperate deciduous forest. *Geophysical Research Letters* **2017**, *44* (1), 542-552. DOI: 10.1002/2016gl070923.
(37) Kavassalis, S. C.; Murphy, J. G. Understanding ozone-meteorology correlations: A role for dry deposition. *Geophysical Research Letters* **2017**, *44* (6), 2922-2931. DOI: 10.1002/2016gl071791.
(38) Kurpius, M. R.; McKay, M.; Goldstein, A. H. Annual ozone deposition to a Sierra Nevada ponderosa pine plantation. *Atmospheric Environment* **2002**, *36* (28), 4503-4515. DOI: 10.1016/s1352-2310(02)00423-5.
(39) Panek, J. A.; Goldstein, A. H. Response of stomatal conductance to drought in ponderosa pine: implications for carbon and ozone uptake. *Tree Physiology* **2001**, *21* (5), 337-344. DOI: 10.1093/treephys/21.5.337.
(40) Panek, J. A. Ozone uptake, water loss and carbon exchange dynamics in annually drought-stressed Pinus ponderosa forests: measured trends and parameters for uptake modeling. *Tree Physiology* **2004**, *24* (3), 277-290. DOI: 10.1093/treephys/24.3.277.
(41) Fares, S.; Savi, F.; Muller, J.; Matteucci, G.; Paoletti, E. Simultaneous measurements of above and below canopy ozone fluxes help partitioning ozone deposition between its various sinks in a Mediterranean Oak Forest. *Agricultural and Forest Meteorology* **2014**, *198-199*, 181-191. DOI: 10.1016/j.agrformet.2014.08.014.
(42) Lin, M.; Horowitz, L. W.; Payton, R.; Fiore, A. M.; Tonnesen, G. US surface ozone trends and extremes from 1980 to 2014: quantifying the roles of rising Asian emissions, domestic controls, wildfires, and climate. *Atmospheric Chemistry and Physics* **2017**, *17* (4), 2943-2970. DOI: 10.5194/acp-17-2943-2017.

(43) Wang, H. S., S. . Causes of the Extreme Dry Condition over California during Early 2013. Explaining Extreme Events of 2013 from a Climate Perspective, *American Society*, **201,** *95* (S7-S11).
(44) Funk, C. H., A.; Stone, D. The Contribution of the Observed Global Warming Trend to the California Droughts of 2012/13 and 2013/14. Explaining Extreme Events of 2013 from a Climate Perspective, *American Meteorlogical Society*, **2014**; *9* (S11-S15).
(45) Griffin, D.; Anchukaitis, K. J. How unusual is the 2012-2014 California drought? *Geophysical Research Letters* **2014**, *41* (24), 9017-9023. DOI: 10.1002/2014gl062433.
(46) State of the Air **2019**, *American Lung Association*: April 24, 2019.
(47) Ambient Monitoring Technology Information Center (AMTIC)*, Environmental Protection Agency, Near-road MOnitoring Sites (Excel), Near-road NO2 Monitoring* (accessed September 15 2019).
(48) Dunlea, E. J.; Herndon, S. C.; Nelson, D. D.; Volkamer, R. M.; San Martini, F.; Sheehy, P. M.; Zahniser, M. S.; Shorter, J. H.; Wormhoudt, J. C.; Lamb, B. K.; et al. Evaluation of nitrogen dioxide chemiluminescence monitors in a polluted urban environment. *Atmospheric Chemistry and Physics* **2007**, *7* (10), 2691-2704. DOI: 10.5194/acp-7-2691-2007.
(49) Russell, A. R.; Valin, L. C.; Bucsela, E. J.; Wenig, M. O.; Cohen, R. C. Space-based Constraints on Spatial and Temporal Patterns of NOx Emissions in California, 2005-2008. *Environmental Science & Technology* **2010**, *44* (9), 3608-3615. DOI: 10.1021/es903451j.
(50) DELWICHE, C. F.; SHARKEY, T. D. Rapid appearance of 13C in biogenic isoprene when 13CO2 is fed to intact leaves. *Plant, Cell & Environment* **1993**, *16* (5), 587-591. DOI: 10.1111/j.1365-3040.1993.tb00907.x.
(51) Schnitzler, J. P., Graus, M., Kreuzwieser, J., Heizmann, U., Rennenberg, H., Wisthaler, A., Hansel, A.,. Contribution of Different Carbon Sources to Isoprene Biosynthesis in Poplar Leaves. *Plant Physiology* **2004**, *135* (1), 152-160. DOI: 10.1104/pp.103.037374.
(52) Ferrieri, R. A.; Gray, D. W.; Babst, B. A.; Schueller, M. J.; Schlyer, D. J.; Thorpe, M. R.; Orians, C. M.; Lerdau, M. Use of carbon-11 in Populus shows that exogenous jasmonic acid increases biosynthesis of isoprene from recently fixed carbon. *Plant, Cell & Environment* **2005**, *28* (5), 591-602. DOI: 10.1111/j.1365-3040.2004.01303.x.
(53) Guenther, A. B.; Zimmerman, P. R.; Harley, P. C.; Monson, R. K.; Fall, R. Isoprene and monoterpene emission rate variability: Model evaluations and sensitivity analyses. *Journal of Geophysical Research* **1993**, *98* (D7), 12609. DOI: 10.1029/93jd00527.
(54) Unger, N.; Harper, K.; Zheng, Y.; Kiang, N. Y.; Aleinov, I.; Arneth, A.; Schurgers, G.; Amelynck, C.; Goldstein, A.; Guenther, A.; et al. Photosynthesis-dependent isoprene emission from leaf to planet in a global carbon-chemistry-climate model. *Atmospheric Chemistry and Physics* **2013**, *13* (20), 10243-10269. DOI: 10.5194/acp-13-10243-2013.
(55) Fang, C.; Monson, R. K.; Cowling, E. B. Isoprene emission, photosynthesis, and growth in sweetgum (Liquidambar styraciflua) seedlings exposed to short- and long-term drying cycles. *Tree Physiology* **1996**, *16* (4), 441-446. DOI: 10.1093/treephys/16.4.441.
(56) Funk, J. L.; Mak, J. E.; Lerdau, M. T. Stress-induced changes in carbon sources for isoprene production in Populus deltoides. *Plant, Cell and Environment* **2004**, *27* (6), 747-755. DOI: 10.1111/j.1365-3040.2004.01177.x.
(57) Monson, R. K.; Trahan, N.; Rosenstiel, T. N.; Veres, P.; Moore, D.; Wilkinson, M.; Norby, R. J.; Volder, A.; Tjoelker, M. G.; Briske, D. D.; et al. Isoprene emission from terrestrial ecosystems in response to global change: minding the gap between models and observations.

Philosophical Transactions of the Royal Society. Series A, Mathematical, Physical & Engineering Sciences **2007**, *365* (1856), 1677-1695. DOI: 10.1098/rsta.2007.2038.
(58) *North American Drought Monitor*. National Drought Mitigation Center, http://droughtmonitor.unl.edu/nadm/Home.aspx (accessed 2018 July 8).
(59) Division of Flood Management: Hydrology BRanch Tulare Basin 6 Station, Chronological Monthly Precipitation. Resources, D. o. W., Ed.
(60) Monson, R. K.; Jaeger, C. H.; Adams, W. W.; Driggers, E. M.; Silver, G. M.; Fall, R. Relationships among Isoprene Emission Rate, Photosynthesis, and Isoprene Synthase Activity as Influenced by Temperature. *Plant Physiology* **1992**, *98* (3), 1175-1180. DOI: 10.1104/pp.98.3.1175.
(61) Monson, R. K.; Harley, P. C.; Litvak, M. E.; Wildermuth, M.; Guenther, A. B.; Zimmerman, P. R.; Fall, R. Environmental and developmental controls over the seasonal pattern of isoprene emission from aspen leaves. *Oecologia* **1994**, *99* (3-4), 260-270. DOI: 10.1007/bf00627738.
(62) Pusede, S. E.; Steiner, A. L.; Cohen, R. C. Temperature and Recent Trends in the Chemistry of Continental Surface Ozone. *Chemical Reviews* **2015**, *115* (10), 3898-3918. DOI: 10.1021/cr5006815.
(63) Loivamäki, M.; Gilmer, F.; Fischbach, R. J.; Sörgel, C.; Bachl, A.; Walter, A.; Schnitzler, J.-P. Arabidopsis, a Model to Study Biological Functions of Isoprene Emission? *Plant Physiology* **2007**, *144* (2), 1066-1078. DOI: 10.1104/pp.107.098509.
(64) Guenther, A.; Karl, T.; Harley, P.; Wiedinmyer, C.; Palmer, P. I.; Geron, C. Estimates of global terrestrial isoprene emissions using MEGAN (Model of Emissions of Gases and Aerosols from Nature). *Atmospheric Chemistry and Physics* **2006**, *6* (11), 3181-3210. DOI: 10.5194/acp-6-3181-2006.
(65) Vilagrosa, A.; Bellot, J.; Vallejo, V. R.; Gil-Pelegrín, E. Cavitation, stomatal conductance, and leaf dieback in seedlings of two co-occurring Mediterranean shrubs during an intense drought. *Journal of Experimental Botany* **2003**, *54* (390), 2015-2024. DOI: 10.1093/jxb/erg221.
(66) Limousin, J. M.; Rambal, S.; Ourcival, J. M.; Rocheteau, A.; Joffre, R.; Rodriguez-Cortina, R. Long-term transpiration change with rainfall decline in a MediterraneanQuercus ilexforest. *Global Change Biology* **2009**, *15* (9), 2163-2175. DOI: 10.1111/j.1365-2486.2009.01852.x.
(67) Tyree, M. T.; Sperry, J. S. Vulnerability of Xylem to Cavitation and Embolism. *Annual Review of Plant Physiology and Plant Molecular Biology* **1989**, *40* (1), 19-36. DOI: 10.1146/annurev.pp.40.060189.000315.
(68) Misztal, P. K.; Karl, T.; Weber, R.; Jonsson, H. H.; Guenther, A. B.; Goldstein, A. H. Airborne flux measurements of biogenic isoprene over California. *Atmospheric Chemistry and Physics* **2014**, *14* (19), 10631-10647. DOI: 10.5194/acp-14-10631-2014.
(69) Alves, E. G.; Tóta, J.; Turnipseed, A.; Guenther, A. B.; Vega Bustillos, J. O. W.; Santana, R. A.; Cirino, G. G.; Tavares, J. V.; Lopes, A. P.; Nelson, B. W.; et al. Leaf phenology as one important driver of seasonal changes in isoprene emissions in central Amazonia. *Biogeosciences* **2018**, *15* (13), 4019-4032. DOI: 10.5194/bg-15-4019-2018.
(70) Joiner, J.; Guanter, L.; Lindstrot, R.; Voigt, M.; Vasilkov, A. P.; Middleton, E. M.; Huemmrich, K. F.; Yoshida, Y.; Frankenberg, C. Global monitoring of terrestrial chlorophyll fluorescence from moderate-spectral-resolution near-infrared satellite measurements: methodology, simulations, and application to GOME-2. *Atmospheric Chemistry and Physics* **2013**, *6* (10), 2803-2823. DOI: 10.5194/amt-6-2803-2013.
(71) Joiner, J.; Yoshida, Y.; Guanter, L.; Middleton, E. M. New methods for the retrieval of chlorophyll red fluorescence from hyperspectral satellite instruments: simulations and application

to GOME-2 and SCIAMACHY. *Atmospheric Measurement Techniques* **2016**, *9* (8), 3939-3967. DOI: 10.5194/amt-9-3939-2016.
(72) Zhang, Y.; Joiner, J.; Gentine, P.; Zhou, S. Reduced solar-induced chlorophyll fluorescence from GOME-2 during Amazon drought caused by dataset artifacts. *Global Change Biology* **2018**, *24* (6), 2229-2230. DOI: 10.1111/gcb.14134.
(73) Russell, A. R.; Valin, L. C.; Bucsela, E. J.; Wenig, M. O.; Cohen, R. C. Space-based Constraints on Spatial and Temporal Patterns of NOx Emissions in California, 2005−2008. *Environmental Science & Technology* **2010**, *44* (9), 3608-3615. DOI: 10.1021/es903451j.
(74) Russell, A. R.; Valin, L. C.; Cohen, R. C. Trends in OMI NO2 Observations over the United States: Effects of Emission Control Technology and the Economic Recession. *Atmospheric Chemistry and Physics* **2012**, *12* (24), 12197-12209. DOI: 10.5194/acp-12-12197-2012.
(75) Pusede, S. E.; Cohen, R. C. On the observed response of ozone to NOx and VOC reactivity reductions in San Joaquin Valley California 1995–present. **2012**, *12* (18), 8323-8339. *Atmospheric Chemistry and Physics* DOI: 10.5194/acp-12-8323-2012.
(76) Rasmussen, D. J.; Hu, J.; Mahmud, A.; Kleeman, M. J. The Ozone–Climate Penalty: Past, Present, and Future. *Environmental Science & Technology* **2013**, *47* (24), 14258-14266. DOI: 10.1021/es403446m.
(77) Baidar, S.; Hardesty, R. M.; Kim, S. W.; Langford, A. O.; Oetjen, H.; Senff, C. J.; Trainer, M.; Volkamer, R. Weakening of the weekend ozone effect over California's South Coast Air Basin. *Geophysical Research Letters* **2015**, *42* (21), 9457-9464. DOI: 10.1002/2015gl066419.
(78) Duncan, B. N.; Yoshida, Y.; Olson, J. R.; Sillman, S.; Martin, R. V.; Lamsal, L.; Hu, Y.; Pickering, K. E.; Retscher, C.; Allen, D. J.; et al. Application of OMI observations to a space-based indicator of NOx and VOC controls on surface ozone formation. *Atmospheric Environment* **2010**, *44* (18), 2213-2223. DOI: 10.1016/j.atmosenv.2010.03.010.
(79) Marr, L. C.; Harley, R. A. Spectral analysis of weekday–weekend differences in ambient ozone, nitrogen oxide, and non-methane hydrocarbon time series in California. *Atmospheric Environment* **2002**, *36* (14), 2327-2335. DOI: 10.1016/s1352-2310(02)00188-7.
(80) McDonald, B. C.; Dallmann, T. R.; Martin, E. W.; Harley, R. A. Long-term trends in nitrogen oxide emissions from motor vehicles at national, state, and air basin scales. *Journal of Geophysical Research: Atmospheres* **2012**, *117* (D21), DOI: 10.1029/2012jd018304.
(81) Pusede, S. E.; Gentner, D. R.; Wooldridge, P. J.; Browne, E. C.; Rollins, A. W.; Min, K. E.; Russell, A. R.; Thomas, J.; Zhang, L.; Brune, W. H.; et al. On the temperature dependence of organic reactivity, nitrogen oxides, ozone production, and the impact of emission controls in San Joaquin Valley, California. *Atmospheric Chemistry and Physics* **2014**, *14* (7), 3373-3395. DOI: 10.5194/acp-14-3373-2014.
(82) Gentner, D. R.; Ford, T. B.; Guha, A.; Boulanger, K.; Brioude, J.; Angevine, W. M.; De Gouw, J. A.; Warneke, C.; Gilman, J. B.; Ryerson, T. B.; et al. Emissions of organic carbon and methane from petroleum and dairy operations in California's San Joaquin Valley. *Atmospheric Chemistry and Physics* **2014**, *14* (10), 4955-4978. DOI: 10.5194/acp-14-4955-2014.
(83) Gentner, D. R.; Ormeño, E.; Fares, S.; Ford, T. B.; Weber, R.; Park, J. H.; Brioude, J.; Angevine, W. M.; Karlik, J. F.; Goldstein, A. H. Emissions of terpenoids, benzenoids, and other biogenic gas-phase organic compounds from agricultural crops and their potential implications for air quality. *Atmospheric Chemistry and Physics* **2014**, *14* (11), 5393-5413. DOI: 10.5194/acp-14-5393-2014.

(84) Park, J. H.; Goldstein, A. H.; Timkovsky, J.; Fares, S.; Weber, R.; Karlik, J.; Holzinger, R. Active Atmosphere-Ecosystem Exchange of the Vast Majority of Detected Volatile Organic Compounds. *Science* **2013**, *341* (6146), 643-647. DOI: 10.1126/science.1235053.
(85) Emission Standards and Supplemental Requirements for 2007 and Later Model year Diesel Heavy-Duty Engines and Vehicles. In *Code of Federal Regulations*.
(86) *Regulation to Reduce Emissions Diesel Particulate Matter, Oxides of Nitrogen and other Criteria Pollutants, From In-Use Heavy-Duty Diesel Fueled Vehicles.* http://www.arb.ca.gov/msprog/onrdiesel/regulation.htm (accessed.
(87) Haugen, M. J.; Bishop, G. A. Long-Term Fuel-Specific NOx and Particle Emission Trends for In-Use Heavy-Duty Vehicles in California. *Environmental Science & Technology* **2018**, *52* (10), 6070-6076. DOI: 10.1021/acs.est.8b00621.
(88) Bishop, G. A.; Schuchmann, B. G.; Stedman, D. H.; Lawson, D. R. Emission changes resulting from the San Pedro Bay, California Ports Truck Retirement Program. *Environmental Science and Technology* **2012**, *46* (1), 551-558. DOI: 10.1021/es202392g.
(89) Dixit, P.; Miller, J.; Cocker, D.; Oshinuga, A.; Jiang, Y.; Durbin, T.; Johnson, K. Differences between emissions measured in urban driving and certification testing of heavy-duty diesel engines. *Atmospheric Environment* **2017**, *166*. DOI: 10.1016/j.atmosenv.2017.06.037.
(90) Jiang, Z.; McDonald, B. C.; Worden, H.; Worden, J. R.; Miyazaki, K.; Qu, Z.; Henze, D. K.; Jones, D. B. A.; Arellano, A. F.; Fischer, E. V.; et al. Unexpected slowdown of US pollutant emission reduction in the past decade. *Proceedings of the National Academy of Sciences* **2018**, *115* (20), 5099-5104. DOI: 10.1073/pnas.1801191115.
(91) Almaraz, M.; Bai, E.; Wang, C.; Trousdell, J.; Conley, S.; Faloona, I.; Houlton, B. Z. Agriculture is a major source of NOxpollution in California. *Science Advances* **2018**, *4* (1), eaao3477. DOI: 10.1126/sciadv.aao3477.
(92) Abatzoglou, J. T.; Williams, A. P. Impact of anthropogenic climate change on wildfire across western US forests. *Proceedings of the National Academy of Sciences* **2016**, *113* (42), 11770-11775. DOI: 10.1073/pnas.1607171113.
(93) Westerling, A. L. Warming and Earlier Spring Increase Western U.S. Forest Wildfire Activity. *Science* **2006**, *313* (5789), 940-943. DOI: 10.1126/science.1128834.
(94) Buysse, C. E.; Munyan, J. A.; Bailey, C. A.; Kotsakis, A.; Sagona, J. A.; Esperanza, A.; Pusede, S. E. On the Effect of Upwind Emission Controls on Ozone in Sequoia National Park. *Atmospheric Chemistry and Physics.* **2018**, *18* (23), 17061-17076. DOI: 10.5194/acp-18-17061-2018.
(95) Steiner, A. L.; Davis, A. J.; Sillman, S.; Owen, R. C.; Michalak, A. M.; Fiore, A. M. Observed Suppression of Ozone Formation at Extremely High Temperatures Due to Chemical and Biophysical Feedbacks. *Proceedings of the National Academy of Sciences* **2010**, *107* (46), 19685-19690. DOI: 10.1073/pnas.1008336107.
(96) Steiner, A. L.; Tonse, S.; Cohen, R. C.; Goldstein, A. H.; Harley, R. A. Influence of Future Climate and Emissions on Regional Air Quality in California. *Journal of Geophysical Research-Atmospheres* **2006**, *111* (D18). DOI: 10.1029/2005jd006935.
(97) Murphy, J. G.; Day, A.; Cleary, P. A.; Wooldridge, P. J.; Cohen, R. C. Observations of the Diurnal and Seasonal Trends in Nitrogen Oxides in the Western Sierra Nevada. *Atmospheric Chemistry and Physics* **2006**, *6*, 5321-5338. DOI: 10.5194/acp-6-5321-2006.
(98) Farmer, D. K.; Perring, A. E.; Wooldridge, P. J.; Blake, D. R.; Baker, A.; Meinardi, S.; Huey, L. G.; Tanner, D.; Vargas, O.; Cohen, R. C. Impact of Organic Nitrates on Urban Ozone

Production. *Atmospheric Chemistry and Physics* **2011**, *11* (9), 4085-4094. DOI: 10.5194/acp-11-4085-2011.
(99) Mao, J.; Ren, X.; Zhang, L.; Van Duin, D. M.; Cohen, R. C.; Park, J. H.; Goldstein, A. H.; Paulot, F.; Beaver, M. R.; Crounse, J. D.; et al. Insights into Hydroxyl Measurements and Atmospheric Oxidation in a California Forest. *Atmospheric Chemistry and Physics.* **2012**, *12* (17), 8009-8020. DOI: 10.5194/acp-12-8009-2012.
(100) Beaver, M. R.; Clair, J. M. S.; Paulot, F.; Spencer, K. M.; Crounse, J. D.; LaFranchi, B. W.; Min, K. E.; Pusede, S. E.; Wooldridge, P. J.; Schade, G. W.; et al. Importance of Biogenic Precursors to the Budget of Organic Nitrates: Observations of Multifunctional Organic Nitrates by CIMS and TD-LIF during BEARPEX 2009. *Atmospheric Chemistry and Physics* **2012**, *12* (13), 5773-5785. DOI: 10.5194/acp-12-5773-2012.
(101) Perring, A. E.; Pusede, S. E.; Cohen, R. C. An Observational Perspective on the Atmospheric Impacts of Alkyl and Multifunctional Nitrates on Ozone and Secondary Organic Aerosol. *Chemical Reviews* **2013**, *113* (8), 5848-5870. DOI: 10.1021/cr300520x.
(102) Thornton, J. A.; Wooldridge, P. J.; Cohen, R. C.; Martinez, M.; Harder, H.; Brune, W. H.; Williams, E. J.; Roberts, J. M.; Fehsenfeld, F. C.; Hall, S. R.; et al. Ozone Production Rates as a Function of NOx Abundances and HOx Production Rates in the Nashville Urban Plume. *Journal of Geophysical Research: Atmospheres* **2002**, *107* (D12), ACH 7-1-ACH 7-17. DOI: doi:10.1029/2001JD000932.
(103) Val Martin, M.; Heald, C. L.; Arnold, S. R. Coupling Dry Deposition to Vegetation Phenology in the Community Earth System Model: Implications for the Simulation of Surface O3. *Geophysical Research Letters* **2014**, *41* (8), 2988-2996. DOI: 10.1002/2014GL059651.
(104) Wu, S.; Mickley, L. J.; Kaplan, J. O.; Jacob, D. J. Impacts of Changes in Land Use and Land Cover on Atmospheric Chemistry and Air Quality over the 21st Century. *Atmospheric Chemistry and Physics* **2012**, *12* (3), 1597-1609. DOI: 10.5194/acp-12-1597-2012.
(105) Stella, P.; Loubet, B.; Lamaud, E.; Laville, P.; Cellier, P. Ozone Deposition onto Bare Soil: A New Parameterisation. *Agricultural and Forest Meteorology* **2011**, *151* (6), 669-681. DOI: https://doi.org/10.1016/j.agrformet.2011.01.015.
(106) Horton, D. E.; Skinner, C. B.; Singh, D.; Diffenbaugh, N. S. Occurrence and Persistence of Future Atmospheric Stagnation Events. *Nature Climate Change* **2014**, *4*, 698-703. DOI: 10.1038/nclimate2272 PMC.
(107) Vukovich, F. M. Regional-Scale Boundary Layer Ozone Variations in the Eastern United States and Their Association with Meteorological Variations. *Atmospheric Environment* **1995**, *29* (17), 2259-2273. DOI: https://doi.org/10.1016/1352-2310(95)00146-P.
(108) Leibensperger, E. M.; Mickley, L. J.; Jacob, D. J. Sensitivity of US air quality to mid-latitude cyclone frequency and implications of 1980–2006 climate change. *Atmospheric Chemistry and Physics* **2008**, *8* (23), 7075-7086. DOI: 10.5194/acp-8-7075-2008.
(109) Reddy, P. J.; Pfister, G. G. Meteorological factors contributing to the interannual variability of midsummer surface ozone in Colorado, Utah, and other western U.S. states. *Journal of Geophysical Research: Atmospheres* **2016**, *121* (5), 2434-2456. DOI: doi:10.1002/2015JD023840.
(110) Pusede, S. E.; Duffey, K. C.; Shusterman, A. A.; Saleh, A.; Laughner, J. L.; Wooldridge, P. J.; Zhang, Q.; Parworth, C. L.; Kim, H.; Capps, S. L.; et al. On the Effectiveness of Nitrogen Oxide Reductions as a Control over Ammonium Nitrate Aerosol. *Atmospheric Chemistry and Physics* **2016**, *16* (4), 2575-2596. DOI: 10.5194/acp-16-2575-2016.

(111) Miller, G. R.; Chen, X.; Rubin, Y.; Ma, S.; Baldocchi, D. D. Groundwater Uptake by Woody Vegetation in a Semiarid Oak Savanna. *Water Resources Research* **2010**, *46* (10), W10503. DOI: 10.1029/2009WR008902.
(112) Damesin, C.; Rambal, S. Field Study of Leaf Photosynthetic Performance by a Mediterranean Deciduous Oak Tree (Quercus pubescens) during a Severe Summer Drought. *The New Phytologist* **1995**, *131* (2), 159-167.
(113) Osuna, J. L.; Baldocchi, D. D.; Kobayashi, H.; Dawson, T. E. Seasonal Trends in Photosynthesis and Electron Transport during the Mediterranean Summer Drought in Leaves of Deciduous Oaks. *Tree Physiology* **2015**, *35* (5), 485-500. DOI: 10.1093/treephys/tpv023.
(114) Koteen, L. E.; Raz-Yaseef, N.; Baldocchi, D. D. Spatial Heterogeneity of Fine Root Biomass and Soil Carbon in a California Oak Savanna Illuminates Plant Functional Strategy across Periods of High and Low Resource Supply. *Ecohydrology* **2015**, *8* (2), 294-308. DOI: 10.1002/eco.1508.
(115) Velikova, V. B. Isoprene as a Tool for Plant Protection against Abiotic Stresses. *Journal Plant Interactions* **2008**, *3* (1), 1-15, Review. DOI: 10.1080/17429140701858327.
(116) Vickers, C. E.; Gershenzon, J.; Lerdau, M. T.; Loreto, F. A Unified Mechanism of Action for Volatile Isoprenoids in Plant Abiotic Stress. *Nature Chemical Biology* **2009**, *5*, 283, Perspective. DOI: 10.1038/nchembio.158.
(117) Fares, S.; Barta, C.; Brilli, F.; Centritto, M.; Ederli, L.; Ferranti, F.; Pasqualini, S.; Reale, L.; Tricoli, D.; Loreto, F. Impact of High Ozone on Isoprene Emission, Photosynthesis and Histology of Developing Populus Alba Leaves Directly or Indirectly Exposed to the Pollutant. *Physiologia Plantarum* **2006**, *128* (3), 456-465. DOI: 10.1111/j.1399-3054.2006.00750.x.
(118) Wang, B.; Shugart, H. H.; Shuman, J. K.; Lerdau, M. T. Forests and Ozone: Productivity, Carbon Storage, and Feedbacks. *Scientific Reports* **2016**, *6*, 22133, Article. DOI: 10.1038/srep22133
https://www.nature.com/articles/srep22133#supplementary-information.
(119) Fiore, A. M.; Naik, V.; Spracklen, D. V.; Steiner, A.; Unger, N.; Prather, M.; Bergmann, D.; Cameron-Smith, P. J.; Cionni, I.; Collins, W. J.; et al. Global Air Quality and Climate. *Chemical Society Reviews* **2012**, *41* (19), 6663-6683. DOI: 10.1039/c2cs35095e.
(120) Guenther, A. B.; Jiang, X.; Heald, C. L.; Sakulyanontvittaya, T.; Duhl, T.; Emmons, L. K.; Wang, X. The Model of Emissions of Gases and Aerosols from Nature version 2.1 (MEGAN2.1): an extended and updated framework for modeling biogenic emissions. *Geoscientific Model Development* **2012**, *5* (6), 1471-1492. DOI: 10.5194/gmd-5-1471-2012.

(122) *National Air Toxics Assessment 2014*; U.S. Environmental Protection Agency, https://www.epa.gov/national-air-toxics-assessment/2014-nata-assessment-results (accessed August 25, 2019).
(123) Collins, T. W.; Grineski, S. E.; Chakraborty, J.; Montgomery, M. C.; Hernandez, M. Downscaling Environmental Justice Analysis: Determinants of Household-Level Hazardous Air Pollutant Exposure in Greater Houston. *Annals of the Association of American Geographers* **2015**, *105* (4), 684-703. DOI: 10.1080/00045608.2015.1050754.
(124) Collins, T. W.; Grineski, S. E.; Morales, D. X. Sexual Orientation, Gender, and Environmental Injustice: Unequal Carcinogenic Air Pollution Risks in Greater Houston. *Annals of the American Association of Geographers* **2017**, *107* (1), 72-92. DOI: 10.1080/24694452.2016.1218270.
(125) Hernandez, M.; Collins, T. W.; Grineski, S. E. Immigration, mobility, and environmental injustice: A comparative study of Hispanic people's residential decision-making and exposure to

hazardous air pollutants in Greater Houston, Texas. *Geoforum* **2015**, *60*, 83-94. DOI: 10.1016/j.geoforum.2015.01.013.
(126) Bullard, R. D. *Invisible Houston : the Black experience in boom and bust*; Texas A & M University Press, 1987.
(127) Linder, S. H.; Marko, D.; Sexton, K. Cumulative Cancer Risk from Air Pollution in Houston: Disparities in Risk Burden and Social Disadvantage. *Environmental Science and Technology* **2008**, *42* (12), 4312-4322. DOI: 10.1021/es072042u.
(128) Sansom, G. P., J.; Parras, A.; Nieto, Y.; Arellano, Y.; Berke, P.; McDonald, T.; Shipp, E.; Horney, J. A. The Impacts of Exposure to Environmental Risk on Physical and Mental Health in a Small Geographic Community in Houston, TX. *Journal Community Health* **2017**, *48*, 813-818. DOI: 10.1007/s10900-017-0322-y.
(129) Clark, L. P.; Millet, D. B.; Marshall, J. D. Changes in Transportation-Related Air Pollution Exposures by Race-Ethnicity and Socioeconomic Status: Outdoor Nitrogen Dioxide in the United States in 2000 and 2010. *Environmental Health Perspectives* **2017**, *125* (9). DOI: 10.1289/ehp959.
(130) Clark, L. P.; Millet, D. B.; Marshall, J. D. National Patterns in Environmental Injustice and Inequality: Outdoor NO2 Air Pollution in the United States. *PLoS ONE* **2014**, *9* (4), e94431. DOI: 10.1371/journal.pone.0094431.
(131) Levy, I.; Mihele, C.; Lu, G.; Narayan, J.; Brook, J. R. Evaluating Multipollutant Exposure and Urban Air Quality: Pollutant Interrelationships, Neighborhood Variability, and Nitrogen Dioxide as a Proxy Pollutant. *Environmental Health Perspectives* **2014**, *122* (1), 65-72. DOI: 10.1289/ehp.1306518.
(132) Jerrett, M.; Burnett, R. T.; Ma, R. J.; Pope, C. A.; Krewski, D.; Newbold, K. B.; Thurston, G.; Shi, Y. L.; Finkelstein, N.; Calle, E. E.; et al. Spatial analysis of air pollution and mortality in Los Angeles. *Epidemiology* **2005**, *16* (6), 727-736. DOI: 10.1097/01.ede.0000181630.15826.7d.
(133) Morello-Frosch, R.; Jesdale, B. M. Separate and unequal: residential segregation and estimated cancer risks associated with ambient air toxics in U.S. metropolitan areas. *Environmental Health Perspectives* **2006**, *114* (3), 386-393. DOI: 10.1289/ehp.8500 PubMed.
(134) *PROFILE OF VERSION 1 OF THE 2014 NATIONAL EMISSIONS INVENTORY*; Office of Air Quality Planning and Standards, Emissions Inventory and Analysis Group, 2017. https://www.epa.gov/sites/production/files/2017-04/documents/2014neiv1_profile_final_april182017.pdf (accessed August 28, 2019).
(135) Kim, S. W.; McKeen, S. A.; Frost, G. J.; Lee, S. H.; Trainer, M.; Richter, A.; Angevine, W. M.; Atlas, E.; Bianco, L.; Boersma, K. F.; et al. Evaluations of NOx and highly reactive VOC emission inventories in Texas and their implications for ozone plume simulations during the Texas Air Quality Study 2006. *Atmospheric Chemistry and Physics* **2011**, *11* (22), 11361-11386. DOI: 10.5194/acp-11-11361-2011.
(136) Rivera, C.; Mellqvist, J.; Samuelsson, J.; Lefer, B.; Alvarez, S.; Patel, M. R. Quantification of NO2 and SO2 emissions from the Houston Ship Channel and Texas City industrial areas during the 2006 Texas Air Quality Study. *Journal of Geophysical Research: Atmospheres* **2010**, *115* (D8). DOI: 10.1029/2009jd012675.
(137) Washenfelder, R. A.; Trainer, M.; Frost, G. J.; Ryerson, T. B.; Atlas, E. L.; de Gouw, J. A.; Flocke, F. M.; Fried, A.; Holloway, J. S.; Parrish, D. D.; et al. Characterization of NOx, SO2, ethene, and propene from industrial emission sources in Houston, Texas. *Journal of Geophysical Research: Atmospheres* **2010**, *115* (D16). DOI: 10.1029/2009jd013645.
(138) Institute, H. E. Traffic-Related Air Pollution: A Critical Review of the Literature on Emissions, Exposure, and Health Effects. **2010**, (Special Report 17).

(139) Brook, J. R.; Burnett, R. T.; Dann, T. F.; Cakmak, S.; Goldberg, M. S.; Fan, X. H.; Wheeler, A. J. Further interpretation of the acute effect of nitrogen dioxide observed in Canadian time-series studies. *Journal of Exposure Science and Environmental Epidemiology* **2007**, *17*, S36-S44. DOI: 10.1038/sj.jes.7500626.
(140) Brunekreef, B.; Holgate, S. T. Air pollution and health. *Lancet* **2002**, *360* (9341), 1233-1242. DOI: 10.1016/s0140-6736(02)11274-8.
(141) Burnett, R. T.; Stieb, D.; Brook, J. R.; Cakmak, S.; Dales, R.; Raizenne, M.; Vincent, R.; Dann, T. Associations between short-term changes in nitrogen dioxide and mortality in Canadian cities. *Archives of Environmental Health* **2004**, *59* (5), 228-236. DOI: 10.3200/aeoh.59.5.228-236.
(142) Crouse, D. L.; Peters, P. A.; Hystad, P.; Brook, J. R.; van Donkelaar, A.; Martin, R. V.; Villeneuve, P. J.; Jerrett, M.; Goldberg, M. S.; Pope, C. A.; et al. Ambient PM2.5, O-3, and NO2 Exposures and Associations with Mortality over 16 Years of Follow-Up in the Canadian Census Health and Environment Cohort (CanCHEC). *Environmental Health Perspectives* **2015**, *123* (11), 1180-1186. DOI: 10.1289/ehp.1409276.
(143) Edwards, J.; Walters, S.; Griffiths, R. K. Hospital Admissions for Asthma in Pre-school Children - Relationship to Major Roads in Birmingham, United Kingdom. *Archives of Environmental Health* **1994**, *49* (4), 223-227. DOI: 10.1080/00039896.1994.9937471.
(144) Gauderman, W. J.; Avol, E.; Lurmann, F.; Kuenzli, N.; Gilliland, F.; Peters, J.; McConnell, R. Childhood asthma and exposure to traffic and nitrogen dioxide. *Epidemiology* **2005**, *16* (6), 737-743. DOI: 10.1097/01.ede.00001813087.51440.75.
(145) Lin, S.; Munsie, J. P.; Hwang, S. A.; Fitzgerald, E.; Cayo, M. R. Childhood asthma hospitalization and residential exposure to state route traffic. *Environmental Research* **2002**, *88* (2), 73-81. DOI: 10.1006/enrs.2001.4303.
(146) Adar, S. D.; Kaufman, J. D. Cardiovascular disease and air pollutants: Evaluating and improving epidemiological data implicating traffic exposure. *Inhalation Toxicology* **2007**, *19*, 135-149. DOI: 10.1080/08958370701496012.
(147) Lipfert, F. W.; Wyzga, R. E. On exposure and response relationships for health effects associated with exposure to vehicular traffic. *Journal of Exposure Science and Environmental Epidemiology* **2008**, *18* (6), 588-599. DOI: 10.1038/jes.2008.4.
(148) Wu, J.; Ren, C. Z.; Delfino, R. J.; Chung, J.; Wilhelm, M.; Ritz, B. Association between Local Traffic-Generated Air Pollution and Preeclampsia and Preterm Delivery in the South Coast Air Basin of California. *Environmental Health Perspectives* **2009**, *117* (11), 1773-1779. DOI: 10.1289/ehp.0800334.
(149) Choi, W.; He, M.; Barbesant, V.; Kozawa, K.; Mara, S.; Winer, A.; Paulson, S. Prevalence of wide area impacts downwind of freeways under pre-sunrise stable atmospheric conditions. *Atmospheric Environment* **2012**, *62*, 318-327. DOI: 10.1016/j.atmosenv.2012.07.084.
(150) Karner, A. A.; Eisinger, D. S.; Niemeier, D. A. Near-Roadway Air Quality: Synthesizing the Findings from Real-World Data. *Environmental Science & Technology* **2010**, *44* (14), 5334-5344. DOI: 10.1021/es100008x.
(151) Bechle, M. J.; Millet, D. B.; Marshall, J. D. Remote sensing of exposure to NO2: Satellite versus ground-based measurement in a large urban area. *Atmospheric Environment* **2013**, *69*, 345-353. DOI: https://doi.org/10.1016/j.atmosenv.2012.11.046.
(152) Rowangould, G. M. A census of the US near-roadway population: Public health and environmental justice considerations. *Transportation Research Part D-Transport and Environment* **2013**, *25*, 59-67. DOI: 10.1016/j.trd.2013.08.003.

(153) Boersma, K. F.; Jacob, D. J.; Trainic, M.; Rudich, Y.; DeSmedt, I.; Dirksen, R.; Eskes, H. J. Validation of urban NO2 concentrations and their diurnal and seasonal variations observed from the SCIAMACHY and OMI sensors using in situ surface measurements in Israeli cities. *Atmospheric Chemistry and Physics* **2009**, *9* (12), 3867-3879. DOI: 10.5194/acp-9-3867-2009.
(154) Geddes, J. A.; Martin, R. V.; Boys, B. L.; van Donkelaar, A. Long-Term Trends Worldwide in Ambient NO2 Concentrations Inferred from Satellite Observations. *Environmental Health Perspectives* **2016**, *124* (3), 281-289. DOI: 10.1289/ehp.1409567.
(155) Larkin, A.; Geddes, J. A.; Martin, R. V.; Xiao, Q.; Liu, Y.; Marshall, J. D.; Brauer, M.; Hystad, P. Global Land Use Regression Model for Nitrogen Dioxide Air Pollution. *Environmental Science & Technology* **2017**, *51* (12), 6957-6964. DOI: 10.1021/acs.est.7b01148.
(156) Novotny, E. V.; Bechle, M. J.; Millet, D. B.; Marshall, J. D. National Satellite-Based Land-Use Regression: NO2 in the United States. *Environmental Science & Technology* **2011**, *45* (10), 4407-4414. DOI: 10.1021/es103578x.
(157) Su, J. G.; Jerrett, M.; Beckerman, B.; Wilhelm, M.; Ghosh, J. K.; Ritz, B. Predicting traffic-related air pollution in Los Angeles using a distance decay regression selection strategy. *Environmental Research* **2009**, *109* (6), 657-670. DOI: https://doi.org/10.1016/j.envres.2009.06.001.
(158) Nowlan, C. R.; Liu, X.; Janz, S. J.; Kowalewski, M. G.; Chance, K.; Follette-Cook, M. B.; Fried, A.; González Abad, G.; Herman, J. R.; Judd, L. M.; et al. Nitrogen dioxide and formaldehyde measurements from the GEOstationary Coastal and Air Pollution Events (GEO-CAPE) Airborne Simulator over Houston, Texas. *Atmospheric Measurement Techniques Discussions* **2018**, 1-36. DOI: 10.5194/amt-2018-156.
(159) Nowlan, C. R.; Liu, X.; Leitch, J. W.; Chance, K.; González Abad, G.; Liu, C.; Zoogman, P.; Cole, J.; Delker, T.; Good, W.; et al. Nitrogen dioxide observations from the Geostationary Trace gas and Aerosol Sensor Optimization (GeoTASO) airborne instrument: Retrieval algorithm and measurements during DISCOVER-AQ Texas 2013. *Atmospheric Measurement Techniques* **2016**, *9* (6), 2647-2668. DOI: 10.5194/amt-9-2647-2016.
(160) Souri, A. H.; Choi, Y.; Pan, S.; Curci, G.; Nowlan, C. R.; Janz, S. J.; Kowalewski, M. G.; Liu, J.; Herman, J. R.; Weinheimer, A. J. First Top-Down Estimates of Anthropogenic NOx Emissions Using High-Resolution Airborne Remote Sensing Observations. *Journal of Geophysical Research: Atmospheres* **2018**, *123* (6), 3269-3284. DOI: 10.1002/2017jd028009.
(161) U.S. Census Burea, P. D. *Annual Estimates of Resident Population: April 1, 2010 to July 1, 2018*. April 2019. https://factfinder.census.gov/faces/tableservices/jsf/pages/productview.xhtml?src=bkmk (accessed 2019 August 1).
(162) Anonymous. *Texas State Energy Profile*. 2019. https://www.eia.gov/state/print.php?sid=TX (accessed 2019 October 7, 2019).
(163) Ports, S. S. C. o. T. *Overview of Texas Ports and Waterways*; E1.012; 2016.
(164) Darby, L. S. Cluster Analysis of Surface Winds in Houston, Texas, and the Impact of Wind Patterns on Ozone. *Journal of Applied Meteorology* **2005**, *44* (12), 1788-1806. DOI: 10.1175/jam2320.1.
(165) (HEI), H. E. I. *State of Global Air 2019*; Boston, MA, 2019. www.stateofglobalair.org.
(166) Sexton, K.; Linder, S. H.; Marko, D.; Bethel, H.; Lupo, P. J. Comparative assessment of air pollution-related health risks in Houston. *Environmental Health Perspectives* **2007**, *115* (10), 1388-1393. DOI: 10.1289/ehp.10043 PubMed.

(167) Leitch, J. W. D., T.; Good, W.; Ruppert, L.; Murcray, F.; Chance, K.; Liu, X.; Nowlan, C.; Janz. S. J.; Krotkov, N. A.; Pickering, K. E.; Kowalewski, M.; and Wang, J. *The GeoTASO airborne spectrometer project*; 92181H; **2014**.
(168) van Geffen, J. H. G.; Boersma, K. F.; Eskes, H. J.; Maasakkers, J. D.; Veefkind, J. P. TROPOMI ATBD of the total and tropospheric NO2 data products. *Royal Netherlands Meteorological Institute* **2018**. http://www.tropomi.eu (accessed 2018 12 May).
(169) Veefkind, J. P.; Aben, I.; McMullan, K.; Förster, H.; de Vries, J.; Otter, G.; Claas, J.; Eskes, H. J.; de Haan, J. F.; Kleipool, Q.; et al. TROPOMI on the ESA Sentinel-5 Precursor: A GMES mission for global observations of the atmospheric composition for climate, air quality and ozone layer applications. *Remote Sensing of Environment* **2012**, *120*, 70-83. DOI: https://doi.org/10.1016/j.rse.2011.09.027.
(170) Boersma, K. F.; Eskes, H. J.; Dirksen, R. J.; van der A, R. J.; Veefkind, J. P.; Stammes, P.; Huijnen, V.; Kleipool, Q. L.; Sneep, M.; Claas, J.; et al. An improved tropospheric NO2column retrieval algorithm for the Ozone Monitoring Instrument. *Atmosphere Measurement Techniques* **2011**, *4* (9), 1905-1928. DOI: 10.5194/amt-4-1905-2011.
(171) Lorente, A.; Folkert Boersma, K.; Yu, H.; Dörner, S.; Hilboll, A.; Richter, A.; Liu, M.; Lamsal, L. N.; Barkley, M.; De Smedt, I.; et al. Structural uncertainty in air mass factor calculation for NO2 and HCHO satellite retrievals. *Atmosphere Measurement Techniques* **2017**, *10* (3), 759-782. DOI: 10.5194/amt-10-759-2017.
(172) van Geffen, J. H. G. M.; Boersma, K. F.; Van Roozendael, M.; Hendrick, F.; Mahieu, E.; De Smedt, I.; Sneep, M.; Veefkind, J. P. Improved spectral fitting of nitrogen dioxide from OMI in the 405–465 nm window. *Atmosphere Measurement Techniques* **2015**, *8* (4), 1685-1699. DOI: 10.5194/amt-8-1685-2015.
(173) Zara, M.; Boersma, K. F.; De Smedt, I.; Richter, A.; Peters, E.; van Geffen, J. H. G. M.; Beirle, S.; Wagner, T.; Van Roozendael, M.; Marchenko, S.; et al. Improved slant column density retrieval of nitrogen dioxide and formaldehyde for OMI and GOME-2A from QA4ECV: intercomparison, uncertainty characterisation, and trends. *Atmosphere Measurement Techniques* **2018**, *11* (7), 4033-4058. DOI: 10.5194/amt-11-4033-2018.
(174) Boersma, K. F.; Eskes, H. J.; Richter, A.; De Smedt, I.; Lorente, A.; Beirle, S.; van Geffen, J. H. G. M.; Zara, M.; Peters, E.; Van Roozendael, M.; et al. Improving algorithms and uncertainty estimates for satellite NO2 retrievals: results from the quality assurance for the essential climate variables (QA4ECV) project. *Atmosphere Measurement Techniques.* **2018**, *11* (12), 6651-6678. DOI: 10.5194/amt-11-6651-2018.
(175) Boersma, K. F.; Eskes, H. J.; Brinksma, E. J. Error analysis for tropospheric NO2 retrieval from space. *Journal of Geophysical Research: Atmospheres* **2004**, *109* (D4). DOI: 10.1029/2003jd003962.
(176) Williams, J. E.; Boersma, K. F.; Le Sager, P.; Verstraeten, W. W. The high-resolution version of TM5-MP for optimized satellite retrievals: description and validation. *Geosciences Model Development* **2017**, *10* (2), 721-750. DOI: 10.5194/gmd-10-721-2017.
(177) Kleipool, Q. L.; Dobber, M. R.; de Haan, J. F.; Levelt, P. F. Earth surface reflectance climatology from 3 years of OMI data. *Journal of Geophysical Research: Atmospheres* **2008**, *113* (D18). DOI: 10.1029/2008jd010290.
(178) Eskes, H.; Geffen, J. v.; Boersma, F.; Eichmann, K.-U.; Apituley, A.; Pedergnana, M.; Sneep, M.; Veefkind, J. P.; Loyola, D. *Sentinel-5 precursor/TROPOMI Level 2 Product User Manual Nitrogendioxide*; Royal Netherlands Meteorological Institute, Ministry of Infrastructure and Water Management, 2019. http://www.tropomi.eu/sites/default/files/files/publicS5P-KNMI-

L2-0021-MA-Product_User_Manual_for_the_Sentinel_5_precursor_Nitrogen_dioxide-3.0.0-20190327.pdf (accessed October 31, 2019).
(179) Sun, K.; Zhu, L.; Cady-Pereira, K.; Chan Miller, C.; Chance, K.; Clarisse, L.; Coheur, P. F.; González Abad, G.; Huang, G.; Liu, X.; et al. A physics-based approach to oversample multi-satellite, multispecies observations to a common grid. *Atmosphere Measurement Techniques* **2018**, *11* (12), 6679-6701. DOI: 10.5194/amt-11-6679-2018.
(180) Dunlea, E. J.; Herndon, S. C.; Nelson, D. D.; Volkamer, R. M.; San Martini, F.; Sheehy, P. M.; Zahniser, M. S.; Shorter, J. H.; Wormhoudt, J. C.; Lamb, B. K.; et al. Evaluation of nitrogen dioxide chemiluminescence monitors in a polluted urban environment. *Atmospheric Chemistry and Physics* **2007**, *7* (10), 2691-2704. DOI: 10.5194/acp-7-2691-2007.
(181) American Lung Association (ALA), State of the Air-2017. **2017**. (acccessed 24 February, 2018).
(182) Steven Manson, J. S., David Van Riper, and Steven Ruggles. IPUMS National Historical Geographic Information System: Version 13.0. Minneapolis: University of Minnesota, 2018.
(183) Hennemuth, B.; Lammert, A. Determination of the Atmospheric Boundary Layer Height from Radiosonde and Lidar Backscatter. *Boundary Layer Meteorology* **2006**, *120* (1), 181–200.
(184) Dai, C.; Wang, Q.; Kalogiros, J. A.; Lenschow, D. H.; Gao, Z.; Zhou, M. Determining Boundary-Layer Height from Aircraft Measurements. *Boundary-Layer Meteorology* **2014**, *152* (3), 277-302, journal article. DOI: 10.1007/s10546-014-9929-z.
(185) McDonald, B. C.; McKeen, S. A.; Cui, Y. Y.; Ahmadov, R.; Kim, S.-W.; Frost, G. J.; Pollack, I. B.; Peischl, J.; Ryerson, T. B.; Holloway, J. S.; et al. Modeling Ozone in the Eastern U.S. using a Fuel-Based Mobile Source Emissions Inventory. *Environmental Sciences and Technology* **2018**, *52* (13), 7360-7370. DOI: 10.1021/acs.est.8b00778.
(186) Frost, G. J.; McKeen, S. A.; Trainer, M.; Ryerson, T. B.; Neuman, J. A.; Roberts, J. M.; Swanson, A.; Holloway, J. S.; Sueper, D. T.; Fortin, T.; et al. Effects of changing power plant NOx emissions on ozone in the eastern United States: Proof of concept. *Journal of Geophysical Research: Atmospheres* **2006**, *111* (D12). DOI: 10.1029/2005jd006354.
(187) Judd, L. M.; Al-Saadi, J. A.; Janz, S. J.; Kowalewski, M. G.; Pierce, R. B.; Szykman, J. J.; Valin, L. C.; Swap, R.; Cede, A.; Mueller, M.; et al. Evaluating the impact of spatial resolution on tropospheric NO2 column comparisons within urban areas using high-resolution airborne data. *Atmospheric Measurement Techniques Discuss.* **2019**, *2019*, 1-25. DOI: 10.5194/amt-2019-161.
(188) Griffin, D.; Zhao, X.; McLinden, C. A.; Boersma, F.; Bourassa, A.; Dammers, E.; Degenstein, D.; Eskes, H.; Fehr, L.; Fioletov, V.; et al. High-Resolution Mapping of Nitrogen Dioxide With TROPOMI: First Results and Validation Over the Canadian Oil Sands. *Geophysical Research Letters* **2019**, *46* (2), 1049-1060. DOI: 10.1029/2018gl081095.
(189) Pope, R. J.; Graham, A. M.; Chipperfield, M. P.; Veefkind, J. P. High resolution satellite observations give new view of UK air quality. *Weather* **2016**, *0* (0). DOI: 10.1002/wea.3441.
(190) Goldberg, D. L.; Lu, Z.; Streets, D. G.; de Foy, B.; Griffin, D.; McLinden, C. A.; Lamsal, L. N.; Krotkov, N. A.; Eskes, H. Enhanced Capabilities of TROPOMI NO2: Estimating NOX from North American Cities and Power Plants. *Environmental Science & Technology* **2019**. DOI: 10.1021/acs.est.9b04488.
(191) Ialongo, I.; Virta, H.; Eskes, H.; Hovila, J.; Douros, J. Comparison of TROPOMI/Sentinel 5 Precursor NO2 observations with ground-based measurements in Helsinki. *Atmospheric Measurement Techniques Discuss.* **2019**, *2019*, 1-18. DOI: 10.5194/amt-2019-329.
(192) Zhang, Y.; Wang, Y.; Chen, G.; Smeltzer, C.; Crawford, J.; Olson, J.; Szykman, J.; Weinheimer, A. J.; Knapp, D. J.; Montzka, D. D.; et al. Large vertical gradient of reactive nitrogen

oxides in the boundary layer: Modeling analysis of DISCOVER-AQ 2011 observations. *Journal of Geophysical Research: Atmospheres* **2016**, *121* (4), 1922-1934. DOI: 10.1002/2015jd024203.
(193) McDonald, B. C.; Dallmann, T. R.; Martin, E. W.; Harley, R. A. Long-term trends in nitrogen oxide emissions from motor vehicles at national, state, and air basin scales. *Journal of Geophysical Research: Atmospheres* **2012**, *117* (D21). DOI: https://doi.org/10.1029/2012JD018304.
(194) Houston, D.; Li, W.; Wu, J. Disparities in Exposure to Automobile and Truck Traffic and Vehicle Emissions Near the Los Angeles–Long Beach Port Complex. *American Journal of Public Health* **2014**, *104* (1), 156-164. DOI: 10.2105/ajph.2012.301120.
(195) Houston, D.; Wu, J.; Ong, P.; Winer, A. Structural disparities of urban traffic in Southern California: Implications for vehicle-related air pollution exposure in minority and high-poverty neighborhoods. *Journal of Urban Affairs* **2004**, *26* (5), 565-592. DOI: 10.1111/j.0735-2166.2004.00215.x.
(196) Houston, D.; Krudysz, M.; Winer, A. Diesel Truck Traffic in Low-Income and Minority Communities Adjacent to Ports:Environmental Justice Implications of Near-Roadway Land Use Conflicts. *Transportation Research Record* **2008**, *2067* (1), 38-46. DOI: 10.3141/2067-05.
(197) Lena, T. S.; Ochieng, V.; Carter, M.; Holguín-Veras, J.; Kinney, P. L. Elemental carbon and PM(2.5)levels in an urban community heavily impacted by truck traffic. *Environmental health perspectives* **2002**, *110* (10), 1009-1015. DOI: 10.1289/ehp.021101009 PubMed.
(198) Karner, A.; Eisinger, D.; Bai, S.; Niemeier, D. Mitigating Diesel Truck Impacts in Environmental Justice Communities:Transportation Planning and Air Quality in Barrio Logan, San Diego, California. *Transportation Research Record* **2009**, *2125* (1), 1-8. DOI: 10.3141/2125-01.
(199) Marr, L. C.; Harley, R. A. Modeling the Effect of Weekday−Weekend Differences in Motor Vehicle Emissions on Photochemical Air Pollution in Central California. *Environmental Science & Technology* **2002**, *36* (19), 4099-4106. DOI: 10.1021/es020629x.
(200) Nassar, R.; Napier-Linton, L.; Gurney, K. R.; Andres, R. J.; Oda, T.; Vogel, F. R.; Deng, F. Improving the temporal and spatial distribution of CO2 emissions from global fossil fuel emission data sets. *Journal of Geophysical Research: Atmospheres* **2013**, *118* (2), 917-933. DOI: 10.1029/2012jd018196.
(201) Zoogman, P.; Liu, X.; Suleiman, R. M.; Pennington, W. F.; Flittner, D. E.; Al-Saadi, J. A.; Hilton, B. B.; Nicks, D. K.; Newchurch, M. J.; Carr, J. L.; et al. Tropospheric emissions: Monitoring of pollution (TEMPO). *Journal of Quantitative Spectroscopy and Radiative Transfer* **2017**, *186*, 17-39. DOI: https://doi.org/10.1016/j.jqsrt.2016.05.008.
(202) Ard, K. Trends in exposure to industrial air toxins for different racial and socioeconomic groups: A spatial and temporal examination of environmental inequality in the U.S. from 1995 to 2004. *Social Science Research* **2015**, *53*, 375-390. DOI: https://doi.org/10.1016/j.ssresearch.2015.06.019.
(203) Gwynn, R. C.; Thurston, G. D. The Burden of Air Pollution: Impacts among Racial Minorities. *Environmental Health Perspectives* **2001**, *109*, 501-506. DOI: 10.2307/3454660 (acccessed 2022/11/19/).JSTOR.
(204) Tessum, C. W.; Apte, J. S.; Goodkind, A. L.; Muller, N. Z.; Mullins, K. A.; Paolella, D. A.; Polasky, S.; Springer, N. P.; Thakrar, S. K.; Marshall, J. D.; et al. Inequity in consumption of goods and services adds to racial–ethnic disparities in air pollution exposure. *Proceedings of the National Academy of Sciences* **2019**, *116* (13), 6001-6006. DOI: 10.1073/pnas.1818859116.

(205) Di, Q.; Wang, Y.; Zanobetti, A.; Wang, Y.; Koutrakis, P.; Choirat, C.; Dominici, F.; Schwartz, J. D. Air Pollution and Mortality in the Medicare Population. *New England Journal of Medicine* **2017**, *376* (26), 2513-2522. DOI: 10.1056/nejmoa1702747.
(206) Lin, S.; Munsie, J. P.; Hwang, S.-A.; Fitzgerald, E.; Cayo, M. R. Childhood Asthma Hospitalization and Residential Exposure to State Route Traffic. *Environmental Research* **2002**, *88* (2), 73-81. DOI: https://doi.org/10.1006/enrs.2001.4303.
(207) Demetillo, M. A. G.; Navarro, A.; Knowles, K. K.; Fields, K. P.; Geddes, J. A.; Nowlan, C. R.; Janz, S. J.; Judd, L. M.; Al-Saadi, J.; Sun, K.; et al. Observing Nitrogen Dioxide Air Pollution Inequality Using High-Spatial-Resolution Remote Sensing Measurements in Houston, Texas. *Environmental Science & Technology* **2020**, *54* (16), 9882-9895. DOI: 10.1021/acs.est.0c01864.
(208) Houston, D.; Ong, P.; Jaimes, G.; Winer, A. Traffic exposure near the Los Angeles–Long Beach port complex: using GPS-enhanced tracking to assess the implications of unreported travel and locations. *Journal of Transport Geography* **2011**, *19* (6), 1399-1409. DOI: https://doi.org/10.1016/j.jtrangeo.2011.07.018.
(209) Levy, J. I.; Greco, S. L.; Melly, S. J.; Mukhi, N. Evaluating Efficiency-Equality Tradeoffs for Mobile Source Control Strategies in an Urban Area. *Risk Analysis* **2009**, *29* (1), 34-47, https://doi.org/10.1111/j.1539-6924.2008.01119.x. DOI: https://doi.org/10.1111/j.1539-6924.2008.01119.x (acccessed 2022/11/19).
(210) Nguyen, N. P.; Marshall, J. D. Impact, efficiency, inequality, and injustice of urban air pollution: variability by emission location. *Environmental Research Letters* **2018**, *13* (2), 024002. DOI: 10.1088/1748-9326/aa9cb5.
(211) (HEI), H. E. I. *Traffic-related air pollution: A critical review of the literature on emissions, exposure and health effects*; 2010.
(212) Kravitz-Wirtz, N.; Crowder, K.; Hajat, A.; Sass, V. The Long-term Dynamics of Racial/Ethnic Inequality in Neighborhood Air Pollution Exposure, 1990 - 2009 *Du Bois Review: Social Science Research on Race* **2016**, *13* (2), 237-259. DOI: 10.1017/S1742058X16000205 From Cambridge University Press Cambridge Core.
(213) Rosofsky, A.; Levy, J. I.; Zanobetti, A.; Janulewicz, P.; Fabian, M. P. Temporal trends in air pollution exposure inequality in Massachusetts. *Environmental Research* **2018**, *161*, 76-86. DOI: https://doi.org/10.1016/j.envres.2017.10.028.
(214) Southerland Veronica, A.; Anenberg Susan, C.; Harris, M.; Apte, J.; Hystad, P.; van Donkelaar, A.; Martin Randall, V.; Beyers, M.; Roy, A. Assessing the Distribution of Air Pollution Health Risks within Cities: A Neighborhood-Scale Analysis Leveraging High-Resolution Data Sets in the Bay Area, California. *Environmental Health Perspectives 129* (3), 037006. DOI: 10.1289/EHP7679 (acccessed 2022/11/19).
(215) Burnett, R. T.; Stieb, D.; Brook, J. R.; Cakmak, S.; Dales, R.; Raizenne, M.; Vincent, R.; Dann, T. Associations between short-term changes in nitrogen dioxide and mortality in Canadian cities. *Arch Environ Health* **2004**, *59* (5), 228-236. DOI: 10.3200/aeoh.59.5.228-236 From NLM.
(216) McDonald, B. C.; McKeen, S. A.; Cui, Y. Y.; Ahmadov, R.; Kim, S.-W.; Frost, G. J.; Pollack, I. B.; Peischl, J.; Ryerson, T. B.; Holloway, J. S.; et al. Modeling Ozone in the Eastern U.S. using a Fuel-Based Mobile Source Emissions Inventory. *Environmental Science & Technology* **2018**, *52* (13), 7360-7370. DOI: 10.1021/acs.est.8b00778.
(217) Apte, J. S.; Messier, K. P.; Gani, S.; Brauer, M.; Kirchstetter, T. W.; Lunden, M. M.; Marshall, J. D.; Portier, C. J.; Vermeulen, R. C. H.; Hamburg, S. P. High-Resolution Air Pollution Mapping with Google Street View Cars: Exploiting Big Data. *Environmental Science & Technology* **2017**, *51* (12), 6999-7008. DOI: 10.1021/acs.est.7b00891.

(218) Harkins, C.; McDonald, B. C.; Henze, D. K.; Wiedinmyer, C. A fuel-based method for updating mobile source emissions during the COVID-19 pandemic. *Environmental Research Letters* **2021**, *16* (6), 065018. DOI: 10.1088/1748-9326/ac0660.
(219) Reardon, S. F.; Firebaugh, G. 2. Measures of Multigroup Segregation. *Sociological Methodology* **2002**, *32* (1), 33-67. DOI: 10.1111/1467-9531.00110 (acccessed 2022/11/19).
(220) Theil, H.; Finizza, A. J. A note on the measurement of racial integration of schools by means of informational concepts. *The Journal of Mathematical Sociology* **1971**, *1* (2), 187-193. DOI: 10.1080/0022250X.1971.9989795.
(221) Reardon, S. F.; O'Sullivan, D. Measures of Spatial Segregation. *Sociological Methodology* **2004**, *34* (1), 121-162. DOI: https://doi.org/10.1111/j.0081-1750.2004.00150.x.
(222) Chodrow, P. S. Structure and information in spatial segregation. *Proceedings of the National Academy of Sciences* **2017**, *114* (44), 11591-11596. DOI: 10.1073/pnas.1708201114.
(223) McDonald, B. C.; McBride, Z. C.; Martin, E. W.; Harley, R. A. High-resolution mapping of motor vehicle carbon dioxide emissions. *Journal of Geophysical Research: Atmospheres* **2014**, *119* (9), 5283-5298, https://doi.org/10.1002/2013JD021219. DOI: https://doi.org/10.1002/2013JD021219 (acccessed 2022/11/19).
(224) York, D.; Evensen, N. M.; Martínez, M. L.; De Basabe Delgado, J. Unified equations for the slope, intercept, and standard errors of the best straight line. *American Journal of Physics* **2004**, *72* (3), 367-375. DOI: 10.1119/1.1632486 (acccessed 2022/11/19).
(225) Lee, B. A.; Reardon, S. F.; Firebaugh, G.; Farrell, C. R.; Matthews, S. A.; O'Sullivan, D. Beyond the Census Tract: Patterns and Determinants of Racial Segregation at Multiple Geographic Scales. *American Sociological Review* **2008**, *73* (5), 766-791. DOI: 10.1177/000312240807300504 (acccessed 2022/11/19).
(226) Bechle, M. J.; Millet, D. B.; Marshall, J. D. Effects of Income and Urban Form on Urban NO2: Global Evidence from Satellites. *Environmental Science & Technology* **2011**, *45* (11), 4914-4919. DOI: 10.1021/es103866b.
(227) Bechle, M. J.; Millet, D. B.; Marshall, J. D. Does Urban Form Affect Urban NO2? Satellite-Based Evidence for More than 1200 Cities. *Environmental Science & Technology* **2017**, *51* (21), 12707-12716. DOI: 10.1021/acs.est.7b01194.
(228) Callahan, C. W.; Mankin, J. S. Globally unequal effect of extreme heat on economic growth. *Science advances* **2022**, *8* (43), eadd3726. DOI: 10.1126/sciadv.add3726 PubMed.
(230) Abeleira, A. J.; Farmer, D. K. Summer Ozone in the Northern Front Range Metropolitan Area: Weekend–Weekday Effects, Temperature Dependences, and the Impact of Drought. *Atmospheric Chemistry and Physics* **2017**, *17* (11), 6517-6529. DOI: 10.5194/acp-17-6517-2017.
(231) Mollner, A. K.; Valluvadasan, S.; Feng, L.; Sprague, M. K.; Okumura, M.; Milligan, D. B.; Bloss, W. J.; Sander, S. P.; Martien, P. T.; Harley, R. A.; et al. Rate of Gas Phase Association of Hydroxyl Radical and Nitrogen Dioxide. *Science* **2010**, *330* (6004), 646-649. DOI: 10.1126/science.1193030.
(232) Sander, S. P.; Finlayson-Pitts, B. J.; Friedl, R. R.; Golden, D. M.; Huie, R. E.; Keller-Rudek, H.; Kolb, C. E.; Kurylo, M. J.; Molina, M. J.; Moortgat, G. K.; et al. Chemical Kinetics and Photochemical Data for Use in Atmospheric Studies, Evaluation Number 15 in JPL Publication 06-2, Jet Propulsion Laboratory. **2006**.
(233) Perring, A. E.; Bertram, T. H.; Farmer, D. K.; Wooldridge, P. J.; Dibb, J.; Blake, N. J.; Blake, D. R.; Singh, H. B.; Fuelberg, H.; Diskin, G.; et al. The Production and Persistence of SRONO2 in the Mexico City Plume. *Atmospheric Chemistry and Physics* **2010**, *10* (15), 7215-7229. DOI: 10.5194/acp-10-7215-2010.